Trine Asklund Larssen

Prereduction of Comilog- and Nchwaning-ore

Doctoral thesis

NTNU
Norwegian University of
Science and Technology

Trine Asklund Larssen

Prereduction of Comilog- and Nchwaning-ore

Thesis for the Degree of Philosophiae Doctor

Trondheim, December 2020

Norwegian University of Science and Technology
Faculty of Natural Sciences
Department of Materials Science and Engineering

NTNU
Norwegian University of
Science and Technology

Preface

This thesis is submitted to the Norwegian University of Science and Technology (NTNU) as a partial fulfillment of the requirements for the degree of Philosophiae Doctor. The work has mainly been performed at the department of materials science and engineering (IMA) at NTNU under the supervision of Professor Tangstad within the period of August 2017-September 2020. Parts of the work were conducted at the Steel Institute at RWTH Aachen under the supervision of Professor Senk.

The main purpose of the presented work was to investigate the prereduction behavior of two commercial manganese ores through experimental work. The raw materials were provided by ERAMET Norway AS and the experiments were done by the author.

Parts of the work presented in this thesis have also been included in the following published or to be published scientific papers:

- Larssen, T.A., Tangstad, M. and Kero, I.T., 2019. Energy distribution in HC FeMn and SiMn energy vs exergy analyses. Journal of the Southern African Institute of Mining and Metallurgy, 119(12), pp.1071-1076 (paper also presented at INFACON XV)
- Larssen, T.A., Tangstad, M. and Kero, I.T., 2018. Gaseous Reduction of Mn Ores in $CO\text{-}CO_2$ Atmosphere. In Extraction 2018 (pp. 1093-1101). Springer, Cham.
- Larssen, T.A., Tangstad, M. and Kero, I.T., 2019. Energy distribution in HC FeMn and SiMn - energy vs exergy analyses. The 15th International Ferro-Alloys Congress (INFACON XV)
- Larssen, T.A., Senk, D. and Tangstad, M. Reduction of Manganese ores in $CO\text{-}CO_2$ atmospheres. *Metallurgical and materials transactions B*, 2020 (DOI :10.1007/s11663-020-02018-0)
- Larssen, T.A., Senk, D. and Tangstad, M. Reaction rate analysis of the prereduction of manganese ores in $CO\text{-}CO_2$ atmosphere (submitted to *Metallurgical and materials transactions B*, 2020)
- Larssen, T.A. and Tangstad, M. Kinetics of the prereduction zone in a ferromanganese furnace: literature review (submitted to *Journal of Mineral Processing and Extractive Metallurgy Review*, 2020)
- Larssen, T. A. and Tangstad, M., Estimation of off-gas characteristics for varying conditions in the prereduction zone of a ferromanganese furnace using mass- and energy-balances. INFACON XVI, 2021 (abstract accepted)

Acknowledgements

Abstract

Manganese ferroalloys are mainly used as an alloying element in steel production and are normally produced in submerged arc furnaces. Raw materials such as manganese ore, metallurgical coke and fluxes (and quartz for SiMn) are premixed in proper ratios and fed to the charge top. As the manganese ore descends in the furnace, it will experience increasing temperatures and an ascending furnace gas, which is largely composed of $CO(g)$ and $CO_2(g)$. In addition, the gas contains smaller amounts of water vapor and/or hydrogen, which may be introduced through the moisture in the raw materials. These gas components are thus mainly present in the upper parts of the industrial furnace. While in solid state, higher manganese and iron oxides in the ore will be reduced to MnO and Fe. The gas-solid reaction between the ore and the furnace gas is largely decisive of the energy consumption and the characteristics of the off-gas, including amount, composition and temperature. This is due to two main factors. Firstly, manganese ores have varying oxygen levels, where a high oxidation level correlates to a larger extent of the exothermic reduction of higher manganese oxides to MnO. This further implies that high oxygen ores will have a larger influence on the CO/CO_2 ratio in the gas phase. Secondly, the reaction between the ore and the furnace gas is governed by kinetics, which is affected by the characteristics of the given ore. The ore-gas kinetics is important as it decides the extent of reduction that occurs in the active region of the Boudouard reaction, which is said to be at temperatures exceeding 800°C in an industrial ferromanganese furnace. The Boudouard reaction is highly endothermic, carbon consuming, and gas producing. It further leads to an increased energy in the off-gas. As such, a higher furnace efficiency is obtained when the Boudouard reaction is minimized, i.e. the prereduction of the manganese ore is completed at temperatures below 800°C. The prereduction behavior of manganese ores has been studied previously, however there is still a lack of knowledge on the topic. This is partly credited to the high number of manganese ores, as the prereduction behavior is dependent on the ore characteristics. Furthermore, the focus of previous investigations has largely been the final step of reduction, i.e. Mn_3O_4 to MnO, where the ores were precalcined and investigated at high temperatures. As such, the information on how the ores behave at low temperatures as they are fed to the furnace is scarce. An increased understanding of this part of the furnace could potentially reveal measures leading to increased energy efficiency and lower CO_2 emissions.

This work focused on the prereduction behavior of two commercial manganese ores, i.e. Comilog- and Nchwaning-ore. Comilog is a high oxygen ore, where the majority of the ore is composed of MnO_2-minerals. Nchwaning is a semi-oxidized ore, containing various Mn_2O_3-oxides, hematite and calcite. Furthermore, Comilog and Nchwaning differ in physical properties, such as porosity. Due to these differences, the ores show different reduction behaviors, and will have different effects on energy efficiency and gas characteristics. The goal was to elucidate the reaction behavior and quantify the effect of parameters that may vary in an industrial furnace, e.g. particle size, gas composition and temperature. The results were further used to estimate the effect on the off-gas characteristics through simulated mass and energy balances.

When heated in reducing atmosphere, the tetravalent oxides in Comilog reduced to manganosite(MnO) in an overall single step. When the temperature reached approximately 580-600°C, any present MnO_2 was rapidly decomposed to Mn_2O_3, which further reduced to MnO. The reduction rate in the initial stages, i.e.

prior to rapid reduction step, was found to be proportional to the inverse particle size ($1/r_p$) and the partial pressure of CO to the power of 0.7. The reaction rate of the rapid decomposition step was merely dependent on the amount of MnO_2 that was present when threshold temperature was reached. The reduction was observed to proceed through similar reaction steps in both isothermal(400-600°C) and non-isothermal heating(25-1000°C). It is suggested that a denser structure is formed when the ore is subjected to isothermal heating, as a topochemical reaction front was formed. This was not observed in non-isothermal experiments. This may either be due to the rapid initial temperature increase, or due to the low reaction temperatures.

The manganese and iron oxides in Nchwaning ore were found to reduce at highly similar temperature ranges, however the manganese oxide reduction was initiated prior to the iron oxides in small particle sizes(< 4 mm). Trivalent oxides reduced to MnO in a single step, and the reduction of hematite subsided with the formation of wüstite(FeO). It was found that the reduction rate was proportional to the inverse particle size ($1/r_p$) and the partial pressure of CO to the power of 1.5. Carbonates were found to decompose at temperatures 800-1000°C regardless of particle size and CO-concentration. The reduction behavior of Nchwaning ore was less reproducible compared to Comilog ore, due to a more heterogeneous nature. It was found that representative investigations may not be performed using small sample sizes. Chemical analysis showed that the ore reduced through similar reaction steps when reduced isothermally(600-900°C) and non-isothermally(25-1000°C). Nchwaning ore particles did not appear to follow a shrinking core behavior, as a reaction front was not observed at any evaluated conditions.

Comilog ore is reduced at a lower temperature range compared to Nchwaning ore. Furthermore, the temperatures of Comilog ore is largely affected by the heat production accompanying the reduction, whereas Nchwaning ore largely follows the furnace temperature. This is both due to the higher oxygen level of Comilog ore, and the faster reduction rate of MnO_2 to MnO in Comilog compared to Mn_2O_3 to MnO in Nchwaning. A simple model was constructed for the reduction of Nchwaning- and Comilog-ore, which was able to describe the reduction extent with reasonable agreement. The model included the quantified dependency on the particle size and partial pressure of CO. Further, the reduction rate was described according to a first order reaction. Activation energies were determined to be 17 kJ/mol for Comilog ore and 63 kJ/mol for Nchwaning ore. Due to the different reduction behavior, it was found that the use of Nchwaning ore generally leads to an increased energy and carbon consumption, as a larger extent of the reduction occurred in the active region of the Boudouard reaction. Furthermore, this leads to a higher content of CO(g) in the off-gas.

A certain amount of moisture is present in the raw materials, which gives rise to water vapor and potentially hydrogen, where the latter depends on the kinetics of the water-gas shift reaction. Comilog- and Nchwaning-ore responded differently to the presence of hydrogen and water vapor in the gas mixture. For Comilog, it was found that hydrogen promoted the reduction rate, both when added as H_2(g) and H_2O(g) in a CO-CO_2 mixture for a fixed oxygen pressure, where the effect was larger for the former. It was found that the water-gas-shift reaction proceeded to some extent, but was not at equilibrium at temperatures between 25-750°C. The reduction of Nchwaning ore appeared to be insignificantly affected by the presence of hydrogen. As such, it is believed that the water-gas shift reaction was close to or at equilibrium. Surface moisture will rapidly evaporate at 100°C, and it was further found that the chemically bound moisture in Comilog was expelled at temperatures 200-400°C. Hence, the presence of water vapor and/or hydrogen will have a low effect on the reaction rates in an industrial furnace, as it is removed prior to the initiation

of the ore reduction. For a given charge mixture containing 10% of moisture, the energy in the off-gas will increase with increasing extent of the water-gas shift reaction. Compared to no reaction between water vapor and $CO(g)$, the energy in the off-gas is increased 1.5% relative to the total energy consumption of the furnace if the water-gas shift reaction is at equilibrium.

It was found that both ores are subjected to disintegration during heating in reducing atmosphere, where Nchwaning showed a lower extent compared to Comilog. A close correlation between the reduction extent and decrepitation was observed. The decrepitation of Comilog ore was not related to the thermal stresses resulting from the rapid decomposition step. It was found that a decreasing heating rate correlated to an increased disintegration. It is suggested that when the reduction proceeds at lower temperatures, a denser structure is formed, which in turn makes the ore more susceptible towards decrepitation.

Contents

x

List of figures

List of tables

1 Introduction

1.1 Production of manganese ferroalloys

Manganese ferroalloys are produced in submerged arc furnaces where the electricity is fed through three Söderberg electrodes installed in a triangle orientation. High carbon ferromanganese (HC FeMn) and silicomanganese (SiMn) are the two most common alloys, which mainly differs in their content of silicon. Both are used in steel industry as an alloying element and for deoxidation and desulphurization of steel products[1]. The raw materials are typically manganese ore and/or sinter, coke as reductant, and fluxes (and quartz for SiMn). Premixed materials enter the furnace from the top at ambient temperature, from which they descend towards increasing temperatures in the lower part. The furnace can be viewed as two separate zones, as illustrated in Figure 1.1. The materials are in solid state while they are in the prereduction zone. As the name indicates, the main feature of this zone is the reduction of the manganese oxides that constitutes the ore. The manganese exists in the ore as oxides, where the manganese mainly has a valence of 3+(Mn_2O_3) or 4+(MnO_2). These higher oxides will reduce to a valence of 2+(MnO) by reacting with the $CO(g)$ present in the furnace gas. In addition to the manganese oxide reduction, iron oxides are reduced to metallic iron, carbonates are decomposed, and moisture is evaporated in the prereduction zone.
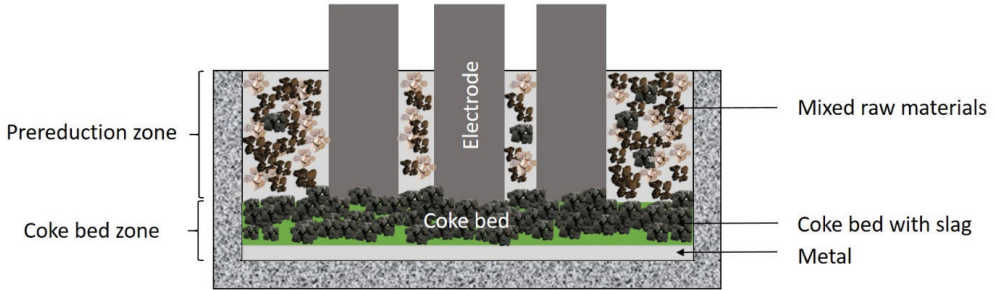
Figure 1.1: Illustration of a ferromanganese furnace

At higher temperatures, the materials will melt and form a slag phase. This part of the process is referred to as the coke bed zone and it is located in the lower parts of the furnace, close to the electrode tips. MnO and SiO_2 will be reduced from the liquid slag by solid carbon as shown in reaction 1.1 and 1.2, respectively. The reactions produce CO-gas that will ascend in the furnace and function as reductant in the prereduction zone. The energy consumption of the coke-bed zone is largely fixed for the production of a specific alloy composition, implying that variations in energy consumption, and thus the energy efficiency, mainly occurs in the prereduction zone.

$$MnO(l) + C = Mn(l) + CO(g) \qquad \Delta H^0_{298} = 259\ kJ \qquad 1.1$$
$$SiO_2(l) + 2C = Si(l) + 2CO(g) \qquad \Delta H^0_{298} = 751\ kJ \qquad 1.2$$

1.1.1 Prereduction zone

The raw materials will always contain a certain amount of water, which could be at a surface level or chemically bound in the material. Certain materials are stored outside on a daily basis, which implies that the moisture content can show large variations depending on weather change. The surface temperature of the furnace should always be higher than 100°C, and as a result evaporation of water will take place. The amount of surface moisture will affect the overall energy consumption of the furnace as evaporation is an endothermic process, and it may have a potential impact on the temperature gradient of the furnace. According to Swamy and Robertson, a higher content of free moisture will merely lead to a lower off-gas temperature and have no further impact on the system[2]. Higher temperatures are required to vaporize chemically bound water, e.g. 400°C, and it may as such be of further significance in the system. The water vapor may further react according to the water-gas shift reaction, as shown in reaction 1.3, which proceeds to the right at temperatures up to approximately 800°C. A certain amount of hydrogen gas is always detected in the off-gas system of industrial furnaces[3], which is likely a product of this reaction. Hydrogen may also enter the system through volatiles in the coke, or from the electrode paste. The potential influence of hydrogen and water is further discussed in section 2.2.2.

$$H_2O(g) + CO(g) = H_2(g) + CO_2(g) \qquad \Delta H^0_{298} = -41 \ kJ \qquad 1.3$$

The manganese in the ores exists as different minerals of varying oxidation level, including pyrolusite(MnO_2), bixbyite(Mn_2O_3) and hausmannite(Mn_3O_4). These oxides will be reduced stepwise to manganosite(MnO) by the CO-gas ascending from the smelting zone according to reactions 1.4-1.6. Reduction of MnO to metallic manganese by CO-gas is not thermodynamically feasible. The reduction of higher manganese oxides by CO-gas is highly exothermic, and the reactions will thus contribute to heat the charge material. This implies that a higher oxygen level of the ore will result in a lower energy consumption as less electric energy is required for heating.

$$MnO_2 + \frac{1}{2}CO(g) = \frac{1}{2}Mn_2O_3 + \frac{1}{2}CO_2(g) \qquad \Delta H^0_{298} = -101 \ kJ \qquad 1.4$$

$$\frac{1}{2}Mn_2O_3 + \frac{1}{6}CO(g) = \frac{1}{3}Mn_3O_4 + \frac{1}{6}CO_2(g) \qquad \Delta H^0_{298} = -29 \ kJ \qquad 1.5$$

$$\frac{1}{3}Mn_3O_4 + \frac{1}{3}CO(g) = MnO + \frac{1}{3}CO_2(g) \qquad \Delta H^0_{298} = -17 \ kJ \qquad 1.6$$

The $CO_2(g)$ produced in the final step of reduction, reaction 1.6, may react with solid carbon if the temperature is sufficiently high. The reaction between $CO_2(g)$ and solid carbon to form two moles of CO-gas is known as the Boudouard reaction(reaction 1.7). In a manganese furnace, the Boudouard reaction is catalyzed by the presence of alkalis, causing it to have significant rates at temperatures as low as 800°C[4]. This means that in this temperature region, the overall reduction of Mn_3O_4 is by solid carbon according to reaction 1.8. As the Boudouard reaction is highly endothermic and carbon consuming, the extent of the reaction has a great impact on the overall efficiency of the process.

$$\frac{1}{3}C + \frac{1}{3}CO_2(g) = \frac{2}{3}CO(g) \qquad \Delta H^0_{298} = 57 \ kJ \qquad 1.7$$

$$\tfrac{1}{3}Mn_3O_4 + \tfrac{1}{3}C = MnO + \tfrac{1}{3}CO(g) \qquad\qquad \Delta H^0_{298} = 40\ kJ \qquad\qquad 1.8$$

It may be mentioned that while the $CO_2(g)$ released from the reduction of Mn_3O_4 is the main source of reactant in the Boudouard reaction, all $CO_2(g)$ released at these temperature may potentially react with the solid carbon. The manganese materials fed to the furnace contain a considerable amount of iron oxides, which similar to the manganese oxides will reduce in subsequent steps (Fe_2O_3-Fe_3O_4-FeO-Fe) by the CO-gas ascending from the melting zone and release $CO_2(g)$. In addition, limestone and dolomite are commonly used fluxes, which also produce to $CO_2(g)$ when decomposed.

1.2 Scope of thesis

This work is part of the research activities in the HighEFF center, which is a collaborative effort in the Norwegian industry to increase energy efficiency and decrease climate gas emissions. The thesis will present parts of the work dedicated to the manganese ferroalloy process within the center.

The efficiency of a ferromanganese furnace, both in terms of materials and energy, is largely determined by the behavior of the materials in the prereduction zone. The main purpose of this work will be to increase the knowledge and understanding of how manganese ores behave while in the prereduction zone, and the effects on off-gas characteristics. An experimental investigation simulating the industrial furnace in small scale will form the basis of the work. Two commercial manganese ores will be investigated under varying conditions, where evaluated parameters will include ore particle size, gas atmospheres, and temperature. Kinetic analysis of the experiments will be performed to evaluate the trends and quantify the variables' effect on the reaction behavior. Finally, mass and energy balances will be used to estimate the effect of the results on the industrial operation.

The thesis includes the following chapters:

Chapter 2 presents the relevant theoretical background and existing literature. This includes characteristics of manganese ores, and the reduction behavior of various manganese sources in gas atmospheres. The main focus is CO-CO_2 atmospheres in accordance with the main gas components in an industrial furnace, however some attention is paid to atmospheres containing $H_2(g)$ and $H_2O(g)$. The basis of gas-solid reaction analysis is also covered. Lastly, mass and energy balances constructed for the production process of HC FeMn and SiMn are presented.

Chapter 3 describes the characteristics of the utilized materials, the details of the equipment, and the specific procedure used to obtain the experimental data regarding manganese ore prereduction behavior. The experiments were conducted using two different thermogravimetric furnaces. The majority of the work was conducted at NTNU, whereas parts (isothermal experiments) were performed at RWTH Aachen. Equipment specifics and procedure for the two set-ups are presented separately.

Chapter 4 presents the results obtained through the experimental work performed in this study. The chapter has been divided into two main sections, correlating to the two industrial manganese ores that were

investigated, i.e. Comilog ore and Nchwaning ore. These sections are further divided according to the different experimental series: non-isothermal reduction in CO-CO_2 atmosphere, isothermal reduction in CO-CO_2 atmosphere, non-isothermal reduction – effect of inert material, and lastly non-isothermal reduction – effect of H_2/H_2O. Thermogravimetric curves, decrepitation extents, and characterization of reduction products are presented consecutively for each individual series.

Chapter 5 provides the discussion of the experimental procedures and results of this work. The chapter is comprised of four main sections. In the first section, the observed reaction steps and mechanisms are presented for the two ores. Section two elaborates on the reaction rate behavior, where the effect of the evaluated variables is quantified. This section includes the results of the model that was found to satisfactorily describe the reduction data. Subsequently, a section has been attributed to the decrepitation behavior. Lastly, the results are discussed in relation to the industrial operation, in a section named industrial significance.

Finally, **Chapter 6** will finalize the thesis by summarizing the main observations and conclusions. In addition, recommendations for further work are included.

2 Literature review

This chapter comprises the theoretical background and existing literature relevant for the work conducted in this study. According to the scope of this work being the behavior of manganese ores in the prereduction zone, the main focus of the following chapter is existing literature on the reduction behavior of different manganese ores in different particle sizes in CO-CO_2 atmospheres. In addition, attention has been paid to the potential effect of hydrogen gas and/or water vapor and the role of iron oxides. In order to determine kinetic parameters and reduction mechanisms, the results will be interpreted mathematically. Thus, existing theory of tools for gas-solid reaction analysis are covered. The chapter is finalized with the presentation of mass and energy balances for the production of HC FeMn and SiMn.

2.1 Manganese ores

Chemical composition and mineralogy

Ores that contain more than 35% of manganese are classified as manganese ores. Further, ores with manganese content in the range of 38-55% are categorized as metallurgical grade ores. The manganese in the ores exists in the form of minerals, and the mineralogy is complex as manganese can be found in both divalent, trivalent, and tetravalent oxidation state. The most common manganese minerals can be seen in Table 2.1, reprinted from Olsen et al[3]. Despite the wide range of manganese minerals in existence, studies show that certain minerals are observed to a much higher extent than others. This includes pyrolusite, braunite, hausmannite and bixbyite. Excluding braunite, this gives MnO_2, Mn_2O_3 and Mn_3O_4, which is how the oxidation levels of manganese usually is reported in reduction studies.

Table 2.1: Most common manganese minerals presented by name, chemical formula, and manganese content[3].

Mineral	Chemical formula	Mn content
Pyrolusite	MnO_2	63.2
Braunite	$3(Mn,Fe)_2O_3 \cdot MnSiO_3$	48.9[5]-56.1[6]
Braunite II	$7(Mn,Fe)_2O_3 \cdot CaSiO_3$	52.6[6], [7]
Manganite	$\Upsilon\text{-}MnOOH$	62.5
Psilomelane	$(K,Ba)(Mn^{2+}Mn^{4+})_8O_{16}(OH)_4$	48.6-49.6[5]
Cryptomelane	$(K,Ba)Mn_8O_{16} \cdot xH_2O$	55.8-56.8[5]
Hollandite	$(Ba,K)Mn_8O_{16} \cdot xH_2O$	42.5
Todorokite	$(Ca,Na,K)(Mn^{2+}Mn^{4+})_6O_{12} \cdot xH_2O$	49.4-52.2[5]
Hausmannite	$(Mn,Fe)_3O_4$	64.8[7]
Jacobsite	Fe_2MnO_4	23.8[6]
Bixbyite	$(Mn,Fe)_2O_3$	55.6[6]
Rhodochrosite	$MnCO_3$	47.6

The ores are extracted from land-based deposits, of which some of the most important ones are located in South Africa, Australia, Gabon, Brazil, China and India. The Kalahari manganese field in South Africa is

the world's largest manganese deposit, and the origin of several different commercial ores, such as Nchwaning (sometimes referred to as Assmang in Norwegian studies[8]), Mamatwan and Wessels. In spite of originating from the same deposit, these ores may differ significantly in mineralogy[7], [9]. Mamatwan has a high content of carbonates and the manganese-bearing mineral is mainly braunite. Wessels is an oxide ore containing braunite and braunite II, potentially minor amounts of hausmannite, bixbyite and hematite. Other deposits of great importance are the mine in Gabon, from which the commercial ore known as Comilog ore originates, and the Groote Eylandt in Australia from where BHP ore originates. Table 2.2 presents an overview of reported mineralogy of some commercial manganese ores, which shows that many ores exhibit complex mineralogy.

Table 2.2: Mineralogy of common manganese ores

Ore	Reported minerals
Comilog/Gabon	• Pyrolusite, Cryptomelane[10] • Cryptomelane, Nsutite, Pyrolusite, Lithiopherite, Quartz, Goethite, Ramsdellite, Hematite, Gibbsite[11]
CVRD	• Nsutite, Todorokite, Kaolinite, Cryptomelane, Hematite, Lithiophorite, Pyrolusite, Quartz, Gibbsite[11]
Mamatwan	• Braunite, Hausmannite, Hematite, Manganite[10]
Nchwaning(Assmang)	• Braunite I, Braunite II, Bixbyite, Calcite, Kutnahorite, Hausmannite, Hematite, Barite, Manganite, Marokite[12] • Braunite II[10]
Wessel	• Bixbyite, braunite, manganite, hausmannite, calcite[13] • Bixbyite, manganite, hausmannite, calcite[11]
Wessel (ASM) – calcined	• Braunite, braunite II, bixbyite, hausmannite, hematite[14]
Groote Eylandt (BHP)	• Pyrolusite (+ silica inclusions)[13] • Pyrolusite, cryptomelane[10] • Pyrolusite, cryptomelane, quartz[14] • Pyrolusite, iron silica, silica[11]
Groote Eylandt (BHP) - calcined	• Bixbyite, pyrolusite, quartz, hausmannite[14]
Gloria	• Braunite I (+carbonates)[12] • Rhodochrosite[10]
Namibian ore	• Braunite, pyrolusite, quartz, barite[14]

It is mentioned that previous studies show that characterization of mineralogy in manganese ores is not a straight-forward procedure. This is due to the high number of constituting minerals, as well as similar chemical composition of several of the minerals, cation substitution, heterogeneity of the ore, and geometric effects, such as porosity and cracks. Furthermore, according to Varentsov and Grasselly, several of the minerals are frequently intergrown[15]. Sørensen et al.[16] showed that while XRD identified merely

pyrolusite in Groote Eylandt ore, further inspection in optical microscope and SEM gave considerable abundance of both pyrolusite, cryptomelane, iron alumo-silicates, and quartz. It was further observed that XRD identified bixbyite as main mineral of Wessels ore, whereas SEM and EDS investigations showed that the mineral identified as bixbyite was in fact braunite in two different modifications.

When exposed to the conditions of the prereduction zone, the manganese oxides in the ore will reduce according to reaction 1.4-1.6. The extent of each reaction, and thus heat produced, is given by the oxidation level of the ore. Some ores have a relatively high oxygen level, which would be beneficial in terms of the energy consumption, as excessive amounts of heat are released, thus minimizing the electrical energy need. Having the manganese content existing as MnO_2 compared to Mn_3O_4 may reduce the energy consumption of the process with 600 kWh/ton HC FeMn[17]. Nonetheless, large amounts of oxygen released could lead to an unstable furnace operation in closed furnaces, and it is thus common in industrial practice to use a combination of high oxygen level ores and low oxygen level ores. CVRD, Comilog, and Groote Eylandt (BHP) are ores with a high oxygen level, close to MnO_2, and a low content of iron oxides. In general, South African ores can be classified as semi-oxidized ores, with an oxygen level close to that of Mn_2O_3, while also having a higher content of iron compared to the highly-oxidized ores[12]. The use of Comilog, a high oxygen ore, in industrial operation was evaluated by Tangstad et. al[10]. The content of Comilog ore was increased from 15% to 50% by substituting low oxygen manganese sources. This resulted in a higher $CO_2(g)$ concentration in the off-gas due to the higher oxygen level and a decrease in the power consumption, of which the latter may be observed in Figure 2.1.
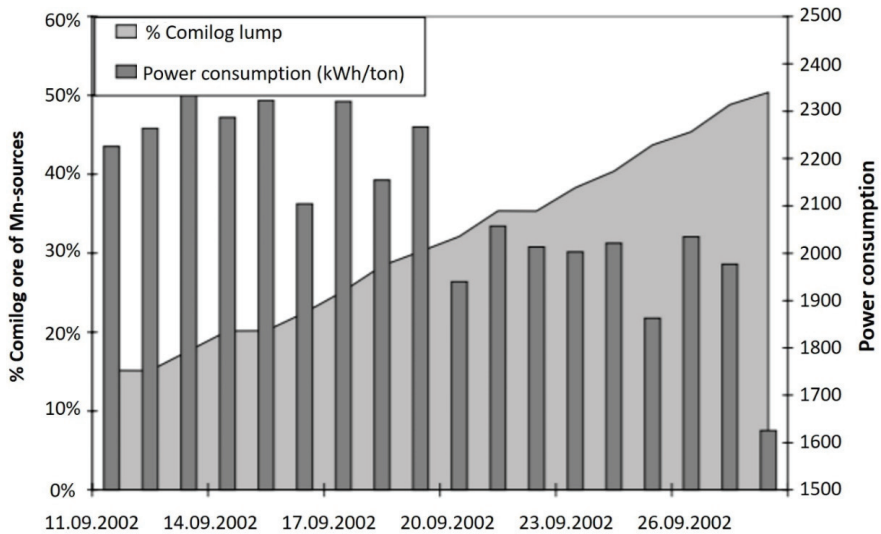
Figure 2.1: Decrease of power consumption with increasing amount of Comilog ore in manganese raw materials[10]

In addition to manganese, the ores always contain a certain amount of iron, which may typically exist as hematite (Fe_2O_3). Further, iron atoms are often found partially substituting manganese atoms in certain minerals, e.g. bixbyite being $(Mn,Fe)_2O_3$[11]. The manganese to iron ratio of the ores is an important parameter, where a weight ratio of 7.5 is required to produce a standard ferromanganese alloy with 78 wt% Mn[3]. Other components of considerable size in the ores are typically oxides as CaO, MgO, SiO_2 and Al_2O_3, of which the two former are categorized as basic oxides and the two latter as acidic oxides. The ratio of basic oxides to acidic oxides is known as the *basicity*. The basicity will describe certain physical properties of the slag, such as viscosity, which is important for an optimal alloy-slag separation during tapping. Today's industrial practice usually involves a basic slag. This can be obtained either by using an appropriate combination of basic and acidic ores, or by addition of fluxes (dolomite or limestone) to increase the content of basic oxides. It has also been seen that the amount of MnO in the end slag, and thus Mn in the alloy, is determined by the slag chemistry (and temperature), where a higher basicity gives a lower MnO content in the slag[18], [19]. As such, basic slags help to secure a good furnace operation, and optimizes the manganese yield. Nonetheless, in the case of silicomanganese production, an increasing content of basic oxides will at the same time have a retarding effect on the activity of SiO_2. Oxides as K_2O, BaO, and TiO_2 may be present in the ore in minor amounts. Further, important trace elements are typically phosphorous (P) and sulphur (S). Phosphorous is of particular importance, as all P in the ore will end up in the alloy, whereas sulphur will remain in the slag as manganese sulphide (MnS). Blended manganese sources are usually necessary in order to meet the phosphorous requirement of the produced alloy, where South-African ores generally has a low content[3].

The bulk chemical composition of some of the more common manganese ores is shown in Table 2.3. In addition to manganese ores, sinter and HC FeMn slag also represent sources of manganese in the production of ferromanganese alloys. As these materials remain relatively stable in the prereduction zone, not much attention has been paid. Nonetheless, the chemical composition of Gabonese sinter and HC FeMn slag have been included in the table. Sinter is high quality ore fines that have been agglomerated through a sintering process to ensure good furnace permeability. This process cause alterations to the chemical composition, mainly by decreasing the oxygen level of manganese. HC FeMn slag is the byproduct in production of high-carbon ferromanganese alloys, and as it still contains high levels of MnO it is often used as a raw material in the production of silicomanganese.

In respect to the chemical compositions, it should be mentioned that ores are heterogeneous. Chemical analysis of 10 lumps of Groote Eylandt ore reported by Berg[14] showed a variation in manganese content between 29.7-56.1 % and iron content between 1.1-26.3%. Similarly, 10 lumps of Wessels ore showed 40.5-56.7% for manganese and 5.1-17.3% for iron.

Physical properties

In terms of furnace operation, granulometry of the ore is an important aspect. The permeability of the charge depends on the distribution and concentration of fines. If the charge contains considerable amounts of fines, the gas will encounter difficulties to flow evenly throughout the charge layer and may rather form channels. This may inhibit evaporation of water and reduction of oxides at an early stage, which could give an

increased energy consumption due to off-gas with high temperature and CO-content. There are limitations on size fractions that can be fed to the furnace, and as such, many plants have separate sinter plants that agglomerate the generated fines. According to Pochart et al. [20], in order to maintain a stable operation, the manganese sources added to a sealed HC FeMn furnace should only have an oxygen level exceeding 12% above MnO, and the amount of particles smaller than 6 mm should be lower than 15%. From Figure 2.2, it can be seen that Comilog exhibits a widespread granulometry ranging from smaller than 5 mm to larger than 80 mm, where 80% is smaller than 40 mm.

Table 2.3: Chemical composition of commercial manganese ores

	Gabonese ore [8]	CVRD ore [8]	Nchwaning ore [8], [12]	Gloria ore [12]	Groote Eylandt ore [21]	Gabonese sinter [10]	HC FeMn slag[22]
Mn, tot	51.7	44.1	42.7-48.9	35.2-36.2	45.2	58.5	27.3
MnO_2*	78.2	63.7	29.1-35.3	17.2-24.8	67.4	19.7	-
Fe, tot	1.3	7.6	6.5-12.4	5.4-6.3	3.3	3.5	-
SiO_2	4.4	4.9	4.7-7.5	6.1-6.3	10.6	7.0	25.5
Al_2O_3	5.3	7.4	0.3-0.4	0.2-0.3	5.1	6.5	11.4
MgO	0.1	0.1	0.5-1.3	3.7-4.1	0.1	0.0	7.5
CaO	0.1	0.2	7.1-8.9	14.2-14.9	0.1	0.1	18.5
CO_2	0.1	0.1	2.7-4.3	16.9-17.8	0.2	0.0	-
S	-	0.1	0.0-0.4	0.1-0.2	0.01		0.5
P	-	0.01	0.0-0.1	0.0	0.07	0.1	
H_2O	8.7	2.5	0.1-0.2	0.1-0.2	-	1.5	

*All excess oxygen relative to MnO is reported as MnO_2
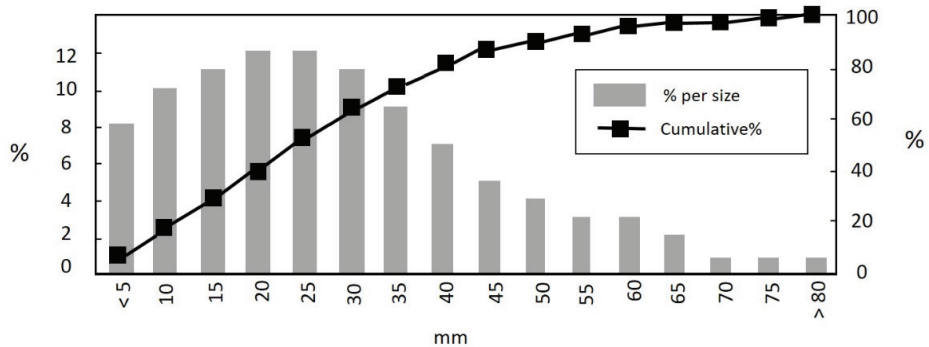
Figure 2.2: Grain size distribution of Comilog ore. Figure after Pochart et al.[20]

The mechanical strength of the ore will determine the amount of fines that are generated. Fines can be generated both in cold state, i.e. during mining and transportation, or in the furnace at high temperatures and reducing atmosphere. Generation of fines during heating, also known as decrepitation, may be expressed through the cohesion index and the thermal abrasion index. The cohesion index is defined as the fraction of ore sample that remains in original size after heating in reduced atmosphere. For determination of thermal abrasion index, the reduced sample will be tumbled in a Hannover drum and subsequently sieved, which will then simulate the strength of the ore in the furnace. Figure 2.3 shows the thermal abrasion index (TI) of different manganese materials (ores and sinter) in particle size 10-15 mm reduced in 70%CO-30%CO$_2$ from room temperature up to 1100°C[10]. The results show that Mamatwan and Nchwaning (Assman) ore exhibit a higher mechanical strength compared to Comilog ore and Comilog sinter, as less fines are generated. In general, it was seen that the largest amount of fines, i.e. lowest mechanical strength, corresponded to the more porous ores. Visser et al. [12] did similar testing on Nchwaning and Gloria South-African ores. After heating and reduction, approximately 50-65% of the ores remained at a size fraction larger than 5 mm (TI5), which correlates with the high-strength ores in Figure 2.3. Thus, porosity and mechanical strength are closely related parameters, and it may be mentioned that highly-oxidized ores generally have a higher porosity compared to semi-oxidized ores[8]. The porosity of some commercial manganese ores is presented in Table 2.4.
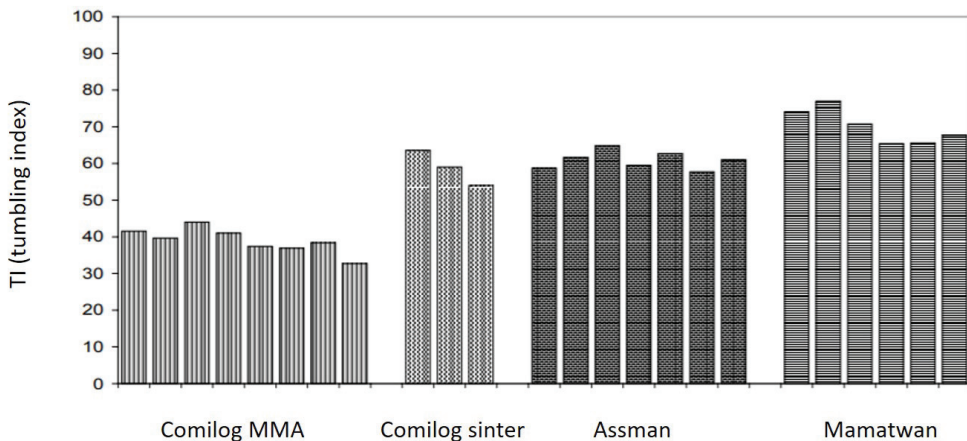
Figure 2.3: Variation in strength shown by the thermal abrasion index (TI) after heating and tumbling of different manganese ores and sinter[10]

Faria with colleagues published several papers from investigations on the decrepitation behavior of manganese ores, mainly Brazilian[23]–[26]. Evaluation of three different Brazilian ores (two oxide (mainly cryptomelane) ores and one silcate-carbonate) and one South African (Wessels) ore showed that the highest decrepitation indexes were observed for ores that experienced some mineralogical phase transformation

during heating. The results indicated three main factors responsible for the decrepitation of manganese ores: moisture elimination, decomposition of hydrated minerals, and decomposition of higher oxides and braunite. It was suggested that the thermal decompositions of manganese oxides were the main contributing factor. This was supported by Biswas et al., who investigated primary reasons for decrepitation of low grade manganese ore lumps from Indian mines[27].

Table 2.4: Porosity for some commercial manganese ores[21], [28]

Ore	Porosity [%]
Comilog lump	30-50
Comilog crushed	15-25
CVRD	38.5
Groote Eylandt	9.4
Nchwaning	0.1
Gloria[12]	< 7
Wessel	2-10

The heat exchange between raw materials and hot gases in the prereduction zone is dependent on the ores thermophysical properties, such as thermal conductivity, thermal diffusivity, thermal expansion and heat capacity. These parameters were investigated for solid ore samples, as well as compacted powder, by a Laser laser-flash method by Ksiazek et. al. [29], [30]. It was found that the thermal diffusivity of manganese ores was strongly influenced by temperature, mineralogy, and to some extent porosity. All ores exhibited a decreasing diffusivity with increasing temperature. Semi-oxidized ores showed a gradual decrease, whereas highly oxidized ores experienced a rapid decrease at 600°C, likely related to the decomposition of MnO_2 to Mn_2O_3. The bulk thermal conductivity of Comilog- and Nchwaning-ore was found to be affected by the particle size fraction. It was suggested that this correlated to the bulk void fraction, where the conductivity decreased with increasing void fraction. Obtained values were used to calculate temperature behavior of clusters and single particles. Figure 2.4 shows the result of the simulation of the upper part of the prereduction zone, i.e. when room temperature ore particles are exposed to the hot (250-300°C) gases in top of the burden. The figure (left) shows that the two quartz types and Wessels ore exhibit a high thermal diffusivity as these materials have nearly reached the ambient temperature while Groote Eylandt ore remains at 100°C. It is also observed that a lower thermal diffusivity correlates to a higher temperature gradient within the material.

2.2 Gaseous reduction of manganese ores and oxides

As the energy consumption attributed to the coke-bed zone is largely fixed for a given alloy composition, variations in energy efficiency in a ferromanganese furnace mainly arise from the behavior in the prereduction zone, which will generally depend on two characteristics. Firstly, the oxygen level of the ore determines the extent of exothermic heat produced from reactions 1.4-1.6. The correlation between oxidation level and overall power consumption was evident from Figure 2.1, which showed the influence of high oxygen Comilog ore on behalf of low oxidized sources in industrial furnace operation. Secondly,

the energy efficiency is strongly dependent on what is known as the CO-reactivity of the ores, which reflects how easily the ore is reduced in CO-atmosphere, i.e. the kinetics of reactions 1.4-1.6. The minimum carbon- and energy consumption will be obtained when oxides in the manganese ore are fully reduced to MnO and Fe prior to entering the active region of the Boudouard reaction. For convenience, it is repeated that the presence of alkalis in the ferromanganese furnace catalyzes the Boudouard reaction, causing the threshold temperature for sufficient kinetics to be approximately 800°C[4]. The CO-reactivity of ores and ore blends in industrial practice is often quantified through the *prereduction degree*, which is usually defined as the amount of released $CO_2(g)$ from the reduction of Mn_3O_4 and Fe_3O_4 and decomposition of carbonates that does not react with solid carbon through the Boudouard reaction.
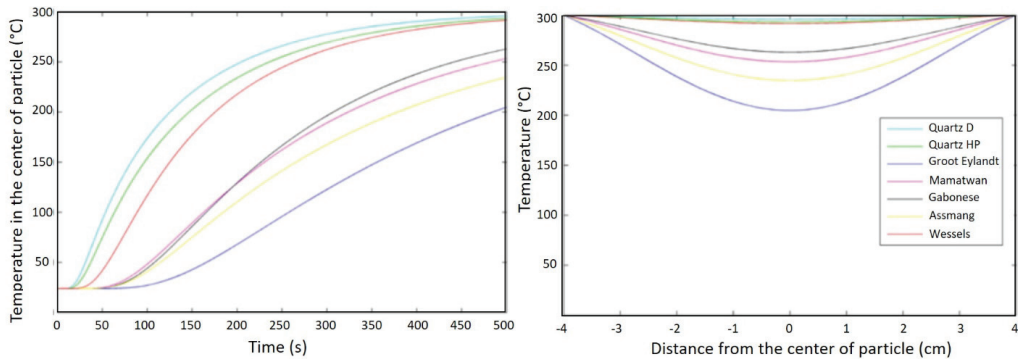
Figure 2.4: Simulations of temperature development in the center of room temperature ore particles (4 cm) exposed to hot gases of temperature 250-300C (left), and temperature profile of particle (right) after 500 sec.[30]

The equilibrium stability of the manganese oxides will be determined by temperature and the oxygen pressure. Figure 2.5 shows the stability of manganese and iron oxides as a function of oxygen partial pressure. The $Mn-O_2$ system is superimposed on the $Fe-O_2$ system, implying that the relations are valid for pure oxides. According to the diagram, higher manganese oxides should easily be converted to MnO at low temperatures in air, and even more easily in reducing atmosphere. At an oxygen pressure of 1 atm, MnO_2 decomposes at approximately 486°C, whereas Mn_2O_3 decomposes at 792°C. It can be mentioned that this figure gives higher temperatures compared to the diagram presented by Olsen et al[3], which is believed to be due to the use of other databases for the equilibrium constants.

The main components of the furnace gas in a conventional manganese ferroalloy furnace is CO(g) and $CO_2(g)$, which coexist at atmospheric pressure. This implies that it is fair to assume that $p(CO) + p(CO_2) = 1$ atm. The equilibrium pressure of oxygen, and thus the reduction potential of the gas, is defined by the Boudouard reaction (equation 1.7). Figure 2.6 shows the oxygen pressure given by equation 1.7 as a function of temperature calculated from HSC Chemistry 10[17]. At temperatures below 700°C, the reaction is shifted to the left, implying that any present CO(g) will decompose to solid carbon and $CO_2(g)$. The reaction proceeds to the right at temperatures exceeding 700°C, meaning that solid carbon and $CO_2(g)$ will react to form CO(g). It should be mentioned that industrially closed Mn-ferroalloy furnaces typically have

an off-gas temperature below 500°C, where considerable concentrations of CO are found in the off-gas. Thus, equilibrium between gas phase and solid carbon is not established at low temperatures.
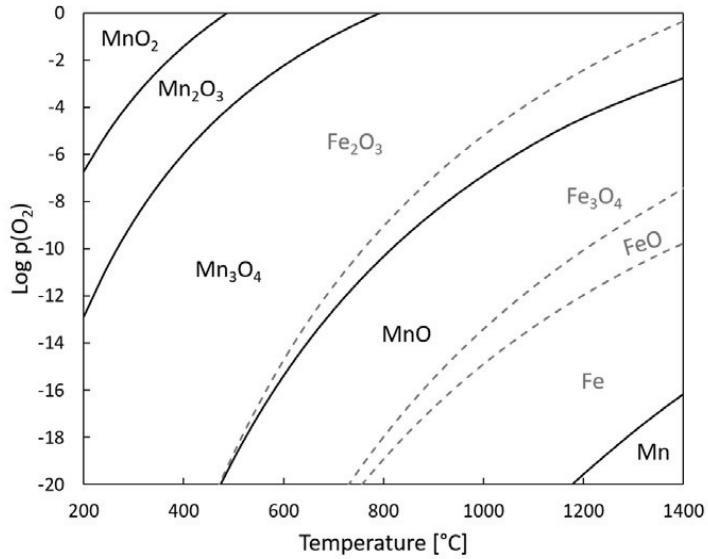
Figure 2.5: Calculated equilibrium relations of the Mn-O₂ system and the Fe-O₂ system. The systems are superimposed. Values from HSC 9[17]
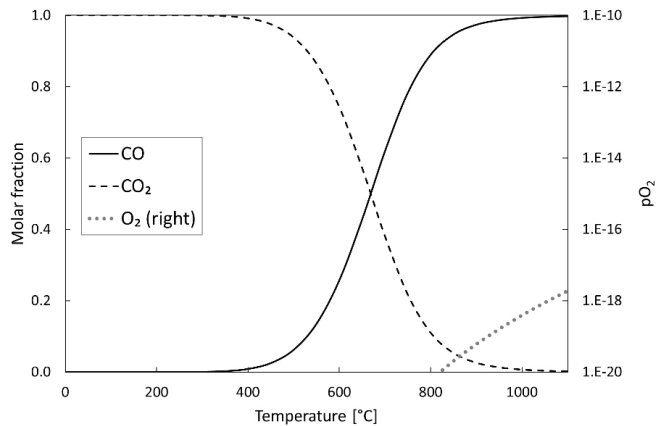
Figure 2.6: Equilibrium molar fractions of CO and CO₂ according to the Boudouard reaction with corresponding oxygen pressure in a gas atmosphere consisting of CO-CO₂. Values from HSC 9[17]

The equilibrium constant (CO_2/CO ratio) for the reduction of Mn_3O_4 to MnO by CO is $1.1 \cdot 10^4$ at 800°C, however laboratory studies show that the majority of the reduction occurs at temperatures exceeding 800°C for several types of ores[8], [12]. Industrial data reporting carbon consumption and CO/CO_2 ratio in the off-gas also support that a considerable amount of the reduction of manganese ores occur at temperatures exceeding 800°C. The degree of prereduction has previously been calculated for three industrial furnaces over a period of six years (1998 to 2004), where it was found that the extent of gas reduction was typically between 10 to 40%[31]. However, a prereduction degree of 50 to 60% was also observed occasionally. The influence of Comilog ore on furnace operation was evaluated at a closed furnace at Eramet Norway Sauda. The content of the high-oxygen ore Comilog was increased from 10 to 37% on behalf of BHP ore, another high-oxygen level ore. Thus, the total oxygen level of the charge did not change considerably, whereas the degree of prereduction increased from a medium to a high level due to the higher reactivity towards CO-gas of Comilog ore compared to BHP ore[32]. Thus, it is clear that the reduction of manganese ores is determined by kinetics rather than thermodynamics.

As the reduction kinetics of manganese ore has a great impact on the efficiency of the furnace process, both in terms of material consumption (carbon) and electrical energy consumption, numerous studies have been reported on the topic during the last decades. Evaluated atmospheres include hydrogen, argon and methane, however the majority of studies are dedicated to CO-containing atmospheres, as it simulates the industrial practice. The following section evaluates available literature on reduction behavior of manganese ores, with the focus on reduction by $CO(g)$.

2.2.1   Reduction in presence of $CO(g)$

Reported studies of manganese ore prereduction include both isothermal and non-isothermal setups. Non-isothermal studies have generally been used to assess the CO-reactivity in terms of oxygen released at temperatures exceeding 800°C. The ores are heated in reducing atmosphere, simulating the industrial practice, and analysed for their oxygen content at a given target temperature. These studies generally provide little or no discussion of any kinetics or mechanisms for different types of ores. A majority of the published studies have been performed under isothermal conditions, as this simplifies the mathematical interpretation of the results and determination of reaction mechanisms. Within these studies, ores with a high oxygen level were frequently calcined prior to investigation of reduction kinetics in order to have the initial oxide be of lower valence, i.e. Mn_2O_3 or Mn_3O_4. This was done to minimize the complexity of the multistep reaction sequence, in addition to ensuring a more stable temperature during the experimental runs. However, it is mentioned that several of the studies show that the prereduction behavior of manganese ores is dependent on the pretreatment of the material, such as calcination temperature, time, and atmosphere[32]–[34]. Results and observations obtained from both temperature regimes will be presented.

One of the earliest in-depth studies on reduction of manganese ores in CO-atmosphere is the Dr. ing dissertation of Berg, who investigated the mineral's potential influence on the reduction behavior of manganese ores[14]. The evaluated ores were Groote Eylandt (BHP), a Wessels type ore (ASM), and a Namibian (NAM) ore. The majority of the work was executed on ore lumps in size 5-10 cm crushed and sieved to pieces smaller than 2 cm. The ore pieces were calcined at 800°C in a muffle furnace prior to reduction experiments in order to decompose MnO_2 to Mn_2O_3, remove volatile components such as bound

water, and make the ore more thermally stable to avoid decrepitation. The samples were reduced in isothermal setups at temperatures in the range of 600-1100°C in CO-CO$_2$ atmosphere. In general, all experimental results showed that the reproducibility was low for all ore types, with the exception of the Namibian (NAM) ore. To evaluate the variation in reduction behavior of BHP ore, 20 pieces of ore (1.2-1.7 cm) from different lumps were selected and reacted under equal conditions (70CO-30CO$_2$ at 900°C). The results are shown in Figure 2.7, where it can be observed that the reduction behavior appears to fall within two distinct categories, where variations are also observed within the categories. No explanation was provided, however chemical analysis of the residue from crushing of lump 1-10 of BHP ore showed large variation in the manganese and iron content of the lumps, ranging from 29.7-56.1% and 1.07-26.33%, respectively.
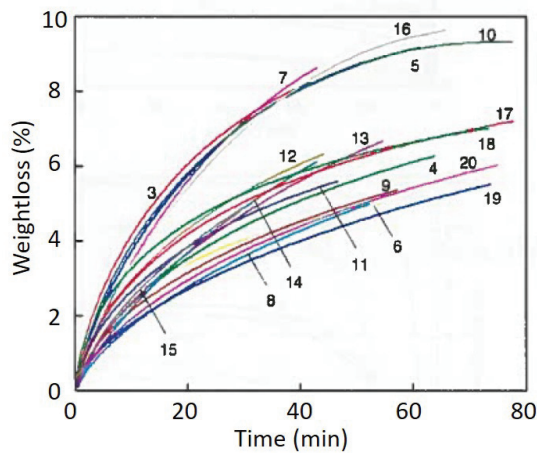
Figure 2.7: Percentage weight loss vs. time for irregular ore pieces (1.2-1.7 cm) of BHP ore in 70%CO+30%CO$_2$ at 900°C as reported by Berg[14]

Berg also investigated the effect of increasing temperature and increasing concentration of CO in the atmosphere for calcined BHP ore, which indicated an increasing reduction rate with increasing %CO for the majority of the experiments. No temperature dependence was observed from 800-1000°C, yet a clearly increased rate was observed at 1100°C, which was also successfully reproduced. Further, it may be mentioned that experiments conducted on BHP ore calcined to Mn$_3$O$_4$ showed a higher reduction rate compared to ores calcined to Mn$_2$O$_3$. Some experiments were conducted on untreated BHP ore consisting mainly of MnO$_2$ in pure CO (4 L/min) in the range of 600-800°C. No distinct stages of reduction was observed at 600°C, however an extremely fast initial reduction rate was observed at 700°C and 800°C up to 9-10% weight loss, which was believed to correlate to the reduction of MnO$_2$ to Mn$_2$O$_3$. Subsequently, a considerably lower rate was observed.

Investigations of microstructure in partially reduced samples showed that all ore types appeared to reduce in a shrinking core behavior, where additional reaction fronts could be observed along cracks of substantial size. An unreduced core of Mn$_2$O$_3$ was surrounded by a distinct layer of MnO. Only a thin rim of Mn$_3$O$_4$ was observed, indicating that the rate of Mn$_3$O$_4$-reduction was as fast as the rate of Mn$_2$O$_3$. Metallic iron

was not detected in any of the investigated samples. Overall, Berg concluded that the rate limiting factors of the reduction were dependent on the mineralogy of the reducing ore, and it was stated that ores containing bixbyite (and hausmannite) reduced faster than braunite ores. These conclusions were mainly based on the observations made from the experimental results of Wessels (ASM) ore reduction, where ore pieces from different lumps of ASM ore were compared. Residue from crushing of the different lumps were analysed by XRD, which indicated that the lumps differed in mineralogy. The difference was reportedly whether braunite, braunite II, or bixbyite was the main constituting mineral. In addition, variation in chemical composition for the 20 lumps of ASM ore were within 40.5-56.7% and 0.7-13.4% for manganese and iron, respectively. The results are shown in Figure 2.8, where the fastest reduction is observed for bixbyite ore (curve 3, 8 and 10) and the slowest reduction was observed for pure braunite ore (curve 7). Braunite ore mixed with hematite or other components (curve 1 and 9) reduced faster than the pure braunite ore. Ores high in braunite II showed an intermediate reduction rate. Further, no apparent correlation was observed between increasing reduction temperature in the range of 800-1100°C, nor any correlation with increasing CO concentration in the range of 50-90% for the ores mainly containing braunite or braunite II. The most important parameter for the reduction bixbyite (and hausmannite) ore was claimed to be the particle size, as the reduction was suggested to be limited by diffusion through the MnO product layer. This conclusion was based on the observation of small pore sizes in the manganosite layer. On the contrary, reduction of braunite minerals were found to be determined by chemical reaction, and the most important parameters were concluded to be the temperature and the melting point of the reduction product due to heavy sintering making the product layer more difficult to penetrate.
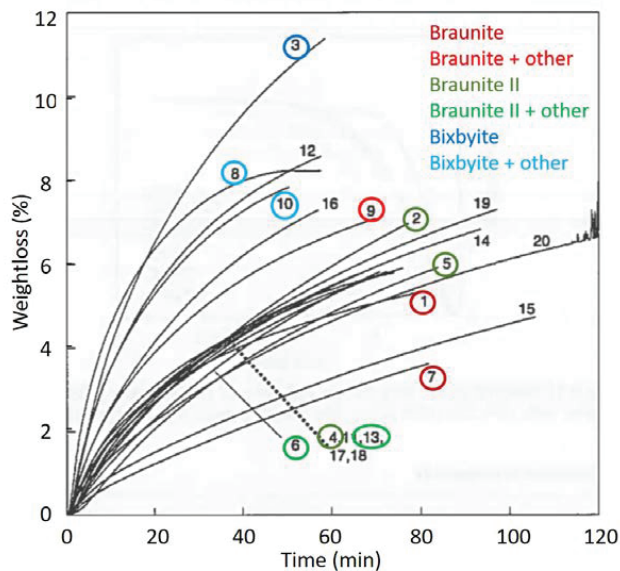
Figure 2.8: Percentage weight loss vs. time for reduction of irregular pieces (1.2-1.7 cm) of Wessels (ASM) ore with CO (30%CO₂) at 900°C as reported by Berg[14]

Regarding the previous paragraph, it is mentioned that the large variation observed for BHP ore (Figure 2.8), where all lumps were found to have bixbyite as main constituting mineral, raises uncertainties regarding the mineral's effect on the reduction rate. The experiments conducted on NAM ore showed increasing reduction rate with increasing temperature and increasing content of CO(g), however no distinction between different minerals were observed. A study supporting the claims of Berg regarding the minerals influence on reduction behavior was reported by Waldemar and Dressel, who investigated the thermal behavior of different manganese minerals in controlled atmospheres[35]. The minerals were evaluated in both neutral, oxidizing and reducing atmospheres, and it was shown that the reduction/decomposition behavior of a specific mineral was affected by the presence of other minerals.

Continued work from Berg conducted on Australian GEMCO (Groote Eylandt) and South African ASSMAN (Nchwaning) ore reported by Berg and Olsen, showed that ASSMAN braunite ore displayed a more rapid reduction compared to GEMCO bixbyite ore[36]. The natural porosity of the ores was evaluated, which indicated that ASMAN ore had a higher natural porosity. As such, the experimental data presented by Berg and Olsen indicated that porosity has a larger effect on the reduction rate than the mineralogy of the ores. Nonetheless, a decrease in reduction rate was observed when the reduction temperature was close to the ore's melting point, suggesting that the reduction rate is affected by mineralogy at high temperatures. Similar change in behavior at high temperatures have been observed by others[34].

Tangstad et al.[32] published a review of six different laboratory investigations on the CO-reactivity of different ores, where a summary of the results is presented in Table 2.5. The review included the work of Berg, whereas the remaining was unpublished work. The studies had been executed with certain dissimilar experimental conditions, and some discrepancies were observed both within a specific study and between the studies. Nonetheless, BHP (Groote Eylandt) or Comilog (Gabon) ore were found to be the most reactive ores in all reviewed investigations, where most of the oxygen had been released at temperatures below 800°C. Further, the review included observations from an industrial furnace changing its raw materials from BHP (Groote Eylandt) ore to Comilog (Gabon) ore. It was seen that Comilog ore resulted in a significantly improved prereduction compared to BHP ore. As BHP was found to be the more reactive ore compared to Comilog in half of the investigations presented by Tangstad, this could indicate that that laboratory studies are not directly comparable to industrial operation.

Table 2.5: Reactivity order of manganese ores according to the review published by Tangstad et al.[32]

Sørsdal lump	Sørsdal pellet	Todd et. al.	Beck	Stahl	Ruud	Berg	Wasbø
BHP	BHP	Com	Com	Com	BHP	BHP	Com
Com	Tem. S	BHP(?)	BHP	BHP	Glo	Asm	Asm
Gh.C	Com	Am	(Asm)		Com		BHP
Tem. S	Wes	Asm			Asm		
Wes	Gh. C	Wes					
Mam	Mam						

Com = Comilog, Gh. C = Ghana Carbonate, Tem. S. = Temco Sinter, Wes = Wessel, Mam = Mamatwan, Am = Amapa, Asm = Asman(Nchwaning), Glo = Gloria

A relatively similar and more recent study was published by Turkova et al.[8], where the focus was dedicated to the relationship between CO-reactivity and porosity of different manganese materials. Eight different manganese materials, including Gabonese ore (Comilog), CVRD ore, Assmang (Nchwaning) ore, and sinter and/or pellets of the mentioned ores were evaluated. Samples in size fraction 10-15 mm were heated at 10°C/min up to 400°C and 800°C. The gas atmosphere was 70 vol% CO and 30 vol% CO_2 with a gas flow rate of 4 l/min. The work of Turkova was continued in the GasFerrosil project, where all materials were evaluated at additional target temperature of 1100°C, while all other experimental conditions remained unchanged[21]. The new results were in high correlation with the trends described by Turkova, and as such the studies are discussed together. Figure 2.9 shows the temperature development in the sample as a function of the furnace wall temperature for Comilog ore, BHP ore, Comilog sinter and Nchwaning ore. The two former are high oxygen ores, whereas the two latter are semi- and low oxidized, respectively. It is evident that the sample temperature is highly affected by the exothermic reactions, where the large exothermic peak in temperature is typical for high oxygen ores.
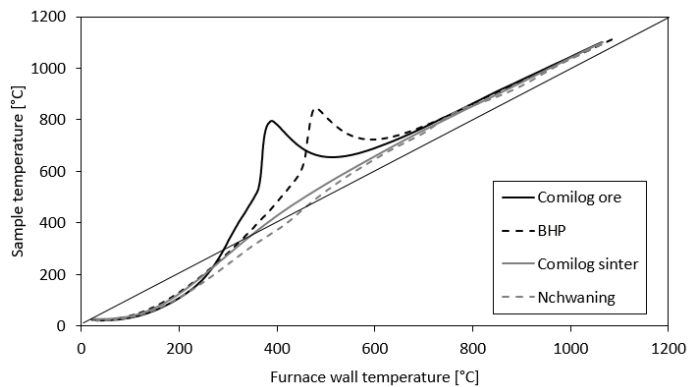
Figure 2.9: Sample temperature as a function of furnace temperature during heating of Comilog-, BHP- and Nchwaning-ore, and Comilog sinter in 70%CO-30%CO₂[8]

The TGA results showed that reduction was initiated at temperatures exceeding 600°C for all materials, except for Gabonese, CVRD and BHP (Groote Eylandt) ore. Nchwaning ore had the lowest CO-reactivity with an x in MnOx value of 1.28 at 800°C. A comparison of the manganese material's initial porosity and the oxygen to manganese ratio at 800°C revealed a general trend of a high initial porosity correlating to a high CO-reactivity, and thus a low oxygen level at 800°C. The results imply that ores with high initial porosity will have higher CO-reactivity compared to their respective pellets and sinter. On the contrary, for Nchwaning, which has a low initial porosity, making an agglomerate with higher porosity will increase the CO-reactivity. Further, it was observed that the porosity of the samples increased during heating in reducing atmosphere, however the slope of increase was highly similar for all materials, implying that a low or high CO-reactivity can be indicated by the initial porosity of the raw ore. The strong apparent correlation between initial porosity and CO-reactivity was not clear for Groote Eylandt (BHP) ore, as it has been seen to have a relatively low porosity and a high CO-reactivity. As such, the work in the GasFerrosil project was extended to include the behavior of Groote Eylandt ore. It was observed that the porosity of Groote Eylandt

18

showed a significantly larger increase with temperature compared to the other manganese materials. The porosity increased from 13.9% at 400°C to 42.4% at 800°C, which was the same porosity as was found for Comilog ore at this temperature. This may explain the high CO reactivity of Groote Eylandt. The O/Mn ratio at 800°C as a function of initial porosity shown in Figure 2.10 includes both the work of Turkova[8] and the data from the GasFerrosil project[21].
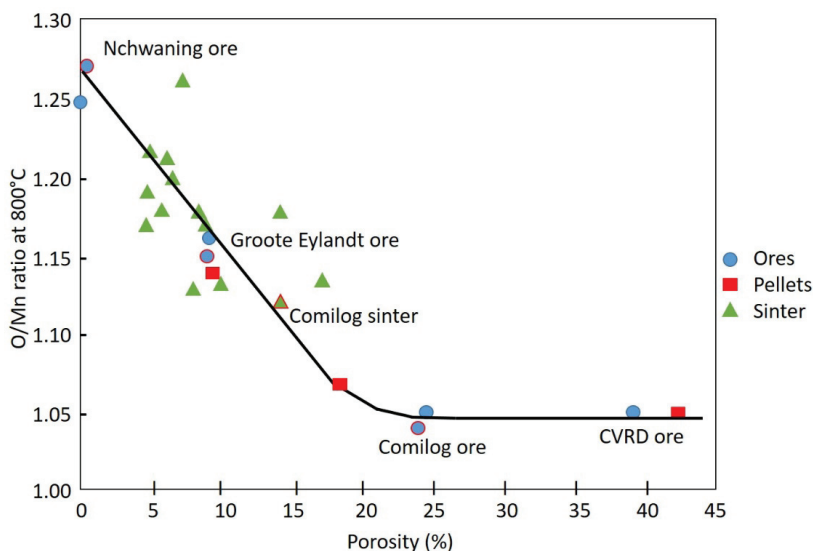
Figure 2.10: O/Mn ratio as obtained by chemical analysis of manganese materials reduced non-isothermally at temperatures up to 800°C as a function of the measured porosity (values outlined in red correlate to work performed in the GasFerrosil project)[21]

Results from similar investigations were presented by Visser et al., who investigated the South African ores Gloria and Nchwaning (Assmang)[12]. Both ores showed an initial oxygen level (O/Mn ratio) of approximately 1.5, correlating to Mn_2O_3. No reduction was observed for any of the experimental runs at temperatures lower than 600°C when reduced in 70%CO-30%CO_2. Gloria ore (Gl) obtained an O/Mn ratio of 1.05 at 850°C, whereas Nchwaning ore obtained the same oxygen level at 1000°C. At 800°C, Nchwaning ore was seen to have an oxygen level of approximately 1.3. It may be mentioned that as Gloria is a carbonate ore, it may still release considerable amounts of CO_2 in the active region of the Boudouard reaction, despite having obtained a complete prereduction of manganese oxides. The study of Visser et al., and the previously mentioned studies of Turkova and Tangstad, respectively, show that South-African ores in general exhibit a low CO-reactivity. As they also have a high thermal strength, it was suggested that both the low CO-reactivity and the high thermal strength are related to the porosity. The oxidation level (x in MnOx) and initial porosity of various commercial manganese ores are shown in Table 2.6.

Table 2.6: Oxidation level (x in MnOx) and initial porosity of various commercial manganese ores[28]

Ore	MnOx	Porosity [%]
Comilog lump	1.92	30-50
Comilog crushed	1.92	15-25
CVRD	1.82	38.5
Groote Eylandt lump	1.94	5-8
Groote Eylandt crushed	1.94	5-8
Nchwaning (Assmang)	1.46	0.1
Gloria[12]	1.40-1.50	< 7

Three different grades of Egyptian manganese ores (<25 mm) from Um Bogma were investigated isothermally at 900 and 1100°C in 60%CO-40%CO$_2$ (1L/min) atmosphere by Fahim et al[37]. XRD analyses of all three ore grades showed that manganese existed as pyrolusite (MnO$_2$) and iron as hematite (Fe$_2$O$_3$), with Mn/Fe ratios being 1.5, 3.3, and 4.5 for low, medium and high grade ore, respectively. Low and medium grade ore had a true porosity in the range of 18-20%, whereas the high grade ore had a porosity of 36%. The reduction extent was determined from the weight recorded by the thermobalance relative to the excess oxygen in the sample assuming a complete reduction to MnO and Fe. For all three ore grades at both 900°C and 1100°C, a highly rapid initial rate up to a 60-70% reduction extent was seen, which may correlate to the reduction of MnO$_2$ to Mn$_3$O$_4$. Subsequently, a lower reduction rate was observed in all cases, leading to a varying total reduction extent for the three ore grades. Higher grade ores showed a higher reduction extent, which was attributed to that solid solution manganese and iron oxides were more difficult to reduce than the individual oxides, and the formation of solid solution would be lower for ores with a lower Mn/Fe ratio. It can however be noted that the porosity was also higher for the high grade ore.

Pochart et al. showed the importance of considering the ore size and the heating rate when studying reducibility of manganese ores[20]. Two different tests based on the same principle, where the main difference was the size of the load, were performed. The former, known as the "Boris" test, evaluated Comilog-, BHP-, and Assmang/Nchwaning-ore in 200 g batches in 60%CO-40%CO$_2$ (400 L/h) at temperatures up to 1100°C. Two different heating rates, 2°C/min and 8°C/min, were used, simulating minimum and maximum heating rates observed in electric furnaces. Further, two different particle sizes were used, i.e. below 5 mm and 10-15 mm. The latter, known as the "CORED" test, evaluated the same ores in 1400 g batches under equal temperature conditions (target temperature and heating rate) and gas composition. Particle size distributions were 10-15 mm and 25-35 mm. The results are reprinted in Table 2.7, which show that the influence of heating rate is more important in coarse ore, except for Comilog which is more sensitive to granulometry. It may also be noted that Nchwaning (Assmang) exhibit a higher CO-reactivity compared to Groote Eylandt (BHP) in the results presented by Pochart et al., which does not align with previous investigations.

Table 2.7: Effect of particle size and heating rate on oxidation level of manganese (x in MnOx) for Comilog, BHP, and Assmang/Nchwaning ore as obtained by two different reducibility tests conducted in CO-CO2 atmosphere[20]

Test type	Ore and size	2°C/min MnOx, x =	8°C/min MnOx, x =
Boris test	Comilog small (< 5 mm)	1.00	1.11
	Comilog medium (10-15 mm)	1.14	1.15
CORED test	Comilog medium (10-15 mm)	1.08	-
	Comilog large (25-35 mm)	1.12	1.25
Boris test	BHP small (< 5 mm)	1.22	1.20
	BHP medium (10-15 mm)	1.22	1.28
CORED test	BHP medium (10-15 mm)	1.22	1.28
	BHP large (25-35 mm)	1.25	1.40
Boris test	Assman small (<5 mm)	1.08	1.09
	Assman medium (10-15 mm)	1.09	1.16
CORED test	Assman medium (10-15 mm)	1.09	-
	Assman large (25-35 mm)	1.13	1.25
CORED test	Mamatwan large (25-35 mm)	-	1.11

Gao et al. investigated the kinetics of reduction of manganese ore by CO-gas[38]. The commercial name of the ore was not presented, however chemical analysis showed the ore to be relatively low in total manganese content (36.6 wt%) and relatively high in iron (12.7 wt%) and acidic oxides ($SiO_2+Al_2O_3$ = 15.7 wt%). The manganese ore was milled to less than 1 mm and sieved into size ranges from 0.5–1.0 mm to < 45 μm before being calcined at 900°C in argon prior to reduction experiments, thus removing volatiles and decomposing MnO_2 phase to Mn_3O_4. Gas composition was varied from 10:90 to 40:60 $CO:CO_2$ and the total flow rate was equal to 1.5 NL/min. It was found that the reduction rate increased slightly with decreasing particle size. Further, it was found that the reduction was initiated at 440°C in 30 vol% CO, and increasing temperature correlated to an increase in the rate of reduction. Further, a higher CO content resulted in a higher reduction rate. Isothermal experiments at 550°C in 70%CO(+CO_2) with 60 minutes holding time was sufficient in reducing Mn_3O_4 to MnO, as well as Fe_2O_3 to Fe_3O_4. No effect of bed depth of the samples was observed in the range of 0.1-0.4 cm bed depth. A topochemical reaction mechanism was not observed and it was shown that the reduction process was best described by the nucleation and growth kinetics equation.

The reduction of Mn_3O_4 to MnO in calcined ore was also investigated by Ishak in his Dr. Ing thesis[34]. The experimental work was carried out isothermally, using Comilog ore precalcined to decompose higher manganese oxides to Mn_3O_4, at temperatures 900-1100°C. Investigated variables were particle size, temperature, reductant, and preparation of manganese ore material. Reductants were either coke, alkali-impregnated coke, CO(g), or a combination of these. From experiments run with coke in addition to CO-gas, no weight loss was observed from coke, indicating an insignificant occurrence of the Boudouard reaction. Nonetheless, a higher initial reduction rate was observed in experiments conducted with coke compared to quartz (to ensure comparable gas flow through charge) in addition to CO-gas. It was found that the reduction rate increased to a small extent with increasing temperature and decreasing particle size,

which was suggested to indicate that both chemical reaction and diffusion affects the reduction rate. It was observed that external mass transport gave a negligible contribution to the rate. The ore particles were found to generally follow a shrinking core behavior during reduction. Further, similar to Berg[14], Ishak observed a change in mechanism at higher temperatures, believed to be due to a sintering effect. It was suggested that the sintering coarsens the product layer, resulting in larger pores. This was supported by pore distribution analysis.

Several studies have been performed where the manganese ore was calcined prior to reduction experiments in order to have the manganese initially existing as Mn_2O_3 or Mn_3O_4, rather than MnO_2. However, it has been observed that the reduction rate of Mn_3O_4 to MnO is considerably slower if the ore is precalcined compared to reduction rate of Mn_3O_4 from green ore[32]. When the Mn_3O_4-layer is formed by calcination at high temperatures, the formed layer has been seen to be denser and hence more difficult to penetrate. The inhibiting effect of calcination on the reduction rate of Mn_3O_4 to MnO was further confirmed by Ishak[34]. Samples calcined in 3 L/min $N_2(g)$ at 1100°C were compared to samples that had been pre-reduced at temperatures 290-300°C in 100% CO (1.5 L/min) atmosphere. In both samples, the majority of the manganese was in the form of Mn_3O_4 after treatment. Porosity measurements showed that the specific surface area was considerably larger for reduced ore compared to calcined ore, i.e. 14.13 m^2/g vs 0.71 m^2/g. The reduction in CO-atmosphere was evaluated in isothermal experiments at 950°C and 1000°C. The retarding effect of calcination compared to pre-reduction was evident at 950°C, where a higher reduction rate was observed for the pre-reduced sample, likely due to the increased reaction area. The results show that evaluation of CO-reduction of manganese ore from calcined samples may give a wrong impression of the rate determining factors.

In relation to manganese ores, several studies have been performed utilizing solid carbon as reductant[39]–[43]. These investigations are generally performed at high temperatures (T>1000°C), outside the scope of this work, as the overall aim has been reduction of manganese oxides to metallic state. Nonetheless, some of the observations made in studies where the starting material had an O/Mn ratio exceeding that of MnO will be covered. Carbothermic reduction of manganese ores is generally agreed to be described by two stages: an initial fast stage where the higher oxides are reduced to MnO and metallic Fe, followed by a slower reduction of MnO to metallic Mn[41]–[44]. All following comments and observations may be assumed to regard the initial reduction step if not stated otherwise.

Ackdogan and Eric[41], [42] stated that the reduction initially starts through direct contact between ore and carbon particles, which forms carbon monoxide. CO continues to act as a reducing agent in addition to carbon, where any produced CO_2 is converted back to CO through the Boudouard reaction. The investigated system was Wessel ore with pure graphite in argon atmosphere at temperatures 1100-1350°C. The initial step was found to be under mixed control, where diffusion of CO/CO_2 in the porous product layer, as well as the chemical reaction of CO at the pore walls were important. The reduction was slightly affected by temperature, and the effect of particle size (-0.044 mm to 0.297 mm) appeared to be small. The insignificant influence of particle size on the initial reaction stage was also reported by Eric and Burucu from studies of Mamatwan ore fines (<300 μm) with graphite in argon atmosphere at temperatures 1100-1300°C[44]. Further, microphotographs of partially reduced particles indicated that the reduction occurred in a shrinking core manner. Mixtures of analytical grade MnO_2 and graphite reacted under argon atmosphere at 1100-

1400°C were modelled by a multistep shrinking core model by Reuter and Deventer[45]. The model relied on several assumptions, including intermediate stable oxides and the governing mechanism. The reduction was assumed to follow the sequence MnO_2-Mn_3O_4-MnO-Mn_5C_2-Mn, where solid carbon was given as reductant for all species. It was indicated that the reduction of MnO_2 to Mn_3O_4 was weakly dependent on temperature.

It is seen that the temperatures used for studying carbothermic reduction of manganese ores are far above that required to initiate reduction of manganese ores, and as a consequence, the effect of e.g. varying particle size is too low to be quantified.

2.2.2   Reduction in presence of H_2(g)/H_2O(g)

As previously mentioned, a certain amount of moisture is present in the raw materials as they are fed to the furnace. The moisture will be surface moisture or chemically bound. The amount of surface moisture held by the ores correlate to its porosity. Comilog ore, with a high porosity, contains about 8% compared to 3% for Groote Eylandt ore, which has a lower porosity. South African ores generally contains less than 2%[2]. Evaporation of surface moisture is an endothermic reaction that occur at low temperatures (T<100°C). Increasing content of surface moisture will thus lead to an increasing energy consumption in the furnace, as well as a lower off-gas temperature. According to Swamy and Robertson, a higher content of free moisture will have no further impact on the system[2]. As chemically bound water may require higher temperatures to be expelled, the water may be present at higher temperatures in the prereduction zone. The specific temperatures will depend on the ore characteristics and the mineral in which the water exist. Li and Robertson[46] stated that chemically bound moisture does not reach the lower parts of the furnace, unless the residence time of the solid charge is much less than 1.8 hours. Industrial measurements show a content of H_2(g) in the range of 6-10 % in the off-gas for both HC FeMn and SiMn[47]. The origin of H_2(g) may be from chemically bound water evaporated at higher temperatures reacting with CO(g) according to the water-gas shift reaction (reaction 1.3)

Hydrogen may reduce the higher manganese oxides to MnO in a similar manner as CO(g), according to reaction 2.1-2.3.

$$MnO_2 + \frac{1}{2}H_2(g) = \frac{1}{2}Mn_2O_3 + \frac{1}{2}H_2O(g) \qquad \Delta H^0_{298} = -80 \; kJ \qquad 2.1$$

$$\frac{1}{2}Mn_2O_3 + \frac{1}{6}H_2(g) = \frac{1}{3}Mn_3O_4 + \frac{1}{6}H_2O(g) \qquad \Delta H^0_{298} = -22 \; kJ \qquad 2.2$$

$$\frac{1}{3}Mn_3O_4 + \frac{1}{3}H_2(g) = MnO + \frac{1}{3}H_2O(g) \qquad \Delta H^0_{298} = -5 \; kJ \qquad 2.3$$

In atmospheres containing CO, CO_2, H_2 and/or H_2O, the equilibrium partial pressure of oxygen is determined by the water-gas shift reaction (CO(g) + H_2O(g) = CO_2(g) + H_2(g)), where the equilibrium constant is expressed as:

$$K_T = \frac{p_{CO} \cdot p_{H_2O}}{p_{CO_2} \cdot p_{H_2}}$$

2.4

The partial pressures may be calculated from the molar relations between the phases, as seen in equation 2.5, in combination with molar elemental balances for carbon, oxygen, and hydrogen.

$$P_x = \frac{n_x}{n_{total}}$$

2.5

As an example, Figure 2.11 shows the equilibrium pressures of CO, CO_2, H_2, H_2O, and resulting oxygen pressure, as a function of temperature for a given input gas composition of $P(CO) = P(H_2) = 0.375$ and $P(CO_2) = p(H_2O) = 0.125$.
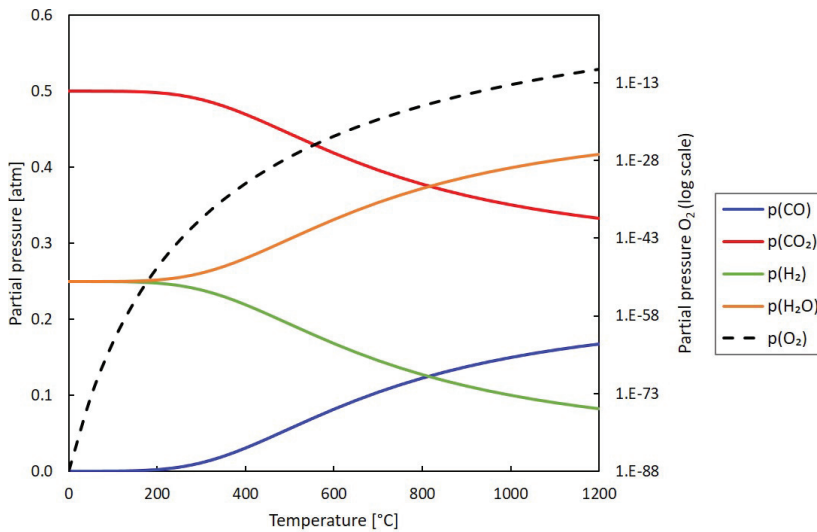
Figure 2.11: Equilibrium partial pressures for starting gas composition of p(CO) = p(H₂) = 0.375 and p(CO₂) = p(H₂O) = 0.125 according to the water-gas shift-reaction. Values from HSC Chemistry 9[17]

Figure 2.12 shows the stability diagram of manganese and iron oxides together with the equilibrium partial pressure of oxygen according to the water-gas shift reaction for given starting gas compositions. As can be seen, MnO is the stable manganese oxide for all evaluated gas compositions, whereas the stable iron phase may be either Fe_3O_4, FeO, or metallic iron. It should be noted that the stability diagram of iron oxides is superimposed on the stability diagram of manganese oxides, implying that pure phases are assumed.

24
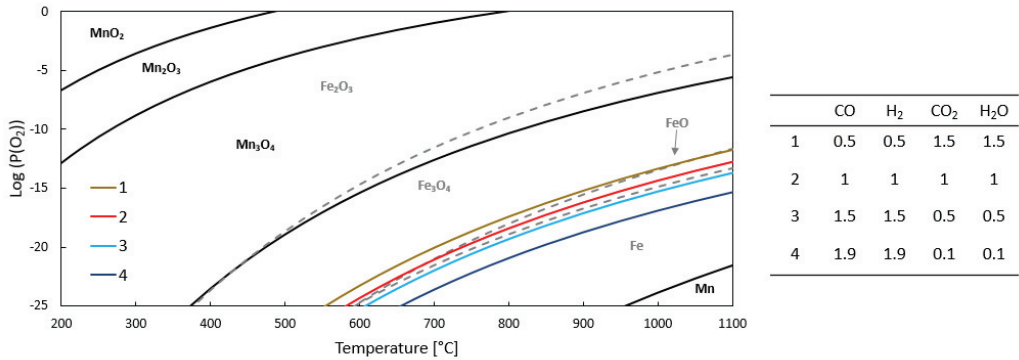
Figure 2.12: Stability diagram for manganese and iron oxides together with the equilibrium partial pressures of oxygen in H_2-H_2O-CO-CO_2 atmosphere for various compositions. Values from HSC 9[17]

Barner and Mantell[48] investigated the reduction of synthetic pyrolusite pellets and particles (0.12-0.21 mm) in hydrogen (1 atm) at temperatures 200-500°C. At low temperatures, XRD showed that the main constituting oxides were MnO_2 and Mn_3O_4, whereas minor amounts of Mn_2O_3 were detected. Due to this, the authors assumed the reduction to occur topochemically through sequence MnO_2-Mn_2O_3-Mn_3O_4. Below 250°C, the reduction proceeded to Mn_3O_4 under a chemically controlled reaction rate. Considerable diffusional resistances were observed between 250-325°C, which was believed to be due to the more protective Mn_3O_4 product layer. Thus, only small amounts of MnO were detected at temperatures below 325°C, whereas MnO was the main phase at higher temperatures. The effect of hydrogen partial pressure was investigated at 226°C, where helium was used as diluent and the total pressure was maintained at 800 mmHg (≈ 1.05 atm). A clear increase in the reaction rate was observed with increasing partial pressure of hydrogen. The results, in terms of apparent rate constant as a function of hydrogen partial pressure, are shown in Figure 2.13 (left). The retarding effect of water vapor was investigated at the same temperature, where 1 and 10 mole% levels of water vapor concentrations were used. The results are shown in Figure 2.13 (right), which showed that small concentrations of water vapor clearly inhibited the reduction process. It was suggested that the inhibiting effect was due to adsorption of water vapor on active reaction sites at the gas-solid reaction interface. The reduction kinetics of a Belgian Congo pyrolusite ore was also briefly mentioned in the study, where it was observed that the ore specimens reduced considerably faster compared to the synthetic pyrolusite samples at all conditions investigated.

De Bruijn et al. [33] investigated the reduction of MnO_2 ore and synthetic Mn_2O_3 and Mn_3O_4 by the use of a thermobalance at various hydrogen pressures in the temperature range 275-400°C. It was found that both MnO_2 ore and synthetic Mn_2O_3 reduced to MnO via the intermediate oxide Mn_3O_4. The Mn_2O_3 phase was not detected. The conversion curves indicated that the reduction was a two-step reaction, where a change in slope was observed at approximately 65% conversion. The majority of the experiments was conducted with size fraction 0.090-0.105 mm, and it was further reported that varying the size fraction within range 0.0675-0.1275 mm resulted in almost identical time-conversion curves. This was attributed to the porous nature of the ore particles. The influence of water vapor was also evaluated, where a decrease in the rate

with increasing water vapor concentration was found. The inhibiting effect of water vapor was of similar magnitude as what was reported by Barner and Mantell[48].
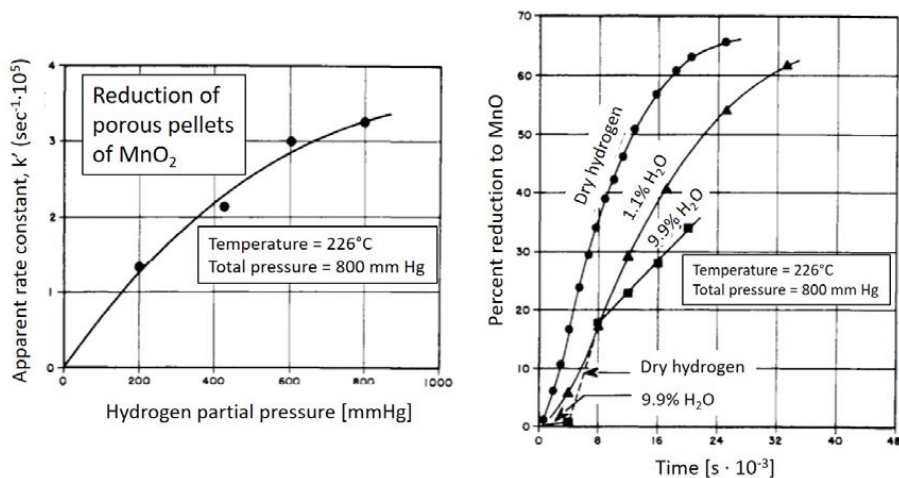
Figure 2.13: Effect of hydrogen partial pressure at 226°C (left) and effect of water vapor at 226°C (right) on the reduction of porous MnO₂ pellets. Figure after Barner and Mantell[48]

Konov et al. investigated Wessels ore and two grades of Groote Eylandt ore(GE-PF and GE-PS) isothermally at 1000°C in hydrogen atmosphere[49]. In addition, some non-isothermal experiments were conducted with a heating rate of 5°C/min in the temperature range 300-1500°C. Ore particles in size fraction -45-150 mm were preheated in air for 3 hours prior to reduction, giving Mn_2O_3 and Mn_3O_4 as main phases for Wessels and GE-PF ores, and Mn_2O_3, Mn_3O_4, and SiO_2 for GE-PS ore. The reduction of Mn_2O_3 and Fe_2O_3 by H_2 to MnO and Fe with water evolution started at temperatures lower than 300°C, and were completed at approximately 950°C. For GE-PF ore, a rapid increase in reduction rate, in terms of water evolution, was observed before peak at approximately 500°C followed by a slow and steady decrease in the rate. Similar behavior was seen for GE-PS, however the peak was observed at a somewhat lower temperature, i.e. 400°C. For Wessels ore, the increase and decrease in rate was relatively symmetrical with a peak point at 750°C.

Briquettes made from low grade manganese ore consisting mainly of pyrolusite, hematite, and quartz was reduced by different flow rates of hydrogen at temperatures 800-950°C in the work presented by El-Gawad et al[50]. The pellets were made from ore of particle size less than 75 μm mixed with molasses. It was seen that the reduction rate increased with increasing temperature, and a slight increase in the rate was observed when the flow rate was increased in the range of 0.5-2 L/min. Further, it was suggested that the initial stages of reduction were controlled by diffusion through the product layer, whereas final stages were controlled by nucleation and growth. XRD analysis of the reduced samples showed that all manganese oxides were reduced to MnO, and iron oxides reduced to metallic iron.

The effect of hydrogen on the reduction of Comilog ore was investigated by Beck through isothermal experiments conducted at 750°C[51], [52]. Single particles in size 4.00-6.68 mm and 25.00 mm were evaluated in pure CO, pure H_2, as well as in gas mixtures with 50:50 $CO:H_2$ and 33:67 $CO:H_2$. The ore was calcined prior to the reduction experiments, decomposing higher manganese oxides to Mn_3O_4. The increasing hydrogen content appeared to have a promoting effect on the reduction rate. Beck also observed that the weight curves converged at a higher total weight loss with increasing hydrogen content in the atmosphere, which could indicate a higher reduction extent. In a separate study, Beck investigated the reduction of Groote Eylandt ore (BHP), Assmang (Nchwaning) ore and Comilog ore in $CO(g)$ and $H_2(g)$ atmosphere, respectively[53]. The experiments were conducted with single particles of size 1-2 cm heated at 6 °C/min up to 1000°C. The experiments resulted in an increased reaction rate, as well as increased reduction extent, for all three evaluated ores. Isothermal reduction of calcined Nchwaning ore particles (1-2 cm) in $H_2(g)$ indicated that particles rich in braunite were more temperature dependent and encountered larger diffusional resistances compared to particles rich in bixbyite.

The reduction of Nchwaning manganese ore was investigated isothermally by varying the oxygen pressure in blends of CO, H_2, CO_2, and H_2O by Lobo[54]. The ore was evaluated in lump and pellet form, both in sizes 10-14 mm, where pellets were roasted at 800°C for 2 hours prior to reduction experiments. The experiments were conducted with 200g batches of material reduced at 950°C for 2 hours. The initial porosity of the materials was measured, and it was found that the pellets had a porosity between 30-34%, whereas the lumped material only had about 3%. It was seen that a higher oxidation level of the gas (higher oxygen pressure) gave a slower reduction rate for the ore lumps. Further, it also resulted in a lower total weight loss, where total weight loss ranged from 7% to 12%. For the pellets, a highly similar reduction rate was observed for all gas compositions, however the total obtained weight loss differed. A higher oxidation degree in the gas (higher oxygen pressure) correlated with a lower total weight loss. The highest weight loss was obtained with 100% $H_2(g)$, which stabilized at 12.5%. In contrast, the lowest was obtained using 25% of each gas component, giving a weight loss of 7.5%. From chemical analysis of the reduced samples, it was seen that higher manganese oxides had been reduced to MnO in all cases, whereas the varying weight loss was due to a varying reduction extent of iron oxides. This implies that manganese oxides are more easily reduced than iron oxides in Nchwaning ore. The observed iron phase in the reduced sample was in good agreement with the predicted phases from thermodynamic data.

Pyrolusite ore was decomposed into a mixture of bixbyite, hausmannite and manganosite through calcination by Perreault and Patience[55]. The background was to evaluate pyrolusite as an alternative oxygen carrier in chemical looping combustion, so the sample was sequentially reduced and oxidized by H_2 and O_2 15 times at 800°C prior to the first experiment, and the same reduction-oxidation routine was used on the same sample to investigate all variables. Reduction kinetics of pyrolusite was evaluated in 5-25 vol% CO (diluted by argon), in addition to combined CO/H_2 tests where CO was varied between 15-25 vol% and hydrogen between 12-20 vol%, still diluted by Argon. Results were evaluated in terms of the oxygen transfer from solid to gas during reduction. The experimental data showed a decrease in oxygen transfer with increasing temperature when reduction was carried out in CO. It was also seen that increasing the CO concentration increased the oxygen transfer up to a limit. However, in a combination of CO and H_2 ($CO:H_2$ ratio of 5:4), compared to pure CO, the oxygen transfer was increased by 50% at 810°C. At 960°C, the oxygen transfer increased with as much as 86% when reducing with 20 vol% CO. These numbers only

consider the oxygen transfer related to CO/CO_2, as the oxygen transfer was calculated from a mole balance on the measured CO_2. These results indicate that in addition to its function as a reductant, H_2 also increases the overall reduction by increasing the oxygen diffusion associated with CO-reduction, in accordance with the results of Lobo[54] and Beck[53].

The effect of hydrogen on the reduction of manganese ores Comilog and Nchwaning was recently studied by Ngoy through non-isothermal experiments[56]. The gas atmospheres contained CO-CO_2 and CO-CO_2-H_2, respectively, where the gas compositions correlated to similar equilibrium oxygen pressures. 100 g of ore samples in size fraction 9.5-16.0 mm were reduced at 6°C/min at temperature range 25-1000°C. To avoid carbon deposition, the samples were heated to 500°C in pure CO_2 before the reducing gas was introduced. The evaluated gas atmospheres correlated to two different oxygen pressures. $p(O_2)_1$ was 70%CO-30%CO_2 (total 2.85 L/min), as well as 41%CO-41%H_2-18%CO_2 (total 4.85 L/min). $p(O_2)_2$ was 50%CO-50%CO_2 (total 4 L/min), and 41%CO-18%H_2-41%CO_2 (total 4.85 L/min). For Nchwaning ore, it was observed that the reduction was initiated at the same temperature for a given oxygen pressure, regardless of the species constituting the gas. The weight reduction behavior indicated that the reaction rate was slightly faster in the hydrogen containing gas. A highly similar weight reduction behavior and extent was observed for 50%CO-50%CO_2 and 70%CO-30%CO_2, indicating that the reduction of Nchwaning ore is insensitive to oxygen partial pressure. Another potential reason is that the gas flow played a larger role than the oxygen partial pressure, as both atmospheres were conducted with a gas flow of CO equal to 2 L/min. The results obtained for Comilog ore for oxygen pressure composition 1 are shown in Figure 2.14. The reduction is initiated at 500°C when the reducing gas is introduced to the system. A clear difference is seen in the weight behavior as a function of time and temperature, respectively. This is due to the extent of heat production accompanying Comilog ore reduction, causing the sample temperature to increase. This gives the weight vs temperature curves a "Z-shape", which is characteristic for high oxygen ores. An example of the temperature development was presented previously in Figure 2.9. The figure shows that the reaction rate is higher in the experiments conducted with hydrogen. At approximately 90 minutes process time, i.e. 650°C, a weight increase is observed in the hydrogen experiments. This is believed to be due to carbon deposition.
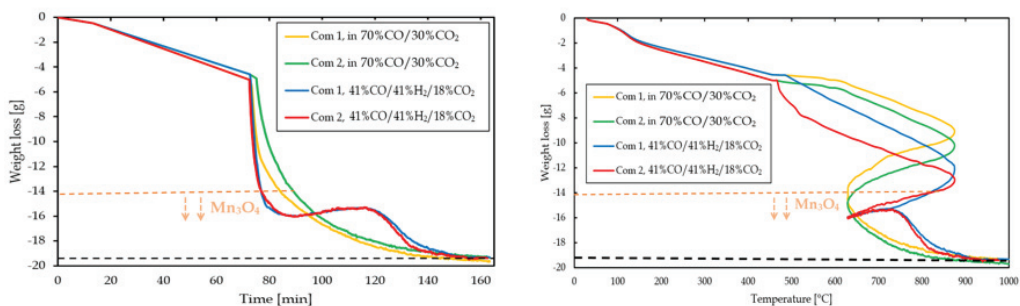
Figure 2.14: Weight reduction of Comilog ore in CO-CO_2 and CO-CO_2-H_2 atmospheres correlating to similar equilibrium oxygen pressures[56]

Comilog ore, Comilog sinter, and Assmang (Nchwaning) ore were reduced with 2L/min CO, 2:2 L/min CO:H$_2$, 2.8:1.2 L/min CO:CO$_2$, 2:0.85 L/min CO:CO$_2$, and 2:0.85:2 L/min CO:CO$_2$:H$_2$ in the *GasFerrosil* project[21]. Ore in size fraction +9.5-13.2 mm were heated from room temperature to 1100°C over a period of 120 minutes. It was observed that the presence of hydrogen had a large effect on the reaction rate. The time at which 90% reduction is obtained was reduced from 55 minutes to 35 minutes in 2 L/min CO compared to 2-0.85-2 L/min CO-CO$_2$-H$_2$. The reduction temperatures were however highly similar, indicating that the temperature is a result of the reaction rate.

2.2.3   Kinetic descriptions

Several of the studies presented in the previous sections has included discussions of kinetics and mechanisms, and the calculation of kinetic parameters. An overview of the studies in terms of experimental conditions, model, and resulting activation energy is presented in Table 2.8. The presented studies have been divided into three categories: reduction in CO-CO$_2$, reduction in H$_2$, and reduction in the presence of a solid carbon source. The reasoning and procedures for some of the more relevant studies are commented, whereas others are merely listed in the table. It is reminded that the studies involve the use of various materials, synthetic and calcined ore, and it has been found by several that the reduction behavior is highly dependent on the pretreatment of the ore[32], [34], [48].

The reduction of Mn$_2$O$_3$ to MnO was investigated in ore calcined prior to isothermal reduction by Berg[14]. Single particles reduced in CO-CO$_2$ atmosphere at 700-900°C were found to reduce through the formation of a product layer/reaction front, which was observed in optical microscope. As such, Berg decided to utilize the shrinking core model to describe the experimental data. It was assumed that the reaction was of mixed control by pore diffusion and chemical reaction at the interface, where the chemical reaction was assumed to be first order with respect to reactant gas (CO). In general, there was large variation between parallels, and the model was also only able to describe a smaller portion of the experiments. Rate constants and diffusivities were calculated, which also showed large variance. In general, bixbyite particles were more successfully described compared to braunite particles. The activation energy was calculated for braunite particles of Wessels (ASM) ore and found to be 41 kJ/mol, whereas 50-70 kJ/mol was found for Namibian ore. The R^2 of the Arrhenius plot was quite low. For the majority of the experiments, it was decided that further interpretation of mechanism and calculation of activation energies was not reasonable.

Kinetics and mechanism were also reported by Berg and Olsen[36]. This was a continuation of Berg's work, implying that experimental conditions and modelling framework were highly similar as to that previously described by Berg. Single particles were used, which resulted in considerable variance between parallels. The shrinking core model was applied to the reduction of bixbyite at temperatures 700-900°C, which provided a good fit for parts of the reaction course. A large scatter of rate constants was obtained, whereas obtained diffusivities were in the range of 0.01-0.12 cm^2/s. The shrinking core model was found to be unsuitable to evaluate the reaction kinetics of the braunite ore slabs, suggested to be due to non-ideal reaction topochemistry. As such, Arrhenius plots were constructed from the reaction rate evaluated from the weight loss vs time curves. The reaction rates and corresponding Arrhenius plot of braunite ore slabs are seen in Figure 2.15. Calculated activation energies were in the range of 30-45 kJ/mol, however, the large scattering of values raises large uncertainties.

A larger sample size was used by Ishak[34] when investigating the reduction of Mn_3O_4 to MnO in calcined Comilog ore, where 50 g calcined ore was reduced in $CO-CO_2$ at 900-1100°C. Ishak evaluated the experimental data with both the shrinking core model and the grain model, which both seemed fit to describe the reduction. The activation energy was calculated by assuming that the reaction was a first order chemical reaction with respect to reactant gas (CO). The models were used to calculate the effective diffusivity and reaction rate constant, as well as the reaction modulus (σ^2), which gives the contribution of pore diffusion and chemical reaction, respectively, to the reaction mechanism. The activation energy could not be calculated at temperatures 900-950°C, as the rate was observed to decrease with increasing temperature. Activation energies at temperatures 950-1100°C were determined to be within 12-230 kJ/mol for particle size 2.4-4.8 mm, and 32-144 kJ/mol for size 6.7-9.5 mm. Ishak found diffusivities that were generally slightly larger compared to that reported by Berg[14], which may be due to that different ores were used. Nonetheless, the rate constants were of similar magnitude.
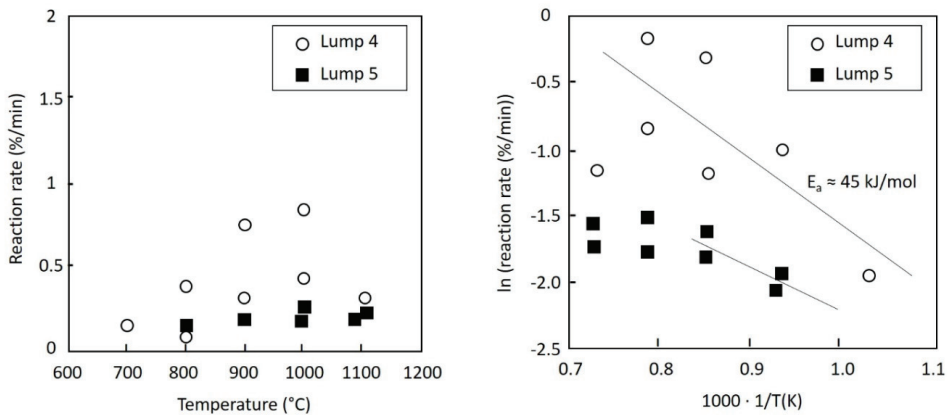
Figure 2.15: Reaction rates and corresponding Arrhenius plot for braunite ore slabs from values presented by Berg and Olsen[36]

Based on the observation of all oxidation states ($MnO_2-Mn_2O_3-Mn_3O_4-MnO$) by XRD in partially reduced single porous MnO_2 pellets and synthetic MnO_2 in hydrogen, Barner and Mantell assumed a topochemical reaction mechanism[48]. From the slope of the reaction rate plotted towards the inverse temperature (Arrhenius plot), the activation energy was determined to be approximately 92 kJ/mole below 250°C, and 117-125 kJ/mole at temperatures exceeding 325°C. A transition region was observed at temperatures 250-325°C. Rate constants were also calculated from assuming a chemical reaction control, where the resulting activation energy was 112 kJ/mol, agreeing well with the activation energy determined from the Arrhenius plot.

De Bruijn et al. evaluated both a shrinking core model and a crackling core model to the reduction of MnO_2 to MnO (via Mn_3O_4) by hydrogen[33]. A distinct change in reduction rates was observed at approximately 67% conversion, indicating a two-step reduction. An induction stage was observed, which was found to have an activation energy of 76 kJ/mol. A two-step shrinking core model gave kinetic values similar to those obtained from modelling the overall reduction with a crackling core model. The total curve modelled

by the crackling core model resulted in an activation energy of 77 kJ/mol for MnO_2 to Mn_3O_4, whereas 103 kJ/mol was found for Mn_3O_4 to MnO. Correspondingly, 79 kJ/mol and 106 kJ/mol was obtained for the two reaction stages with the two-step shrinking core.

Reuter and Deventer[45] proposed a multistep shrinking core model to describe the kinetics of reduction of MnO_2 in the presence of carbon (graphite) at 1100-1400°C. The assumed reduction path was MnO_2-Mn_3O_4-MnO-Mn/Mn_5C_2. As such, four different reactions with individual rates were evaluated, and it was assumed that rates were controlled by chemical reaction in all cases. Further, it was assumed that the temperatures were sufficient for the Boudouard reaction to be completely shifted to the right, meaning that only $CO(g)$ was present. The proposed model fit the experimental reduction data well. The activation energy of reduction of MnO_2 to Mn_3O_4 was determined to be 71.3 kJ/mol. The following three subsequent reactions were found to have activation energies in the region of that previously reported for the Boudoaurd reaction, indicating that the Boudouard reaction affected the kinetics.

An investigation of the reduction kinetics of an unspecified calcined ore in CO-CO_2 at 400-700°C was presented by Gao et al.[38]. Through conventional model-fitting of isothermal experiments, it was found that the reduction was described by nucleation and growth kinetics. The effect of varying particle size and CO partial pressure was determined from the apparent rate constants as a function of the variable. The reduction was found to be unaffected by changing particle size (in range <45 μm to 500-1000 μm) and proportional to the CO partial pressure. An activation energy of 66 kJ/mol was calculated for the reduction of Mn_3O_4 to MnO.

It is clear that the most popular approach to modelling prereduction of manganese ores is by the use of the conventional shrinking core model. An issue with this is the fact that the shrinking core model is defined for nonporous species, whereas manganese ores are porous. Further, most of the kinetic values are found from the use of calcined materials, which has been shown to display quite dissimilar reaction characteristics compared to untreated ore. As such, it is evident that there is a lack of reliable and representative kinetic values for the prereduction of manganese ores.

2.3   Reduction of iron oxides

Manganese ores contain various amounts of iron oxides, which will reduce in the same temperature range as the manganese oxides. Most of the studies concerning manganese ore reduction pay little attention to the simultaneous reduction of iron oxides, despite considerable concentrations in certain ores. Iron is generally found as hematite in manganese ores where the content of iron is of significant magnitude. When heated in a reducing atmosphere, hematite will reduce stepwise by $CO(g)$ in a similar manner as to manganese oxides, according to equation 2.6-2.8. The difference is that a complete reduction of iron oxides to metallic iron is possible in CO-atmosphere[11], [54].

$$Fe_2O_3 + 1/3\,CO = 2/3\,Fe_3O_4 + 1/3\,CO_2 \qquad \Delta H^0_{298} = -13\,kJ \qquad\qquad 2.6$$

$$2/3\,Fe_3O_4 + 2/3\,CO = 2FeO + 2/3\,CO_2 \qquad \Delta H^0_{298} = 25\,kJ \qquad\qquad 2.7$$
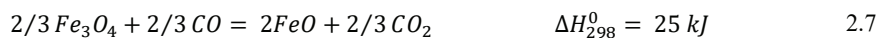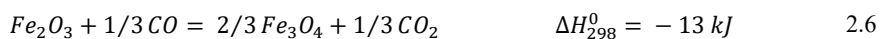
Table 2.8: Summary of kinetic descriptions of gaseous reduction of manganese ores (in presence or absence of solid carbon source)

Material	Gas	Solid carbon	Temperature [°C]	Size [mm]	Initial	Product	Model/rate controlling mechanism	Reasoning	Ea [kJ/mol]	Ref.
Calcined BHP, NAM & ASMAN ore	$CO:CO_2$	-	700-1100	10-20	Mn_3O_4	MnO	Shrinking core: Combined chemical reaction and pore diffusion	SEM (product layer observed in BHP and ASM)	41 (ASM ore) 50-70 (NAM ore)	Berg[14]
Calcined Asman & Gemco ore	$7CO:3CO_2$	-	700-1100	3-5 (plates)	Mn_3O_4	MnO	Shrinking core: Combined chemical reaction and pore diffusion	SEM	30-45	Berg&Olsen[36]
Calcined Comilog ore	CO	-	950-1100	•2.4-4.8 •6.7-9.5	Mn_3O_4	MnO	Shrinking core: Combined chemical reaction and pore diffusion	SEM	•12-230 •32-144	Ishak[34]
Unspecified calcined ore	$3CO:7CO_2$	-	400-700	0.105-0.150	Mn_3O_4	MnO	Nucleation and growth	Model-fitting	66	Gao et. al.[38]
Baharia iron ore	$4CO:CO_2$	-	600-1000	1-4	MnO_2	MnO	1: Diffusion 2: Chemical reaction	Magnitude of activation energy/model-fitting	1. 9.61 2. 36.4	El-Geassy et. al.[57]
Synthetic MnO_2	H_2	-	1. 200-250 2. 250-325 3. 325-400	13x3	1. MnO_2, Mn_2O_3, Mn_3O_4 3. MnO	1. Shrinking core: Chemical reaction 2. Pore diffusion 3. Chemical reaction	XRD (all oxides detected)	1. 92 2. - 3. 117-125	Barner&Mantell[48]
Calcined ore	H_2	-	275-400	0.090-0.105	MnO_2	MnO (via Mn_3O_4)	Two-step shrinking core Crackling core	Model-fitting/XRD	Shrinking core: 1. step: 79 2. step: 106 Crackling core: 1. step: 77 2. step: 103	De Bruijn et. al.[33]
Low grade oxide pellet from Egyptian ore	H_2		750-950	5-7	MnO_2	MnO	Chemical reaction	Model-fitting	79.78	El-Hussiny et. al.[58]
Preheated Mamatwan ore fines	Ar	X	1100-1350	< 0.42	Mn_2O_3, Mn_3O_4, MnO	MnO	Diffusion	Magnitude of activation energy	61	Eric&Burucu[44]
Wessels	Ar	X	1100-1350	0.044-0.297	Mn_2O_3	MnO	Pore diffusion and chemical reaction	Relation between particle size and rate/Model-fitting	81.3-94.6	Akdogan&Eric[40]–[42]
MnO_2	Ar	X	1100-1400	Not specified	MnO_2	Mn_3O_4	Multistep shrinking core	Assumption	71.3	Reuter&Deventer[45]

$$FeO + CO = Fe + CO_2 \qquad\qquad \Delta H^0_{298} = -18\,kJ \qquad 2.8$$

As the literature on iron oxide reduction in manganese ore is scarce, this section will also include literature on reduction of iron ore. Due to the extensive global consumption of iron and steel products, a substantial amount of literature on iron ore reduction has been published throughout the years. Numerous studies have been conducted in relation to the direct reduction (DR) of iron ore, which may be somewhat similar conditions as the prereduction zone of a ferromanganese furnace. The direct reduction (DR) of iron ore followed by electric arc steel making forms an alternative to the standard blast furnace route for making steel.

In a DR furnace, pelletized or lump iron ore, descends through a syngas mixture of hydrogen and carbon monoxide, where the reduction of iron oxides occur in the upper parts at temperatures below 950°C. The content of iron oxides in manganese ores is considerably lower compared to ores used for iron production. Thus, it may be expected that iron oxides are more difficult to reduce from manganese ores due to a low activity when it is in solid solution with manganese oxides. This section does not provide a full review of literature on iron ore reduction. Rather, it has been attempted to provide a short summary of the more recent and relevant studies.

Isothermal reduction experiments were conducted by El-Geassy et al. [57], who investigated the reduction of Baharia iron ore samples (1-4 mm) with a high content of manganese in $CO-CO_2$-atmosphere at temperatures 600-1000°C. The total iron and manganese content were 50.2 wt% and 4.5 wt%, respectively. The influence of gas composition was evaluated at 700°C by varying the CO content from 10-80%. It was seen that the reduction stopped at 19-26% conversion in 20% CO (+ CO_2), where hematite (Fe_2O_3) was reduced to magnetite (Fe_3O_4), and MnO_2 had been decomposed to MnO, Mn_2O_3 and/or Mn_3O_4. At 900-1000°C, wüstite (FeO) was partially formed with the magnetite. At 800-1000°C, analysis showed that metallic iron was produced in 80% CO (+ CO_2). Conversion curves showed a rapid initial reduction step, followed by a considerable decrease in the rate. An increasing reaction rate with increasing temperature and CO-concentration was observed for both stages. The initial stage was shown to have an activation energy of approximately 10 kJ/moles for 20-80%CO (+ CO_2), whereas the final stage resulted in ca. 24 kJ/mole in 20%CO and 36 kJ/mole in 80%CO. From the magnitude of the activation energies calculated from Arrhenius plots, it was suggested that the reduction in 20%CO-80%CO_2 was controlled by gaseous diffusion, whereas reduction in 80%CO-20%CO_2 was controlled by gaseous diffusion in the initial stages and mixed control in the latter stages. Results from conventional model-fitting agreed with the previously suggested mechanisms.

El-Geassy with colleagues continued the work of simultaneous reduction of manganese and iron oxides through investigating isothermal reduction of compact briquettes in hydrogen atmosphere at 1073-1373K[59]. Pure Fe_2O_3 and Fe_2O_3 doped with 2, 4, and 6 mass% MnO_2 (> 99%), all in particle size <50μm, were annealed at 1473 K for 6 h prior to reduction experiments. Annealing lead to the formation of $MnFe_2O_4$ in manganese containing samples. Increasing content of manganese in the briquettes correlated to an increasing retardation of the reduction rate and the overall reduction extent. The lower reduction rate in the initial stages were attributed to the presence of the dense $MnFe_2O_4$ phase, which retarded diffusion. Pure Fe_2O_3 samples obtained a complete reduction to metallic iron, whereas the $MnFe_2O_4$ phase reduced to iron

manganese oxide ((FeO)$_{0.899}$(MnO)$_{0.101}$). A total gas flow of 1 L/min was used, shown to be sufficient to overcome the gas boundary layer effect. Rate controlling mechanisms of both initial and final stages were evaluated from the correlation between the apparent activation energies, conventional model-fitting of gas-solid reaction models, and microscopic examinations of partially and completely reduced compacts. An activation energy of approximately 40 kJ/mol was found for the initial stage, and 59-69 kJ/mol was found for the latter stage. According to the authors, this revealed that the initial stages were under mixed control (diffusion and chemical reaction), whereas final stage reduction was controlled by the interfacial chemical reaction. Similar conclusions were made from the model-fitting, however increasing deviation from the reaction models was observed with decreasing temperature.

A slower reduction of iron in the presence of manganese was also observed by Eric and Burucu[44] and Leith and Howden[60], respectively. The former investigated the reduction of Mamatwan ore fines (< 0.42 mm) in the presence of graphite in argon atmosphere at 1300-1350°C[44]. It was observed that the ore reduced faster than pure Mn_3O_4 oxide, and slower than pure Fe_2O_3 oxide, potentially indicating that the iron in the ore catalyzes the reduction process.

A review of experimental and mathematical investigations of the gaseous (mainly CO and H_2) reduction of iron oxide pellets in relation to DRI was presented by Ghadi et al.[61]. It was shown that rate controlling factors and governing mechanism appear to be dependent on the experimental conditions utilized. Results from several studies were reprinted with the respective author's permission, including the work of Joseph[62], which showed that the porosity was one of the most important factors in terms of iron ore reducibility. Further mentioned was the work of McKewan[63] who investigated the rate-controlling mechanism of a dense hematite pellet, who stated that the reduction proceeded topochemically, where the overall rate was controlled by the interfacial chemical reactions. Turkdogan and Vinters[64], [65] and Turkdogan et al.[66] claimed that the reduction of iron ore by hydrogen at temperatures 200-1200°C may proceed through three regimes, i.e. uniform internal reduction, limited mixed control, and gas diffusion in porous iron-layer, respectively. Uniform internal reduction was found to be independent of particle size. It was further observed that the reduction of both dense and porous hematite lead to the formation of porous wüstite. The authors concluded that a single rate equation could not be derived due to the complexity of the reduction.

Bonalde et al. [67] found the reduction of fired hematite pellets at 850°C in hydrogen or carbon monoxide to be a mixed controlled system. Chemical reaction and internal gas diffusion were competing at the initial stages of reduction, where internal gas diffusion became the dominating mechanism at the latter stages of reduction. It was found that the reduction was fastest in pure hydrogen, slowest in pure CO, and intermediate with a mixture of CO-CO_2-H_2-CH_4, as shown in Figure 2.16. A faster reduction in hydrogen compared to CO atmosphere was also observed by Pineau et al.[68], who studied the reduction of Fe_2O_3 by hydrogen at temperatures 220-680°C. The authors also presented a review of existing literature on kinetic parameters of hematite reduction, which showed that values varied with starting material, nature of reducing gas, temperature range, reaction step, presence of water vapor in the gas mixture, impurities, physical shape, etc. Nonetheless, activation energies obtained for iron oxide reduction with CO appeared to be comparable to that of H_2.
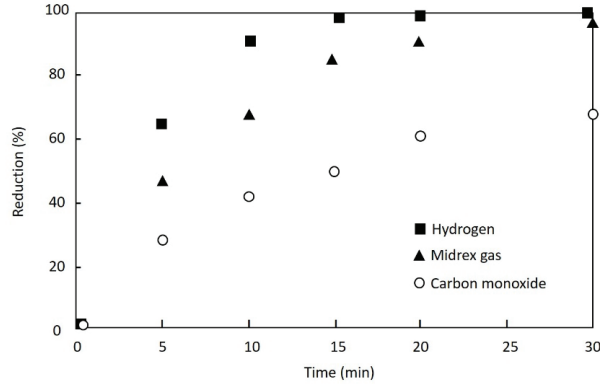
Figure 2.16: Reduction of hematite pellets with H_2, CO, and mixture of CO-H_2-CH_4-CO_2 at 850°C in 2 L/min total gas flow.
Figure after Bonalde et al.[67]

2.4 The Boudouard reaction

The reaction between solid carbon and CO_2, known as the Boudouard reaction, is an important reaction in many metallurgical processes. The Boudouard reaction is not directly investigated in this study, however as a majority of the experiments is conducted in CO-CO_2 atmosphere, the occurrence of the left and right shifted Boudouard reaction may be expected. As ferromanganese production relies on the usage of metallurgical coke, the focus of this section will be accordingly.

The stoichiometric Boudouard reaction is defined as reaction 1.7. From Figure 2.6 it was seen that most of the $CO_2(g)$ present will react with carbon at temperatures above 700°C, and the gas will be approximately 100% $CO(g)$ at 900°C. However, these values are only valid at established equilibrium. The reaction rate has been seen to be determined by kinetics, and has been found to be affected by temperature, gas flow, particle size, carbon structure, and mineral composition[69]–[71]. Sakurovs and Burke evaluated the effect of gas composition (in CO, CO_2, N_2 mixtures) by the investigation of nine different Australian coals[72]. They concluded that the gas composition had little effect on the gasification rate of cokes for a wide concentration range of gases and coke. Nonetheless, a decreasing CO_2 level correlated to a decreased reaction rate.

Aderbigbe and Szekely evaluated coke reactivity in CO-CO_2 atmosphere at temperatures 850-1000°C[73]. Their results indicated that the Boudourard reaction requires temperatures exceeding 1000°C in order to obtain significant rates. In respect to ferromanganese production, it is well known that alkalis, and especially potassium, entering the furnace as a constituent of manganese ores (and coke), influence the Boudouard reaction. Ishak published a literature survey on the reported effect of alkalis (potassium particularly) on the Boudouard reaction[34]. Some of the mentioned studies were Aderibigde and Szekely[73], Rao et al.[74], and Alam and DebRoy[75], all of which showed that the reaction rate of the Boudouard reaction increased significantly by the influence of potassium in the temperature range of 800-

1200°C. Kaczorowski et al. showed that the catalytic effect of potassium had a larger impact on the reaction rate compared to temperature, partial pressure of CO_2, and particle size[4].

Ishak investigated the reactivity of both metallurgical coke and coke impregnated with potassium at temperatures 800-1000°C[34]. The results from experiments conducted in 25%CO_2-75% CO atmosphere at 1000°C is shown in Figure 2.17. The promoting effect of the potassium on the reduction rate is easily observed when comparing the results from untreated metallurgical coke (O-1000 and O-1000-2) with the impregnated metallurgical coke samples (I-1000, 1-1000-2 and 1-1000-3). Thus, the reaction rate of the Boudouard reaction may be significant at temperatures down to 800°C in a ferromanganese furnace. Nonetheless, the extent of the Boudouard reaction is also dependent on the amount and concentration of CO_2 present, which will be affected by the potentially ongoing reduction of manganese ores.
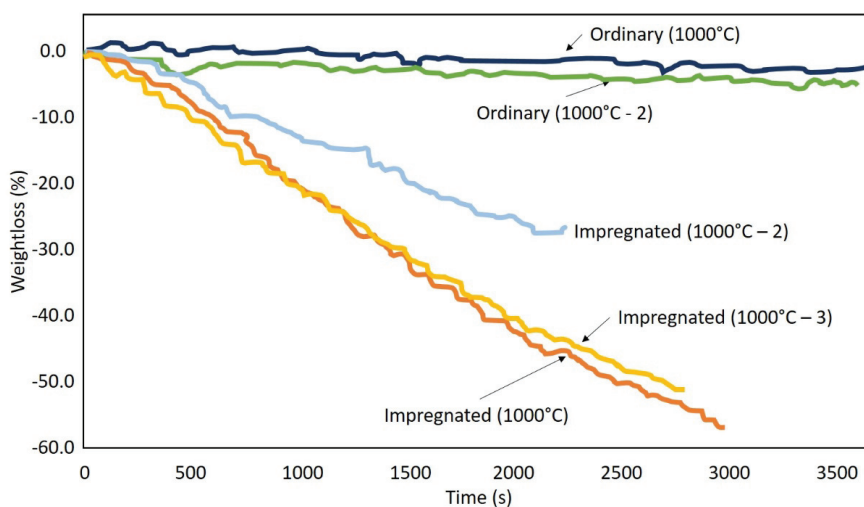
Figure 2.17: Effect of potassium on the kinetics of the Boudouard reaction, shown by weight changes registered for experiments done at 1000°C with either ordinary or impregnated coke. Figure after Ishak [34]

At temperatures below 700°C, the equilibrium of the reaction is shifted towards decomposition of CO into CO_2 and solid carbon. This may also influence the prereduction of manganese ores, as solid carbon may deposit on the ore surface, covering the reactive sites, and thus inhibit reduction. Carbon deposition have been observed in several metallurgical reduction studies conducted in CO-containing atmosphere, where several studies have been published in relation to iron production in the blast furnace. A kinetic study of carbon deposition in the presence of iron pellets in carbon monoxide atmosphere was presented by Haas et al.[76]. Investigated variables included CO pressure and gas flow, types of catalyst, temperature, and the presence of hydrogen, water vapor, and carbon dioxide. The extent of carbon deposition varied with the type of catalyst, where no evidence of carbon deposition on wüstite or magnetite was found, whereas considerable deposition occurred on iron-impregnated firebrick. The carbon deposition reaction rate

appeared to increase with increasing catalyst surface area, whereas changing CO gas flow between 0.25-0.85 L/min appeared to have no effect. Further, it was found that the deposition rate and extent increased with increasing CO pressure between 0.5-2.0 atm. By investigating the effect of temperature, it was found that the carbon deposition rate reached its maximum at 550°C.

El-Geassy and Nasr observed carbon deposition at temperatures below 900°C in isothermal reduction of porous Fe_2O_3 with pure carbon monoxide[77]. Experiments conducted at 700-900°C were stopped before completion and the amount of carbon deposition was seen to be greater than the amount of oxygen removal due to reduction. Carbon deposition was also observed in green and dense compacts, respectively. Jozwiak et al. investigated the reduction of various iron oxides and found that a three step CO reduction of hematite occurred at temperatures 200-600°C. The reduction was accompanied by carbon deposition at temperatures exceeding 400°C[78].

Similar results were presented by Towhidi and Szekely[79], where the influence of carbon deposition on the reduction of hematite pellets with CO, H_2, and N_2 was investigated. Carbon deposition was observed at temperatures below 900°C, where the maximum rate was between 500-600°C. Compared to pure CO atmosphere, it was found that hydrogen (in the presence of CO) had a promoting effect on the carbon deposition. The deposition occurred simultaneously as the reduction process, and was dominating at 500-600°C.

2.5 Gas-solid reaction phenomena

The behavior of the low temperature zone of a ferromanganese furnace is described by gas-solid kinetics and mechanisms. Gas-solid reactions are heterogeneous in nature, implying that geometric factors and transport phenomena may affect the system, in addition to the chemical kinetics. The reactions usually occur at a phase boundary, which implies that transportation of reactants and products, including mass and heat, must be transported to and from the boundary.

The most common gas-solid reactions can be expressed as[80]:

$$A_{(g)} + bB_{(s)} = cC_{(g)} + dD_{(s)} \qquad 2.9$$

These reactions are generally influenced by four main stages, where the influence of each stage may depend on the specific reaction under evaluation:

1. Gaseous diffusion (mass transfer) of reactants/products between bulk and interface (external mass transfer)
2. Diffusion of gaseous reactants/products through the pores of the solid
3. Adsorption/desorption of reactants/products
4. Chemical reaction between the adsorbed gas and the solid

Where it is assumed that diffusion of species to and from, respectively, bulk is considered to be the same mechanism, and is known as external mass transfer. The same applies to diffusion of species through the pores of the solid. Further, stage 3 and 4 are assumed to be represented by the chemical reaction, implying

that external mass transfer, pore diffusion, and chemical reaction are the three main mechanisms. Further, the rate of these phenomena may be affected by other factors, such as heat transfer (for endothermic or exothermic reactions) and structural changes of the solid (e.g. sintering). In addition, nucleation affects gas-solid reactions when a second solid phase is formed. Thus, gas-solid reactions can be considered complex and potentially difficult to analyze. Often the rate of one of the mentioned reaction stages may be significantly lower than the others and hence be the rate-determining step. However, the rate-determining stage may also change during the reaction course. Figure 2.18 shows a representation of how temperature and size of reacting pellet/lump may determine the rate-controlling step in a gas-solid reaction[80]. At small pellet sizes and low temperatures, nucleation effects govern the reaction, whereas an increasing pellet size at low temperature leads to chemical reaction control. At high temperatures, at a pellet particle size above a minimum threshold, diffusional resistance in the solid particle limits the reaction rate. The low and high temperature range is often separated by an intermediate section, where a mixed reaction control occurs.

While there are several phenomena that may affect the reaction in a gas-solid system, the majority of situations are governed by chemical reaction and pore diffusion. These factors will be further elaborated, whereas external mass transfer and temperature effects will be covered briefly. For the following information, the work by Szekely et al.[80] and Levenspiel[81], respectively, is referred to.
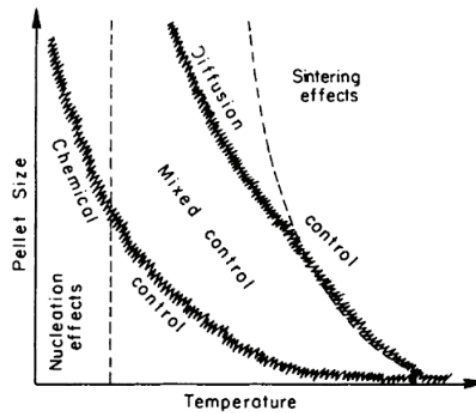
Figure 2.18: Representation of how temperature and pellet size determine the rate-controlling step and the significance of nucleation and sintering effects in gas-solid reactions[80]

External mass transfer describes the diffusion of gas species to and from bulk to particle surface. For a gaseous transferred species A, with concentration C_{As} at the solid surface and C_{A0} in the bulk, the rate of mass transfer from the solid into the gas per unit solid surface area is given as:

$$N_A = h_D(C_{As} - C_{A0}) \qquad \text{2.10}$$

Where h_D is the mass transfer coefficient. This expression assumes equimolar counter-diffusion, i.e. rate of gas diffusion towards surface equals the diffusion rate of gas from surface. In general, external mass transfer rarely limits the overall rate.

Chemical reaction describes the reaction surface kinetics, and includes the adsorption, reaction between species, and lastly desorption of product. More often, the kinetics of adsorption and desorption is not described by the rate equation in a chemical reaction mechanism, as most data can be described by nth-order rate expressions.

A general expression for the reaction rate according to the chemical reaction 2.9 is expressed as (with activity of unity for solids):

$$r_A = k_C \left(C_A^m a_B^n - \frac{C_C^p a_D^q}{K} \right) = k_C \left(C_A^m - \frac{C_C^p}{K} \right) \qquad \text{2.11}$$

Where k_c is the chemical rate constant, K is the equilibrium constant, and C_A and C_C denote the concentrations of reactant and product gases at the particle surface. a_B and a_D are the activities of the solids, and m, n, p, and q, give the reaction orders for species A(g), B, C(g), and D.

If the rate is controlled by chemical kinetics and resistance due to mass transfer is negligible, the gas concentrations at the particle surface will be equal to the bulk concentration.

For irreversible reactions with large equilibrium constants, the rate expression can be simplified to:

$$r_A = k_C \cdot C_A^m \qquad \text{2.12}$$

The chemical rate constant, as appeared in equation 2.11 and 2.12 is described by the Arrhenius equation:

$$k = k_0 e^{-E_a/RT} \qquad \text{2.13}$$

Where k_0 is the pre-exponential factor, a constant for the chemical reaction, E_a is the activation energy for the reaction, R is the universal gas constant and T is the temperature.

Pore diffusion describes the movement of gaseous species within a porous solid. The diffusion of gases through a solid is significantly more complex than the diffusion through a fluid. Two main complicating factors are that the solid volume is not available for diffusive transfer and that the structure of the solid may exhibit varying porosity causing the diffusive path to be more or less tortuous.

If the diffusion resistance in bulk flow, and potential pressure gradients are neglected, the flow of gaseous reactant A in a porous solid may be expressed as:

$$N_A = -D_{eff} \nabla C_A \qquad \text{2.14}$$

Where D_{eff} is the effective diffusivity and ∇C_A is the concentration gradient. The effective diffusivity is affected by two possible mechanisms, which can contribute to varying extent during the reduction course.

The mechanisms are molecular diffusivity and Knudsen diffusivity, where the inverse of the effective diffusivity can be viewed as the sum of the resistance from the effective molecular diffusivity and the Knudsen diffusivity, respectively:

$$\frac{1}{D_{A,eff}} = \left(\frac{1}{D_{AB,eff}} + \frac{1}{D_{A,K}} \right)$$

2.15

When the pores are large, the diffusion will be defined by the molecular diffusion, whereas Knudsen diffusion dominates at small pore sizes. The effective molecular diffusivity is the molecular diffusivity multiplied with the porosity of the solid (ε) divided by the tortuosity (τ) of the solid:

$$D_{AB,eff} = \left(\frac{\varepsilon}{\tau} \right) D_{AB}$$

2.16

The molecular diffusivity can be approximated from the Chapman-Enskog equation:

$$D_{AB}(cm^2 s^{-1}) = 0.0018583 \frac{\sqrt{T^3 \left(\frac{1}{M_A} + \frac{1}{M_B} \right)}}{p\sigma_{AB}^2 \Omega_{AB}}$$

2.17

Where D_{AB} is the molecular diffusivity, T is the temperature, M_A and M_B is the molar mass of species A and B, respectively, p is the pressure, σ_{AB} is a constant, and Ω_{AB} is the collision integral.

The Knudsen diffusivity is found from gas theory:

$$D_{A,K} = \frac{4}{3} \left(\frac{8RT}{\pi M_A} \right)^{1/2} K_0$$

2.18

Where $D_{A,K}$ is the Knudsen diffusivity, R is the ideal gas constant, T is the temperature, M_A is the molar mass of species A, and K_0 is a parameter characteristic of the solid.

The extent to which the reaction rate is lowered due to resistance to pore diffusion is often given through the quantity known as the effectiveness factor:

$$\eta = \frac{(actual\ mean\ reaction\ rate\ within\ pore)}{(rate\ if\ not\ slowed\ by\ pore\ diffusion)}$$

2.19

Heat effects during reaction may arise when the reaction rate is fast and the heat released is not removed at sufficient rate, causing the temperature of the particle to deviate from the ambient/fluid. The exothermic or endothermic reaction may result in both a temperature variation within the particle, as well as a temperature difference between particle and bulk gas.

The convective heat transfer between a particle surface and a gas stream can be expressed as:

$$q_y = h(T_s - T_0) \qquad\qquad 2.20$$

Where q_y is the heat flux and h is the heat transfer coefficient. The heat transfer coefficient is normally estimated from empirical relations for different systems.

The conductive heat transfer in porous solids is described by Fourier's law:

$$q_y = -k\nabla T \qquad\qquad 2.21$$

2.5.1 Gas-solid reaction analysis

Gas-solid reactions are studied experimentally either isothermally or non-isothermally. As the names indicate, isothermal experiments are conducted at constant temperatures, whereas non-isothermal experiments involve heating the sample at a rate, which is commonly linear. The reaction extent is usually expressed in terms of a conversion degree, which for thermogravimetric analysis may be defined as:

$$\alpha = \frac{m_0 - m_t}{m_0 - m_\infty} \qquad\qquad 2.22$$

Where m_0 is the initial weight of the sample, m_t is the weight at time t (or temperature T for non-isothermal), and m_∞ is the theoretical weight loss. The conversion degree thus expresses the extent of reactants transformed to product.

The general equation for kinetic analysis under isothermal conditions is described according to 2.23 in differential form[82]. The equation is valid for a single-step reaction scheme.

$$\frac{d\alpha}{dt} = k(T) \cdot f(\alpha) \cdot h(P) \qquad\qquad 2.23$$

Where α is the conversion of reactant, and dα/dt is the conversion rate, k(T) is the rate constant, and f(α) is the reaction model in differential form. Reaction models describe the relation between the conversion rate and conversion extent. The pressure dependence h(P) is commonly ignored in most computational methods. When gaseous species are involved as reactants or products, the pressure may potentially have a large effect on the kinetics. Nonetheless, the rate is commonly assumed to be a function of only two variables, the temperature through the rate constant, and the conversion through the reaction model:

$$\frac{d\alpha}{dt} = k(T) \cdot f(\alpha) \qquad\qquad 2.24$$

The integrated form of equation 2.24 becomes:

$$g(\alpha) = k(T) \cdot t \qquad\qquad 2.25$$

41

The temperature dependence of the rate constant is commonly given by the Arrhenius equation:

$$k(T) = Ae^{-\frac{Ea}{RT}} \qquad\qquad 2.26$$

Where A is the preexponential factor, E_a is the activation energy, and R is the universal gas constant. The rate's dependence on the conversion is expressed through a suitable reaction model. Reaction models are characteristic for the governing mechanism of solid-state reactions, e.g. first order chemical reaction or three-dimensional diffusion. Some of the most common reaction models are presented in Table 2.9[83].

Table 2.9: Common reaction models[83], [84]. α is the conversion degree, often also denoted X

	Reaction model	Differential form: $f(\alpha) = 1/k\ d\alpha/dt$	Integral form: $g(\alpha) = kt$
	Nucleation models		
1	Power law (P2)	$2 \cdot \alpha^{(1/2)}$	$\alpha^{1/2}$
2	Power law (P3)	$3 \cdot \alpha^{(2/3)}$	$\alpha^{1/3}$
3	Power law (P4)	$4 \cdot \alpha^{(3/4)}$	$\alpha^{1/4}$
4	First order kinetics or random nucleation followed by an instantaneous growth of nuclei (Avrami-Erofe'ev eq. n=1)	$(1-\alpha)$	$-\ln(1-\alpha)$
5	Random nucleation and growth of nuclei through different nucleation and nucleus growth models. (Avrami-Erofeev eq. n $\neq$1.)	$n(1-\alpha)[-\ln(1-\alpha)]^{1-1/n}$	$[-\ln(1-\alpha)]^{1/n}$
6	Avrami-Erofe'ev (n=2)	$2(1-\alpha)[-\ln(1-\alpha)]^{1/2}$	$[-\ln(1-\alpha)]^{1/2}$
7	Avrami-Erofe'ev (n=3)	$3(1-\alpha)[-\ln(1-\alpha)]^{2/3}$	$[-\ln(1-\alpha)]^{1/3}$
8	Avrami-Erofe'ev (n=4)	$4(1-\alpha)[-\ln(1-\alpha)]^{3/4}$	$[-\ln(1-\alpha)]^{1/4}$
	Diffusion models		
9	1D-diffusion	$1/2\alpha$	α^2
10	2D-diffusion	$[-\ln(1-\alpha)]^{-1}$	$[(1-\alpha)\ln(1-\alpha)]+\alpha$
11	3D-diffusion	$3(1-\alpha)^{2/3}/2(1-(1-\alpha)^{1/3})$	$[1-(1-\alpha)^{1/3}]^2$
	Geometrical contraction models		
12	Contracting area	$2(1-\alpha)^{1/2}$	$1-(1-\alpha)^{1/2}$
13	Contracting sphere	$3(1-\alpha)^{2/3}$	$1-(1-\alpha)^{1/3}$
	Reaction order models		
14	Zero order	1	α
15	First order	$(1-\alpha)$	$-\ln(1-\alpha)$
16	Second order	$(1-\alpha)^2$	$(1-\alpha)^{-1}-1$
17	Third order	$(1-\alpha)^3$	$0.5((1-\alpha)^{-2}-1)$

For non-isothermal studies, the temperature is varied as a function of time, which for linear heating is expressed as:

$$T = T_0 + \beta t \qquad \qquad 2.27$$

Where T is the temperature at time t, T_0 is the starting temperature, and β is the linear heating rate (K/min). The relation between conversion rate with respect to time and temperature, respectively, may be expressed as:

$$\frac{d\alpha}{dT} = \frac{d\alpha}{dt} \cdot \frac{dt}{dT} \qquad \qquad 2.28$$

The differential form of the non-isothermal rate law is then expressed according to equation 2.29.

$$\frac{d\alpha}{dT} = k(T)f(\alpha) = \frac{A}{\beta} exp\left(\frac{-E}{RT}\right)f(\alpha) \qquad \qquad 2.29$$

Which in integrated form gives rise to the temperature integral, as shown in 2.30:

$$g(\alpha) = \frac{A}{\beta} \int_0^T exp\left(\frac{-E_a}{RT}\right)dT \qquad \qquad 2.30$$

The temperature integral in equation 2.30 does not have an analytical solution, however several approximate solutions have been utilized in the past, e.g. the trapezoidal method and the Doyle-approximation.

The aim of the mathematical description of the process rates is to obtain information on the reaction mechanism, the activation energy, and the frequency factor, sometimes referred to as the *kinetic triplet*. The available methods for interpretation of the experimental data are generally categorized as model-fitting or model-free methods, where methods exist for both isothermal and non-isothermal data.

Model-fitting involves an evaluation of the different existing reaction models (diffusion, nucleation, chemical reaction etc.) applied to the experimental data, where the model resulting in the more optimal statistical fit is assumed to be representative. The isothermal model-fitting method (conventional method) involves two fits, where the first determines the rate constant. The rate constant is deduced from the slope of the reaction model that obtains the best fit. The second fit is from the Arrhenius relation, from which the activation energy (E_a) and the frequency factor (A) is deduced from the slope and intercept with the y-axis. Model-fitting methods have also been developed and utilized for non-isothermal data, including the direct differential method, and the methods developed by Freeman-Carroll and Coats-Redfern, respectively. Non-isothermal model-fitting methods have been highly criticized, as utilizing the model-fitting method to a single non-isothermal curve will not produce reliable kinetic values[85]–[89]. This procedure is not recommended as it assumes a constant triplet (A, Ea, and model), and they involve the simultaneous fitting of these three parameters from a single curve. In addition, they involve a single heating rate, which is not always sufficient to observe representative reaction kinetics[83]. Arrhenius parameters obtained from

isothermal studies have often shown to disagree with parameters determined from non-isothermal experiments. According to Vyazovkin and Wight[90], there are two main reasons for this. Firstly, for non-isothermal data, the model-fitting approach often fails to obtain a separation between the dependence on temperature and the reaction model. As such, a large number of reaction models will obtain a high-degree fit. Secondly, isothermal and non-isothermal experiments are generally conducted in different temperature ranges. If the evaluated reaction occurs through several steps having different activation energies, this would not be reflected by a model-fitting method, as this provides a single value describing an overall process. Jiménez et al. [84] showed that a set of non-isothermal curves recorded from different heating rates was required in order to employ the model-fitting method successfully for non-isothermal experiments. The authors showed that by evaluating single-curve data, an apparent optimal fit was obtained for nine different reaction models, which gave rise to a large variance in activation energies. This was also observed by The Kinetics Committee of the International Confederation for Thermal Analysis and Calorimetry (ICTAC) which presented an extensive comparison of various methods used to determine kinetic parameters, leading to the recommendation of multiple heating rate programs[85].

Model-free methods are often referred to as isoconversional methods, although not all model-free methods are isoconversional. Another commonly used notation is multicurve-methods, as multiple curves are required to perform the analysis. This implies several temperatures for isothermal experiments, and several heating rates for non-isothermal experiments. These methods allow for the determination of activation energies as a function of conversion extent, as well as temperature. Further, the activation energy is determined without relying on a pre-determined reaction model, which is why this method is often referred to as a model-free approach. The basic assumption of the isoconversional method is that the reaction model is not dependent on temperature or heating rate. Vyazovkin and Wight showed that by applying this method, similar dependencies of the activation energy for isothermal and non-isothermal experiments were obtained[90]. In order to obtain frequency factors, an assumption regarding the governing mechanism is required. As the isoconversional method calculates the activation energy at progressive reduction, it may reveal complex reaction schemes involving multiple steps.

The standard isoconversional method for isothermal data is performed by taking the natural logarithm of 2.25, as expressed in 2.31. A plot of (-lnt) vs 1/T at each conversion α will yield the activation energy from the slope, regardless of the model.

$$-\ln t = ln\left(\frac{A}{g(\alpha)}\right) - \frac{E_a}{RT} \qquad 2.31$$

Another isoconversional method is the Friedman's method, which is based on the natural logarithm of equation 2.24, i.e. the rate equation in differential form. As was mentioned, isoconversional methods may reveal steps constituting complex reaction schemes. However, Khawam and Flanagan have shown that artifactual variations in activation energy may be observed from the calculation methods employed in both isothermal and non-isothermal systems[91], [92]. Two types of variation in activation energy was observed for simulated data, where a true variation due to complex nature of the process was observed in combination with an artifactual resulting from calculation methods. The latter referred to e.g. experimental variables of low control giving in a shift of the conversion-time curve.

For complex reaction schemes, there are two potential approaches for analysis. As already mentioned, the isoconversional method may reveal distinct steps in a reaction scheme. Secondly, if possible, the overall observed data may be separated by deconvolution of the individual reaction steps if the overall observed data consists of distinct peaks or areas indicating multistep. Deconvolution is to use the trend of the overall reaction behavior to express the individual contributing steps using an appropriate fitting function. Literature shows the use of different fitting functions, such as Gaussian and Lorentzian. The majority of these fitting functions, including Gaussian (equation 2.32) and Lorentzian, assume a symmetrical behavior of the kinetic curves. Other fitting functions, as the Fraser-Suzuki (equation 2.33) allows for asymmetrical behavior. Deconvolution is only possible when the reaction data consists of clear distinct peaks.

$$y = a_0 \cdot exp\left[-\frac{1}{2}\left(\frac{x - a_1}{a_2}\right)^2\right] \qquad 2.32$$

$$y = a_0 \cdot exp\left[-ln2\left[\frac{\ln\left(1 + 2a_3\frac{x - a_1}{a_2}\right)}{a_3}\right]^2\right] \qquad 2.33$$

The presented relations for non-isothermal temperature regimes includes the explicit value of the heating rate, which means that the equations are limited to systems where the sample temperature does not deviate significantly from the reference temperature. A computational method applicable to arbitrary temperature variation was presented by Vyazovkin[93]. The method uses the isoconversional principle, and includes numerical integration of the temperature integral presented in equation 2.30 over the actual temperature variation as a function of time, according to equation 2.34:

$$J[E, T(t)] = \int_0^t \exp\left[-\frac{E}{RT(t)}\right] dt \qquad 2.34$$

Assuming that the reaction model is independent of temperature variation, a given set of conversions obtained at n different heating programs gives the relation:

$$\phi(E_\alpha) = \sum_{i \neq i}^{n} \sum^{n} \frac{J[E_\alpha, {}_i(t_\alpha)]}{J[E_\alpha, {}_j(t_\alpha)]} = min \qquad 2.35$$

From which the activation energy may be obtained by varying E_α until minimum is attained.

2.5.2 Models

Several different kinetic models describing gas-solid reactions exist. The choice of model relies on the specific system under evaluation and the valid assumptions that can be made. A good model illustrates reality in the most accurate manner without introducing overly complex mathematical considerations. Models describing a general gas-solid reaction generally fall within three categories: where the solid is assumed non-porous, where the solid is porous, and where the solid is composed of several non-porous subunits (particles/grains), respectively. Modelling of gas-solid systems is an extensive field, and a full review of all existing models and the extension and development of these has not been performed. Rather, this section aims to provide a short overview of the topic.

Most commonly used is the shrinking core model, which generally describes gas-solid reactions involving an initially non-porous solid. The work by Szekely et al.[80] and Sohn[94] may be referred to for further details on the information provided in the following paragraphs if not other stated.

The shrinking core model describes topochemical reaction mechanisms, where the reaction proceeds from the outer surface towards the center, leading to the formation of a product layer surrounding the unreacted core. This model generally describes initially non-porous solids as reactants, implying that the reaction interphase is considered sharp. As all mathematical models, the shrinking core follows certain assumptions and limitations. Firstly, as already mentioned, the reactant solid is assumed to be non-porous. Secondly, the conventional shrinking core model may only be used to describe isothermal systems. Finally, the reaction is assumed to be first-order with respect to gaseous reactants, and transportation of reactant and product gases occurs via equimolar diffusion.

The model incorporates contributions from chemical reaction kinetics, diffusion through porous product layer, and external mass transfer. The general expression including all three factors is expressed as[80]:

$$t^* = g_{F_p}(X) + \sigma_s^2 \left(p_{F_p}(X) + \frac{4X}{Sh^*} \right) \qquad 2.36$$

Where X is the conversion, t* is the dimensionless reaction time (t* = 1 for full conversion of solid reactant) and F_p is the shape factor describing the geometry of the solid reactant (= 1, 2, or 3 for a slab, a long cylinder, or a sphere, respectively). The function g is the reaction model for chemical reaction, and σ_s^2 is the shrinking core modulus, which gives the ratio between the influence of the chemical reaction vs the influence of mass transfer (pore diffusion and external mass transfer). This implies that the two components in the brackets in relation to the shrinking core modulus represents diffusion resistances, where the left component represents diffusion in particle and the right component represents mass transfer through bulk.

Relation between the dimensionless time and the specific reaction time, as well as the fully described shrinking core modulus is found in the literature. Inserting the relations, and assuming a negligible resistance from external mass transfer through boundary layer, gives the following shrinking core equation valid for a particle of spherical geometry:

$$t = \frac{\rho_s r_p}{k_c} \frac{1}{C_{CO}^0} g(X) + \frac{\rho_s}{6D_E} \frac{r_p^2}{C_{CO}^0} p(X) \qquad 2.37$$

Where t is the specific reaction time, ρ is the particle density, r is the particle radius, k_C is the chemical rate constant, C^0 is the bulk gas composition, g(X) is the reaction model for chemical reaction with contracting volume, D_E is the diffusion constant, and p(X) is the reaction model for 3D diffusion.

In contrast to the sharp interface between reacted and unreacted non-porous solid in the shrinking core model, a variation in conversion throughout the solid is expected in an initially porous solid. If the chemical reaction rate is slower than the diffusion rate, the gas is uniform throughout the solid, causing the reaction to occur at the same rate throughout the solid. This system may be described by the so-called homogeneous volume reaction model, in which the reaction is independent of particle size[95]. When the diffusion rate is lower than the chemical reaction rate, the reaction may take place in a more narrow region between reacted and unreacted parts of the solid[96]. This situation is similar to the non-porous shrinking core model under pore diffusion control. An intermediate system may also exist, where the reaction-diffusion interaction is such that the outer layers of the particle is exhausted while the reaction may still take place throughout the solid. Different models applies to different structures, where Figure 2.19 shows an illustration of concentration profiles and solid particle structure for volumetric reaction model, grain model, and pore model, respectively.
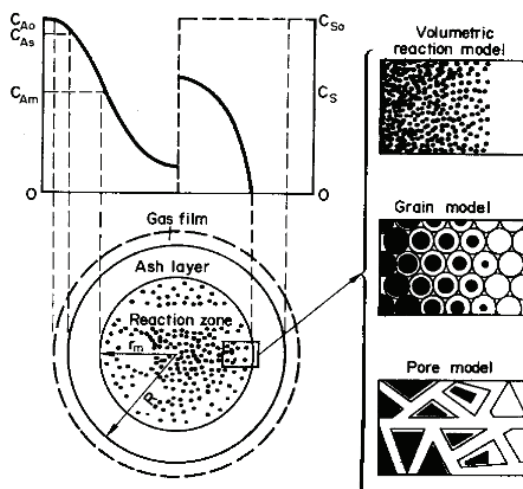
Figure 2.19: Schematic diagram of concentration profile and solid structure in particle for different reaction mechanisms[97]

The grain model is an extension of the shrinking core model, and was developed by Szekely and Evans[98] and further generalized by Sohn and Szekely[99]. In general, assumptions and limitations listed for the shrinking core model is also valid in terms of the grain model. The reaction according to the grain model can be viewed as a set of shrinking core mechanism occurring throughout the particle. The overall reduction of the particle may also be viewed in a shrinking core manner, where grains closer to the particle surface is more reacted than grains in the center. It was also assumed that the diffusion of reactant gas through the

product layer around the individual grains provides negligible resistance to the rate. The generalized formula for the grain model may be expressed as equation 2.36, where the modulus is dissimilar from the shrinking core modulus. A model describing the reaction of a porous solid where the pores are subjected to enlargement is the random-pore model presented by Bhatia and Perlmutter[100]. The model allows for arbitrary pore size distributions in the reacting solid.

An important aspect of the modeling of gas-solid reactions is the law of additive reaction times. For gas-solid reaction systems governed by mixed control of chemical reaction and pore diffusion, Sohn[101] showed that the time required to attain a certain conversion was the sum of the time required to attain the conversion under full chemical reaction control and full diffusion control, respectively. It was further shown that the law was valid regardless of the relation between the rate and solid conversion.

2.6   Mass and energy balances

This section presents staged material and energy balances for the production of 1 tonne of HC FeMn and SiMn, respectively, by the use of HSC Chemistry 9[17]. Material and energy balances represent important tools in process industry. They may provide information on energy consumption, the energy distribution between the various input and output streams, or the effect of different parameters on e.g. the off-gas characteristics. In this section, the energy recovery potentials within the various output streams will be commented on. While conventional energy balances are expressed through enthalpies, another way of assessing a process is through exergy, which is the amount of energy that may be converted to useful work. The mass balances presented in this section will be presented both in terms of energy (enthalply) and exergy, to determine the potential difference between the two types of system assessment. This work was also published as a scientific paper[102].

Process chemistry

The production processes of high-carbon ferromanganese and silicomanganese in the submerged arc furnace are very similar, however different raw materials are used and hence the products are different. Raw materials in HC FeMn are commonly manganese ore and/or sinter, coke and fluxes. Similar raw materials are also used for SiMn, in addition to others: quartz is added to obtain a sufficient Si-content in the alloy and the end slag from HC FeMn production, with a relatively high content of MnO, is often used as a source of manganese in SiMn. (Fe)Si-remelt or off-grade qualities may also be added.

The submerged arc furnace may be divided into two main areas, i.e. the prereduction zone and the coke-bed zone. The prereduction zone is defined as the part of the furnace where the materials remain in solid state. The reactions and characteristics of this zone was presented in section 1.1.1, and will thus not be reprinted here. When the temperature reaches 1200-1400°C, the charge will have formed a liquid slag from which the final reduction of MnO to manganese metal will occur at the slag/coke bed interface. Similarly, SiO_2 will be reduced to silicon. This part of the furnace is known as the coke-bed zone. The product metals are saturated with carbon and the C content is thus 7% and 1.5% for a typical HC FeMn and SiMn alloy,

respectively. The reactions occurring in the coke-bed zone are shown in equation 2.38-2.39. In addition, some carbon is dissolved in the alloy.

$$MnO(l) + C = Mn(l) + CO(g) \qquad\qquad 2.38$$
$$SiO_2(l) + 2C = Si(l) + 2CO(g) \qquad\qquad 2.39$$
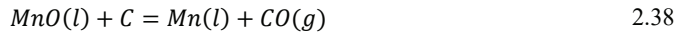
The CO-gas formed in the metal producing reactions will partly be consumed in the low temperature zone in the reduction of the higher oxides. A typical HC FeMn alloy contains 78% Mn, 7% C and %Si < 1, whereas SiMn has a silicon content of 17-20%. Due to this, SiMn production requires a higher process temperature compared to HC FeMn. Typical temperatures are 1500°C for HC FeMn and 1600°C for SiMn.

Mass and energy balance

The energy consumption of a process can be determined by the net effect of exothermic and endothermic reactions in the process, or by evaluating the enthalpy of the materials going in and out of the furnace. The energy used in the process will be transformed into heat or energy in the substance.

Assumptions made to construct the energy balances valid for both processes are as follows:

- Mixing enthalpies were not included for any of the species
- Losses related to furnace operation (heat loss, cooling water, fines etc.) were not included
- Prereduction degree was set to 25% (75% of CO_2 produced from reduction of Mn_3O_4, iron oxides and carbonate decomposition reacts according to Boudouard).
- Alkali circulation was not included
- Evaporation of Mn and Si was not evaluated

HC FeMn

The charge mixture is based on two different manganese ores (ore 1 and 2) and sinter in a ratio approximately 1:0.4:1. Ore 1 and sinter are considered acidic (high in silica and alumina), whereas ore 2 is high in CaO. Average oxygen level is $MnO_{1.7}$ and a total of 17.95 kmol Mn is added. Dolomite is added as flux, corresponding to 10 wt% of the total input charge. Coke is used as reductant and the added amount gives a fixed carbon of 358 kg. A water content of approximately 10% in the raw materials was assumed. The relation between the MnO liquidus content and the slag basicity (CaO+MgO/ SiO_2+Al_2O_3) has previously been calculated[3] and was used to predict the distribution of manganese between alloy and slag. The alloy will be saturated in carbon, correlating to 7%. Raw materials enter the furnace at 25°C, whereas slag and alloy is tapped at 1500°C and the off-gas is assumed to 200°C. The defined input of raw materials and corresponding output are presented in Table 2.10.

The specified system has a total energy consumption, and required electric feed, of 2456 kWh per tonne of alloy. The energy streams of the furnace are presented in a Sankey diagram in Figure 2.20. The streams are given both by specific energy content in kWh and as percentage of total.

Table 2.10: Input and output of staged material and energy balance for production of ca. 1 tonne of HC FeMn. All raw materials are entering the furnace at 25°C. Output temperatures are 1500°C for slag and alloy and 200°C for off-gas

INPUT			OUTPUT		
Species	kmol	kg	Species	kmol	kg
MnO_2	9.50	826.16	Mn(l)	14.34	787.99
Mn_3O_4	2.82	644.56	Si(l)	0.01	0.40
Fe_3O_4	0.84	193.33	Fe(l)	2.51	139.89
SiO_2	2.88	172.98	C(l)	5.82	69.87
Al_2O_3	0.74	75.04			
CaO	0.41	22.71	MnO(l)	3.61	256.13
MgO	0.20	8.02	SiO_2(l)	2.87	172.12
C	29.85	358.56	Al_2O_3(l)	0.74	75.04
$CaCO_3$	2.20	220.19	CaO(l)	2.61	146.08
$MgCO_3$	1.36	114.67	MgO(l)	1.56	62.84
H_2O	11.00	198.17			
			CO(g)	16.54	463.26
			CO_2(g)	11.06	486.59
			H_2O(g)	9.50	171.15
			H_2(g)	1.50	3.02
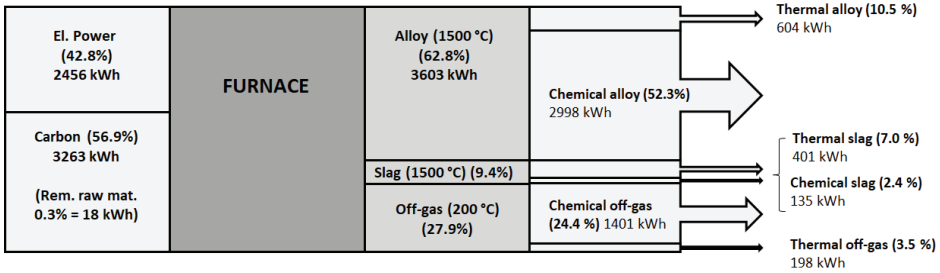
Figure 2.20: Sankey diagram showing energy (enthalpy) streams for production of ca. 1 tonne of HC FeMn alloy. All percentages are given respective to the total energy input/output. Solidification enthalpy is included in thermal streams

SiMn

The staged balance is based on raw materials as Assman ore, slag and embedded metallics from the HC FeMn process, quartz, coke (Polish and Chinese), dolomite and silicon sculls. 390 kg remelt material is circulating in the process. Oxygen level in Mn-sources, given by x in MnOx, is 1.2 and the total amount of consumed carbon is 274 kg. The alloy is carbon saturated, corresponding to 1.5%. It was assumed that the end slag contains 8% MnO and 43% SiO_2. The charge mixture corresponds to the production of

approximately 1 tonne of alloy, excluding the metal embedded in slag (approximately 37 kg in this case). Compositions of input and output streams are presented in Table 2.11.

Table 2.11: Input and output of staged material and energy balance for production of ca. 1 tonne of SiMn. All raw materials are entering the furnace at 25C. Output temperatures are 1600°C for slag and alloy and 400°C for off-gas

Input			Output		
Species	kmol	kg	Species	kmol	kg
MnO_2	1.58	137.36	Mn(l)	13.23	726.70
MnO	9.77	692.70	Si(l)	7.56	212.33
Mn	3.17	173.88	Fe(l)	1.47	82.20
Fe_2O_3	0.39	61.48	C(l)	1.30	15.55
Fe	0.70	39.20			
SiO_2	12.89	774.43	MnO(l)	1.28	90.97
Si	2.82	79.06	SiO_2(l)	8.14	489.32
Al_2O_3	1.77	180.37	Al_2O_3(l)	1.77	180.37
CaO	3.82	213.94	CaO(l)	4.33	242.82
MgO	2.14	86.05	MgO(l)	2.55	102.86
C	22.81	273.94	K_2O(l)	0.25	23.74
K_2O	0.25	23.74			
$CaCO_3$	0.52	51.55	CO(g)	19.74	552.87
$MgCO_3$	0.42	35.16	CO_2(g)	2.71	119.12
H_2O	5.33	96.02	H_2O(g)	4.33	78.00
			H_2(g)	1.00	2.02
Remelt		390.54	Remelt		390.54

The energy analysis of SiMn is presented as a Sankey diagram showing the energy streams in Figure 2.21, both in specific energy content in kWh and as percentage of total. The enthalpy balance gives a total energy deficiency and required electrical energy feed of 3419 kWh. The Sankey diagram shows that approximately 21% of the total input energy has been converted into thermal energy, whereas the remaining is found as chemical energy. As for HC FeMn, the key step to improving energy efficiency lies within the chemical energy in the off-gas containing 1631 kWh (20%) of the total energy output. If the chemical energy in alloy, off-gas and remelt is considered recovered, the total energy lost is 22.8%. 1299 kWh (16.1%) of the total energy is found as heat in alloy and slag (1533 kWh (19%) including the remelt).

Exergy analysis

The exergy analyses presented in this section are representative for the HC FeMn and SiMn systems that were described previously in relation to the energy (enthalpy) analyses. A general expression for an exergy balance is defined as follows[103]:
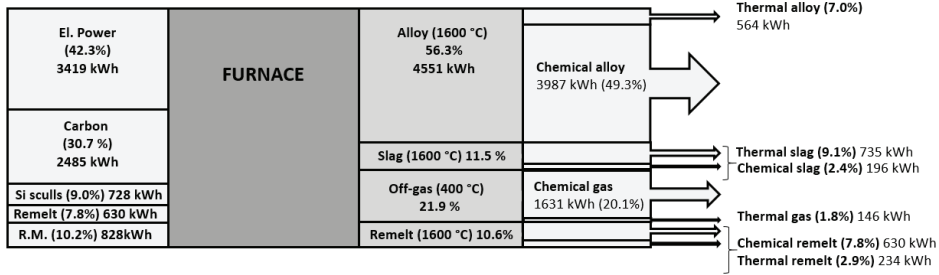
Figure 2.21: Sankey diagram showing energy (enthalpy) streams for production of ca. 1 tonne of SiMn. All percentages are given respective to the total energy input/output. Solidification enthalpy is included in thermal stream. (R.M=remaining materials)

$$\sum_j \left(1 - \frac{T_0}{T_j}\right) Q + W + \sum_i m_i e_i - \sum_o m_o e_0 - E_D = 0 \qquad \text{2.40}$$

Where the first term is the potential work utilized from a heat stream, W is added work (electrical energy) and e denotes the exergy with subscript i for input and o for output. E_D is the destructed exergy. The total exergy of a material stream consists of two different contributions similar to the enthalpy: physical (thermal) exergy and chemical exergy:

$$e = e^{ph} + e^{ch} \qquad \text{2.41}$$

$$e^{ph} = (h - h_0) - T_0(s - s_0) \qquad \text{2.42}$$

$$e^{-ch} = \Delta G_f^0 + \sum_y n_y e_y^{-ch} \qquad \text{2.43}$$

Enthalpies, entropies and Gibbs formation energies needed in the calculations are given by HSC Chemistry 9. e_y^{-ch} is standard chemical exergy respective to a reference environment of $T_0 = 25°C$, $p_0 = 1$ atm and standard concentration of reference substances in the natural environment. These exergies were given by Szargut et al.[104] and is also found in HSC Chemistry 9[17].

HC FeMn

The exergy analysis for HC FeMn is presented as a Grassmann diagram in Figure 2.22. Numbers are valid for production of c. 1 tonne of alloy. The main difference between the exergy balance and the enthalpy balance is that input and output are always equal in terms of enthalpy, whereas the output exergy is always

lower than the input. It can be seen from the diagram that 13.7% of the total input exergy is lost during the process due to irreversibilities. 46.7% of the total exergy was transferred to the product (alloy) as chemical exergy. The remaining exergy has been converted into thermal exergy in various forms and chemical exergy in slag and off-gas, all of which may potentially be recovered. If none of these sources were to be recovered at the plant, the exergy destruction would be 46.2%. As previously mentioned, the HC FeMn slag is often used as a raw material in SiMn production, and the chemical energy in the slag may hence be considered recovered. In addition, the chemical exergy in the off-gas is often utilized. Considering this, the exergy destruction becomes 26.1%.
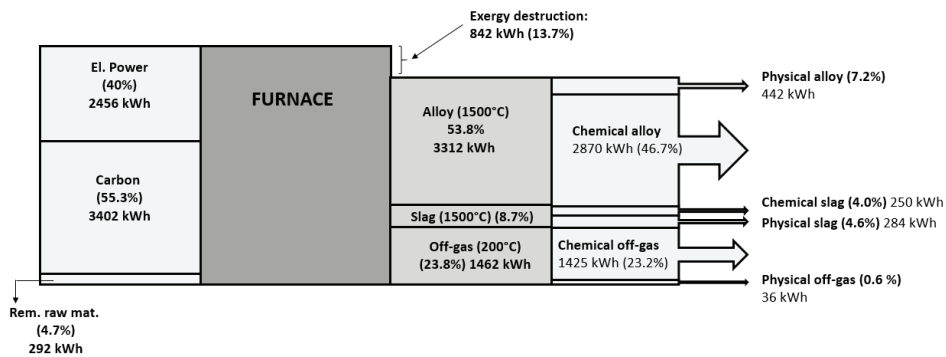
Figure 2.22: Grassmann diagram showing exergy streams for production of 1 tonne of HC FeMn. All percentages are given respective to the total exergy input. Solidification is included in thermal (physical) streams

SiMn

The resulting exergy balance for SiMn is presented as a Sankey diagram in Figure 2.23, where exergy streams are given in both kWh and percentage of total. Numbers are valid for production of approximately 1 tonne of alloy. If all exergy in the output material streams was recovered, the amount of destructed exergy would be 10.8%. By considering all exergy streams that seldom are recovered (all thermal exergy and chemical exergy in slag), the exergy destruction is 28.2%. Other observations are that only 43 kWh (0.5%) may be recovered from the low-temperature thermal exergy in the off-gas. In contrast, the high-temperature thermal exergy of slag, alloy and remelt is 1048 kWh(12.5%).

Observations

Potential recovery of energy lies within all energy reserves that are not chemical energy in the produced alloy. The chemical potential in the slag is relatively low in both processes, however the slag in HC FeMn can be used as a raw material in SiMn and may hence be a useful by-product. The most straightforward potential recovery source is the chemical energy/exergy in the off-gas. The gas may be burned to produce thermal heat or electricity, however burning produces large amounts of CO_2. Plants located in industry

parks may also sell the gas to neighboring industries[105]. The required technologies are well established and utilized at plants today. The available chemical energy is:

- 1401 kWh (24.4% of total output) for HC FeMn
- 1631 kWh (20.1% of total output) for SiMn

These values are valid for an off-gas temperature of 200°C and 400°C for HC FeMn and SiMn, respectively, and a prereduction degree of 25%. Both the temperature and the content of CO will vary from day to day in industrial operation and the potential recoverable energy will hence vary correspondingly.
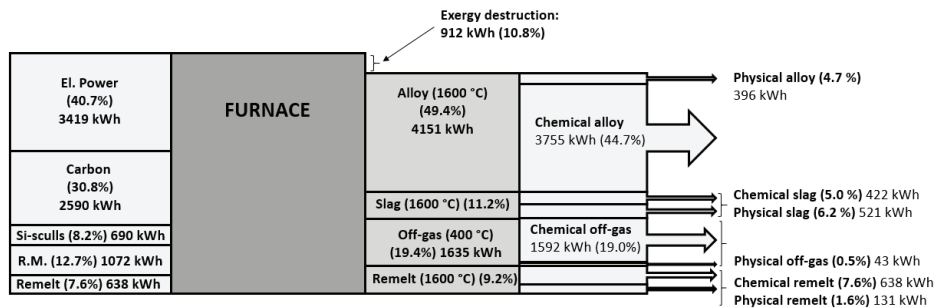
Figure 2.23: Grassmann diagram showing exergy streams for production of 1 tonne of SiMn. All percentages are given respective to the total exergy input. Solidification is included in thermal (physical) streams (R.M. = remaining raw materials)

The main heat source is cooling of high temperature alloy and slag. The heat is produced batchwise which makes recovery challenging, however a Norwegian plant, Eramet Kvinesdal, has implemented recovery through hot water from the molten slag[106]. When cooled and solidified, the available energy in the alloy and slag is:

- 1005 kWh (equal to 17.5% of total energy output) for HC FeMn. The amount that potentially may be recovered is given by the exergy, which is 726 kWh.
- 1299 kWh (equal to 16.1% of total energy output) for SiMn, not including thermal energy in remelt. Corresponding exergy is 917 kWh. Values including remelt are 1533 kWh and 1048 kWh for energy and exergy, respectively.

The exergy analyses showed the reduction in energy quality accompanying the transformations occurring in the furnace. These values were found to be 13.7% for HC FeMn and 10.8% for SiMn. A comparison of the calculated enthalpies and exergies can be seen in Figure 2.24 for HC FeMn(left) and SiMn(right). When calculating an enthalpy balance, it is assumed that species in the respective highest oxidation state, e.g carbon in form of CO_2, has zero enthalpy at $T = 25$°C and $p = 1$ atm regardless of the species' concentration. In exergy calculations, the species will have a certain amount of chemical exergy if the concentration of the compound deviates from the compounds concentration in the natural environment. Due to this, chemical exergy of material streams may be larger compared to the corresponding enthalpy. This is for example seen

for the slag in both systems. Nonetheless, the chemical enthalpy and exergy in off-gas is highly similar. Additional information provided by the diagram is the difference in the available energy from heat streams (enthalpy) compared to the amount potentially recovered (exergy). It can be seen that low-temperature heat sources (such as the off-gas) may to a lesser degree be recovered compared to high-temperature sources.
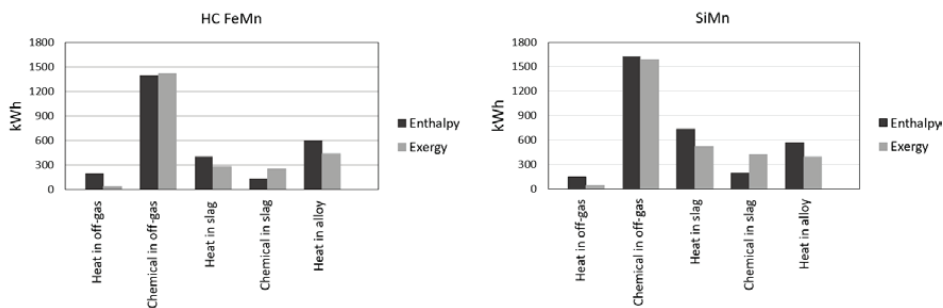
Figure 2.24: Comparison of calculated enthalpies and exergies in output streams for HC FeMn(left) and SiMn(right). Chemical enthalpy and exergy for alloy is included

In industrial operation, parameters related to furnace operation (heat loss from furnace, cooling water, fines etc.) are obviously a major contributor to the overall energy consumption of the process. According to Tangstad and Olsen[107], the losses may result in an efficiency of 80%. This has not been accounted for in these calculations, as the focus was rather on the energy within the material streams. With no losses considered, the electric energy consumption was found to be c. 2460 kWh for HC FeMn and 3420 kWh for SiMn, which agrees well with previously reported energy consumptions[3]. The chemical energy in the off-gas is the largest potential recover source, which is both well-known and implemented in the majority of plants today. Other major sources lies within the thermal energy of the alloy and slag. This energy is more difficult to recover, however technology has been implemented to produce hot water from molten slag beds at a Norwegian plant.

The distribution of energy and exergy between the different material streams are highly similar and key potential recovery sites will be the same regardless of the analysis method utilized. The additional information provided by the exergy analysis compared to the enthalpy is the amount of exergy lost (reduced energy quality) due to irreversible processes within the furnace. These values were found to be 13.7% for HC FeMn and 10.8% for SiMn.

3   Experimental

This chapter provides a detailed description of the utilized equipment and raw materials, along with the techniques used to evaluate the experimental results. The scope of this project was to investigate the prereduction behavior of Comilog- and Nchwaning-ore, to determine the effects the ores may have on furnace operation and off-gas characteristics. As such, the purpose of the experimental work was to evaluate kinetics and mechanisms of the reduction of these ores under conditions simulating the industrial furnace. This was carried out by monitoring the reaction progression through the weight loss or the off-gas composition as a function of time and temperature. The majority of the experimental work was carried out in CO-CO_2 atmosphere. Further, the influence of inert materials on the temperature development, as well as smaller concentrations of H_2 and H_2O in the gas were evaluated. Reaction products were analysed through chemical composition, phase composition, and microstructure development.

The majority of the experimental work has been carried out at NTNU, whereas parts of the work (the isothermal reduction experiments) were conducted at RWTH Aachen. All characterization and investigation of reduced samples were performed at NTNU.

3.1   Equipment

As stated, the focus of this work was the solid state reduction of manganese ores in gaseous atmosphere. This section describes the apparatus used, where the DisVaDri furnace was used for the experiments conducted at NTNU, whereas the Tammann furnace is located at RWTH Aachen. Both furnaces are thermogravimetric, meaning that the sample is suspended from a mass balance. The DisVaDri furnace also has an off-gas analyzer. The equipment measures the mass loss, temperature and/or time, where the mass loss is a direct reflection of the reduction extent.

3.1.1   DisVaDri furnace

A vertical retort tube furnace connected to a mass balance was used for the reduction experiments performed at NTNU. The furnace system set up have been illustrated in Figure 3.1, where the main components are the crucible suspended from a mass balance (PR2003 DELTARANGE by Mettler Toledo) with a mass range of 0-2100 g of accuracy 10 mg. An Entech VTF 80/15 furnace, mounted on a hydraulic lift, is raised to surround the crucible during heating. Another important feature is the off-gas analyzer connected to the gas outlet, which measures the concentration of CO and CO_2.

The crucible is made of stainless steel, is 45 cm high, and has an inner diameter of 4.8 cm. A schematic of the crucible set up is shown in Figure 3.2(left), where the location of sample, thermocouple submerged in sample, and gas inlet and gas outlet is marked. The sample is located in the lower parts of the crucible and placed on top of a grid in order to ensure an even distribution of gas through the sample. The gas inlet is located at the upper part of the crucible, from where the gas moves through the double walls and meets the sample from the bottom. This setup ensures preheating and premixing of the gas before it meets the sample. Figure 3.2 (right) shows the crucible, suspended from the mass balance, and its location in the furnace. The

furnace is lifted to surround the crucible during heating, while the image shows the furnace before it has been lifted.
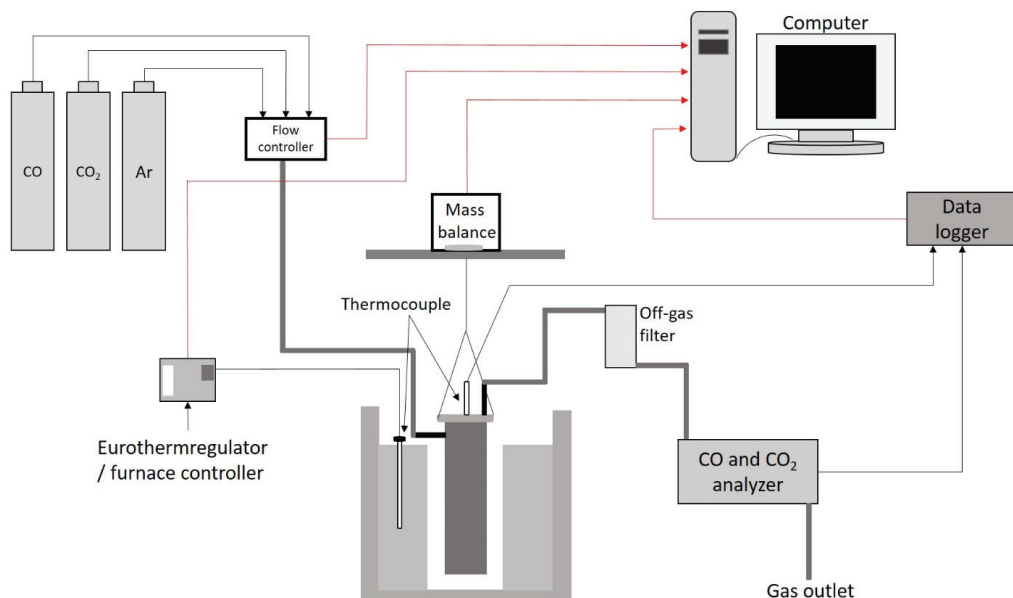
Figure 3.1: Schematic of DisVadri furnace set up

Two different thermocouples are utilized during the experiments, where one is submerged in the sample and the other is located inside the furnace wall. The furnace temperature is controlled by the thermocouple in the furnace wall, which is connected to an Eurotherm 2408 controller, which is further connected to a computer. The furnace can endure temperatures up to 1100°C for isothermal setups, and 1200°C for non-isothermal experiments. Further, the furnace handle heating rates up to 10°C/min. Kanthal heating elements in the furnace heats the exterior of the crucible. There is a deviation between the sample temperature and the furnace wall temperature at all times. Initially, the furnace wall temperature will be higher than the sample temperature, as the heating elements are located outside the crucible. After the center of the crucible has reached the same temperature as the furnace wall thermocouple, the interior of the crucible will continue to increase in temperature, causing it to have a higher temperature than the furnace itself. The behavior is illustrated in Figure 3.3, where an empty crucible was heated at 6°C/min up to 1000°C. This deviation is approximately 40°C when the empty crucible is 1000°C.

Both oxidizing and reducing atmospheres may be used, where gas mixtures may be of the following gases; Ar, N_2, CH_4, CO_2, H_2, CO, and O_2. The input is controlled by flow meters, which can handle flow rates between 0.2-10.0 L/min. Water vapor may also be added using a Bronkhorst Controlled Evaporator Mixture connected to the system. The temperature of the evaporator is set to a temperature exceeding 100°C to ensure that no condensation of the water occur. Temperature, holding time, and gas flow of desired components are programmed in a connected software. During the experiment, time, temperature and weight

58

is measured and recorded at five second intervals. In addition, a connected IR spectrometer gas analyzer measures the CO and CO_2 content exiting the crucible.
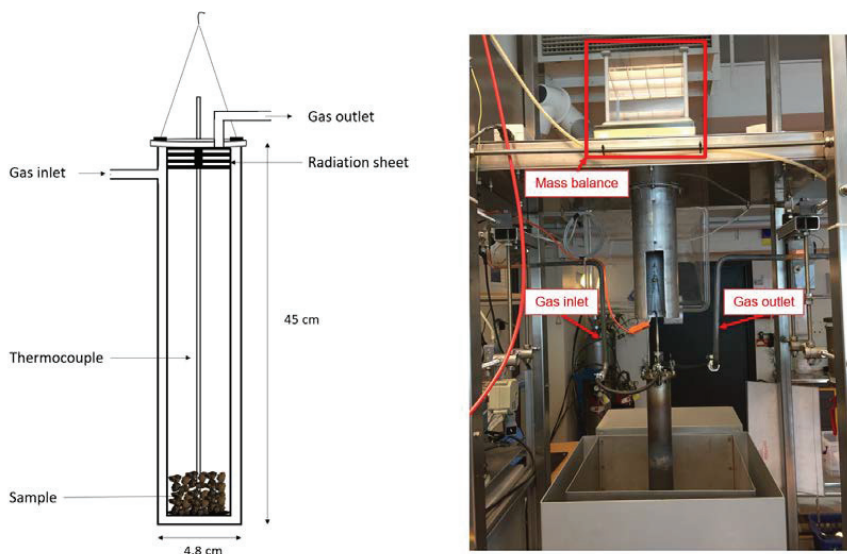
Figure 3.2: Schematic of DisVaDri crucible setup to the left, where gas inlet/outlet, radiation sheet, and placing of sample and thermocouple is marked. Image showing parts of furnace setup to the right. The crucible hangs in a wire connected to a thermobalance, and the furnace is lifted to surround the crucible during heating
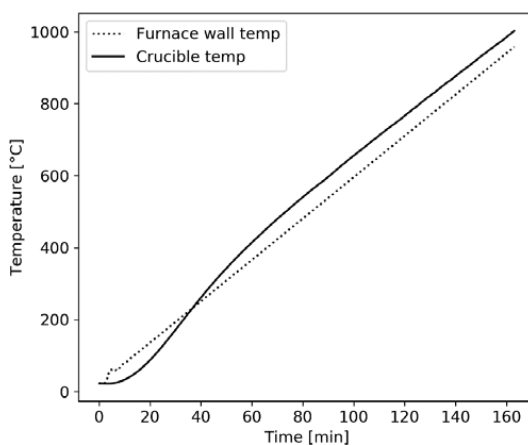
Figure 3.3: Temperature recorded for an empty crucible at furnace wall and crucible interior, respectively

Typical sample size used in the furnace is in the range of 50-200 g. Depending on material and size fraction, this correlates to different heights of sample load. Examplewise, 100 g of Comilog ore in particle size 11.20-15.00 mm correlate to a height of 7 cm. The experimental work was conducted with either Nchwaning- or Comilog-ore. An example of the observed temperatures during experimental run of each ore is presented in Figure 3.4. The temperature development during reduction of Nchwaning ore is consistent with the temperature observed during heating of the empty crucible, indicating that the combination of oxygen level and reaction rate of Nchwaning ore does not result in any heat production detected by the thermocouple. On the contrary, it can be observed that the sample (crucible) temperature during reduction of Comilog ore is strongly affected by the heat production accompanying the reduction reactions. All temperatures later referred to, is the temperature measured at the interior of the crucible, not at the furnace wall.
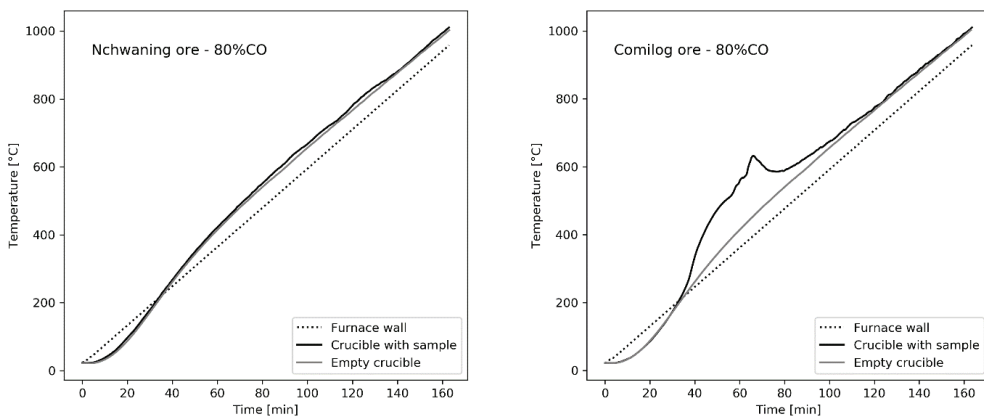
Figure 3.4: Recorded temperatures during reduction of Nchwaning and Comilog ore, respectively, compared with temperature recorded in empty crucible in DisVaDri furnace. Values are valid for reduction of 11.2-15.0 mm particles in 80% CO (remainder CO$_2$)

3.1.2   Tammann furnace

Isothermal reduction experiments were performed by utilizing the Tammann furnace facility at IEHK RWTH in Aachen. The furnace is a thermogravimetric open tube furnace with a furnace chamber diameter of 4 cm. An illustration of the furnace is shown in Figure 3.5. The sample is located in a sample holder made from tungsten or Kanthal mesh wire, which is suspended from an electronic mass balance during the experiments. The mass balance is connected to a computer software, which logs time and weight at a 0.25 s intervals.

The gas mixture is adjusted by mass flow controllers, and the gas enters the furnace chamber from the lower parts. The gas ascends through the chamber and meets the sample before exiting into a ventilation system at the top. A thermocouple is located in the furnace chamber at the same height as the sample, enabling representative temperature measurements. The thermocouple is not connected to the computer software, implying that manual temperature logging is required. Examples of the temperature behavior after the

60

sample holder with Comilog- or Nchwaning-ore was inserted into the furnace are shown in Figure 3.6, which shows values for Comilog ore at 500°C and 600°C, respectively, and Nchwaning at 600°C. For all three cases, the temperature drops in the initial stages. For experiments conducted at 600°C, a 10°C drop in temperature is observed for both ores, whereas a 15°C drop is observed at 500°C for Comilog ore. Subsequent to the initial drop, the temperature increases and stabilize according to the furnace set point for all experiments using Nchwaning ore, as the reaction rate and oxidation level does not provide a combination sufficient to result in any heat production detected by the thermocouple. For Comilog ore, two distinct categories of behavior were observed. At temperatures below 600°C, the behavior was similar to that of Nchwaning ore, whereas experiments conducted at 600°C resulted in a temperature exceeding the set point. The maximum temperature was 617°C, observed after 7.5 minutes holding time.
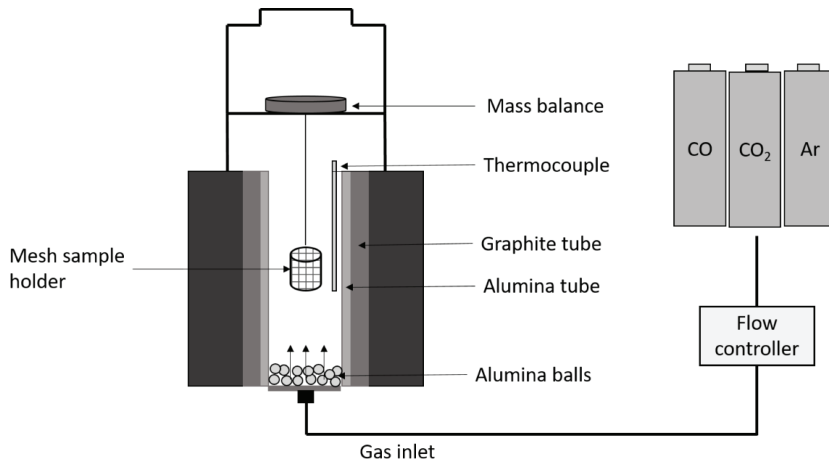
Figure 3.5: Illustration of Tammann furnace set up
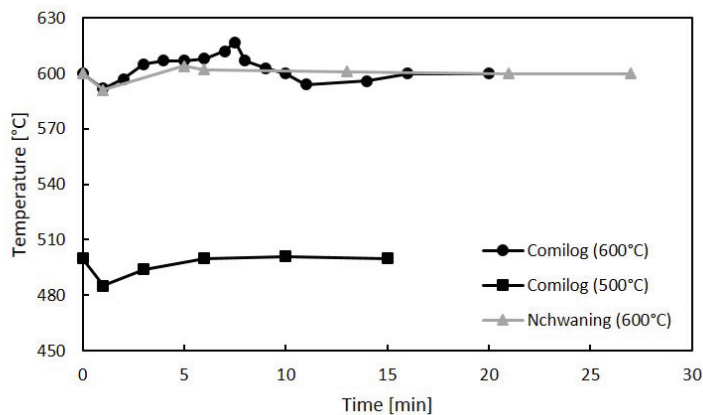
Figure 3.6: Temperature measurements during reduction of Comilog- and Nchwaning-ore, respectively, in Tammann furnace

3.2 Materials

The prereduction of manganese ore was investigated by evaluating Comilog- and Nchwaning-ore supplied by industry. The ores were crushed and sieved into four different size fractions:

- A: 0.50-1.36 mm
- B: 3.33-4.00 mm
- C: 11.20-15.00 mm
- D: 30.00-40.00 mm

The ores were characterized through chemical composition, XRD, and microstructure investigations by scanning electron microscope. The characterization methods are described in detail in section 3.4.

3.2.1 Comilog ore

Comilog is a high-grade ore with a manganese content of approximately 50 wt%, where the oxygen level (x in MnOx) is 1.94-1.95, correlating to the manganese mainly being present in oxidation state similar to MnO_2 with minor amounts of Mn_2O_3. The different size fractions show highly similar composition, however the smallest size fraction has a slightly lower, i.e. 2-3 %, total content of Mn than the larger sizes. The ore contains negligible amounts of CaO and MgO, whereas SiO_2 and Al_2O_3 is present at concentrations between 3.5-6.6%. Further, the ores are dry, where the maximum surface moisture content is found in Comilog B at 0.6%. The content of chemically bound water was estimated to be 5 wt% from the procedure described in section 3.5. The value shows high correlation with reported concentrations of chemically bound moisture by Tangstad et al., which was 4.9-6.5% for various grades of Comilog ore[10].

Table 3.2 shows the theoretical weight loss correlating to the reactions occurring from room temperature to complete prereduction. Considering a complete reduction of iron oxides to metallic iron, reduction of higher manganese oxides to MnO will account for approximately 90% of the total observed weight loss.

X-ray diffraction showed similar phases and abundance for all evaluated particle sizes. The phases identified by XRD were cryptomelane, pyrolusite, ramsdellite, nsutite, gibbsite, goethite, quartz, and lithiopherite. The obtained XRD pattern with identified phases for particle size 11.20-15.00 mm is shown in Figure 3.7, whereas the spectrums for the remaining sizes are shown in appendix. It is observed that the XRD spectrum of Comilog ore exhibits wide diffraction peaks, which complicates the identification process, particularly for phases of minor abundance. The broad peaks may arise from varying cation substitution, small crystallite sizes, peak overlap and/or content of amorphous phase. The results indicated a significant abundance of the mineral nsutite, $(Mn^{4+}_{1-x},Mn^{2+}_x)O_{2-x}(OH)_{2x}$, which does not have a defined crystal structure. The structure is composed of statistically distributed layers of tetragonal pyroluxite and orthorhombic ramsdellite, which gives rise to varying crystallite size, layering structure, as well as deviation from stoichiometric composition. This affects position, profile, and intensity in XRD reflexes[15]. The content of nsutite may be estimated through what is known as peak-shape fitting, however as this requires considerable efforts in order to obtain unreliable results, it was not performed in the present study. Thus, a quantified mineralogy of Comilog ore is not presented. From visual observation of intensities, it is assumed that cryptomelane, nsutite, and pyrolusite are the main constituting minerals of Comilog ore. Estimation of the abundance in terms of major, intermediate and minor, is shown in Table 3.3. Similar minerals were identified in Comilog ore by Sørensen et al.[16], who further performed a peak-shape fitting to estimate the

abundance. Results showed that cryptomelane and nsusite were the main minerals, each present at concentrations within range 32-35%. Further, 12% of pyrolusite, 7% of lithiopherite, and minor amounts of quartz, goethite, ramsdellite, hematite and gibbsite were reported at concentrations 1-6%.

Table 3.1: Chemical analysis of Comilog ore in different size fractions

		0.50-1.36 mm	3.33-4.00 mm	11.20-15.00 mm	30.00-40.00 mm
Mn	TOT	48.4	51.4	51.0	50.8
Fe	TOT	3.5	2.8	3.1	4.1
MnO_2	%	71.7	76.6	76.4	74.7
MnO	%	3.9	3.8	3.5	4.6
Fe_2O_3	%	5.0	4.0	4.4	5.8
SiO_2	%	5.6	3.5	3.5	2.2
Al_2O_3	%	6.6	5.6	5.6	5.0
CaO	%	0.1	0.1	0.1	0.3
MgO	%	0.2	0.2	0.1	0.2
P	%	0.1	0.1	0.1	0.2
S	%	0.0	0.0	0.0	0.0
TiO_2	%	0.2	0.1	0.1	0.2
K_2O	%	1.1	1.1	0.7	0.8
BaO	%	0.2	0.2	0.3	0.3
CO_2	%	0.2	0.2	0.1	0.2
H_2O(surface)	%	0.4	0.6	0.2	0.2
H_2O(bound)*	%	5.0	5.0	5.0	5.0
LOI(950°C)	%	12.8	12.5	13.0	12.2
TOTAL	%	100.3	101.3	100.3	99.9

Table 3.2: Theoretical weight loss correlating to different reactions during temperatures ranging from room temperature to complete prereduction (i.e. 1200°C) for Comilog ore. Weight loss is given relative to the total sample composition.

	0.50-1.36 mm	3.33-4.00 mm	11.20-15.00 mm	30.00-40.00 mm
Reaction	Loss [%]	Loss [%]	Loss [%]	Loss [%]
$MnO_2 + CO = Mn_2O_3 + CO_2$	6.2	6.6	6.6	6.4
$Mn_2O_3 + CO = Mn_3O_4 + CO_2$	2.4	2.5	2.5	2.5
$Mn_3O_4 + CO = MnO + CO_2$	4.7	5.0	5.0	4.9
$Fe_2O_3 + CO = Fe_3O_4 + CO_2$	0.2	0.1	0.2	0.2
$Fe_3O_4 + CO = FeO + CO_2$	0.3	0.3	0.3	0.4
$FeO + CO = Fe + CO_2$	1.0	0.8	0.9	1.2
$H_2O = H_2O(g)$	0.4	0.6	0.2	0.2
CO_2	0.2	0.2	0.1	0.2
Volatile (bound water)	5.0	5.0	5.0	5.0
Total (MnO+FeO)	19.3	20.3	19.9	19.7
Total (MnO+Fe)	20.3	21.1	20.7	20.9
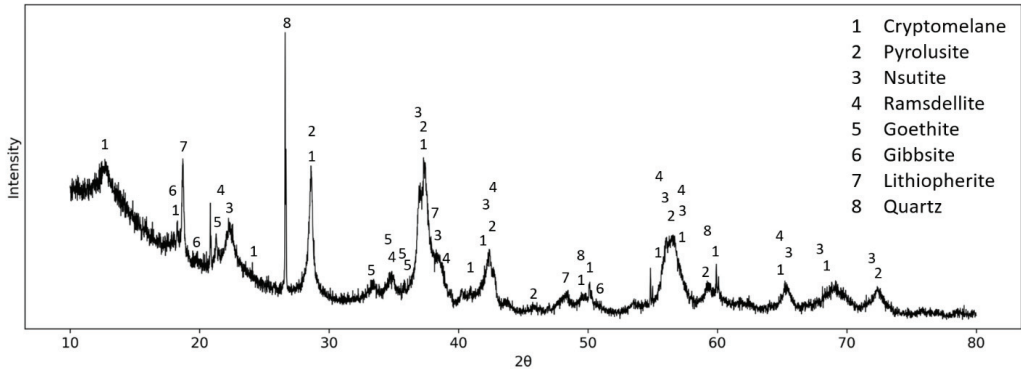
Figure 3.7: XRD pattern of Comilog ore in particle size 11.20-15.00 mm. Peak positions correlating to identified phases are marked

Table 3.3: Mineralogy as identified in BRUKER EVA Software for Comilog ore

Mineral	Formula	Abundance
Cryptomelane	KMn_8O_{16}	Major
Nsutite	$Mn(O,OH)_2$	Major
Pyrolusite	MnO_2	Intermediate
Ramsdellite	MnO_2	Minor
Lithiopherite	$(Al,Li)MnO_2(OH)_2$	Minor
Gibbsite	$Al(OH)_3$	Minor
Goethite	$FeO(OH)$	Minor
Quartz	SiO_2	Minor

In order to get an overview of the microstructures observed in Comilog ore, particles of size fraction 0.50-1.36 mm were mounted in epoxy and investigated in an optical microscope. A large variance of microstructures was observed, where some of these are shown in Figure 3.8. Some showed a homogeneous structure appearing to be composed of a single phase, whereas other contained several phases randomly dispersed throughout. In some particles, a phase separation was seen between the core and the outer layer, giving an appearance similar to a product layer. Similar structures were observed in particle size 3.33-4.00 mm and 11.20-15.00 mm, generally with a higher degree of heterogeneity.

Figure 3.9 shows the microstructure of a Comilog ore particle in size fraction 11.20-15.00 mm. The structure appear similar to that observed for the 0.50-1.36 mm particle that was shown in Figure 3.8 to the right. The backscatter imaging reveals a complex microstructure and mineralogy. Pores of various sizes are observed throughout the particle. Several phases are present, however the phase boundaries are diffuse, as seen in the image to the right with higher resolution. Cryptomelane, pyrolusite, nsutite, and lithiophorite are reported to be frequently intergrown[15], which may contribute to the lack of clear phase boundaries in this particle. The chemical composition as obtained by EDS according to the numbered phases in Figure

3.9 is shown in Table 3.4. Firstly, it is noted that the obtained analytical total of the analyses is relatively low. According to Newbury and Ritchie[108], this could be due to geometric effects, such as porosity and cavities causing irregular surfaces. They further showed that geometric effects could result in large errors, as high as a factor of 10. Aluminum was detected in all phases, where it may be seen that the phase identified as cryptomelane contains 2.7 at% Al. This may be due to substitution, however it is also possible that several phases have been included in the analysis, as underlying phases may be included in the analyses when the grain diameter is small. Element mapping was performed on the same particle in an attempt to see the phase boundaries, where the mapping of the more common elements is shown in Figure 3.10. Aluminium is present throughout the sample, except for areas rich in iron. It is possible that the Al exist in lithiophorite in this particle. As lithiophorite is part of a fine-grained mixture, and the Li-content can not be confirmed by XRF or EPMA, it is not possible to confirm optically or by EPMA[16]. The areas rich in iron correlate to low concentrations of remaining cations. As reliable measurements of oxygen and hydrogen is not possible, it is assumed that this is goethite, as this was the only iron phase detected by XRD. Silicon is observed in areas containing potassium and aluminium. The majority of silicon in Comilog is present as quartz, however due to natural heterogeneity, the quartz phase is not present in all particles.
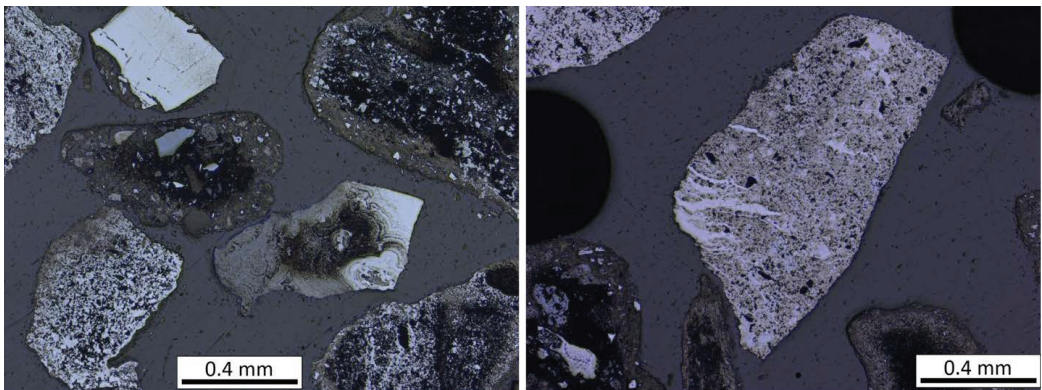
Figure 3.8: Microstructure observed in Comilog ore particles (0.50-1.36 mm) as observed in optical microscope
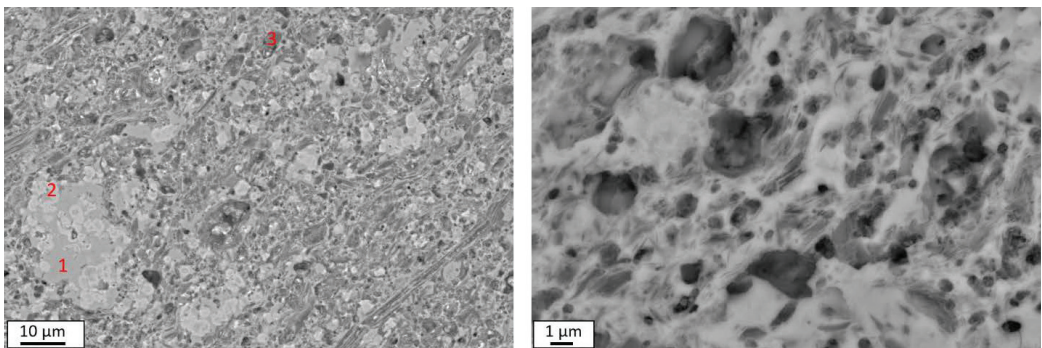
Figure 3.9: Microstructure of Comilog particle (11.20-15.00 mm) from backscatter imaging

Table 3.4: Chemical composition of phases in Comilog ore (11.20-15.00 mm) according to EDS point analysis (average of 3-5 point analyses)

| | Values from EDS | | | | | | | Proposed phase | |
	Mn [at%]	Fe [at%]	Si [at%]	Al [at%]	O [at%]	K [at%]	Total [wt%]	Mineral	Stochiometry
1	38.3	0.0	0.0	2.7	56.6	2.1	85.4	Cryptomelane	$K_xMn^{4+}_{8-x}Mn^{2+}_xO_{16}$
2	6.9	38.6	0.5	1.4	51.9	0.2	90.9	Goethite	FeO(OH)
3	31.6	0.0	4.3	6.7	54.7	2.3	80.5	Mixture	
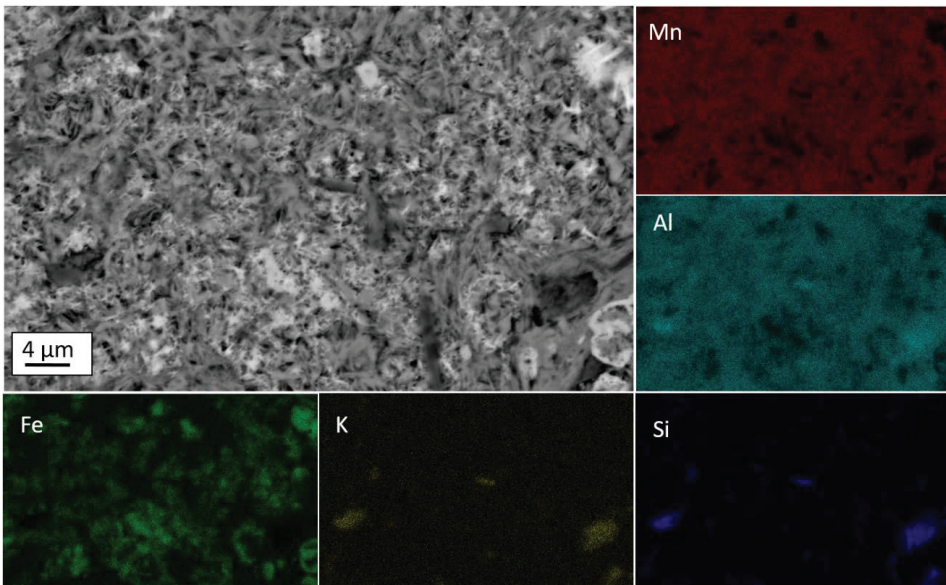
Figure 3.10: Element mapping obtained by EDS of Comilog ore particle (11.20-15.00 mm)

3.2.2   Nchwaning ore

The analyses correlate to an oxygen level (x in MnOx) of 1.46-1.48 for Nchwaning ore. This implies that the manganese oxides can be viewed as a combination of Mn_2O_3 with minor amounts of Mn_3O_4. All four size fractions show highly similar overall chemical composition, where the total manganese content is approximately 46-47wt% and the iron content is 9-10 wt%. CaO is detected at a concentration of 6%, whereas only minor amounts of MgO was observed. Further, approximately 6-7 wt% of SiO_2 was detected. In general, Nchwaning ore was found to contain negligible (< 0.1%) amounts of both surface and bound moisture. The theoretical weight loss is presented in Table 3.6 according to the contribution from the different reactions occurring during solid state reduction of manganese ore. The majority of the weight loss

is due to reduction of higher manganese oxides to MnO and iron oxides to metallic iron, where the latter contributes 40% of the total weight loss considering a complete reduction to metallic state. The theoretical weight loss of reduction of hematite to both wüstite and metallic iron have been presented.

Table 3.5: Chemical analysis of Nchwaning ore in different size fractions

		0.50-1.36 mm	3.33-4.00 mm	11.20-15.00 mm	30.00-40.00 mm
Mn	TOT	46.7	46.5	46.4	46.9
Fe	TOT	9.6	9.5	10.0	8.8
MnO_2	%	35.5	34.2	34.6	34.9
MnO	%	31.3	32.2	31.6	32.1
Fe_2O_3	%	13.7	13.6	13.4	12.6
SiO_2	%	6.4	6.2	6.7	6.8
Al_2O_3	%	0.5	0.5	0.5	0.6
CaO	%	6.2	6.3	5.9	6.3
MgO	%	1.1	1.1	1.0	1.0
P	%	0.0	0.0	0.0	0.0
S	%	0.1	0.2	0.1	0.0
TiO_2	%	0.0	0.0	0.0	0.0
K_2O	%	0.0	0.0	0.0	0.0
BaO	%	0.5	0.5	0.4	0.1
CO_2	%	3.2	3.2	3.0	3.4
H_2O(free)	%	0.0	0.0	<0.1	0.0
H_2O (bound)	%	0.0	0.0	0.0	0.0
LOI (950°C)	%	4.1	4.0	4.0	3.7
TOTAL	%	98.2	97.0	97.3	98.5

In accordance with the highly similar chemical composition of the three size fractions, only minor differences were observed in the XRD analysis. As such, XRD patterns of the two smaller particle sizes can be found in appendix, whereas the results from particle size 11.20-15.00 mm are presented here. Phase identification through the EVA Software indicated that bixbyite, braunite, and braunite II were the main Mn-bearing minerals. These minerals have highly similar XRD-patterns and may only be distinguished in XRD by a few low intensity peaks characteristic for the individual mineral. These characteristic peaks were observed in the XRD pattern (shown in appendix), indicating the presence of all three minerals. Further, hematite, calcite and manganite appeared to be present in considerable concentrations. The XRD spectrum shows several low intensity peaks correlating to phases of minor abundance. According to EVA, these peaks represent hausmannite, johannesite, kutnohorite, (Ca,Mg)-silicate, as well as $AlFe_2O_4$. The XRD-spectrum with identified phases is presented in Figure 3.11.

The abundance was calculated using the TOPAS Software. Although braunite II was identified as the matrix phase by SEM/EDS, the Rietveld analysis provides only minor concentrations of braunite and braunite II, whereas bixbyite has an abundance of approximately 60%. A similar disagreement between XRD and

SEM/EDS was reported by Sørensen et al.[16] in the case of Wessels ore. If one does not differentiate between bixbyite, braunite I and braunite II, the obtained mineralogy shows high correlation with the reported mineralogy of Nchwaning ore by Visser et al.[12]. The quantification shows high correlation with the XRF results, both in terms of oxygen level of manganese, and content of hematite and calcite (if reported CaO from XRF is mainly present as calcite).

Table 3.6: Theoretical weight loss correlating to different reactions during temperatures ranging from room temperature to complete prereduction (i.e. 1200°C) for Nchwaning ore. Weight loss is given relative to the total sample composition.

	0.50-1.36 mm	3.33-4.00 mm	11.20-15.00 mm	30.00-40.00 mm
Reaction	Loss [%]	Loss [%]	Loss [%]	Loss [%]
$MnO_2 + CO = Mn_2O_3 + CO_2$	-	-	-	-
$Mn_2O_3 + CO = Mn_3O_4 + CO_2$	2.0	1.8	1.9	1.8
$Mn_3O_4 + CO = MnO + CO_2$	4.5	4.5	4.5	4.5
$Fe_2O_3 + CO = Fe_3O_4 + CO_2$	0.5	0.5	0.5	0.3
$Fe_3O_4 + CO = FeO + CO_2$	0.9	0.9	1.0	0.7
$FeO + CO = Fe + CO_2$	2.7	2.7	2.9	2.1
$H_2O = H_2O(g)$	0.0	0.0	0.0	0.0
CO_2	3.1	3.1	3.0	7.8
Volatile (bound water)	-	-	-	-
Total (MnO+FeO)	11.0	10.8	10.8	15.1
Total (MnO+Fe)	13.8	13.5	13.7	17.2
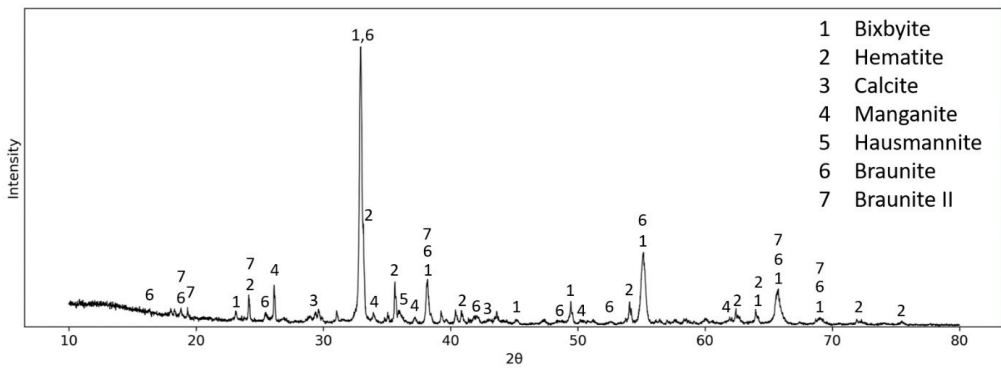
Figure 3.11: XRD spectrum of Nchwaning ore in particle size 11.20-15.00 mm. Peak positions correlating to identified phases are marked

Table 3.7: Identified phases in Nchwaning ore and the respective abundance determined by Rietveld analysis in TOPAS 5

Mineral	Formula	0.50-1.36 mm	3.33-4.00 mm	11.20-15.00 mm
Bixbyite	$(Mn,Fe)_2O_3$	61	61	60
Hematite	Fe_2O_3	10	10	13
Calcite	$CaCO_3$	9	11	9
Braunite I	Mn_7SiO_{12}	6	4	-
Braunite II	$CaMn_{14}SiO_{24}$	3	4	8
Hausmannite	Mn_3O_4	4	3	1
Manganite	$MnO(OH)$	7	7	6

Cross-section examinations of particle size 0.50-1.36 mm, 3.33-4.00 mm, and 11.20-15.00 mm indicated that the microstructures observed in Nchwaning ore were mainly of two types. The two types are shown in Figure 3.12, where Type 1 particles (left) were rich in braunite and carbonate, whereas type 2 contained mainly braunite II. The dark areas in type 1 is a carbonate phase, which was mainly calcite, however a varying concentration of magnesium was detected by EDS point analysis. The brighter areas were identified as braunite, however some regions showed composition correlating to hematite. Type 2 is observed to exhibit a relatively homogeneous structure, where point analysis showed that concentrations of manganese, iron, silicon, and calcium varied throughout the structure. Some of the braunite II particles contained minor amounts of calcite and hematite. Figure 3.13 shows the microstructure of one of these particles as observed by backscatter imaging. EDS analysis indicated the matrix phase was braunite in two different modifications distinguished by the Mn/Fe ratio. The point analysis values can be seen in Table 3.8, where the Mn/Fe ratio is equal to 1.8 and 14.3 in braunite 1 and braunite 2, respectively. Further, minor amounts of barite ($BaSO_4$) were observed in certain single particles, however not displayed in the figure. It may be noted that the quantified oxygen content is consistently lower than the amount correlating to the stoichiometry of the individual phases.
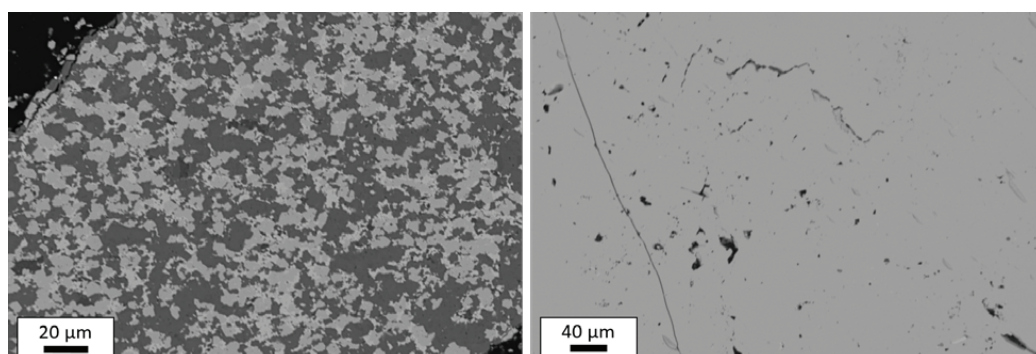
Figure 3.12: Microstructure of the two main types of structures observed in Nchwaning ore
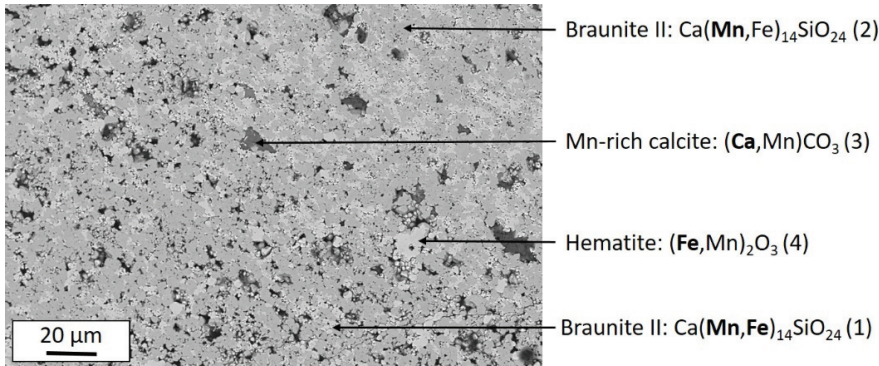
Figure 3.13: Microstructure of Nchwaning ore (11.20-15.00 mm) from backscatter imaging

Table 3.8: Chemical composition of phases in Nchwaning ore particle (11.20-15.00 mm) according to EDS point analysis

	Values from EDS							Proposed phase	
	Mn	Fe	Si	Ca	O	C	Total	Mineral	Stochiometry
	[at%]	[at%]	[at%]	[at%]	[at%]	[at%]	[wt%]		
1	29.8	16.2	3.3	1.0	46.0	3.8	83.8	Braunite II	$Ca(Mn,Fe)_{14}SiO_{24}$
2	39.2	2.4	5.9	3.3	48.9	-	82.3	Braunite II	$Ca(Mn,Fe)_{14}SiO_{24}$
3	4.1	-	-	31.6	49.6	13.7	76.8	Carbonate	$(Ca,Mn)CO_3$
4	3.7	50.4	-	-	41.3	-	90.0	Hematite	$(Fe,Mn)_2O_3$

3.3   Procedure

3.3.1   DisVaDri furnace

The experimental series conducted using the DisVadri furnace were:

- Non-isothermal experiments with Mn ores in CO-CO_2 atmosphere
- Non-isothermal experiments with Mn ores and quartz in CO-CO_2 atmosphere
- Non-isothermal experiments with Mn ores in CO-CO_2 with additions of H_2 or H_2O

The majority of the experiments were conducted with 75 ± 0.5 g of ore. For particle size 30-40 mm, four or five particles were evaluated in each experimental run. This was due to limitations of the crucible, which has a diameter of 48 mm. It is thus likely that there are larger inaccuracies related to these experiments compared to the experiments conducted with smaller particle sizes. Some experiments were conducted with ore mixed with quartz in weight ratio 1:1 and 1:3, respectively. The latter was conducted with 50 g ore and 150 g quartz due to restrictions of maximum load on the mass balance. In experiments with quartz, the materials were added in layers to ensure an even distribution of the two. For all experiments, the samples were weighed in a beaker with diameter similar as the crucible diameter to determine the sample height. An example of the sample weighing in the beaker is shown in Figure 3.14, which shows Comilog ore and

70

quartz mixed in 1:1 ratio. Subsequent to weighing, the sample was loaded into the crucible resting on a steel cage, in order to ensure an even distribution of the gas. The crucible was sealed and suspended from the mass balance.

Figure 3.14: Sample in beaker with diameter similar to crucible diameter. Picture shows Comilog ore mixed with quartz in 1:1 ratio according to weight

A few experiments were also conducted where the Comilog ore particles were wet when added to the crucible. The ore particles were kept submerged in a glass beaker filled with water for approximately 20 minutes, allowing the water to fill pores and cavities in the ore. It was approximated that the ore retained approximately 3-4% of water during this procedure.

A total gas flow of 4 Nl/min was used in all experiments. The majority of the experiments were conducted in CO-CO_2 atmosphere, where the CO concentration was varied between 30-80%. Figure 3.15 shows the stability diagram of the Mn-O_2 system superimposed on the Fe-O_2 system, where the oxygen partial pressures given by the investigated CO-CO_2 gas compositions have been included. It is observed that MnO is the expected manganese oxide for the investigated temperature range and gas atmospheres. Further, when using a gas composition of 50% CO and 50% CO_2, higher iron oxides should be reduced to FeO. When using 80% CO and 20% CO_2, it is expected that iron oxides will be fully reduced to metallic iron. It should be mentioned that both diagrams were calculated from pure oxides, implying that the real activities may be lower for the evaluated system. This may suggest that Fe_3O_4 and FeO are the likely stable oxides for iron at the investigated temperature ranges and gas atmospheres.

Gas atmospheres based on CO-CO_2-H_2 and CO-CO_2-H_2O were also investigated, where the specific gas flow mixture was calculated to give similar oxygen pressures as some of the CO-CO_2 atmospheres. The oxygen pressures in the evaluated CO-CO_2-H_2 and CO-CO_2-H_2O atmospheres were similar to the oxygen lines of 50% CO and 80% CO shown in Figure 3.15. An overview of the investigated gas mixtures are shown in Table 3.9, where gas atmospheres with the same number correlate to similar theoretical oxygen partial pressures. Thus, gas mixture 3a, 3b and 3c, and 4a and 4b, respectively, have similar theoretical oxygen partial pressures throughout the investigated temperature range.
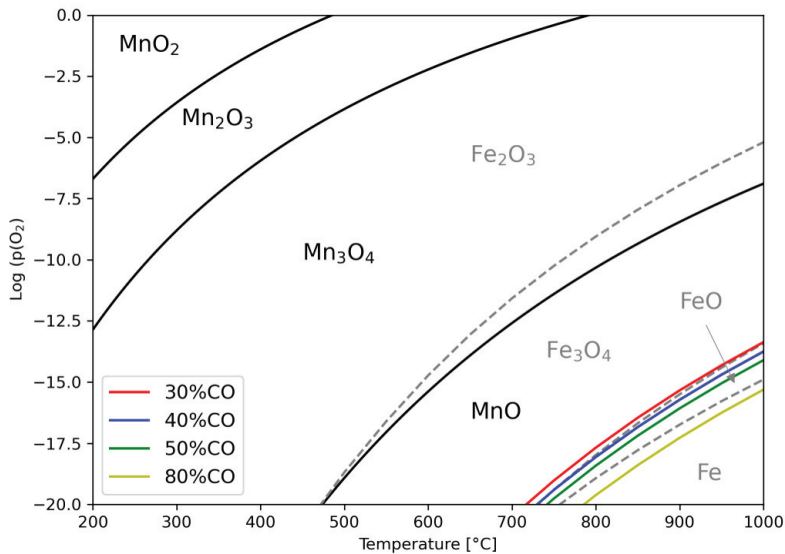
Figure 3.15: Stability diagram of superimposed Mn-O$_2$ and Fe-O$_2$ system including oxygen partial pressures for investigated CO-CO$_2$ atmospheres

The standard non-isothermal experiments were conducted by heating from room temperature to target temperature at a rate of 6°C/min according to the furnace wall temperature. The majority of the experiments were terminated at a sample temperature of 1000°C. According to the previously mentioned deviation between furnace wall temperature and crucible temperature, a sample temperature of 1000°C was obtained at a given set point temperature of 960°C. When target temperature was reached, the power supply was switched off, the furnace was moved to the lower position. Simultaneously, the gas atmosphere was replaced by a flow of argon. The first 10 minutes of the cooling was conducted in a flow of 4 Nl/min argon to rapidly remove the CO-CO$_2$ mixture from the system. Subsequently, the flow was changed to 1 Nl/min and kept for 45 minutes. After the crucible was completely cooled (T<100°C), the sample was removed from the crucible and weighed.

Table 3.9: Gas mixtures used in experiments conducted in DisVaDri furnace

	CO [L/min]	CO$_2$ [L/min]	H$_2$ [L/min]	H$_2$O [L/min]	Total [L/min]	Log(p(O$_2$)) T=800°C
1	1.2	2.8	-	-	4	-17.7
2	1.6	2.4	-	-	4	-18.1
3a	2	2	-	-	4	-18.4
4a	3.2	0.8	-	-	4	-19.6
3b	1.75	1.75	0.5	-	4	-18.4
3c	2.24	1.25	-	0.5	4	-18.4
4b	2.8	0.7	0.5	-	4	-19.6

The reproducibility of the non-isothermal experiments was evaluated, where it was decided to terminate the reproduced experiments at a lower temperature than 1000°C, e.g. 800°C, in the repeated runs. As such, the reproducibility could be evaluated from the correlation between weight reduction curves, and additional information could be obtained from characterization of reduction products at the additional temperature.

Due to unreliable weight balance behavior in the initial stages of the experiments(see appendix A), it was decided to rely on the off-gas composition to evaluate the reduction behavior. The weight behavior was determined from the off-gas analysis by the rectangle integral method according to the following procedure:

The area under the %CO_2-curve at temperature range ΔT is calculated from:

$$Area(T_1 - T_2) = \int_{T_1}^{T_2} CO_2[\%]dT = \frac{1}{2}(\%CO_2(T_1) + \%CO_2(T_2)) \cdot (T_2 - T_1)$$

3.1

The weight is found by the dividing the area at temperature T by the total area, which is then multiplied with the total weight loss (sample weighed before and after experiment).

$$Weight\ [g] = \frac{Area(T_X)}{Area_{total}} \cdot total\ weight\ loss$$

3.2

Comilog contains approximately 5 wt% of bound water, of which the evaporation will not be observed in the off-gas composition. The expected weight loss of Nchwaning ore reduction is attributed to reduction of manganese and iron oxides, respectively, in addition to carbonate decomposition, all of which affects the CO/CO_2 ratio of the off-gas. Example of the weight reduction curves produced from the off-gas analysis is shown for Comilog ore in Figure 3.16. It can be observed that the repeatability of the experiments is high. All weight reduction curves presented beyond this point are calculated from the off-gas analysis, if not stated otherwise.
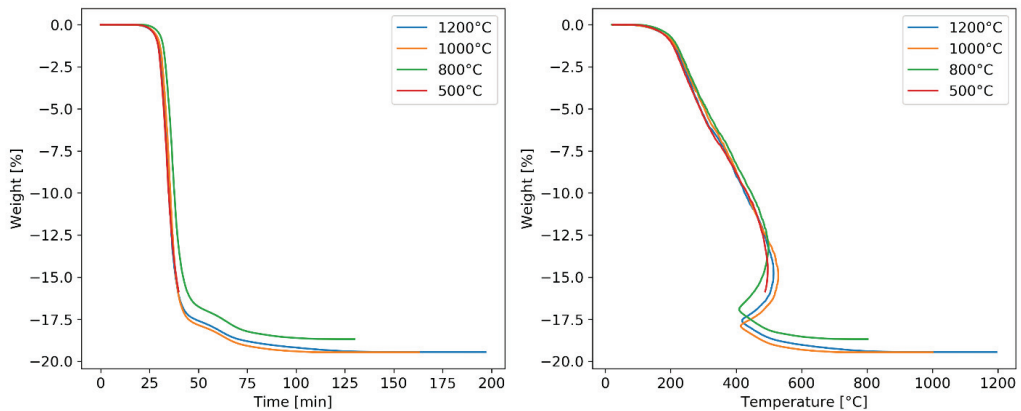
Figure 3.16: Weight calculated from off-gas behavior for Comilog ore (3.33-4.00 mm) in 50%CO-50%CO₂

Carbon deposition/Boudouard reaction

According to thermodynamics, the Boudouard reaction (reaction 3.3) is shifted to the left at temperatures below approximately 700°C, whereas at higher temperatures it will proceed to the right. As such, CO-gas may decompose to solid carbon and $CO_2(g)$ at low temperatures during the reduction experiments. Towards the final stages of the experiments, the temperature may be sufficiently high for the deposited carbon to react with the CO_2 to produce CO-gas.

$$C + CO_2 = 2\ CO \hspace{4cm} 3.3$$

The rate of carbon deposition is mainly influenced by temperature and the CO and CO_2 partial pressures, where a high CO/CO_2 ratio is favorable. According to Figure 2.6, all present CO should decompose to solid carbon and CO_2 at temperatures 0-400°C. As an example, a flow rate of 3.2 L/min CO correlates to a carbon deposition rate of 0.86 g/min at this temperature range. The occurrence of carbon deposition may be difficult to detect from the weight behavior when reduction of higher iron and manganese oxides are occurring simultaneously. As such, an estimation of the temperature ranges at which carbon deposition and the Boudouard reaction occur were evaluated by conducting experiments with similar conditions as to the reduction experiments, where the only changes were the sample material, now being quartz. Thus, 75 g of quartz were heated at 6°C/min up to 1000°C in both 80%CO-20%CO$_2$ and 50%CO-50%CO$_2$. Both experiments were repeated.

Figure 3.17 and Figure 3.18 shows the recorded CO_2 [%] in the off-gas and the weight recorded by the balance for the heating of quartz in CO-CO$_2$ atmosphere. The initial stages of all experiments show a weight increase due to the previously mentioned drifting of the mass balance. For the experiments conducted in 50%CO, it may be observed that the recorded CO_2-concentration in the off-gas is relatively stable throughout. The first run showed a small decline in %CO$_2$ at temperatures exceeding approximately 650°C accompanied by a weight increase. The repeated run shows stable recordings throughout. It can hence be concluded that the extent of carbon deposition is low in 50%CO-50%CO$_2$.
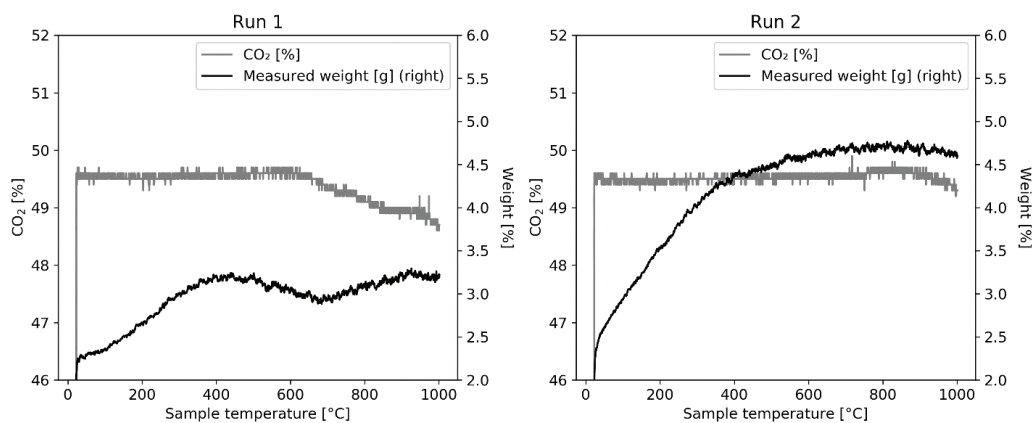
Figure 3.17: Recorded weight and CO$_2$ [%] in off-gas during heating of quartz from ambient to 1000°C at 6°C/min in 50%CO-50%CO$_2$
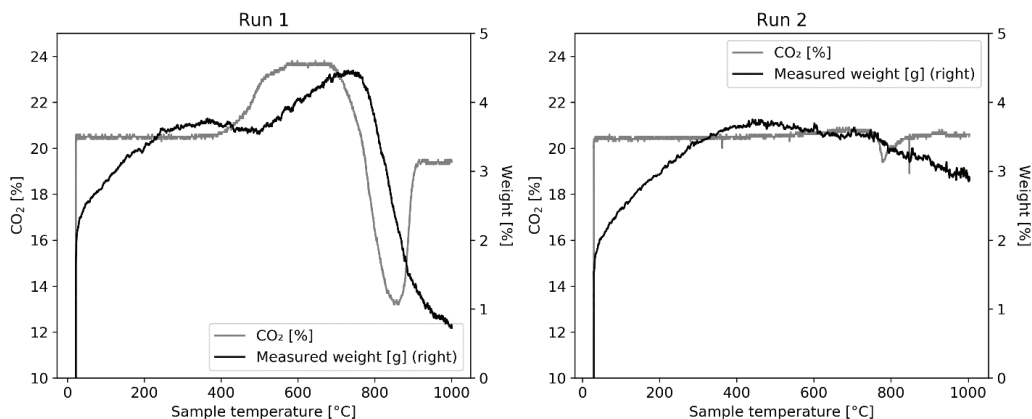
Figure 3.18: Recorded weight and CO_2 [%] in off-gas during heating of quartz from ambient to 1000°C at 6°C/min in 80%CO-20%CO₂

For the first run in 80%CO, it can be seen that the %CO_2 is increased relative to set-point at temperatures 400-780°C, indicating occurrence of the reverse Boudouard reaction. This is supported by the recorded weight, which is seen to increase in the same temperature interval due to the carbon deposition. Further, the recorded CO_2 is decreased below set point, accompanied by a decreasing weight, at temperatures 780-860°C, indicating an ongoing Boudouard reaction. The rate decreases as the consumption of available solid carbon runs to completion, causing the CO_2 to stabilize according to set-point at increasing temperatures. The curves observed for the second run show that the extent of carbon deposition and the following Boudouard reaction that was observed in the first run was not reproduced. Nonetheless, a slight increase of recorded %CO_2 in the off-gas is observed in the same temperature interval as the first run. The Boudouard reaction is initiated at approximately 780°C, as seen by the decreasing content of %CO_2.

Assuming that a CO_2 concentration below set point value correlates to the ongoing Boudouard reaction, the amount of solid carbon consumed may be calculated. Figure 3.19 shows the recorded CO_2-concentration relative to set-point for the different experiments to the left, whereas the figure to the right shows the carbon consumption as a function of temperature. The consumption was calculated by using the molar gas volume (22.4 mol/L) combined with the gas flow of 4L/min. Run 2 in 50% CO and run 1 in 80% CO showed highly stable CO_2-concentrations in the off-gas throughout the experiment, correlating to an insignificant carbon consumption, as seen in the figure to the right. A somewhat higher amount of carbon is consumed in run 1 in 50% CO, i.e. 1.5 g. Nonetheless, if a carbon deposition and consumption of this magnitude occurs during the reduction experiments, it is believed that the effect may be neglected, as it will not cause any considerable changes to the weight- and off-gas recordings accompanying ore reduction. The extent of carbon consumption observed in run 1 in 80%CO correlates to approximately 7.8 g. This extent deviates heavily from the remaining runs and is believed to be an abnormality. The calculated amount of carbon deposition, evaluated from a positive %CO_2 in Figure 3.19, is 7.9 g. As such, the extent of the Boudouard reaction is directly correlated to the extent of carbon deposited at lower temperatures, thus showing that the extent of carbon deposition can be determined from the observed right shifted Boudouard reaction.

In general, the experiments with quartz in CO-CO_2 atmosphere showed that carbon deposition was initiated at temperatures close to 400°C and continued to temperatures up to approximately 780°C. At higher temperatures, the Boudouard reaction was initiated, which continues until the deposited carbon was depleted.
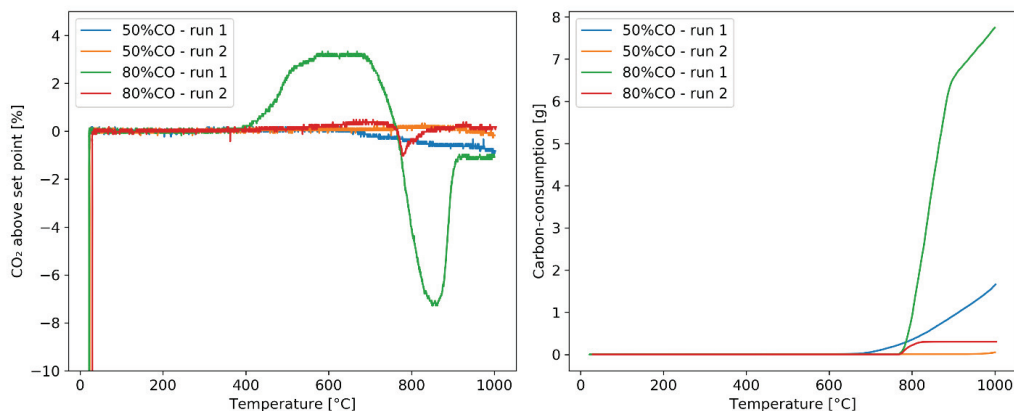
Figure 3.19: CO_2-concentration relative to set-point (left) and correlating calculated carbon consumption (right) for experiments conducted with quartz heated in CO-CO_2 atmosphere (6°C/min)

Assessing the contribution from the Boudouard reaction on the overall observed reduction behavior may be difficult if the reduction of higher manganese and iron oxides are occurring in the same temperature range. Nonetheless, the extent may be estimated by comparison of the off-gas analysis and the weight behavior according to the mass balance, respectively. While both the left shifted Boudouard reaction and the ore reduction increases the CO_2 concentration in the off-gas, the former gives a weight increase whereas the latter gives a weight reduction. Overall, the Boudouard reaction occurred at insignificant extent in the experiments conducted with Comilog ore, regardless of the inlet CO-concentration. This is likely due to reduction of the ore being initiated at a lower temperature than that required by the Boudouard reaction, implying that the CO-concentration had decreased considerably when the active temperature range of the left shifted Boudouard reaction was reached. However, for some of the experiments with Comilog ore, the reaction and the ore reduction occurred in separate temperatures regions. An example of this behavior can be seen in Figure 3.20, which shows experimental data from Comilog ore in particle size 0.50-1.36 mm heated to 1000°C in 80%CO-20%CO_2. The figure shows the recorded fraction of CO_2 in the off-gas relative to set point value (20% CO_2) and recorded weight as a function of temperature, respectively. The large initial peak in produced CO_2 correlates to the reduction of Comilog ore, which converges to set point value at approximately 400°C, indicating a completed ore reduction. At 400-750°C, the %CO_2 increases accompanied by a weight increase, characteristic for the left shifted Boudouard reaction. At temperatures exceeding 750°C, a weight decrease is observed simultaneously as a negative CO_2-concentration, indicating that the Boudouard reaction is shifted to the right. For experiments showing a clear separation between ore reduction and carbon deposition (and subsequent Boudouard reaction), as in Figure 3.20, the recorded CO_2 in off-gas and weight change were adjusted to zero at the regions influenced by the Buduoard reaction.

76

The reduction of Nchwaning ore was initiated at a higher temperature compared to Comilog ore. Furthermore, the reaction rates obtained for Nchwaning ore were considerably lower. As such, the effect of the Boudouard reaction was considerably larger. For experiments conducted in CO-CO_2 atmospheres where the CO-concentration was within 30-50%, the TGA curves were found to be largely representative for the ore reduction. For experiments conducted in 80%CO-20%CO_2, the influence of the Boudouard reaction was more severe. The potential effect of the Boudouard reaction was evaluated for each individual experiment for Nchwaning ore. It is mentioned that the Boudouard reaction have been observed to be catalyzed several different compounds, including iron and potassium, which implies that the use of quartz does not accurately simulate the conditions of the ore, as it contains various amounts of iron. Nonetheless, the temperature ranges of ongoing deposition and Boudouard reaction was highly similar with the use of quartz, Comilog ore, and Nchwnaning ore in this study. This may suggest that the Boudouard reaction is not highly influenced by the presence of iron in the ores.
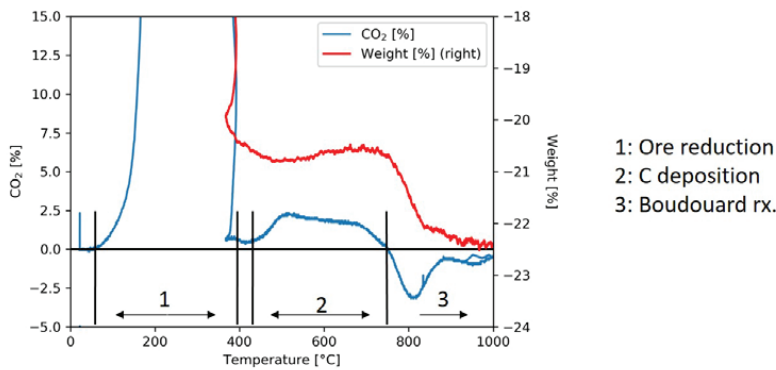
Figure 3.20: Recorded weight and %CO$_2$ relative to set point in off-gas for Comilog in 0.5-1.36 mm in 80% CO heated at 6°C/min up to 1000°C

3.3.2 Tammann furnace

The Tammann furnace is part of the facilities at IEHK RWTH in Aachen, which was utilized for some of the isothermal experiments conducted in this study. The furnace was heated to target temperature while being flushed in CO_2. When target temperature was reached, the desired CO-CO_2 atmosphere was introduced. Two different gas atmospheres were evaluated, i.e. 50% CO and 70% CO (+CO_2) in a total gas flow of 3 L/min. 15-25 g of ore in size fraction 11.20-15.00 mm (4-5 ore particles) were loaded into the sample holder and suspended from the weight balance. The choice of sample size was based on the attempt to minimize self-heating effect due to exothermic reductions, as well as limitations of the furnace geometry. The logging of time and weight values by the software was initiated subsequent to sample loading. After desired holding time, the logging was terminated, the sample was removed from the furnace and flushed in argon while cooling. During the experiment, time and weight are continuously recorded every 0.25-0.50 seconds by the software.

An overview of the experimental conditions is presented in Table 3.10. Figure 3.21 shows the stable manganese and iron oxides for the experimental conditions, where MnO is the stable manganese oxide at all evaluated systems, whereas the stable iron phase varies with temperature and gas composition. Again, it is emphasized that the equilibrium phases are valid for pure iron oxides and manganese oxides, respectively.

Table 3.10: Experimental conditions for isothermal reduction experiments conducted in Tammann furnace

	Temperature [°C]	Time [min]	CO [vol%]	CO_2 [vol%]
Comilog ore	400-600	20-40	50/70	50/30
Nchwaning ore	600-900	30-60	50/70	50/30
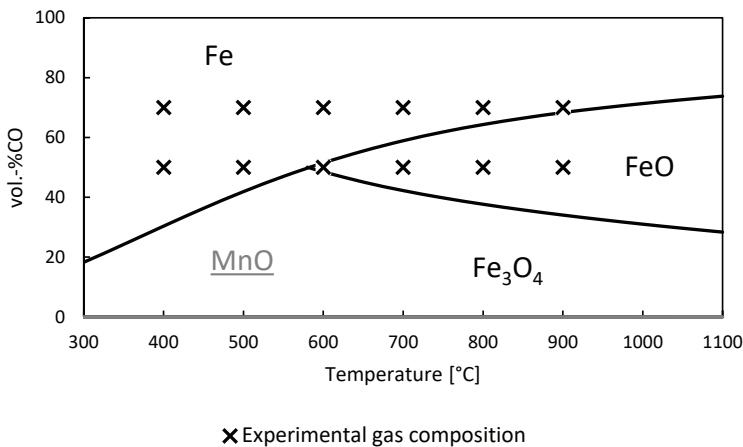
Figure 3.21: Equilibrium phases of manganese and iron oxides as a function of CO-concentration at increasing temperatures

Due to decrepitation in some of the experiments, small pieces of ore were observed to escape the open sample holder. The weight change between every two recordings (0.25 s interval) was evaluated to detect any abnormal weight behavior. Figure 3.22 shows the weight change for Comilog ore in 50%CO-50%CO$_2$ at 500°C and 550°C, respectively. It can be observed that the weight recordings in both experiments generally falls within ± 0.1 g throughout the experiment, with the only exception being a weight change of approximately -1.3 g at 2.8 minutes process time at 550°C. Due to the magnitude of the weight change relative to all remaining observations and the short evaluation interval, it is concluded that the weight change at this instance is a result of sample mass escaping the sample holder. As such, the outlier value(s) was removed for experiments showing this type of behavior, and all following weight recordings were adjusted accordingly. The limit for abnormal behavior, indicating sample mass escaping the sample holder, was set to weight change per 0.25 seconds larger than 0.2 g, which correlates to a loss of 1% per recording and 4%/s for a 20 g sample.

Due to the high sensitivity of the weight balance and the frequency of the software recordings relative to the size of the sample mass loss due to reduction, fluctuations were observed in the produced weight curves.

The fluctuations were generally within the range of ± 0.1 g. The fluctuations were treated in Python by applying a Savitzky-Golay filter. This filter smooths the data without distorting any signal tendency by fitting successive sub-sets of adjacent data points with a low-degree polynomial by the method of linear least squares (convolution). The rolling interval length was set to 2.5 minutes process time. Further, due to potential inhomogeneity of the manganese ore, several repeated runs were performed for the majority of the experimental conditions, were the average weight reduction behavior was assumed to representative. An example of the treatment of weight recording data is shown in Figure 3.23, where the original data obtained for Comilog ore reduced in 50% CO (+CO$_2$) at 550°C for 30 minutes is presented together with the data where decrepitation was removed, and the result of the smoothing by the Savitsky-Golay filter.
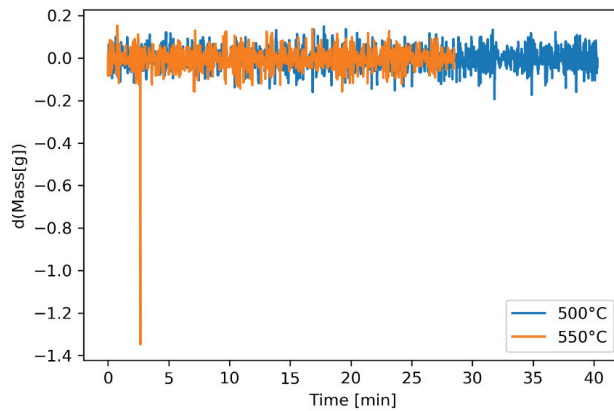
Figure 3.22: Weight change between two subsequent recordings (0.25-0.5 s interval) during isothermal reduction of Comilog ore in 50%CO-50%CO$_2$ at 500°C and 550°C, respectively
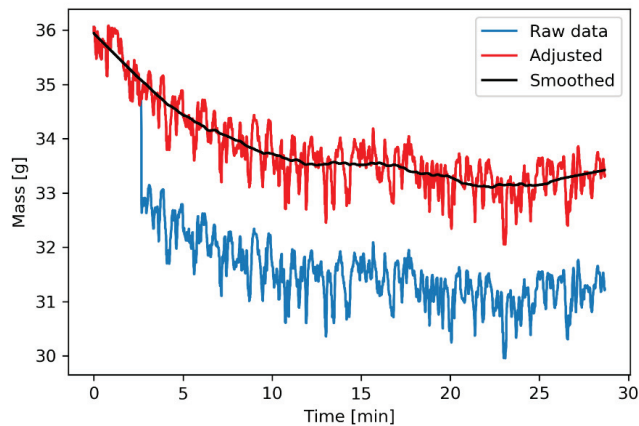
Figure 3.23: Example of treatment of weight recording data obtained from experiments in Tammann furnace, including original data (raw data), data where weight loss due to sample escaping the sample holding is removed (adjusted), and data smoothed by a Savitsky-Golay filter (smoothed). The data was obtained for reduction of Comilog ore in 50% CO - 50% CO$_2$ reduced at 550°C for 30 minutes

3.4 Analysis techniques

Chemical composition

The chemical composition was determined by X-Ray Fluorescence, except for the MnO_2, CO_2, H_2O and LOI content. The MnO_2 is determined by titration according to ASTM 465-11:2017: "Standard test methods for determination of Manganese (IV) in Manganese ores by Redox Titrimetry". Sodium oxalate is added to the solution, where the pH is controlled causing the oxalate to reduce Mn(4+) rather than other valences of manganese. Subsequently, the remaining sodium oxalate is titrated with a $KMnO_4$-solution to determine the amount of oxalate that was consumed by Mn(4+). According to the standard, elements ordinarily present in manganese ores will not interfere with the results[109]. As such, all reported Mn that was not MnO_2 was assumed to be MnO and all reported iron was assumed to be Fe_2O_3. The amount of surface moisture was determined by thermogravimetry, where the mass of moist sample is determined before the sample is dried in an oven at $110 \pm 5°C$ until a constant mass was achieved (ASTM D2216-19). The loss of mass was considered to be water. LOI was determined by measuring the loss of mass when the sample was heated to $950°C$ in a muffle furnace (ASTM D7348-13).

The amount of carbon was determined by Eltra (combustion-IR), which was recalculated to CO_2. The sample is combusted in a carrier gas (oxygen), where the released amounts of CO_2 during combustion is measured in two element selective IR cells. The use of two IR cells enables analysis of both very low and very high concentrations.

X-ray diffraction

The mineral composition of both ore and reduced samples were determined by X-ray diffraction. The specific instrument was a D8 A25 DaVinci X-ray Diffractometer with CuKα-radiation. The DaVinci has a LynxEye™ SuperSpeed Detector. Mineral identification was performed using the PDF database in the BRUKER EVA program. A slit of 0.2 was used throughout angle range 10-80°.

The data was treated by Rietveld analysis using the TOPAS Software, thus giving both mineral and its relative abundance in the sample. The background function was of 10th order. Quantification of phases by the Rietveld method is limited to crystalline phases where the structures are well known. For several of the identified minerals, no information on the crystal structure was available in the utilized database. In these cases, values from publications retrieved from the AMS Crystal Structure Database were used. Table 3.11 shows the database annotation for the identified phases with the reference contributing to crystal structure data for the minerals. This enables crystal structure data for all identified phases, except for nsutite, which was reported to be the a main constituting phase (>35 wt%) in both Gabonese (Comilog) and CVRD ore by Sørensen et al.[11]. Nsutite has a poorly defined crystal structure, which by Sørensen was modeled as a so-called peaks phase[16]. This implies that the nsutite is estimated without considering the X-ray absorption coefficient, causing the results to be semi-quantitative. This procedure was not performed in this study, implying that a quantitative mineralogy was not obtained for samples containing nsutite. This merely applies to untreated Comilog ore.

Table 3.11: Overview of references used where crystal data was not available in standard database

Mineral	Database annotation	Reference for crystal data
Braunite II	PDF 00-041-1368	De Villiers[110]
Manganite	PDF 00-041-1379	Kohler et. al.[111]

It should be mentioned that due to the complexity of manganese minerals, both in quantity of existing phases and potential severe cation substitution, the quantified results should only be used to evaluate trends.

The Rietveld analysis in TOPAS was executed according to following procedure:

- A background function of 10th order was applied
- All cell lengths were kept constant
- All atomic coordinates were kept constant
- Cry size L were allowed to refine within range of 50-200

Scanning electron microscope

Samples were mounted in epoxy and cut to expose the cross-section. Subsequently, they were ground and polished before being coated with carbon. A FE-SEM (Zeiss Ultra 55 LE) with Bruker EDS/NORDIF EBSD system was utilized for investigations of microstructure and analysis of composition. An acceleration voltage of 15 kV was applied. Element mapping of reduced particles was conducted by Electron Probe MicroAnalysis (EPMA). The specific equipment was a FE-EPMA with JEOL WDS system (JEOL JXA 8500).

SEM and EDS analysis of manganese ore is complicated due to several reasons. Certain typical manganese minerals exhibit highly similar compositions, which complicates the identification of the specific mineral by EDS, e.g. pyrolusite, ramsdelite, and nsutite. In addition, it is known that many minerals are subjected to cation substitution, which causes the composition to deviate from the theoretical stoichiometric relation. Lastly, the accuracy of EDS (and EPMA) analyses is affected by geometrical defects of the sample, such as cavities, cracks and porosity. Newbury and Ritchie observed the normalized concentration values obtained by quantitative EDS to be subjected to large errors, as high as a factor of 10, due to the specimen geometry deviating from the ideal flat bulk target[108]. It was also stated that analytical totals outside range of 98-102% indicated factors other than composition affecting the measurements, such as geometric effects.

Decrepitation

Some of the reduced samples were sieved manually into various size fractions to evaluate the mechanical strength and the extent of disintegration upon heating and reduction. The evaluated size fractions were -0.5 mm, + 0.5 mm, + 1.25 mm, +3.33, +4.75 mm, +6.7 mm, +10.0, and +13.2 mm.

3.5 Estimation of chemically bound moisture

As a direct quantification of the amount of chemically bound moisture in the ores is not possible, the content was estimated indirectly. Crushed ore samples (original size 11.20-15.00 mm) were held at high temperatures (940°C/1035°C) for 6 and 12 hours, respectively, in air in a small muffle furnace. Weight loss obtained at the evaluated temperatures is expected to include the removal of volatiles, i.e. surface moisture, bound moisture, and CO_2, in addition to a partial reduction of manganese and iron oxides. The amount of bound water is determined from the registered weight loss during heat treatment by subtracting the contributions from all the remaining components. The content of surface moisture and CO_2 is given by the raw material analysis, whereas further analysis of the heat-treated samples is required to determine whether the manganese and iron oxides have reached equilibrium. The theoretical weight loss for the mentioned components calculated from the raw material analyses was presented in Table 3.2 and Table 3.6 for Comilog- and Nchwaning-ore, respectively. Expected phases for manganese and iron according to thermodynamics (as seen in stability diagram in Figure 2.12) are Mn_3O_4 and Fe_2O_3, if not considering solid solution.

The input and output weight values for the different runs are shown in Table 3.12. All samples were investigated by X-ray diffraction, where abundance of identified phases was quantified by Rietveld analysis using Topas 5. To estimate the accuracy of the Rietveld analysis, the oxygen level of manganese in the Comilog ore sample held at 940°C for 12 hours was also determined by titration.

Table 3.12: Weight prior and subsequent to isothermal heat treatment in muffle furnace for Comilog and Nchwaning ore

	Set point [°C]	Furnace temperature [°C]	Holding time [hours]	Mass initial [g]	Mass out [g]	Loss [%]
	865	940	12	10.02	8.65	13.68
Comilog	950	1035	06	6.71	5.71	14.85
	950	1035	12	7.84	6.72	14.27
Nchwaning	865	940	12	15.99	15.50	3.02

Comilog ore

The obtained XRD spectrums for Comilog ore are shown in Figure 3.24, which shows that similar phases are present in all three samples. The manganese appeared to exist as a combination of Mn_2O_3 and Mn_3O_4, indicating that equilibrium was not reached. The values obtained through quantitative Rietveld analysis are presented in Table 3.13, which show the distribution between Mn_2O_3 and Mn_3O_4 in the individual samples, as well as the corresponding oxygen level (x in MnOx). The calculated oxidation level respective to the initial oxygen level correlates to a weight loss of 8.4wt%, 7.8 wt%, and 7.1 wt% for sample heated at 940°C for 12 hours, 1035°C at 6 and 1035°C at 12 hours respectively. According to the raw material analyses, Comilog only contains 0.12% CO_2 and 0.24% surface H_2O. From these values, the amount of chemically bound water was estimated to 6.1-6.2wt%, with an average of 6.1 wt% for the three runs.
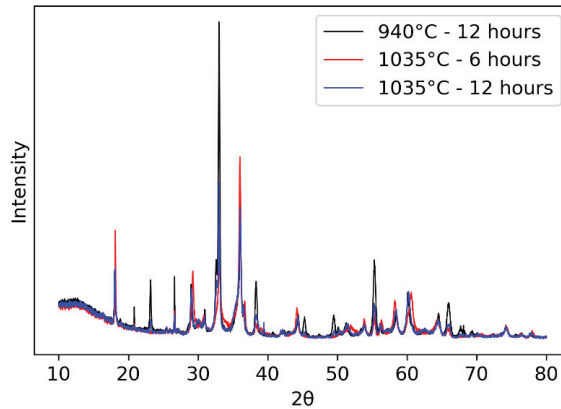
Figure 3.24: XRD spectrum of heat treated Comilog samples

The sample held at 940°C was subjected to a full chemical analysis, including determination of oxidation level of manganese by titration. The obtained x in MnO_x was 1.39, which is lower than that obtained through quantitative XRD analysis, i.e. 1.46. As a result, the estimated amount of bound moisture from utilizing the titration analysis is 5.1 wt%, approximately 14% lower than that obtained from XRD analysis. An overview of the components used to estimate the content of moisture for the different samples is presented in Table 3.14. There is a fair agreement between the values estimated from XRD and the estimation using the titration analysis, however it is assumed that the value estimated from the latter is more representative. The estimated amount of bound water shows high correlation with the values presented by Tangstad et al., where values in range 4.9-6.5% was reported for different types/grade of Comilog ore[10].

Table 3.13: Quantitative Rietveld analysis of Comilog ore samples subjected to isothermal heat treatment in muffle furnace

		940°C – 12 hours	1035°C – 6 hours	1035°C – 12 hours
MnO_2	%	0	0	0
$(Mn,Fe)_2O_3$	%	70	19	41
$(Mn,Fe)_3O_4$	%	24	72	51
MnO	%	0	0	0
x in MnOx (calc)		1.46	1.37	1.41
x in MnOx (titration)		1.39		

The amount of chemically bound moisture in Comilog was estimated without any consideration of the iron oxides present in the ore. According to thermodynamics, any iron oxides should remain stable as hematite under the evaluated conditions, which suggests that it is fair to neglect any weight loss attributed to Fe_xO_y reduction. In addition, from the raw material analysis, it was seen that Comilog contains 4.4 wt% Fe_2O_3,

which merely correlates to a theoretical weight loss of 0.2 wt% when reduced to Fe_3O_4, implying that a potential reduction would not significantly affect the results.

Table 3.14: Overview of weight loss attributions of the various components for Comilog ore held isothermally at 940°C and 1035°C

	940°C – 12 hours [wt%]		1035°C – 6 hours [wt%]	1035°C – 12 hours [wt%]
	XRD	Titration	XRD	XRD
Total weight loss	13.7	13.7	14.9	14.3
Components:				
H_2O(surface)	0.2	0.2	0.2	0.2
CO_2	0.1	0.1	0.1	0.1
MnOx reduction	7.1	8.3	8.4	7.8
Bound moisture (=total – components)	6.2	5.1	6.1	6.1

Nchwaning ore

A weight loss of 3 wt% was obtained after 12 hours holding time at 940°C for Nchwaning ore. Quantitative Rietveld analysis of the XRD spectrum of the treated Nchwaning sample indicated that no reduction of manganese and iron oxides had occurred after 12 hours holding time at 940°C. The calculated oxygen level of manganese (x in MnOx) was calculated to 1.47, which is identical to that analysed in the untreated ore.

The XRD spectrum indicated that carbonates had been decomposed to CaO. According to raw material analysis, the ore originally contains 3 wt% CO_2, which suggests that the obtained weight loss during the isothermal heat treatment may fully be attributed to the decomposition of carbonates. Thus, the results indicate that Nchwaning contains negligible amounts of chemically bound moisture.

3.6   Overview of experiments

This section provides an overview of all experiments conducted in this study, where the experimental series are presented separately for readability. Table 3.14 shows the experiments conducted in CO-CO_2 atmosphere in the DisVaDri furnace at non-isothermal temperature regimes. Experiments with ore and quartz in various ratios is seen in Table 3.16, whereas experiments with CO-CO_2-H_2-H_2O is shown in Table 3.17. Similar overview for experiments conducted utilizing the Tammann furnace at RWTH is presented in Table 3.18.

Table 3.15: Overview of conducted non-isothermal experiments in CO-CO$_2$ atmosphere. All experiments were conducted at 6°C/min heating rate if not other specified

Material	Size	CO:CO$_2$	Temperature [°C]
Nchwaning	0.50-1.36 mm	50:50	1000
		80:20	1000
	3.33-4.00 mm	50:50	300
		50:50	800
		50:50	1000
		80:20	800
		80:20	1000
	11.20-15.00 mm	50:50	700
		50:50	800
		50:50	1000
		50:50	1000 (3°C/min)
		80:20	1000
	30.00-40.00 mm	50:50	800
		50:50	1000
Comilog	0.50-1.36 mm	50:50	1000
		80:20	1000
	3.33-4.00 mm	50:50	300
		50:50	800
		50:50	1000
		50:50	1200
		80:20	300
		80:20	800
		80:20	1000
	11.20-15.00 mm	30:70	1000
		40:60	1000
		50:50	400
		50:50	550
		50:50	1000
		50:50	1000 (2)
		50:50	1000 (3°C/min)
		50:50	1000 (9°C/min)
		80:20	550
		80:20	1000
	11.20-15.00 mm (wet ore)	50:50	770
		50:50	1000
	30.00-40.00 mm	50:50	800

Table 3.16: Overview of non-isothermal experiments conducted with ore and quartz in various ratios

Materials	Mixing ratio by weight
Comilog (3.33-4.00 mm) : quartz	1:0
	1:1
	1:3
Comilog (11.20-15.00 mm) : quartz	1:0
	1:1
	1:3
	1:3 (2)
Nchwaning (3.33-4.00 mm) : quartz	1:0
	1:1
	1:3
Nchwaning (11.20-15.00 mm) : quartz	1:0
	1:1
	1:1 (2)
	1:1 (3)
	1:3
	1:3 (2)
Ore:quartz	0:1

Table 3.17: Overview of experiments non-isothermal experiments conducted in CO-CO$_2$-H$_2$-H$_2$O atmosphere

Ore	Mix	CO:CO$_2$:H$_2$:H$_2$O [L/min]	Furnace setpoint [°C]
Comilog	1a	1.75:1.75:0.50:0.00	500
	1a (2)	1.75:1.75:0.50:0.00	400
	1b	2.24:1.25:0.00:0.50	500
	2a	2.80:0.70:0.50:0.00	500
Nchwaning	1a	1.75:1.75:0.50:0.00	500
	1a (2)	1.75:1.75:0.50:0.00	700
	1b	2.24:1.25:0.00:0.50	700
	2a	2.80:0.70:0.50:0.00	700

Table 3.18: Overview of conducted isothermal experiments at IEHK RWTH. All experiments were conducted with ore in size fraction 11.20-15.00 mm

Ore	Gas	Temperature [°C]	Time [min]
Comilog	50%CO+50%CO$_2$	400	40 (1)
		500	40 (1)
		500	40 (2)
		500	40 (3)
		500	20 (1)
		550	40 (1)
		550	30 (1)
		550	30 (2)
		550	30 (3)
		600	40 (1)
		600	40 (2)
		600	20 (1)
		600	20 (2)
	70%CO+30%CO$_2$	400	40 (1)
		400	40 (2)
		400	20 (1)
		400	20 (2)
		500	40 (1)
		500	40 (2)
		500	20 (1)
		600	40 (1)
		600	40 (2)
Nchwaning	50%CO+50%CO$_2$	600	60 (1)
		600	60 (2)
		600	30 (1)
		700	60 (1)
		700	60 (2)
		700	30 (1)
		700	30 (2)
		800	60 (1)
		800	30 (1)
		800	30 (2)
		800	30 (3)
		800	30 (4)
		900	30 (1)
		900	30 (2)
	70%CO+30%CO$_2$	600	60 (1)
		700	60 (1)
		700	30 (1)
		700	30 (2)
		800	60 (1)
		800	30 (1)

4   Results

This chapter presents the results obtained through the experimental investigation of the prereduction behavior of manganese ore. The results are categorized into to the different experimental series, where weight reduction behavior, decrepitation, and analysis of reduced samples are presented accordingly. Presented weight reduction behavior is data treated according to procedure described in section 3.3.1 and 3.3.2, if not stated otherwise.

4.1   Comilog ore

4.1.1   Non-isothermal reduction in CO-CO$_2$ atmosphere

Weight reduction behavior

Figure 4.1 shows the recorded sample temperature for non-isothermal experiments with a heating rate of 6°C/min with target temperature of 1000°C. The sample temperature is seen to be lagging somewhat in the initial stages of the experiment, which is due to the setup of the furnace. As Comilog is a high oxygen ore, where the majority of the initial manganese is present as MnO$_2$, a large amount of heat is produced during the reduction. This causes the sample temperature to show a positive deviation from the predetermined heating rate of 6°C/min. The deviation is initiated at a lower process time for smaller particle sizes. Considering the reduction in 50%CO-50%CO$_2$, the deviation is initiated at 27 minutes process time for particle size 0.50-1.36 mm, and further at 29 minutes, 34 minutes, and 40 minutes for size 3.33-4.00 mm, 11.2-15.0 mm, and 30.0-40.0 mm, respectively. Similar behavior is observed in 80%CO-20%CO$_2$. With increasing temperature and process time, the effect of the exothermic reactions decreases, and the sample temperature converges according to the heating rate.
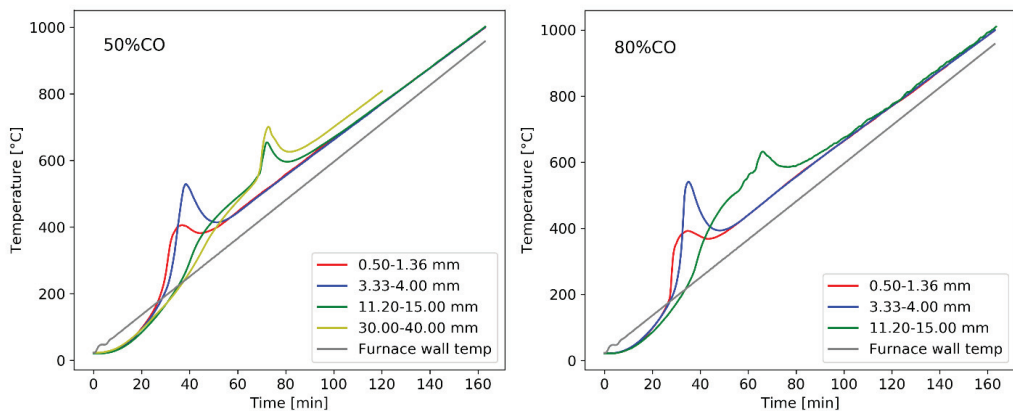
Figure 4.1: Temperature behavior for Comilog ore experiments with target temperature 1000°C at a heating rate 6°C/min

Figure 4.2 shows the calculated weight as a function of process time and sample temperature, respectively, for experiments with target temperature of 1000°C. The four different particle sizes are differentiated by color, whereas dashed lines represent experiments conducted in 50%CO-50%CO$_2$ and solid lines represents 80%CO-20%CO$_2$. Weight reduction is initiated at approximately 150°C, 200°C, 250°C and 300°C for particle size 0.50-1.36 mm, 3.33-4.00 mm, 11.20-15.00 mm and 30.00-40.00 mm, respectively. It is clear that the temperature development is a function of the reaction rate. When evaluated as a function of temperature, a clear distinction in reaction temperatures is observed for all four particle sizes. On the contrary, when evaluating as a function of time, it can be observed that the two smaller particle sizes starts to reduce at similar process times, where the reduction is completed within a few minutes. The two largest particle size reduce significantly slower compared to the two smaller. Particle sizes in range 0.50-15.00 mm appear to have obtained a complete prereduction at 800°C, deduced from the stable weight at exceeding temperatures. A low, but significant dependence on the CO partial pressure is deduced from the curves.
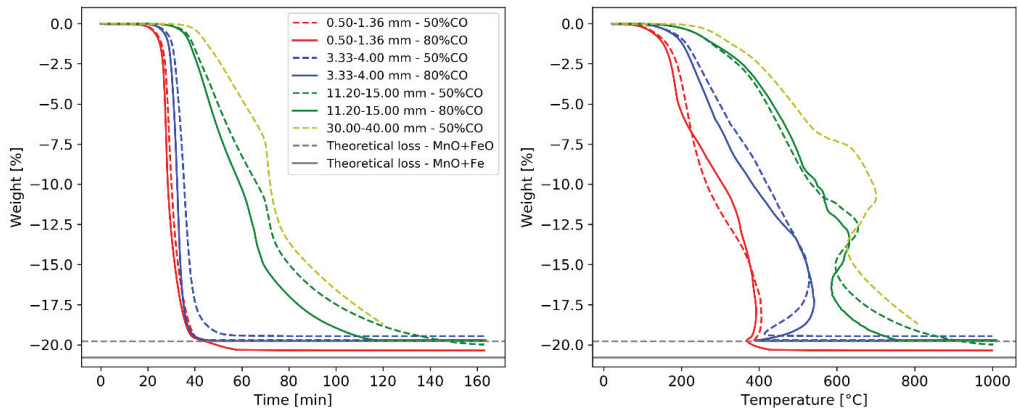
Figure 4.2: Calculated weight as a function of time and temperature, respectively, for Comilog ore heated to 1000°C. Legend is valid for both figures

Figure 4.3 shows the calculated reduction rate correlating to the curves presented in Figure 4.2. For the two smaller particle sizes, a higher reduction rate is obtained for 80% CO compared to 50% CO, however the temperature range at which the rate is larger than zero, confirming ongoing reduction, is the same for both gas atmospheres. The reduction rate for particle size 11.2-15.0 mm and 30.0-40.0 mm indicates the occurrence of at least two individual reduction steps, as several peaks can be observed. The rate starts to increase slowly at approximately 200-250°C, likely due to the reduction of MnO$_2$. The rate shows a small decrease at approximately 300°C, before increasing up to peak at 400°C. When the temperature reaches approximately 580°C, a rapid reduction stage is initiated for the two largest particle sizes. The peak positions of the reaction rate appear to be only slightly affected by gas composition and particle size, as similar trends are observed for 11.2-15.0 mm particles in 50% CO and 80% CO, as well as 30.00-40.00 mm in 50% CO. It can be observed that the reduction rate is significantly lower for the two larger particle

sizes compared to particles of size 0.50-4.00 mm, where maximum obtained rate is approximately 0.7 wt%/min for 11.2-15.0 mm. As a comparison, maximum obtained rate for particle size 0.50-1.36 mm in 80% CO is 3.8 wt%/min. For the experiment with 11.20-15.00 mm particles reduced in 80% CO, the recorded CO_2 was seen to decrease below set-point value at temperatures exceeding 780°C, indicating the occurrence of the Boudouard reaction. The calculated amount of deposited carbon was merely 0.07 g, which may be considered insignificant.
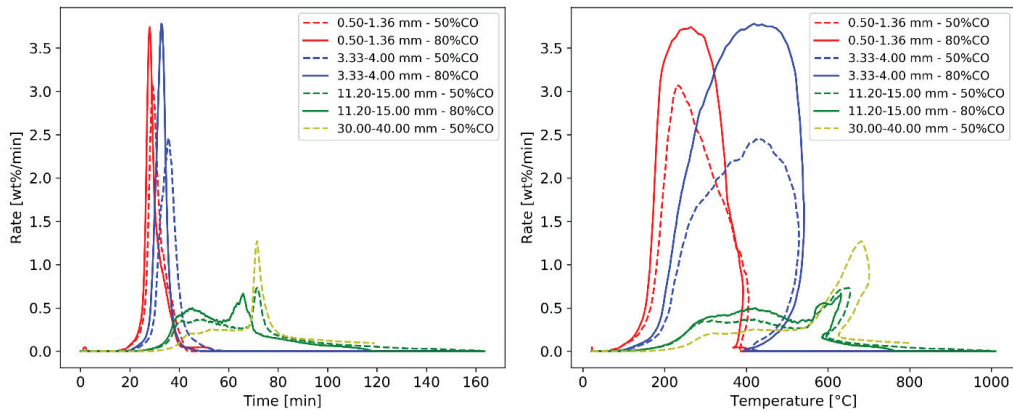
Figure 4.3: Reaction rate (wt%/min) as a function of time and temperature, respectively, for Comilog ore

The effect of CO partial pressure was further evaluated for particle size 11.20-15.00 mm, where the calculated weight and correlating rate are shown in Figure 4.4 and Figure 4.5. It is seen that the reduction is initiated at similar temperature in all atmospheres, where the same trends are observed throughout the experiments. The curves confirm that the reaction rate may be divided into two main regions, occurring at temperature ranges 200-580°C and 580-1000°C, respectively, where a lower rate in the initial stage correlates to a higher rate in the second stage. Further, the curves indicate that the first reaction stage may likely be further separated into two reaction stages, as all curves show a local minima in the rate at temperatures 350-400°C. A rapid reduction stage is initiated at 580°C for all gas atmospheres.

In order to confirm that the trends observed at heating rate 6°C/min was due to reaction behavior, and not the predetermined temperature program, samples of 11.20-15.00 mm reduced in 50%CO-50%CO$_2$ were evaluated at 3°C/min, 6°C/min, and 9°C/min. From the recorded temperature development and the calculated weight as a function of temperature in Figure 4.6, it can be seen that an increasing heating rate correlates to a higher sample temperature. Further, it is observed that a rapid reduction stage is initiated at temperatures close to 600°C at all three heating rates. Thus, the rapid reduction stage is independent of heating rate. The amount of weight loss (reduction) occurring in the rapid stage is dependent on the reduction extent when threshold temperature is reached. As such, the weight loss attributed to the rapid stage is large for experiment conducted at 9°C/min and small for 3°C/min, correlating to the low and high weight loss at threshold temperature, respectively.
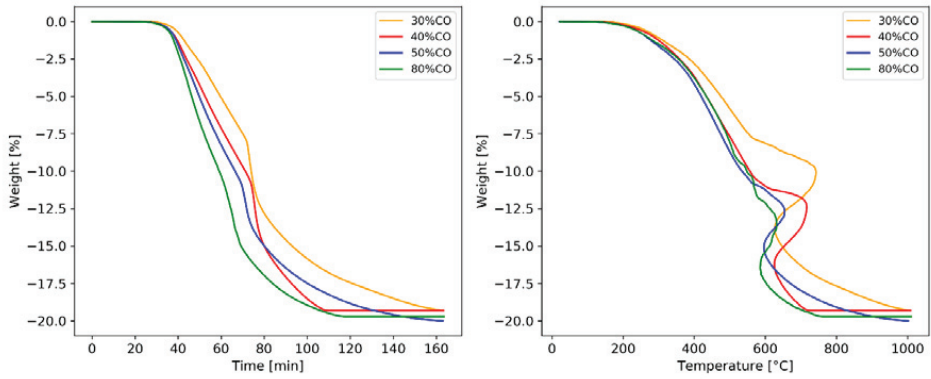
Figure 4.4: Comilog ore (11.20-15.00 mm) in various partial pressures of CO in CO-CO_2 atmosphere. Experiments conducted with heating rate 6°C/min up to 1000°C
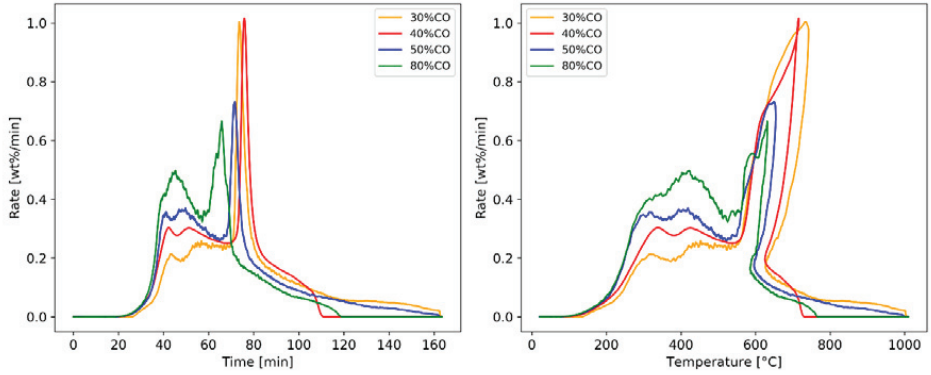
Figure 4.5: Reaction rate [wt%/min] for Comilog ore (11.20-15.00 mm) in various CO partial pressures in CO-CO_2 atmosphere
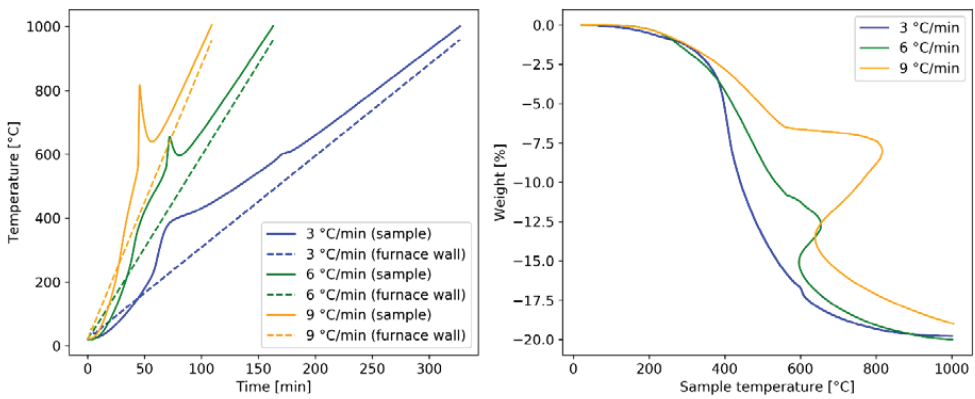
Figure 4.6: Comilog ore in particle size 11.20-15.00 mm heated at 3°C/min, 6°C/min, and 9°C/min, respectively, in 50%CO-50%CO_2. Left: temperature behavior. Right: weight reduction behavior

Reproducibility

The reproducibility of the experiments was evaluated by comparison of the TGA curves where all experimental conditions, except for target temperature, remained constant. In addition to the standard experiments with target temperature of 1000°C, several additional target temperatures were evaluated for particle size 3.33-4.00 mm and 11.20-15.00 mm. The temperatures measured by the thermocouples submerged in the sample, as well as the weight behavior as a function of time and temperature, are shown for all experiments conducted with similar conditions in this section.

The temperatures observed in the experiments conducted with particles of initial size 3.33-4.00 mm at 6°C/min up to various target temperatures are shown in Figure 4.7. The weight as a function of time and temperature are shown in Figure 4.8 and Figure 4.9 for experiments conducted in 50%CO and 80%CO, respectively. Highly similar temperatures and weight behavior were obtained for the experiments in 50%CO-50%CO_2. For the experiments conducted in 80%CO-20%CO_2, the temperatures show highly similar behavior, however the maximum obtained temperature was considerably higher in the experiment terminated at 800°C. As such, the weight as a function of time shows a high degree of overlap for the various runs, whereas the weight as a function of temperature show some dissimilarities. As the chemical analysis of the samples were highly similar, it is not believed that the increased temperature is due to a higher content of MnO_2. A potential explanation is differences in the thermocouple position.
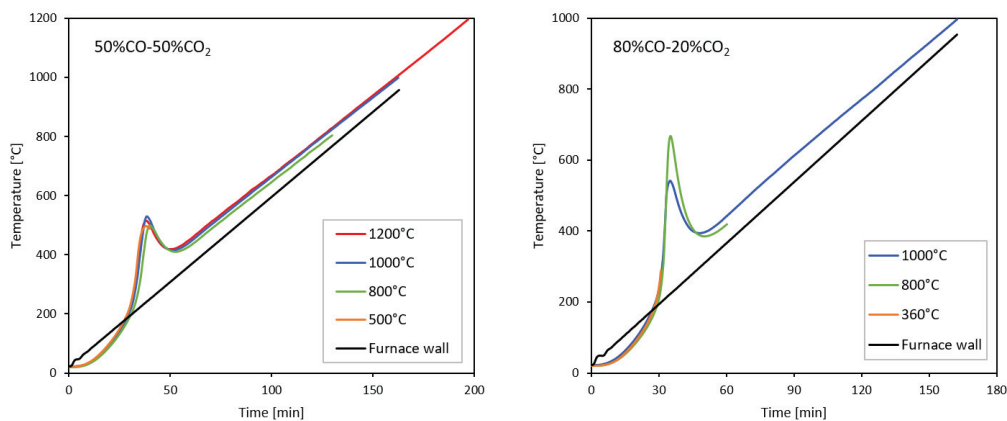
Figure 4.7: Temperature behavior as obtained from thermocouple submerged in sample for Comilog ore in size 3.33-4.00 mm heated in 50%CO-50%CO_2 and 80%CO-20%CO_2, respectively

The temperature measurements for experiments conducted with initial particle size 11.20-15.00 mm are shown in Figure 4.10. In general, similar temperature behavior was observed for the repeated runs with various target temperatures. In the experiment terminated at 400°C in 50%CO and the experiment terminated at 550°C in 80%CO, a constant deviation in the temperature development was introduced from an error in the prescribed temperature program. This deviation is observed in the furnace wall temperatures, which have been included in the figures. From the weight behavior curves shown in Figure 4.11 and Figure

4.12 for experiments in 50%CO and 80%CO, respectively, it is seen that the experiments conducted at similar conditions show high reproducibility. A small deviation is observed for the before mentioned curves which experienced a slightly faster heating rate.
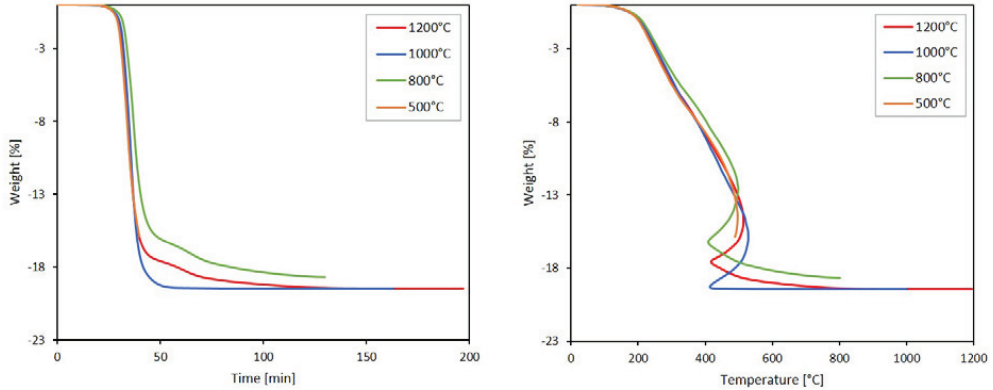
Figure 4.8: Weight as a function of time and temperature, respectively, for Comilog ore in size 3.33-4.00 mm heated in 50%CO-50%CO_2 up to target temperatures in range 500-1200°C
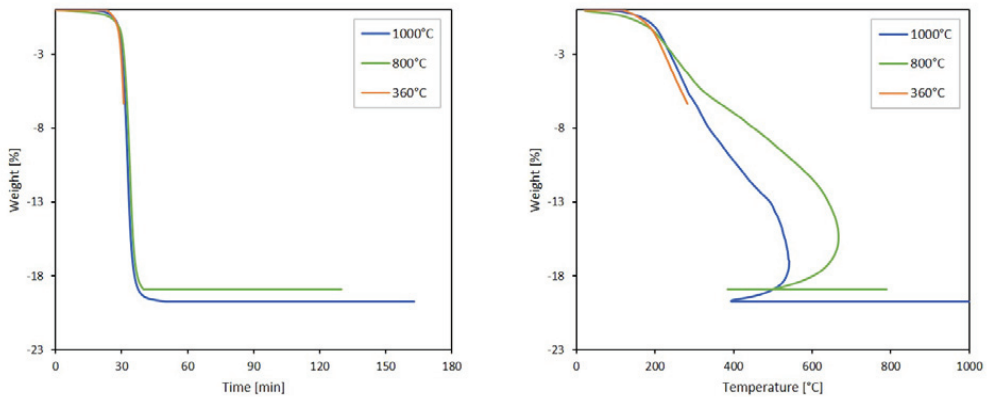
Figure 4.9: Weight as a function of time and temperature, respectively, for Comilog ore in size 3.33-4.00 mm heated in 80%CO-20%CO_2 up to target temperatures in range 360-1000°C

Thus, the comparison of the TGA data obtained for experiments conducted with similar experimental conditions, merely with a change in the target temperature, shows that the reduction of Comilog ore in CO-CO_2 is highly reproducible. A slightly faster weight loss was obtained in a few of the experiments, however, the extent of the deviation is assumed to be of negligible size. The deviation was due to an error in the prescribed temperature program.
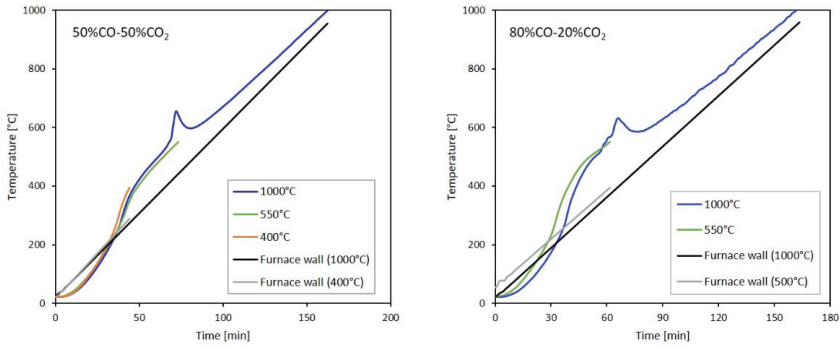
Figure 4.10: Temperature behavior as obtained from thermocouple submerged in sample for Comilog ore in size 11.20-15.00 mm heated in 50%CO-50%CO2 and 80%CO-20%CO2, respectively
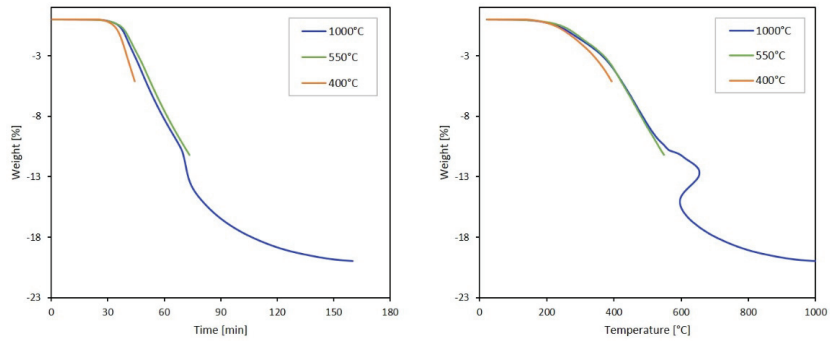
Figure 4.11: Weight as a function of time and temperature, respectively, for Comilog ore in size 3.33-4.00 mm heated in 50%CO-50%CO2 up to target temperatures in range 400-1000°C
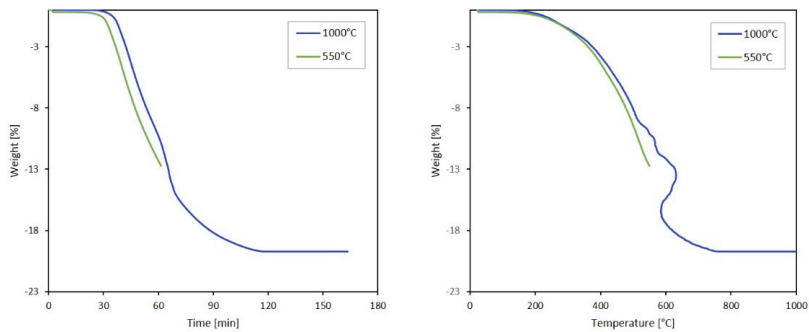
Figure 4.12: Weight as a function of time and temperature, respectively, for Comilog ore in size 3.33-4.00 mm heated in 80%CO-20%CO2 up to target temperatures in range 550-1000°C

95

Decrepitation

Figure 4.13 shows the sample size fraction distribution after reduction of 11.20-15.00 mm particles reduced in 50%CO-50%CO_2 at 6°C/min up to 400°C, 750°C, and 1000°C, respectively. The data indicates that decrepitation increases with increasing temperature, and thus increasing reduction extent. The size fraction distribution was also evaluated for the three different heating rates applied to the reduction of 11.20-15.00 mm particles in 50%CO-50%CO_2 up to 1000°C, where the results are shown in Figure 4.14, which indicates that decrepitation decreases with increasing heating rate. This is contradictory of what is expected, as an increasing heating rate likely correlates to larger thermal stresses in the particles. Furthermore, the increased heating rate was also observed to correlate to a larger exothermic peak (as shown in Figure 4.6), which causes additional thermal stresses. Thus, it is indicated that the rapid reduction step resulting in a large exothermic peak in temperature is not a major factor in the decrepitation of Comilog ore. It is possible that the ore is more susceptible towards decrepitation when the reduction occurs at low temperature.
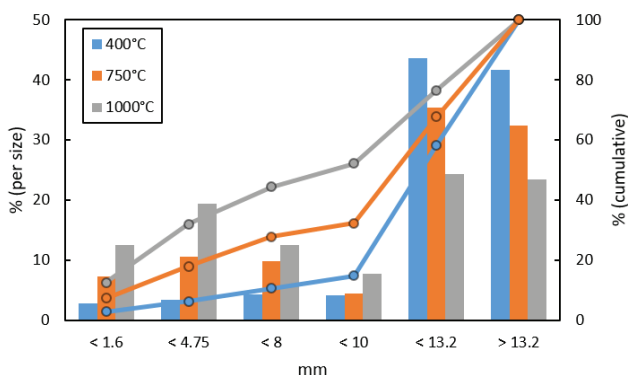
Figure 4.13: Size distribution after reduction of Comilog ore (11.20-15.00) in 50%CO-50%CO_2 heated at 6°C/min up to 400°C, 750°C and 1000°C, respectively
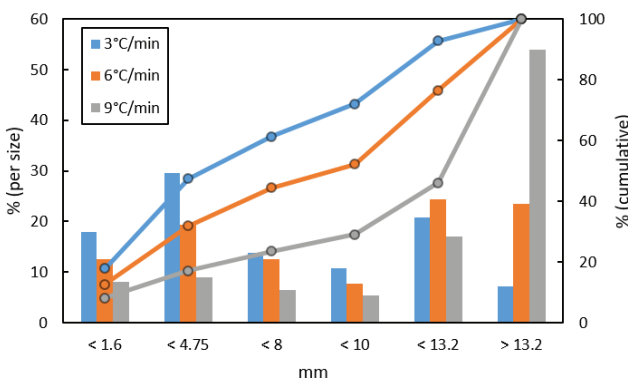
Figure 4.14: Size distribution after reduction of Comilog ore (11.20-15.00) in 50%CO-50%CO_2 heated at 3°C/min, 6°C/min, and 9°C/min, respectively up to 1000°C

Analysis

Table 4.1 shows the chemical composition of the reduced Comilog samples, where only species where quantification exceeds 1 wt% are presented. It can be seen that the analysed x in MnO_x lies between 1.01-1.06 for the experiments heated to 1000°C. As the recorded weight and $\%CO_2$ in the off-gas remained stable at a considerable time and temperature interval prior to termination of several of these experiments, it is believed that a complete reduction was obtained in samples where analysed x in MnOx was within range 1.00-1.05. Figure 4.15 shows the total weight loss (found from weighing sample prior and subsequent to experiment) as a function of analyzed oxidation level of manganese (x in MnOx). A linear regression showing the correlation between the weight loss and analysed oxidation level is included in the figure, which shows that the total observed weight loss behavior may be used to express the reduction behavior of manganese oxides in Comilog ore.

Table 4.1: Chemical analysis of Comilog ore reduced non-isothermally at 6°C/min

Size [mm]	Gas	Temperature	Fe, tot	Mn, tot	MnO_2	MnO	SiO_2	Al_2O_3	K_2O	**MnOx**
0.5-1.36	50% CO	1000°C	4.4	58.8	3.2	73.3	6.7	7.8	1.3	**1.03**
0.5-1.36	80% CO	1000°C	4.4	59.2	0.9	75.7	6.9	7.6	1.3	**1.01**
3.33-4.00	50%CO	500°C	3.7	59.1	24.9	56.0	3.9	6.3	1.3	**1.26**
3.33-4.00	50%CO	800°C	3.7	60.9	9.8	70.6	4.1	6.6	1.4	**1.10**
3.33-4.00	50%CO	1000°C	2.2	62.4	4.0	77.3	4.3	6.5	1.4	**1.04**
3.33-4.00	80%CO	360°C	3.6	60.9	54.9	33.9	4.3	6.8	1.4	**1.57**
3.33-4.00	80%CO	790°C	3.6	60.9	4.4	75.1	4.3	6.8	1.4	**1.05**
3.33-4.00	80%CO	1000°C	3.2	63.5	2.4	80.0	3.9	6.2	1.3	**1.02**
11.2-15.0	30%CO	1000°C	2.1	65.5	6.1	80.0	2.8	5.6	1.4	**1.06**
11.2-15.0	40%CO	1000°C	5.5	61.2	4.0	75.8	3.4	5.1	1.2	**1.04**
11.2-15.0	50%CO	400°C	4.4	53.4	64.7	16.1	3.4	5.7	0.6	**1.77**
11.2-15.0	50%CO	550°C	6.2	55.2	45.1	34.5	3.1	4.9	0.8	**1.52**
11.2-15.0	50%CO	1000°C	3.1	62.9	3.9	78.1	4.2	7.4	1.1	**1.04**
11.2-15.0	80%CO	550°C	2.5	58.7	40.3	42.9	4.1	5.5	1.0	**1.43**
11.2-15.0	80%CO	1000°C	2.2	64.9	5.3	79.6	4.5	6.1	0.8	**1.05**
30.0-40.0	50%CO	800°C	1.5	65.6	25.3	64.1	2.4	4.6	1.0	**1.24**

Some of the samples were subjected to XRD analysis, where a quantitative Rietveld analysis was performed to obtain the abundance of the identified phases. The obtained values for partially reduced samples of particle size 11.20-15.00 mm and 30.00-40.00 mm are shown in Table 4.2. Nsutite and lithiophorite was not detected in any of the particles, indicating that these minerals experience a dehydration at temperatures lower than 400°C under the evaluated conditions. For particle size 11.20-15.00 mm heated in 50% CO it is observed that at 400°C (16% reduced), the reduction product was a combination of bixbyite, hausmannite, and manganosite, where hausmannite was the major phase. At 550°C (45% reduced), the intermediate oxides bixbyite and hausmannite were found only in minor concentrations, and the manganese was

distributed between tetravalent oxides and manganosite. In correlation to the weight reduction behavior, this suggests that the initial stages of reduction is largely attributed to MnO_2-oxides reducing to Mn_3O_4, where a slightly higher temperature is required to further reduce Mn_3O_4 to MnO, resulting in the small decrease in the reaction rate observed at approximately 380°C. The sample is composed of tetravalent oxides and manganosite when the rapid reduction stage is initiated, as observed in the mineralogy for the samples heated in 50% CO and 80% CO terminated at 550°C. The table also shows the mineralogy of particle size 30.00-40.00 mm heated in 50% CO up to 800°C. Chemical analysis correlates to a 74% reduction of higher manganese oxides to MnO for this experiment, and the rate curves show that the experiment was terminated after the rapid reduction stage. The quantified mineralogy shows that all tetravalent oxides has been reduced/decomposed at this temperature, where the manganese was found to be distributed between bixbyite and manganosite. No phases containing aluminium were identified by XRD, and it is believed that the aluminium is present in solid solution in the identified manganese oxides. Prior to reduction, the aluminium was mainly present in lithiophorite. Not much information is available on the thermal behavior of lithiophorite, however some studies indicate that it experience a dehydration at low temperatures and a further conversion to a spinel phase, displayed as broad and weak lines in the XRD spectrum[35], [112]. As such, it is believed that the aluminium is mainly present in solid solution in the hausmannite phase, which is a tetragonal spinel, i.e. $(Mn^{2+})(Mn^{3+}, Al^{3+})_2O_4$, For fully reduced samples, where x in MnOx was 1.00-1.05, it was found that all major peaks were described by manganosite, which according to Rietveld analysis constituted approximately 97% of the reduced ore. The remaining 3% were identified as quartz, kalsilite, and galaxite.
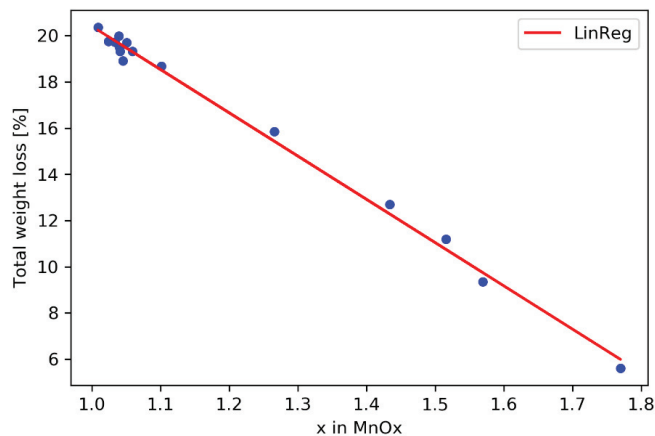
Figure 4.15: Weight loss found from weighing of sample prior and subsequent to experiment as a function of analyzed oxidation level of manganese (x in MnOx). A linear regression (red line) was included to show the relation

Table 4.2: Quantitative Rietveld analysis of mineralogy in partially reduced Comilog samples (11.20-15.00 mm)

Mineral	11.20-15.00 mm			30.00-40.00 mm
	50%CO	50%CO	80%CO	50%CO
	400°C	550°C	550°C	800°C
Manganosite (MnO)	11	54	58	63
Bixbyite (Mn_2O_3)	7	6	7	31
Hausmannite (Mn_3O_4)	18	3	3	5
Pyrolusite (MnO_2)	42	32	28	-
Cryptomelane (KMn_8O_{16})	19	4	4	-
Quartz (SiO_2)	4	2	-	1
Reduction according to titration (MnOx)	16%	45%	54%	74%

Selected particles were mounted in epoxy and cut to expose the cross-section, which was further investigated by scanning electron microscope or by optical microscope. In correlation to the large variance in microstructure observed in untreated Comilog ore (as shown in section 3.2.1), a large variance was also observed in partially reduced samples. Figure 4.16 shows the microstructure observed in three individual particles from the experiment heated in 50%CO-50%CO_2 terminated at 400°C, which according to chemical analysis was 16% reduced. Cracks have formed throughout the surface in all three particles. The particle to the right was homogeneously composed of a single phase, whereas several phases are coexisting in a random distribution in the second particle (center image). A new phase appears to have nucleated in the particle shown to the left, as small regions of a brighter grey phase is dispersed throughout the structure. No indications of a topochemical reaction mechanism was found in the evaluated particles.
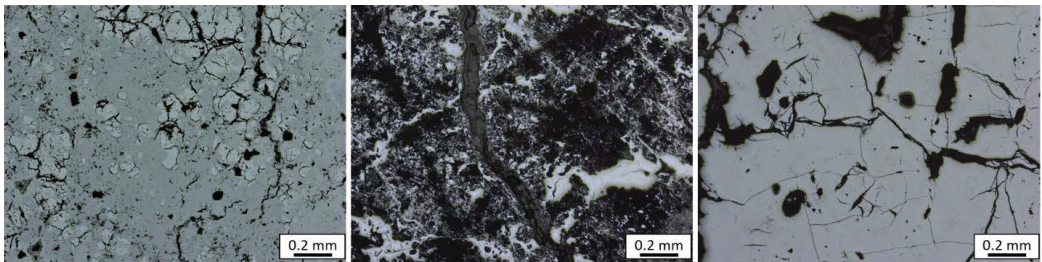
Figure 4.16: Microstructure observed in three different Comilog ore particles (11.20-15.00 mm) reduced at 6°C/min up to 400°C in 50%CO-50%CO_2. Chemical analysis correlate to 16% reduction of manganese oxides

Figure 4.17 and Figure 4.18 shows the microstructure of a single particle reduced in 50%CO and 80%CO, respectively, at 6°C/min up to 550°C. An overview including the outer edge is observed to the left in the figures, whereas a close-up of the center is seen to the right. In line with the observations made from the particles at 400°C, the particles heated up to 550°C do not show any indications of a topochemical reaction mechanism. The sample reduced in 50%CO obtained a reduction of manganese oxides of 45% according

to chemical analysis, where a highly homogenous structure is observed. The matrix is a homogeneous bright grey phase, where smaller regions of a heterogeneous darker grey phase is randomly dispersed in the structure. The particle reduced in 80%CO displays a disorganized structure composed of at least three distinct phases. The phases were analysed by EDS, where the obtained chemical composition is observed in Table 4.3. The analytical total is relatively low for the majority of the analyses, which may be due to geometric effects, such as cracks and porosity[108]. According to the EDS results, the matrix phase of the particle shown in Figure 4.17 and the bright grey phase in Figure 4.18 are MnOx-phases. As reliable quantification of oxygen content is not possible with EDS, the relation between manganese and oxygen cannot be used to determine the oxidation state of manganese. The phases were found to be homogeneous, as a similar oxygen to manganese ratio was found throughout the phase areas. The minor phases were found to contain mainly manganese, aluminium, and oxygen, and silicon in some areas. The concentration of these elements varied throughout the phase. The extent of variation can be seen for the particle reduced in 50% CO, where the composition obtained in three different locations are presented in Table 4.3.
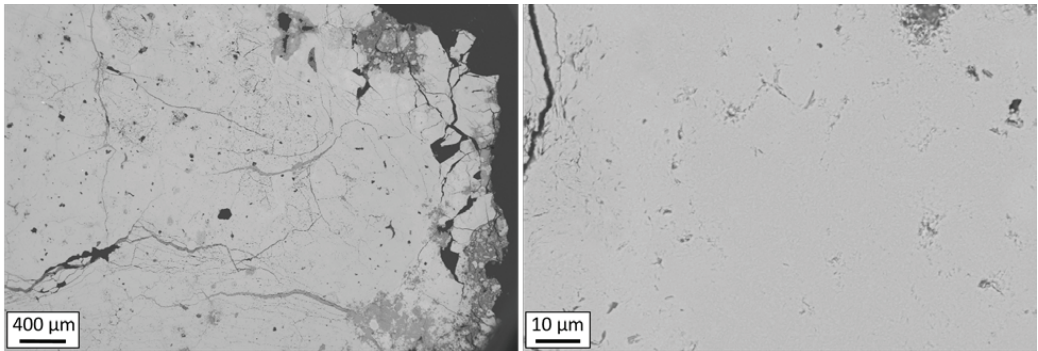
Figure 4.17: Microstructure observed in Comilog ore particle (11.20-15.00 mm) reduced non-isothermally in 50%CO to 550°C. Reduction degree of 45% of higher manganese oxides to MnO according to chemical analysis. Overview including outer edge seen to the left, whereas image to the right shows the center
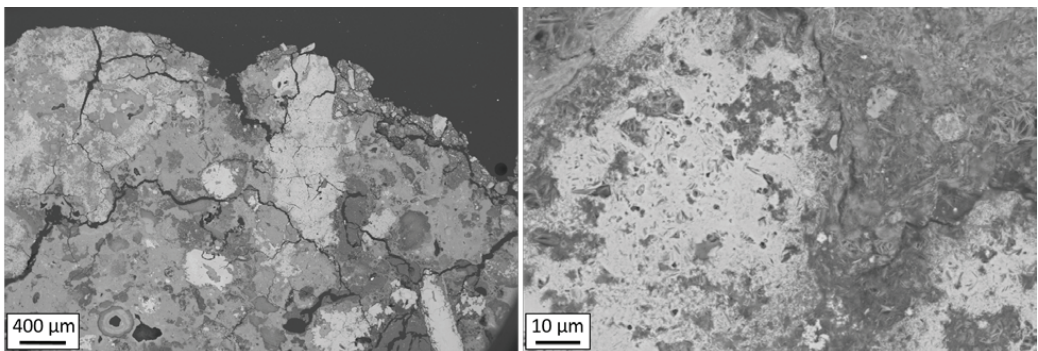
Figure 4.18: Microstructure observed in Comilog ore particle (11.20-15.00 mm) reduced non-isothermally in 80%CO to 550°C. Reduction degree of 54% of higher manganese oxides to MnO according to chemical analysis. Overview including outer edge seen to the left, whereas image to the right shows the center

Table 4.3: Chemical composition as analysed by EDS [at%] of phases observed in microstructure of partially reduced samples shown in Figure 4.17 and Figure 4.18 (Average of 3-5 point analyses)

		Mn [at%]	Fe [at%]	Al [at%]	Si [at%]	O [at%]	Total [wt%]	Suggested phase
50% CO	Matrix	43.1	0.4	-	-	56.0	85.0	MnOx
	Minor #1	12.4	0.3	16.6	0.7	68.6	107.5	
	Minor #2	41.8	0.0	19.0	0.0	38.6	78.8	
	Minor #3	20.0	0.0	17.1	0.4	56.9	82.0	
80%CO	Bright (1)	59.9	0.0	1.7	0.1	35.3	81.0	MnOx
	Medium (2)	22.5	0.9	19.3	4.6	51.3	75.2	
	Dark (3)	23.2	1.4	19.8	5.1	48.9	74.7	

Element mapping of particles in size fraction 0.50-1.36 mm and 3.33-4.00 mm reduced in 50% CO(remainder CO_2) at 6°C/min up to 1000°C is shown in Figure 4.20 and Figure 4.19, respectively. According to chemical analysis, these samples had obtained a complete prereduction. The results illustrate the heterogeneity of Comilog ore, where concentrations of certain elements show a large variance between the particles, in addition to a varying concentration within single particles. Two types of particles are observed in respect to the aluminium concentration, i.e. particles with low/insignificant concentrations and particles with high/considerable concentrations. The aluminium is present throughout the particles, however at varying concentration, which correlates well with that the aluminium is in solid solution in the manganese oxide phases. In addition, the element mapping reveals that the quartz found in Comilog ore is not evenly distributed between the particles. Rather, certain particles are largely composed of quartz, seen as areas high in silicon and oxygen, and low in the remaining elements. The remaining particles show low concentrations of silicon.
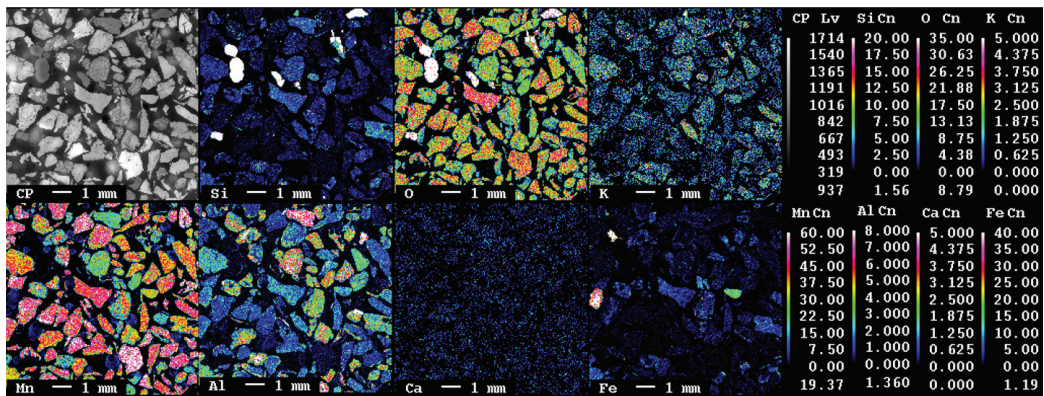
Figure 4.19: Element mapping of Comilog ore particles of initial size 0.50-1.36 mm heated in 50%CO-50%CO2 at temperatures 25-1000°C (6°C/min). Chemical analysis showed that the ore particles obtained a complete prereduction of higher manganese oxides to MnO
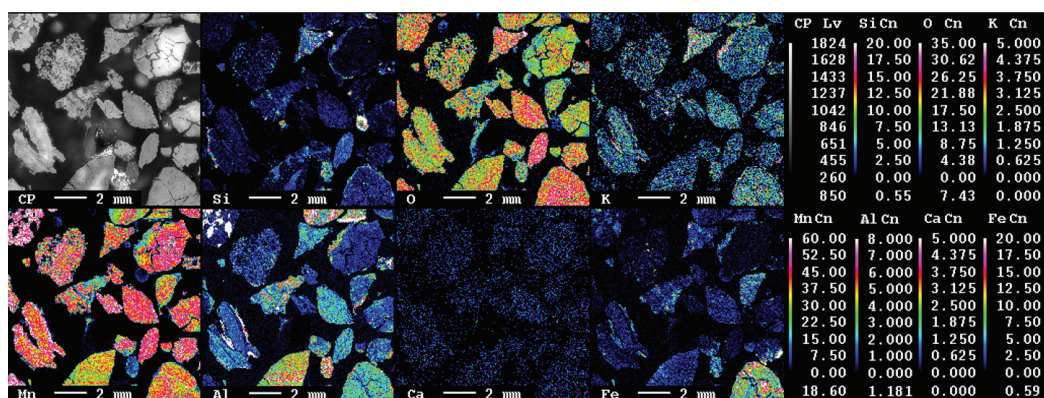
Figure 4.20: Element mapping of Comilog ore particles of initial size 3.33-4.00 mm heated in 50%CO-50%CO₂ at temperatures 25-1000°C (6°C/min). Chemical analysis showed that the ore particles obtained a complete prereduction of higher manganese oxides to MnO

4.1.2   Isothermal reduction - CO-CO₂ atmosphere

Weight reduction behavior

Comilog ore was reduced isothermally at temperatures 400-600°C in 50% CO and 70% CO, remainder being CO_2. Due to limitations in the furnace geometry, the sample size evaluated in each experiment was relatively small. In general, 4 particles were used, correlating to an input weight in the range of 20-25 g. As such, the specific weight loss obtained during reduction is small, e.g. approximately 4 g for a 20 g sample size at a complete prereduction. Due to this, in combination with a high frequency of the weight recordings, fluctuations were observed in the recorded weight behavior. The weight reduction data was recalculated in order to represent the conversion, according to equation 2.22, which is the recorded weight loss relative to the theoretical weight loss. The obtained weight behavior and corresponding conversion are shown in Figure 4.21 and Figure 4.22 for 50% CO and 70% CO, respectively. All experiments show a continuous decrease in weight with increasing holding time, except for experiment conducted at 400°C in 50% CO and the experiment conducted at 600°C in 70% CO. The former shows large fluctuations in the weight, where an increase is observed at approximately 10- and 25-minutes holding time. The latter shows an increase in the weight during the first 5 minutes of the experiment after which a continuous decrease is observed.

Decrepitation

The samples were manually sieved into various size fractions after reduction to estimate the extent of disintegration. As the experiments were conducted in an open furnace, some extent of disintegration could be detected visually, in addition to the distinct decrepitation noise. In some experiments, the decrepitation caused detached pieces of the particle to escape from both sample holder and furnace. This was also confirmed by the weight recordings, which showed a large decrease in weight at a single 0.25 s recording, as was shown in Figure 3.22. The decrepitation appeared to be dependent on time, rather than temperature

in the investigated temperature range. Decrepitation occurred after approximately 2.5-5 minutes process time at 400-600°C. The disintegration is presented through the average of all repeated runs, as ore heterogeneity and small sample size may give a non-representative illustration of potential trends by single experiment comparison. Figure 4.23 shows the results for experiments conducted at 500°C, 550°C, and 600°C, respectively, in 50%CO-50%CO$_2$, where the figure to the left shows the distribution for all repeated runs and the figure to the right shows the average values. It is observed that the variation between the parallels is quite high, and a clear correlation between disintegration and temperature cannot be observed. Further, comparison of samples reduced in 50% CO and 70% CO, respectively, as presented in Figure 4.24 may indicate that increasing CO-concentration correlates with a higher degree of disintegration, however the difference between the distributions is quite low.
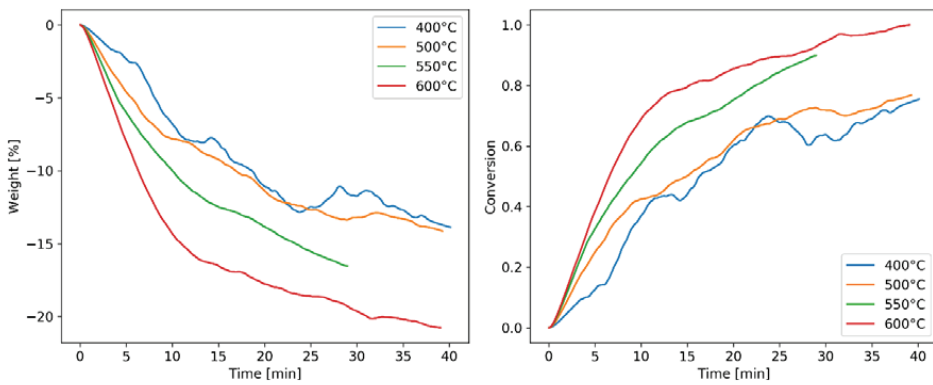
Figure 4.21: Weight [%] and conversion, respectively, as a function of time for isothermal reduction of Comilog ore (11.20-15.00 mm) in gas atmosphere of 50% CO and 50% CO$_2$
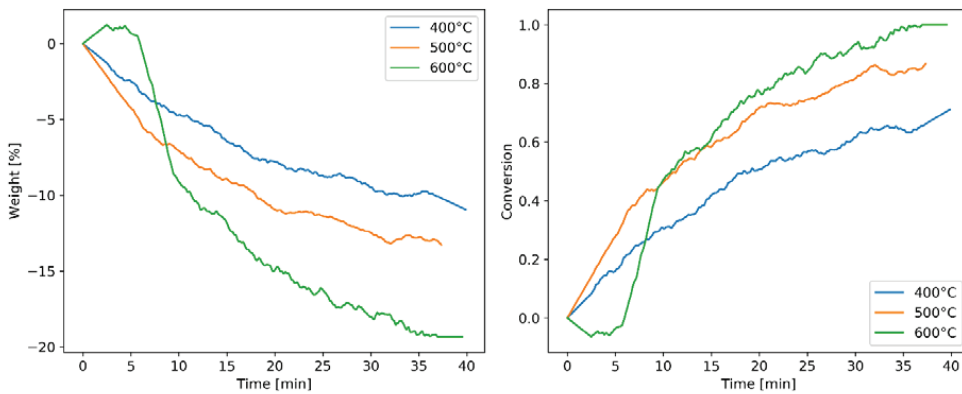
Figure 4.22: Weight [%] and conversion, respectively, as a function of time for isothermal reduction of Comilog ore (11.20-15.00 mm) in gas atmosphere of 70% CO and 30% CO$_2$
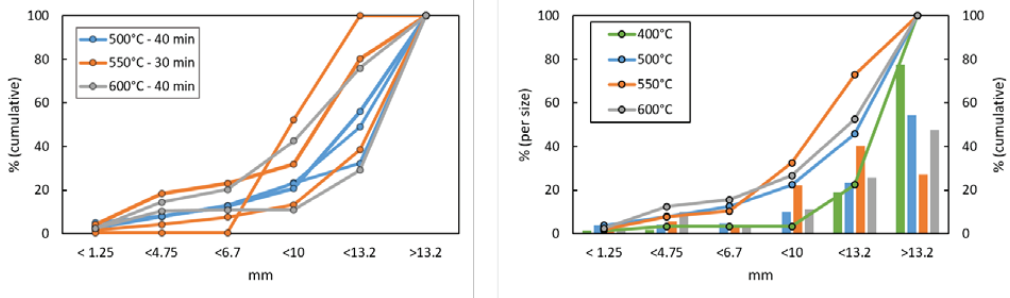
Figure 4.23: Size distribution after reduction experiments conducted at 500°C, 550°C and 600°C, respectively, at 40 minutes holding time in 50%CO-50%CO₂
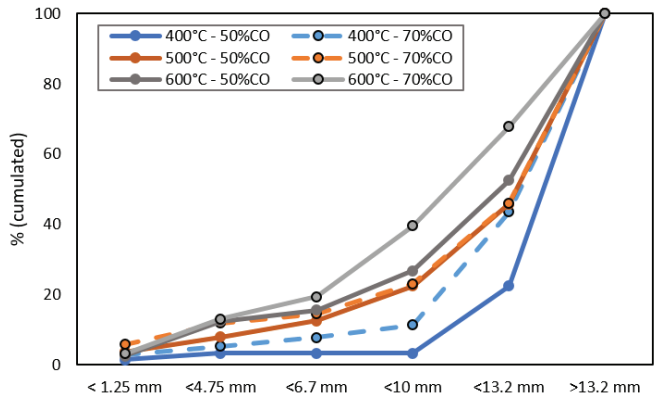
Figure 4.24: Size distribution after reduction experiments at temperatures 400°C, 500°C and 600°C in 50%CO or 70%CO, respectively

Analysis

The chemical composition was analysed for some of the reduced samples, of which the results are presented in Table 4.4. The oxidation level of manganese (x in MnOx) decreases with increasing temperature, where the analyses correlate to a 36%, 40% and 70% reduction for experiments with 40 minutes holding time at 400°C, 500°C, and 600°C, respectively.

Table 4.4: Chemical analysis of Comilog ore (11.20-15.00 mm) reduced isothermally in 50%CO-50%CO₂

Temperature	Holding time [min]	Fe, tot	Mn, tot	MnO₂	MnO	SiO₂	Al₂O₃	K₂O	**MnOx**
400°C	40	2.4	57.7	55.3	29.3	2.8	6.1	0.7	**1.61**
500°C	40	2.0	56.5	50.5	31.7	5.9	5.9	0.8	**1.57**
600°C	40	2.0	62.2	21.3	63.0	3.5	7.0	0.8	**1.22**
600°C	20	1.6	58.4	45.2	38.6	4.2	5.7	2.0	**1.49**

X-ray diffraction analysis indicated that dehydration of nsutite and lithiophorite occurred at low temperatures, as it was not detected in any of the investigated samples. The quantified mineralogy, as obtained through Rietveld analysis using TOPAS 5, is presented in Table 4.5. Pyrolusite and cryptomelane were detected in considerable concentrations at temperatures up to and including 550°C. The tetravalent oxides appeared to be reduced at 600°C, where an abundance of 27% was found after 20 minutes holding time, and further a complete reduction after 40 minutes. Bixbyite was present in minor concentrations, i.e. 5%, at temperatures 400-550°C, whereas 30% is obtained after 20 minutes holding time at 600°C. Thus, this indicates that the MnO_2-oxides (pyrolusite and cryptomelane) reduce to a combination of Mn_3O_4 and MnO at temperatures below 600°C, where the main reduction product is MnO. At 600°C, the MnO_2-oxides reduce rapidly to Mn_2O_3. This implies that the behavior observed for isothermal reduction experiments show high correlation to the behavior observed for non-isothermal reduction. Further, as for the XRD analyses of non-isothermally reduced samples, the identified phases in isothermally reduced samples were manganese oxides in addition to quartz. It is assumed that the aluminium in the ore is present in solid solution in the identified manganese oxides, mainly as $(Mn^{2+})(Mn^{3+}, Al^{3+})_2O_4$.

Table 4.5: Quantitative Rietveld analysis of isothermal reduction products. Samples were reduced in 50%CO-50%CO_2

Mineral [Formula]	400°C (40 min)	500°C (20 min)	500°C (40 min)	550°C (40 min)	600°C (20 min)	600°C (40 min)
Manganosite [MnO]	24	12	29	44	28	69
Hausmannite [Mn$_3$O$_4$]	21	8	16	12	14	17
Bixbyite [Mn$_2$O$_3$]	5	5	5	5	30	13
Pyrolusite [MnO$_2$]	37	66	39	5	7	-
Cryptomelane [KMn$_8$O$_{16}$]	9	8	2	32	20	-
Quartz [SiO$_2$]	4	2	9	3	1	1
Reduction according to titration (MnOx)	36%		40%		48%	77%

Cross-section examinations of reduced particles showed that several of the particles appeared to follow a shrinking core mechanism during reduction. Two of these particles from experiments conducted in 50% CO are shown in Figure 4.25, where the particle to the left was reduced at 400°C, and the particle to the right at 500°C. The observations indicate that the reduction occurs from the exterior towards the center of the particle, however reaction fronts are also observed along the cracks that have formed in the particles. Figure 4.26 shows further inspection of the particle reduced at 500°C, where a close-up of the reaction front is seen, together with the analysed O/Mn ratio at varying radial distance. The oxygen level of manganese (O/Mn ratio) is observed to increase with distance from exterior to center of the particle.

Thus, evidence of a shrinking core mechanism is found in the particles from isothermal reduction experiments, whereas the particles subjected to non-isothermal reduction showed no such indications. Considering the wide variety of microstructures observed in the ore prior to reduction, it is possible that some particle types follow a shrinking core mechanism, whereas other do not. However, the particles investigated from isothermal reduction experiments appear to be of similar type as the particle presented in Figure 4.17 subjected to non-isothermal reduction. As such, a potential explanation is that the rapid

temperature increase the particles were subjected to in the isothermal experiments, caused alterations to the structure. It may also be related to the lower reaction temperature.
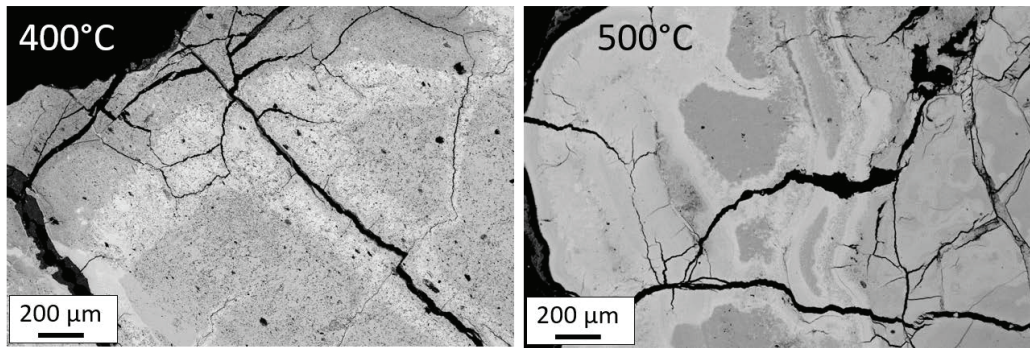
Figure 4.25: Backscatter of sample reduced at 400°C and 500°C in 50% CO showing outer regions of particle surface
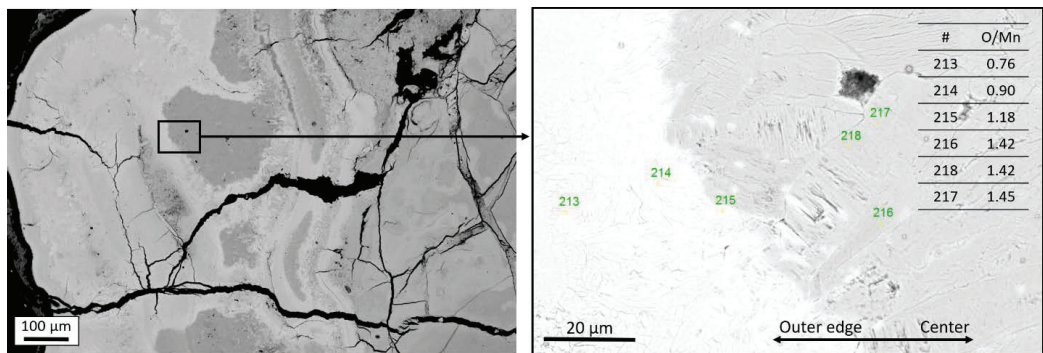
Figure 4.26: Cross-section examination of Comilog ore particle reduced isothermally at 500°C (40 minutes) in 50% CO. Chemical analysis indicated that overall sample was 40% reduced

4.1.3 Non-isothermal reduction – effect of inert material

The ore is fed to the industrial furnace premixed in proper ratios with the remaining required raw materials, such as quartz and coke. While these materials do generally not take part in any reactions at low temperatures in the prereduction zone, they may influence the temperature development, and thus the reduction rates of the ore. This section presents the observations made from the investigation of this potential effect on the temperature development using quartz, which was mixed with the ore in various weight ratios during reduction. At the temperatures used in this investigation, it is assumed that quartz will behave as an inert material.

Weight reduction behavior

All experiments presented in this section have been conducted at 6°C/min up to 1000°C in 50%CO-50%CO₂. The temperature development for experiments with Comilog ore with various amount of quartz can be seen in Figure 4.27. In general, the sample temperature is observed to be lower with increasing amount of quartz in the charge. This is clearly seen for particle size 3.33-4.00 mm, where the maximum temperature obtained in the exothermic peak decreases with increasing content of quartz in the sample charge. For particle size 11.20-15.00 mm, the experiment conducted with merely the ore, and the experiment with ore and quartz in 1:1 ratio exhibit highly similar temperature behavior. The difference is that the exothermic peak occurs at later process time when quartz was added. When ore and quartz was evaluated in a 1:3 weight ratio, the sample temperature was observed to largely follow the temperature of quartz.
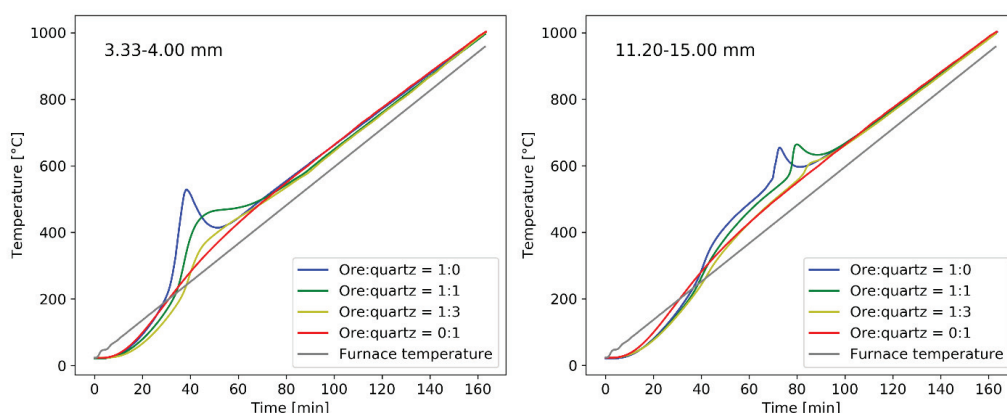
Figure 4.27: Temperature development in experiments conducted with Comilog ore and quartz in various ratios with Comilog ore particle size 3.33-4.00 mm and 11.20-15.00 mm, respectively. All experiments conducted at 6°C/min up to 1000°C in 50%CO-50%CO₂

The weight as a function of time and temperature, respectively, for particle size 3.33-4.00 mm can be seen in Figure 4.28. Evaluating the weight loss as a function of time shows that the experiment conducted with ore has reached a complete prereduction before the weight loss in the experiments with ore and quartz have been initiated. As such, the presence of quartz lowers the temperature, which in turn causes a delay in the reduction. The reduction occurs at similar temperatures, which indicates that the temperature is given by the reduction. The corresponding reaction rate, calculated from the change in weight per time, is presented in Figure 4.29. The maximum rate obtained with merely the ore is nearly twice the magnitude of that obtained with the experiments with mixed ore and quartz. A slight decrease in the rate is observed when the content of quartz is increased from a 1:1 ratio to 1:3.

The weight as a function of time and temperature, respectively, for particle size 11.20-15.00 mm is shown in Figure 4.30, and the corresponding reaction rate is presented in Figure 4.31. The characteristic exothermic peak is observed when ore and quartz is mixed in a 1:1 ratio, however it is not observed at a mixing ratio of 1:3. The absence of the exothermic temperature peak does not appear to have a large effect on the reaction rate. Highly similar weight reduction behavior, both as a function of time and temperature,

is observed for all experiments. The experiments with a 1:3 mixing ratio appear to reduce at slightly lower temperatures.
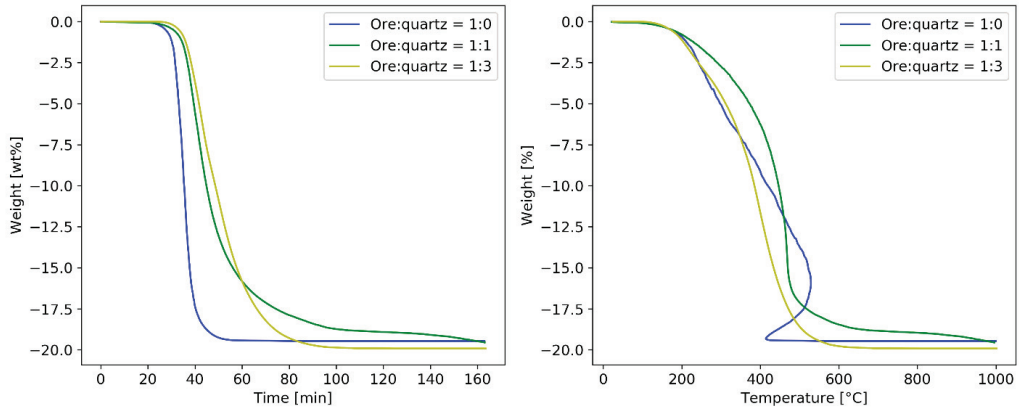
Figure 4.28: Weight as a function of time and temperature, respectively, for Comilog ore (3.33-4.00 mm) mixed with various ratios of quartz
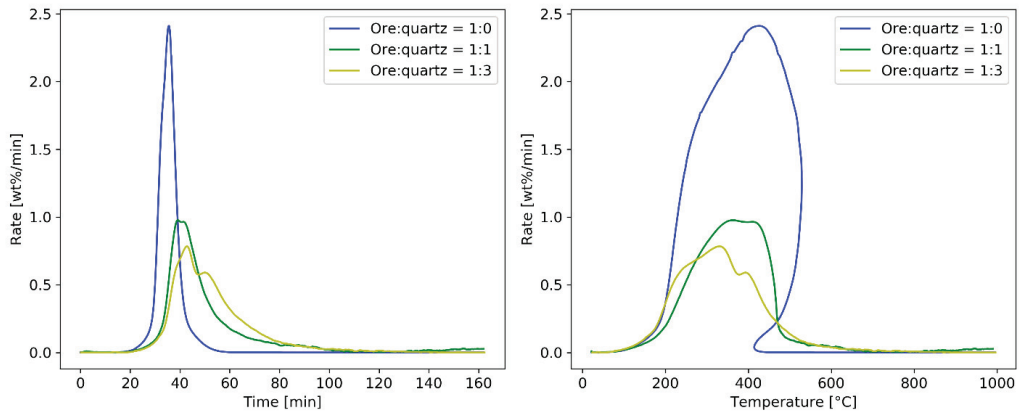
Figure 4.29: Reaction rate [wt%/min] as a function of time and temperature, respectively, for Comilog ore (3.33-4.00 mm) mixed with various ratios of quartz

The effect of quartz on the temperature development was more profound for particle size 3.33-4.00 mm compared to 11.20-15.00 mm. A potential explanation is that the kinetics of larger particles may be to a higher extent governed by gas phase diffusion compared to smaller particles, which may rather be under chemical reaction control. Both mass transport in gas phase and chemical reaction kinetics are promoted by increasing temperature, however chemical reaction is more sensitive towards the temperature compared to gas diffusion. Another factor may be that the heat transfer is different.
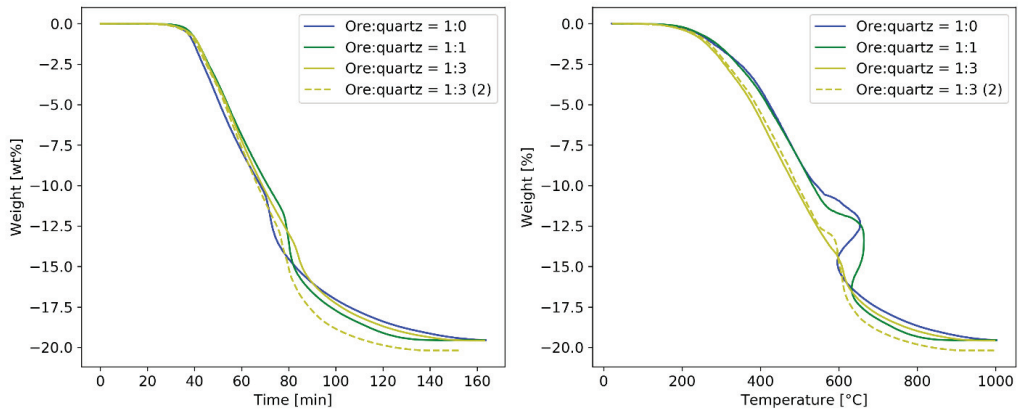
Figure 4.30: Weight as a function of time and temperature, respectively, for Comilog ore (11.20-15.00 mm) mixed with various ratios of quartz
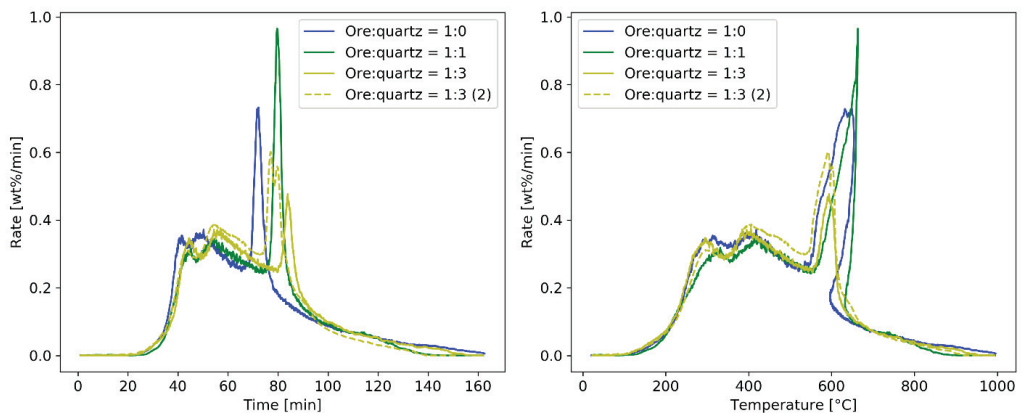
Figure 4.31: Reaction rate [wt%/min] as a function of time and temperature, respectively, for Comilog ore (11.20-15.00 mm) mixed with various ratios of quartz

Decrepitation

Figure 4.32 shows the size distribution of Comilog ore particles after reduction for particles of initial size 3.33-4.00 mm and 11.20-15.00 mm, respectively. No significant difference in the disintegration extent is observed between experiments with 1:1 and 1:3 weight mixing ratio of ore and quartz. For initial particle size 11.20-15.00 mm, 42.3% of the sample was of size smaller than 10 mm after the reduction when ore and quartz was mixed in 1:1 ratio. Similarly, 39.8% and 47.9% was smaller for mixing ratio 1:3 for original and repeated experiment. These values are similar to that obtained for the ore reduced without any quartz in the crucible, where 52.2% was determined to be smaller than 10 mm (Figure 4.14). It is hence shown

that it is not the reduction during the exothermic peak that is disintegrating the ore, but rather the total reduction.
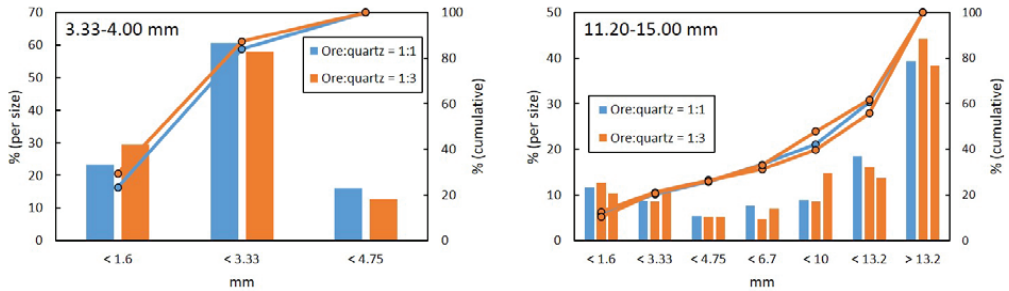
Figure 4.32: Size distribution after reduction experiments where ore and quartz were mixed in 1:1 or 1:3 weight ratio for Comilog ore. Particle size 3.33-4.00 mm (left) and 11.20-15.00 mm (right), respectively

Analysis

The reaction products were analysed for chemical composition, where the obtained values are presented in Table 4.6. The analysed oxidation level (x in MnOx) is between 1.04-1.06, however as the weight and off-gas analysis were stable prior to termination of the experiments, it is assumed that all experiments lead to a complete prereduction, i.e. x in MnOx being 1.00.

Table 4.6: Chemical analysis of Comilog ore mixed with various ratios of quartz reduced in 50%CO-50%CO2 at 6°C/min up to 1000°C

Size [mm]	Ore:quartz	Temperature	Fe, tot	Mn, tot	MnO_2	MnO	SiO_2	Al_2O_3	K_2O	**MnOx**
3.33-4.00	1:1	1000°C	3.8	61.6	4.3	76.0	3.8	6.5	1.3	**1.04**
3.33-4.00	1:3	1000°C	3.6	62.1	4.7	76.3	4.0	6.2	1.2	**1.05**
11.2-15.0	1:1	1000°C	3.0	60.3	4.2	74.4	6.8	7.0	1.2	**1.04**
11.2-15.0	1:3	1000°C	2.7	64.2	5.8	78.2	2.9	6.1	0.8	**1.06**

4.1.4 Non-isothermal reduction – effect of $H_2(g)/H_2O(g)$

The experiments presented in this section include the use of $CO-CO_2$, $CO-CO_2-H_2$, and $CO-CO_2-H_2O$ atmospheres. As a relatively stable and reproducible behavior was observed for the mass balance, both the weight behavior as recorded by the mass balance and the behavior of the CO and CO_2 in the off-gas will be presented in this section.

Five different gas atmospheres correlating to two different theoretical oxygen partial pressures were used in the experiments presented in this section. The standard atmospheres were $50\%CO-50\%CO_2$ ($p(O_2)_1$) and $80\%CO-20\%CO_2$ ($p(O_2)_2$), where gas atmospheres consisting of $CO-CO_2-H_2$ and $CO-CO_2-H_2O$,

respectively, giving the same oxygen partial pressures as $p(O_2)_1$ and $p(O_2)_2$ were investigated. All experiments presented in this section were conducted at a heating rate of 6°C/min using particle size 11.20-15.00 mm. Some of the experiments conducted in CO-CO_2 atmosphere presented in section 4.1.1 are reprinted for comparison.

Effect of $H_2(g)$

Two different theoretical oxygen pressures were evaluated in this section, where the quantity of the components CO-CO_2 and CO-CO_2-H_2 were calculated to correspond to similar oxygen pressures. Figure 4.33 shows the temperatures recorded during the conducted experiments for oxygen partial pressure 1 and 2, respectively. It is observed that the sample temperature increases more rapidly in the initial stages of the experiment when hydrogen is added to the mixture for both oxygen pressures. For oxygen pressure 1 (left figure), the exothermic peak is of lower magnitude in when hydrogen in present, likely explained by the lower reduction temperature in this atmosphere. An exothermic peak is observed in oxygen pressure 2, at a lower process time compared to the CO-CO_2 atmosphere. An overview of the maximum temperatures obtained in furnace and sample, respectively, is shown in Table 4.7.
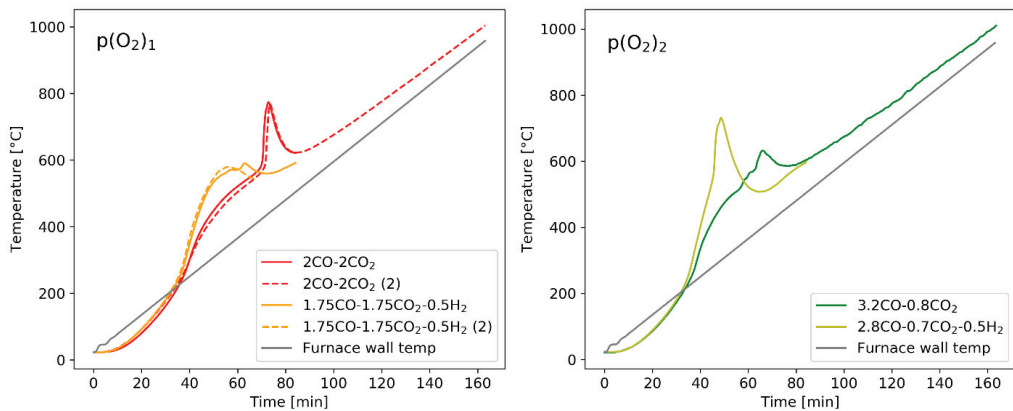
Figure 4.33: Temperature development in Comilog ore reduced in two different oxygen partial pressures at 6°C/min

Table 4.7: Maximum furnace temperature and sample temperature, respectively, for experiments conducted in CO-CO_2, CO-CO_2-H_2, and CO-CO_2-H_2O atmospheres

Gas components	Oxygen pressure	Maximum furnace temperature [°C]	Maximum sample temperature [°C]
CO:CO_2	$p(O_2)_1$	500	774
CO:CO_2:H_2	$p(O_2)_1$	500	592
CO:CO_2:H_2	$p(O_2)_1$	400	479
CO:CO_2:H_2	$p(O_2)_2$	500	731

Figure 4.34 shows the recorded weight as a function of time and temperature, respectively, for the experiments conducted in atmospheres based on $CO-CO_2$ and $CO-CO_2-H_2$, where the gas compositions correlate to two different theoretical oxygen pressures, i.e. $p(O_2)_1$ or $p(O_2)_2$. Thus, this figure shows the effect of hydrogen. The weight was normalized according to the weight loss found from weighing the sample prior and subsequent to the experiments. Parallels for the gas compositions correlating to $p(O_2)_1$ are included in the figure for both $CO-CO_2$ and $CO-CO_2-H_2$ compositions, which shows a high degree of reproducibility in both cases. It can be observed that the reduction is initiated at approximately 200°C for all gas atmospheres. By evaluating the reduction as a function of time, it can be observed that at a certain time after initiation, the experiments conducted in the presence of hydrogen experience a faster weight loss compared to the experiments in $CO-CO_2$ atmosphere. This may suggest that the initial stages of reduction are more affected by the presence of hydrogen compared to the oxygen pressure.
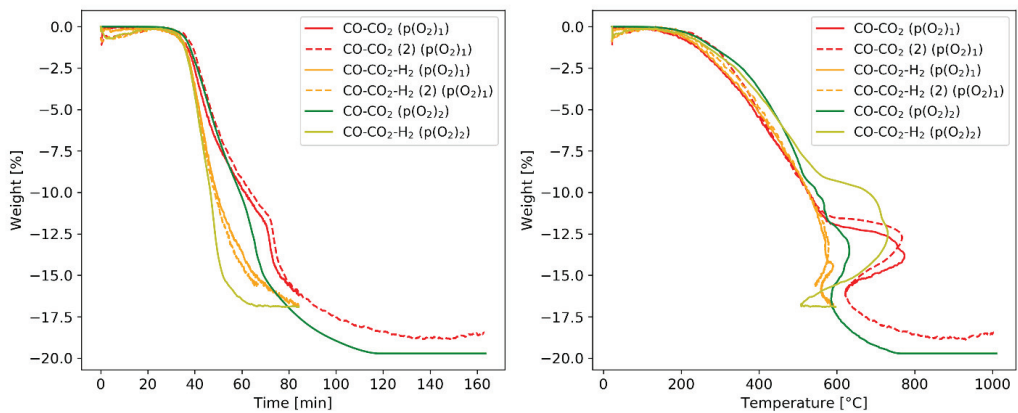
Figure 4.34: Weight (as given by mass balance) behavior of Comilog ore reduced in CO-CO₂ and CO-CO₂-H₂ atmosphere, where gas compositions correlate to two different theoretical oxygen partial pressures

The reduction rate (calculated from change in weight per minute intervals) is presented in Figure 4.35, where the rate shows some fluctuations and noise due to the mass balance, however the trends of the rate are easily observed. It is seen that the reduction is initiated at the same temperature in all evaluated atmospheres, where the reaction rate then continues to increase up to a peak position located at approximately 45 minutes process time for all curves. This process time corresponds to slightly different temperatures in different atmospheres, however all within the range of 300-400°C. Correlating to the exothermic peak in the temperature behavior, a second rapid reduction step is observed when the temperature is close to 600°C. Further, the different gas atmospheres correlate to varying maximum obtained reduction rate, where experiments with hydrogen gas obtains a considerably higher rate compared to the respective atmospheres based on $CO-CO_2$.

The CO_2 and CO concentrations recorded by the off-gas analyzer relative to the set point values for the experiments conducted in 50%CO-50%CO_2 and 80%CO-20%CO_2 and their corresponding atmospheres of $CO-CO_2-H_2$ are shown in Figure 4.36 and Figure 4.37, respectively. To simplify comparison of the trends in the CO and CO_2, the relative CO-concentrations have been presented with an inverted y-axis. The recorded CO_2 shows high correlation with the reaction rate calculated from the weight recorded by the mass

balance (as was presented in Figure 4.35). Some dissimilarities can be seen towards the latter stages of the experimental run for the atmosphere containing CO-CO_2-H_2 of oxygen pressure 2. While the reaction rate shows a continuous decline in the rate from the main peak, the $\%CO_2$ can be seen to decrease to a local minimum at 65 minutes process time, from where a subsequent increase is observed. This increase reaches its maximum at approximately 75 minutes process time, from which the CO_2 appear relatively stable until the experiment was terminated, i.e. 84 minutes process time. Overall, the same observations are made in the CO_2-behavior as in the CO-behavior during the experiments, and it is seen that the two are overall inversely related. The CO-concentration is seen to increase relative to set point in the final stages of the experiments conducted in oxygen pressure 2. This may indicate the occurrence of the Boudouard reaction. For the experiment conducted in CO-CO_2 atmosphere a decrease in CO_2 of similar magnitude as the increase in CO is observed at the same temperature and process time, which further supports the occurrence of the Boudouard reaction.
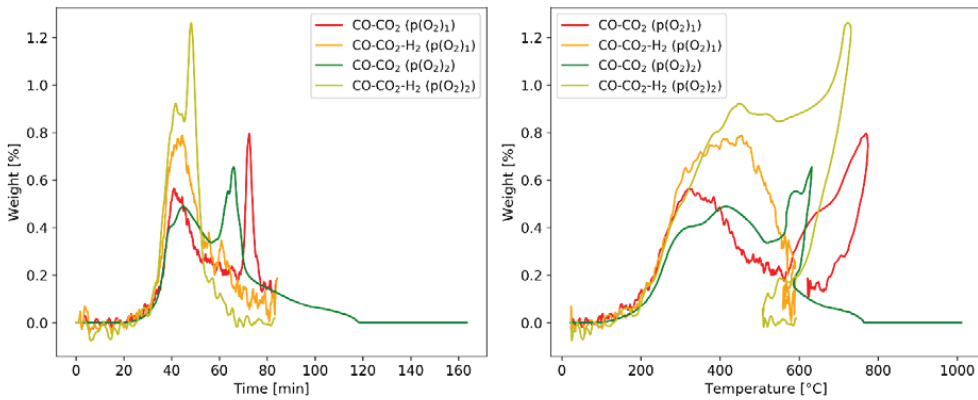
Figure 4.35: Reaction rate of Comilog ore reduced in CO-CO_2 and CO-CO_2-H_2 atmosphere, where gas compositions correlate to two different theoretical oxygen partial pressures
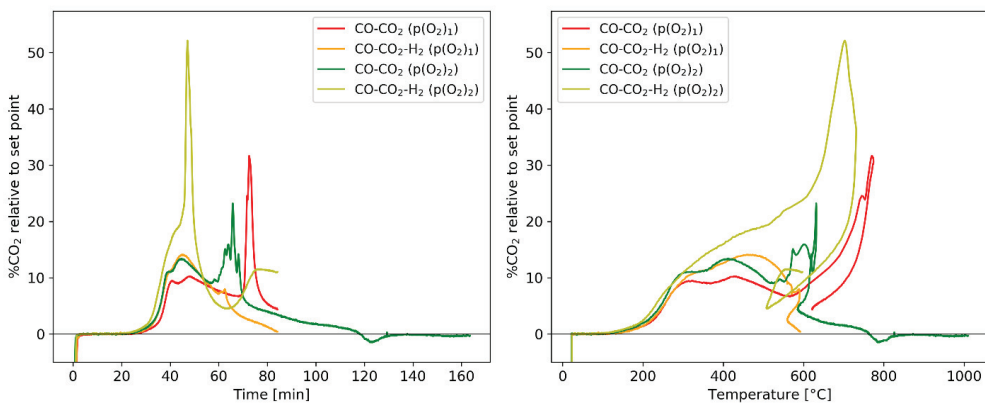
Figure 4.36: $\%CO_2$ relative to set point for experiments with Comilog ore in different gas atmospheres based on CO-CO_2 and CO-CO_2-H_2 correlating to two different theoretical oxygen pressures
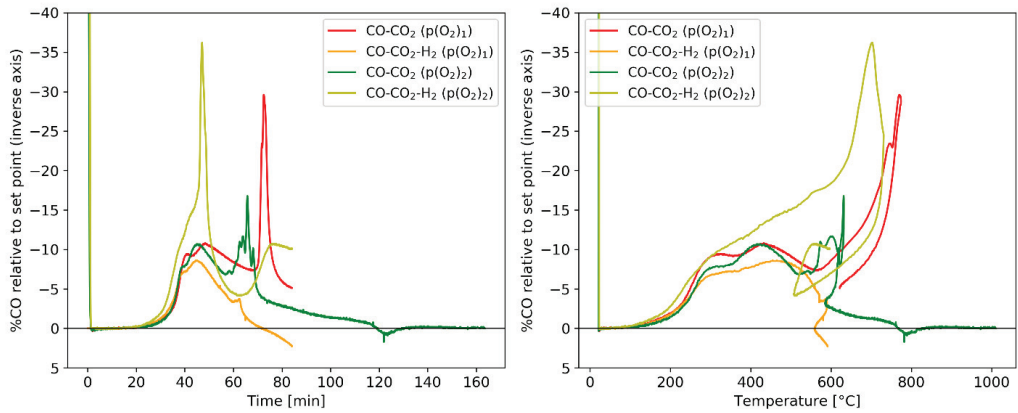
Figure 4.37: %CO relative to set point for experiments with Comilog ore in different gas atmospheres based on CO-CO₂ and CO-CO₂-H₂ correlating to two different theoretical oxygen pressures. Y-axis is inverted

Effect of H₂O

The effect of water on the ore reduction was evaluated by two different approaches. Firstly, the ore particles were soaked in water for a certain amount of time, allowing the ore to retain water in pores and cavities. It was approximated that 3-4% of water was retained in the ore. Secondly, dry ore was evaluated in reducing atmosphere where water vapor was added to the gas mixture. The composition was calculated to obtain similar oxygen pressures as the atmosphere of 50%CO-50%CO₂. The temperature development recorded during the different experiments is shown in Figure 4.38.
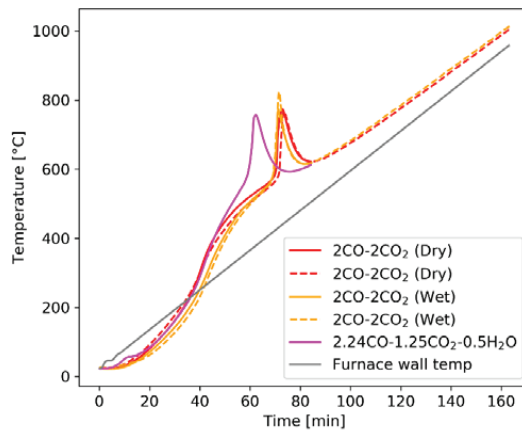
Figure 4.38: Temperature development in Comilog ore reduced in CO-CO₂ (dry or wet) and CO-CO₂-H₂O, where the theoretical oxygen pressure of the two atmospheres are similar

It can be observed that the temperature is slightly higher in the dry ore compared to the wet in the initial stages of the experiment. This is expected, as additional energy is required to evaporate the water in the wet ore. Comparison of the temperature development in the CO-CO_2-H_2O with the correlating CO-CO_2 shows that the temperature behavior is relatively similar, however the exothermic peak occurs at a lower process time in the CO-CO_2-H_2O atmosphere. The furnace target values (set point) and the maximum temperatures obtained in the different experiments are shown in Table 4.8.

Table 4.8: Maximum obtained sample temperature in the different experimental runs

Gas components	Dry/wet	Furnace set point [°C]	Maximum sample temperature [°C]
CO:CO_2	Dry	500	774
CO:CO_2	Dry	1000	1002
CO:CO_2	Wet	500	773
CO:CO_2	Wet	1000	1014
CO:CO_2:H_2O	Dry	500	757

Figure 4.39 shows the weight behavior according to the mass balance recordings for reduction experiments in gas atmospheres of CO-CO_2 with dry or wet ore, and dry ore in CO-CO_2-H_2O. The weight of the wet ore shows a decrease from the initial stages of the experiment, while the dry ore, in both CO-CO_2 and CO-CO_2-H_2O, requires higher process times and temperatures. The experiment conducted with water vapor in the mixture shows a continuous weight increase in the initial stages of the experiment, at temperatures lower than 100°C. It is possible that this weight increase is related to the previously mentioned drifting of the mass balance. Another potential explanation is that the water vapor condenses as it is exposed to the sample, which in this region holds a temperature below 100°C. Further, it is seen that a faster weight loss is obtained in CO-CO_2-H_2O atmosphere compared to CO-CO_2, however highly similar values are obtained at 80 minutes process time. The temperature appears to be a result of the reaction rate, as the two atmospheres show overlapping weight loss as a function of temperature.
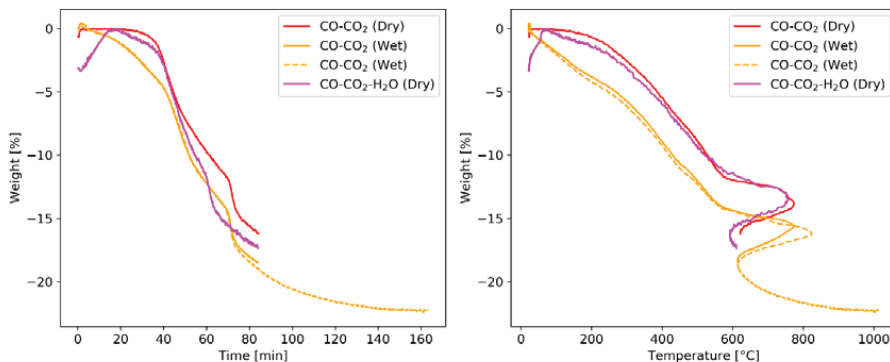
Figure 4.39: Weight behavior of Comilog ore reduced in CO-CO_2 (dry or wet) and CO-CO_2-H_2O, where the theoretical oxygen pressure of the two atmospheres are similar

The corresponding reaction rates calculated from the change in weight per 2 minute intervals are presented in Figure 4.40. The wet and dry ore in CO-CO_2 show similar trends in the reaction rate, where the peak is located at similar process times and temperatures. The difference between the two lies in the weight reduction rate at temperatures lower than 200°C. Further, the peak in reaction rate located at temperatures close to 600°C occurs at a lower process time when water vapor is present in the gas mixture.
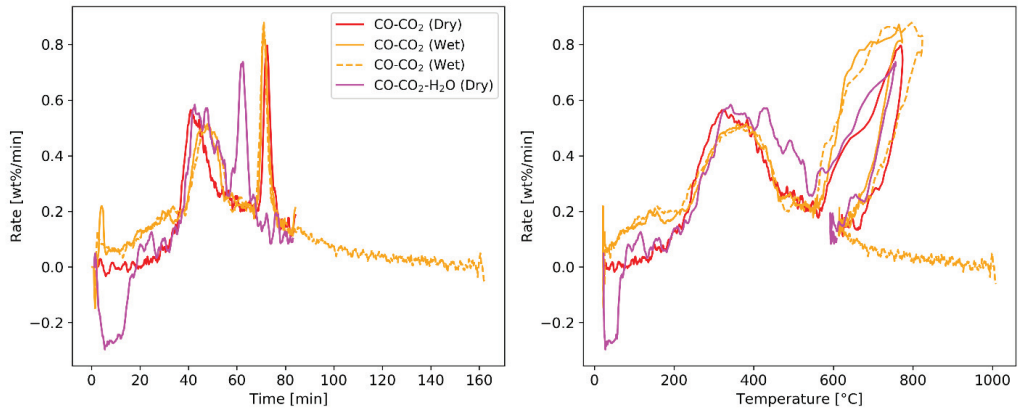
Figure 4.40: Reaction rate [wt%/min] for Comilog ore reduced in CO-CO₂ (dry or wet) and CO-CO₂-H₂O, where the theoretical oxygen pressure of the two atmospheres are similar

The concentrations relative to set point values of CO_2 and CO given by the off-gas analyzer are shown in Figure 4.41 and Figure 4.42, respectively. As previously, the CO has been presented with inverted y-axis values to simplify the visual comparison. The CO_2 starts to increase at a slightly higher process time in the wet ore experiment compared to the dry ore in CO-CO_2 and CO-CO_2-H_2O, respectively, however the temperature at which %CO_2 starts to increase is close to 200°C for all experiments. Similar to the CO_2 concentrations, the recorded CO starts to decrease at the same temperature in all three gas atmospheres. The amount of CO_2 produced is considerably higher in the experiment with water vapor at temperature range 300-600°C compared to the remaining. Further, it can be seen that both the CO and CO_2 shows oscillating trends for the experiment conducted with water vapor present, where the oscillations are mainly observed at temperatures exceeding 450°C, and appear to occur to a larger extent in the recorded CO compared to the CO_2.
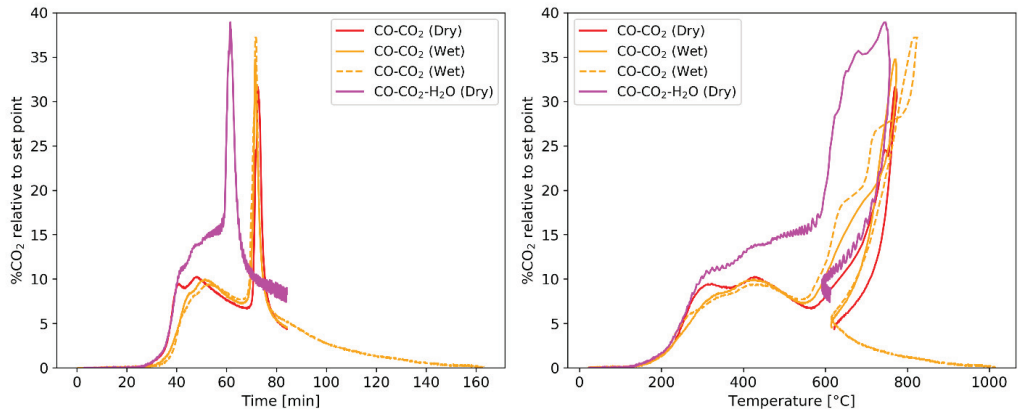
Figure 4.41: %CO₂ relative to set point for experiments with Comilog ore in CO-CO₂ atmosphere (dry or wet) and CO-CO₂-H₂O atmosphere. Inverted y-axis
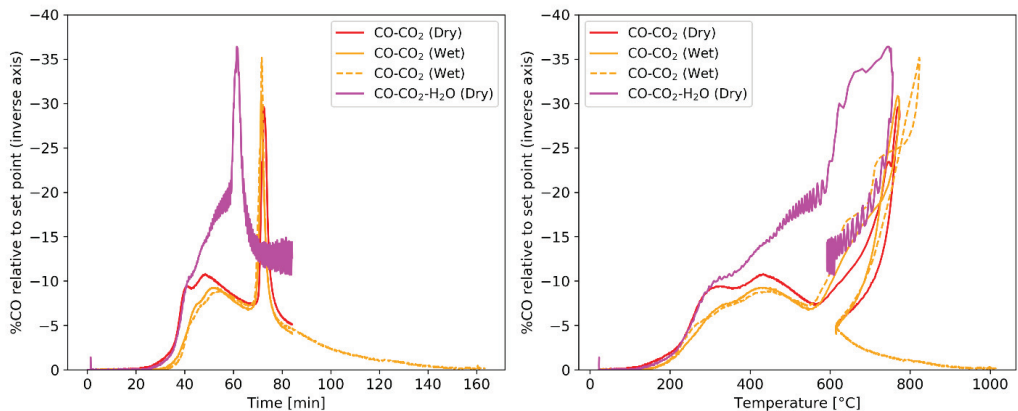
Figure 4.42: %CO relative to set point for experiments with Comilog ore in CO-CO₂ atmosphere (dry or wet) and CO-CO₂-H₂O atmosphere. Inverted y-axis

Decrepitation

The size distribution of the samples after reduction is shown in Figure 4.43. The figure shows the distribution of the experiments conducted in gas atmospheres correlating to oxygen pressure 1, i.e. that of 50%CO-50%CO₂. It is seen that the least amount of decrepitation is experienced in CO-CO₂ atmosphere, while the highest amount is occurred for the atmosphere containing water vapor. However, the difference is relatively small, and the amount of data is scarce, implying that more data should be obtained in order to differentiate between the atmospheres.
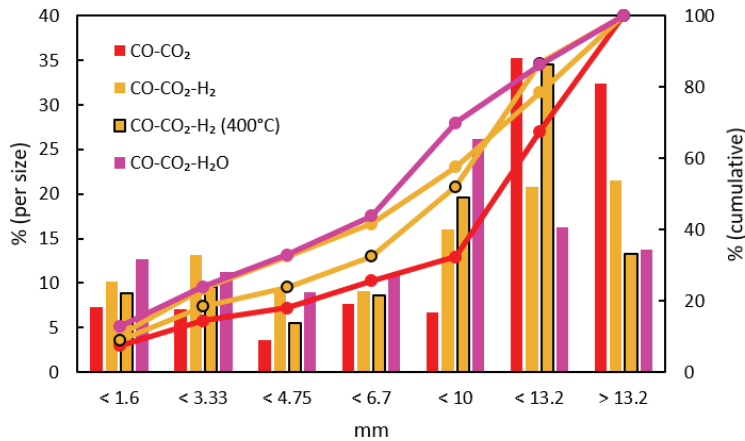
Figure 4.43: Size distribution after reduction experiments for three different gas atmospheres all correlating to the same theoretical oxygen pressure

Analysis

The chemical composition of the reduced samples is presented in Table 4.9. From the experiments conducted in atmospheres correlating to oxygen partial pressure 1 up to 500°C, it is seen that the highest reduction extent was obtained in the atmosphere containing hydrogen, where the analysed oxidation level of manganese (x in MnO_x) was found to be 1.17, followed by $CO-CO_2-H_2O$ of 1.21 and $CO-CO_2$ of 1.27. Comparing the $CO-CO_2$ and $CO-CO_2-H_2$ atmosphere which has similar theoretical oxygen pressure thus shows that hydrogen has a promoting effect on the reaction rate, and hence results in a higher reduction degree. Further, the results indicate that the water-gas shift reaction is not at equilibrium. If equilibrium was obtained, the same reduction degree would be obtained in the $CO-CO_2-H_2O$ atmosphere as the $CO-CO_2-H_2$ atmosphere ($p(O_2)_1$). The two atmospheres would be composed of highly similar concentrations of the constituting gas species were at equilibrium. At 500°C, the equilibrium partial pressure of hydrogen is 0.1250 in the $CO-CO_2-H_2$ atmosphere, and 0.1249 in the $CO-CO_2-H_2O$ atmosphere. This slightly larger hydrogen pressure is not likely to be the cause of the higher reduction obtained in the hydrogen atmosphere.

From the two different oxygen pressures based on $CO-CO_2-H_2$ gas components, the obtained x in MnO_x at 500°C is relatively similar, where 1.17 was obtained in the atmosphere correlating to 50%CO-50%CO_2 compared to 1.14 in the atmosphere correlating to 80%CO-20%CO_2. However, the analysis show that the content of CO_2 is considerably higher in the latter, quantified at 3.9% compared to 0.4-0.7% for the other experiments. The high content of CO_2 is believed to be due to carbon that has deposited on the ore surface, as carbon is analysed and recalculated to CO_2. This may have inhibited the reduction of the ore by decreasing the available reaction area in this specific experiment. Carbon deposition also likely occurred in the experiment conducted in 80%CO-20%CO_2, however the deposited carbon was likely consumed at temperatures close to 800°C in the Boudouard reaction, which explains the low amount of carbon detected by chemical analysis.

Table 4.9: Chemical analysis of reduced Comilog ore (11.20-15.00 mm) samples

Gas	°C	Fe, tot [wt%]	Mn, tot [wt%]	MnO_2 [wt%]	MnO [wt%]	SiO_2 [wt%]	Al_2O_3 [wt%]	K_2O [wt%]	CO_2 [wt%]	**MnOx**
$CO:CO_2$ ($p(O_2)_1$)	500	1.8	63.8	27.5	59.9	2.0	5.1	1.0	0.4	**1.27**
$CO:CO_2:H_2$ ($p(O_2)_1$)	400	2.2	61.9	29.2	56.2	3.9	5.4	0.8	0.7	**1.30**
$CO:CO_2:H_2$ ($p(O_2)_1$)	500	2.7	62.7	16.6	67.4	2.5	5.6	1.0	0.6	**1.17**
$CO:CO_2:H_2O$ ($p(O_2)_1$)	500	2.0	61.7	20.2	63.2	7.1	5.9	1.2	0.3	**1.21**
$CO:CO_2:H_2$ ($p(O_2)_2$)	500	2.1	62.8	13.5	70.1	4.2	5.6	0.8	3.9	**1.14**

The observed microstructures in particles reduced in $CO-CO_2-H_2$ up to set point temperatures of 400°C and 500°C are shown in Figure 4.44. Both particles exhibit a highly disorganized structure, where several phases appear to coexist at a random distribution. The microstructure observed in a particle reduced in $CO-CO_2-H_2O$ is shown in Figure 4.45, which is observed to be relatively homogeneous, where smaller areas of a darker grey phase is dispersed in a brighter grey matrix. The structures presented in Figure 4.44 and Figure 4.45 appear similar to those observed for samples reduced in $CO-CO_2$, as was presented in Figure 4.17 and Figure 4.18.
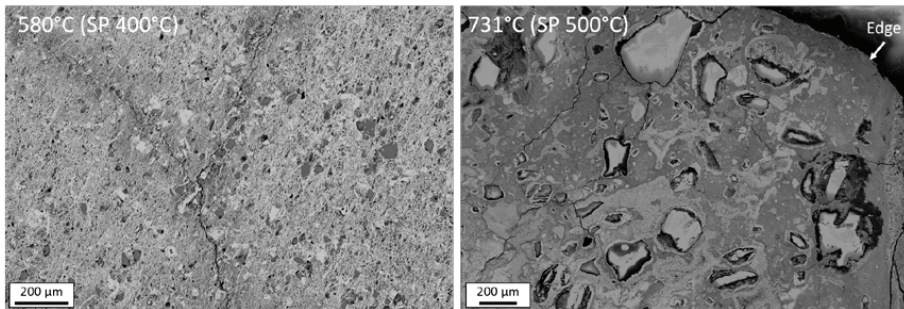
Figure 4.44: Microstructure in Comilog ore particles reduced in $CO-CO_2-H_2$ atmosphere at 6°C/min up to set point temperatures 400°C and 500°C, respectively
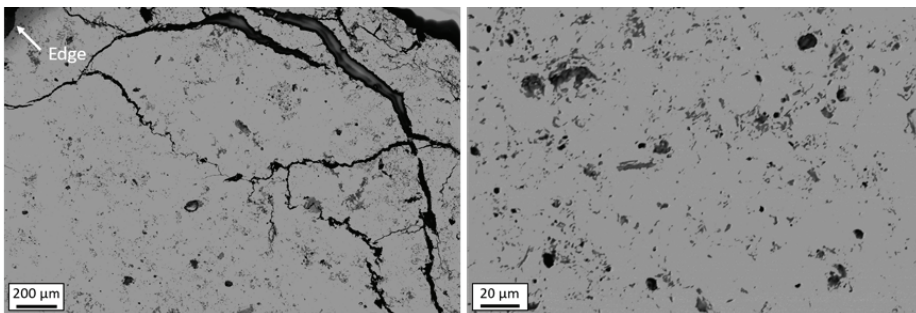
Figure 4.45: Microstructure in Comilog ore particle reduced in $CO-CO_2-H_2O$ at 6°C/min up to set point temperature 500°C (corresponding sample temperature of 757°C)

4.2 Nchwaning ore

4.2.1 Non-isothermal reduction - CO-CO₂ atmosphere

Weight reduction behavior

Figure 4.46 show the recorded sample temperatures for Nchwaning ore heated at 6°C/min up to 1000°C. The sample temperatures are highly similar for all experiments and appear to be unaffected by gas composition and ore size. For comparison, the temperatures recorded for the heating of quartz under similar conditions is added in the figures, which confirms that the temperatures were not affected by any ongoing reactions during reduction of Nchwaning ore. It can be seen that the crucible temperature is lagging somewhat relative to the furnace wall temperature at low temperatures, as it requires a certain process time for the heating to reach the center of the crucible.
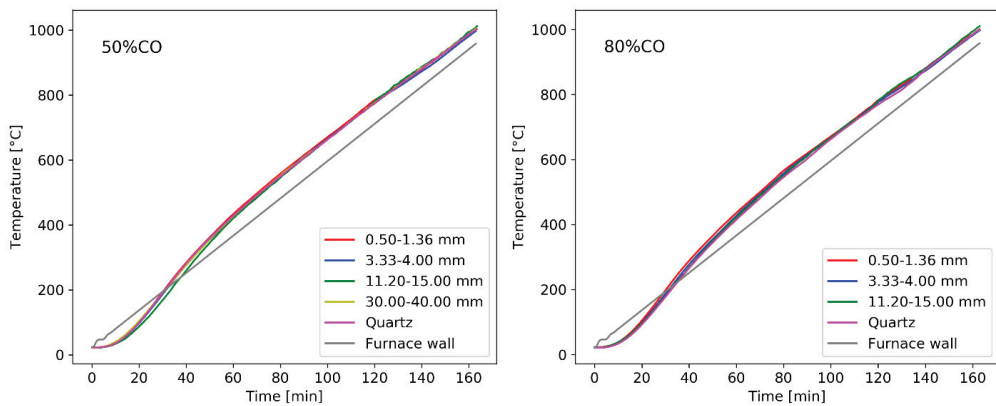
Figure 4.46: Temperature behavior during non-isothermal reduction of Nchwaning ore heated to 1000°C

Figure 4.47 shows the calculated weight as a function of time and temperature for the various particle size fractions heated in CO-CO₂ atmosphere with varying concentration of CO. As the reduction of Nchwaning ore follows the prescribed linear temperature program, the weight behavior as a function of time and temperature, respectively, show similar behavior. While the repeated experiments of smaller particle sizes showed consistent weight reduction behavior, some variation was observed for the larger particle sizes, i.e. 11.2-15.0 mm and 30.0-40.0 mm. As such, the parallels are included in the figure. The curves indicate that the reaction is promoted by decreasing particle size and increasing CO-concentration.

The reaction rates, shown in Figure 4.48, were calculated from the weight change at every 2-minute interval, where it was observed that all characteristics present at shorter time periods remained conserved. As previously mentioned, the weight reduction, and thus reaction rates, were calculated from the CO_2-concentrations recorded in the off-gas. For particle size 0.50-1.36 mm, it was observed that the recorded concentration of CO_2 in the off-gas was subjected to a rapid decrease, resulting in values below set-point, at temperatures exceeding 800°C and 870°C for experiments in 50% CO and 80% CO, respectively. The %CO₂ was adjusted to zero in regions where it decreased below set point, resulting in a stable weight, as

120

seen in the weight curves. The "negative" CO_2-concentration suggests the occurrence of the Boudouard reaction ($C + CO_2 = 2CO$), as all reactions related to the prereduction of the ore produce CO_2. This further indicates potential carbon deposition (from reverse Boudouard reaction) at lower temperatures. The reduction rate of particle size 0.50-1.36 mm reduced in 50% CO started to increase at approximately 280°C. At 380-410°C, the rate increased with a steeper slope, followed by a plateau. The experiments conducted with quartz (presented in section 3.3.1) showed that carbon deposition was initiated at 400°C in both 80% CO and 50% CO (+CO_2). At temperatures exceeding 800°C, the fraction of CO_2 in the off-gas was observed to decrease below set-point, indicating that the Boudouard reaction proceeded to the right. As such, it is believed that the initial peak observed in the reaction rate curves of Nchwaning ore, located at temperatures close to 400°C, is due to carbon deposition.
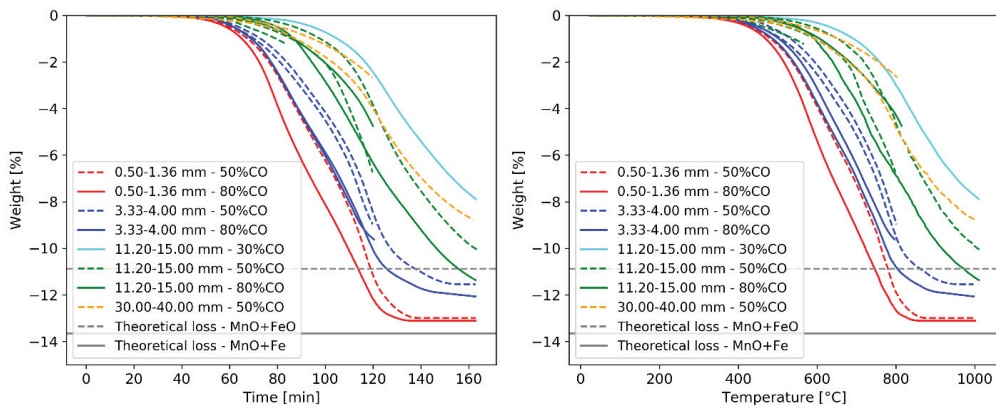
Figure 4.47: Calculated weight as a function of time and temperature, respectively, for Nchwaning ore heated in 50%CO-50%CO2
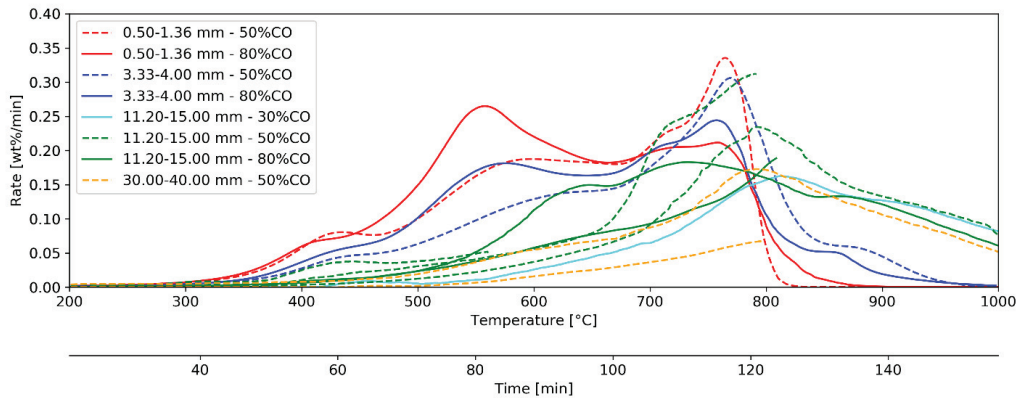
Figure 4.48: Reaction rate curves (wt%/min) for non-isothermal (6°C/min) reduction of Nchwaning ore as calculated from weight reduction curves

The extent of this carbon deposition was estimated by using a Gaussian fitting function to the recorded CO_2 in the off-gas, which was then removed from the rate curves. Figure 4.49 shows the reaction rate curves, where the estimated contribution of left shifted Boudouard reaction has been omitted. The CO_2 consumption correlating to the Bouduoard reaction at temperatures close to 800°C is more difficult to separate, as a CO_2 production from ore reduction occurs at the same temperature range.
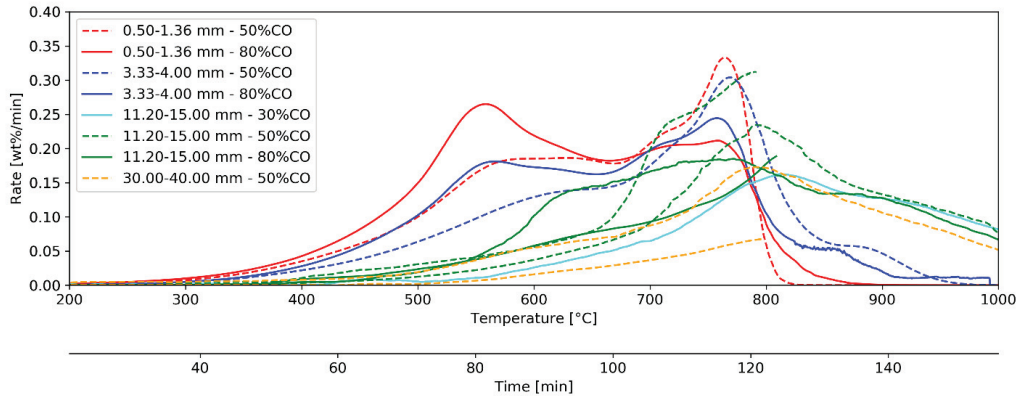
Figure 4.49: Reaction rate curves (wt%/min) for non-isothermal (6 °C/min) reduction of Nchwaning ore, where carbon deposition at low temperature is removed

The reduction is slowly initiated at approximately 300°C for particle size 0.50-1.36 mm and 3.33-4.00 mm, whereas a sample temperature closer to 500°C is required to initiate reduction of size 11.20-15.00 mm and 30.00-40.00 mm. The reaction rate behavior shows that the reduction of Nchwaning ore is characterized by two main stages, as two distinct peaks were observed for the majority of the experiments. The two stages show varying extent of overlap depending on experimental conditions, where the initial peak becomes less profound with increasing particle size and decreasing CO-concentration. Two distinct peaks are seen at temperatures 580°C and 780°C, respectively, for the smaller particles, where a lower reaction rate in the first step correlates to a higher reaction rate in the second step. The steps may be due to a change in reaction mechanism, or due to different chemical reactions. Concerning the latter, the peaks may be related to the reduction of Mn_2O_3 oxides proceeding via the intermediate state Mn_3O_4. However, it is also possible that the two peaks represent the reduction of manganese and iron oxides, respectively. For particle size 0.50-1.36 mm, the rate experiences a rapid decrease at temperatures close to 800°C as the CO_2 is consumed by the Boudouard reaction. For the remaining particle sizes, the rate shows a an overall slow continuous decrease from peak position, where a slight increase in the rate is seen at approximately 850-880°C. This may be due to the decomposition of carbonates, as the equilibrium decomposition temperature for calcite is 886°C for pure species.

The reduction of 11.20-15.00 mm particles in 50% CO was also conducted with a heating rate of 3°C/min, where the temperature development and the calculated weight behavior are shown in Figure 4.50 together with the data obtained at 6°C/min. From the weight behavior it is observed that a slower heating rate

correlates to a slightly higher weight loss at a given temperature. For these two experiments, the reaction rate was calculated from the change in weight per temperature increase (wt%/°C), where the temperature used was the furnace wall temperature, and not the sample temperature. The rate curves are presented in Figure 4.51, which shows that a highly similar rate behavior is obtained. Maximum rate is observed at 800°C for both heating rates, where the rate displays a steeper increase up to peak position for the lower heating rate. While a highly similar reaction rate behavior was obtained, the lower heating rate reveals some additional characteristics of the reduction compared to the higher reaction rate. A continuous increase in the reaction rate is observed from room temperature up to peak at 800°C for heating rate of 6°C/min, whereas a change in the rate behavior is observed at approximately 750°C when the sample was heated at 3°C/min. A change in the rate is also observed at 880°C for both heating rates, believed to be due to carbonate decomposition.
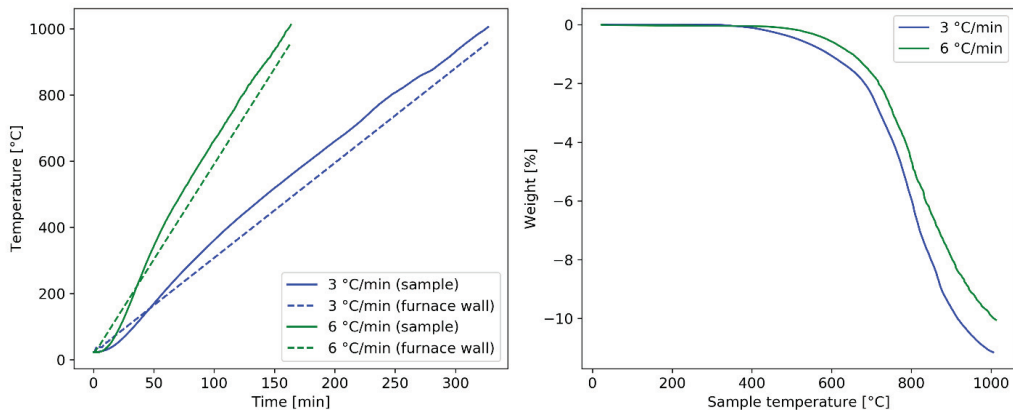
Figure 4.50: Temperature development and weight behavior for Nchwaning ore (11.20-15.00 mm) reduced in 50% CO – 50% CO₂ at 3°C/min and 6°C/min, respectively
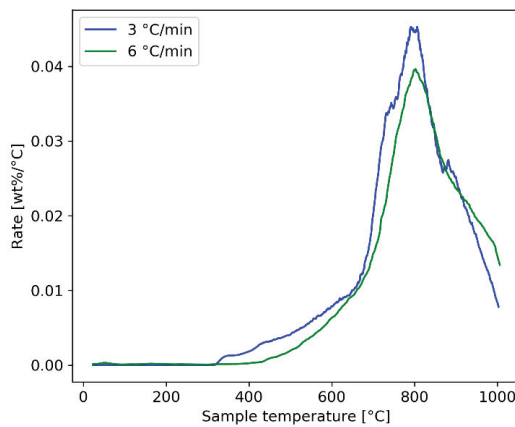
Figure 4.51: Reaction rate [wt%/°C] for Nchwaning ore (11.20-15.00 mm) reduced in 50% CO – 50% CO₂ at 3°C/min and 6°C/min, respectively

Reproducibility

The reproducibility of the experiments was evaluated by comparison of the TGA curves where all experimental conditions, except for target temperature, remained constant. A high consistency between the parallels were observed for particle size 3.33-4.00 mm in both gas atmospheres. The weight curves have been reprinted in Figure 4.52. A larger discrepancy was observed between the various target temperatures of particle size 11.20-15.00 mm and 30.0-40.0 mm, where the reaction rates are reprinted in Figure 4.53 for comparison. As the weight curves were calculated from the increased CO_2 concentration in the off-gas composition, it is possible that the variation on initiation temperature is due to a varying degree of carbon deposition. However, the extent of carbon deposition was observed to be low in atmospheres containing 50%CO, which also displays variation. Furthermore, a highly stable rate is observed at the temperatures where the carbon deposition was generally observed (400-500°C). As such, it is not believed that the variation is not attributed to carbon deposition. A potential explanation for the variance in the parallels is the natural heterogeneity of the ore. Larger particle sizes imply fewer particles evaluated in each experimental run, which increases the effect of the natural variation. A large variance in reduction behavior for single particles of Nchwaning ore has also been observed by others in previous works[14]. For particle size 30.00-40.00 mm, the experiment terminated at 1000°C shows a considerably higher reaction rate compared to the one terminated at 800°C. In these particular experiments, it was observed that the particles heated up to 1000°C had experienced a high degree of decrepitation, whereas the particles terminated at 800°C remained intact in original size. As the reduction rate has been seen to be dependent on particle size, the difference in the reaction rate may be fully or partly attributed to the decrepitation.

In general, it is observed that the TGA data obtained for smaller particle sizes (3.33-4.00 mm) shows a higher degree of reproducibility compared to larger sized particles. This is expected, as the effect of the ore's heterogeneity becomes more profound with increasing particle size in a constant sample mass.
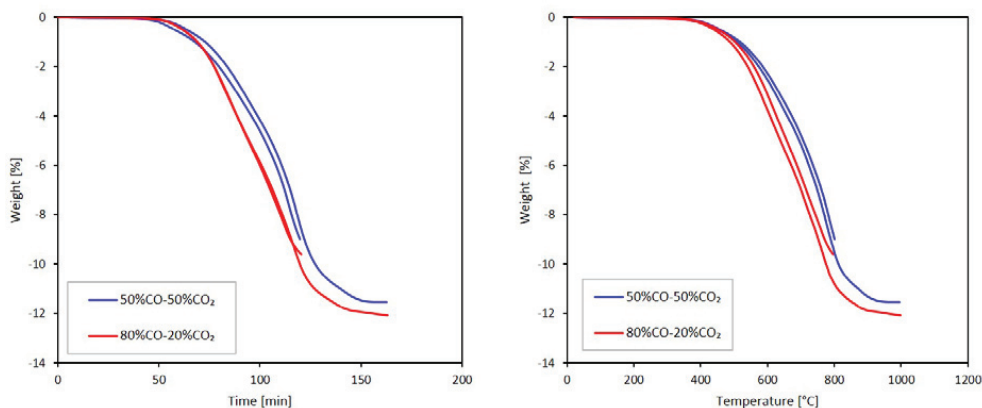
Figure 4.52: Weight as a function of time and temperature, respectively, for Nchwaning ore in size 3.33-4.00 mm heated in 50%CO-50%CO2 and 80%CO-20%CO2 at 6°C/min at 800-1000°C
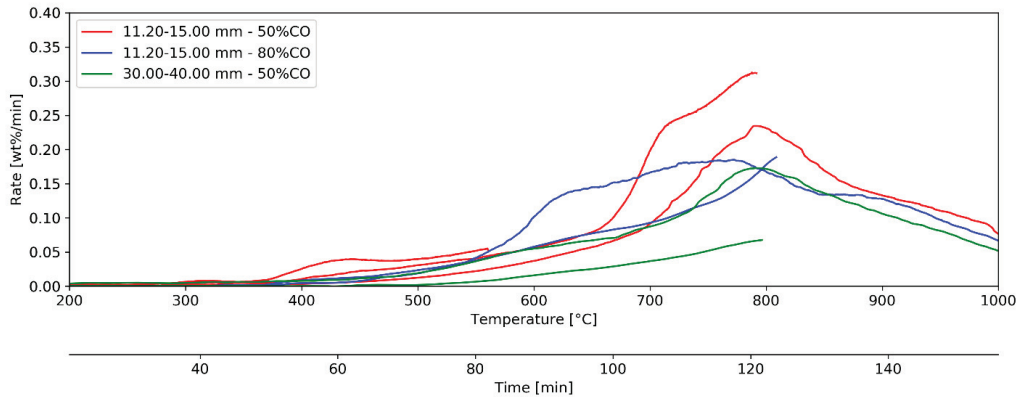
Figure 4.53: Rate [wt%/min] as a function of time and temperature, respectively, for Nchwaning ore in size 11.20-15.00 mm heated in 50%CO-50%CO₂ at 6°C/min at 570-1000°C

Decrepitation

As was shown in the previous section, two experiments were conducted with particle size 30.00-40.00 mm heated at 6°C/min in 50% CO. The two experiments showed dissimilar weight behavior, where the sample terminated at 800°C reduced considerably slower compared to the experiment terminated at 1000°C. It was observed that the sample terminated at 800°C remained intact in the original particle size after the reduction experiment, whereas the sample terminated at 1000°C had experienced intensive decrepitation, as can be seen in Figure 4.54. This may indicate that the particle size highly influences the reaction rate of Nchwaning ore. Larger particles are more subjected to decrepitation, which may explain why the reproducibility of smaller particle sizes was higher compared to larger particle sizes.
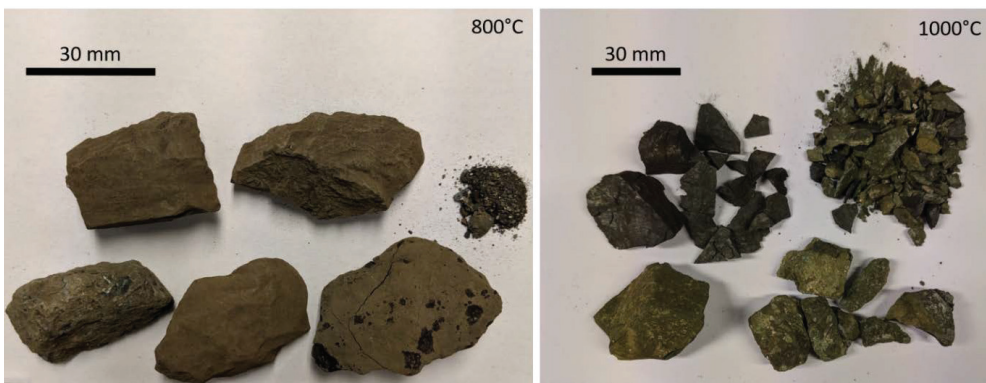
Figure 4.54: Visual of samples subsequent to reduction experiments of initial sample size fraction 30.00-40.00 mm reduced at 6°C/min in 50%CO-50%CO₂ up to 800°C and 1000°C, respectively

Analysis

Table 4.10 shows the chemical composition of the Nchwaning ore samples reduced non-isothermally, where only species quantified at concentrations larger than 1 wt% are presented. A complete prereduction of higher manganese oxides to MnO has been obtained at 1000°C for all conditions, except for particle size 11.2-15.0 mm and 30.00-40.00 mm reduced in 50% CO.

Table 4.10: Chemical composition of Nchwaning ore samples reduced non-isothermally in CO-CO₂ atmosphere

Size [mm]	%CO	Temp. [°C]	Fe, tot [wt%]	Mn, tot [wt%]	MnO_2 [wt%]	MnO [wt%]	SiO_2 [wt%]	CaO [wt%]	MgO [wt%]	CO_2 [wt%]	**MnOx**
0.5-1.36	50	1000	11.3	52.4	0.05	67.6	6.9	6.9	1.1	NA	**1.00**
0.5-1.36	80	1000	11.4	53.7	0.05	67.9	7.1	7.0	1.1	NA	**1.00**
3.33-4.00	50	300	10.5	46.2	34.1	31.9	5.7	6.3	1.0	NA	**1.47**
3.33-4.00	50	800	11.0	50.5	0.05	65.1	6.6	6.6	1.1	NA	**1.00**
3.33-4.00	50	1000	11.6	52.0	0.05	67.1	6.9	6.8	1.1	NA	**1.00**
3.33-4.00	80	800	10.4	51.2	0.05	66.1	6.9	7.2	1.1	NA	**1.00**
3.33-4.00	80	1000	11.4	52.6	0.05	67.9	7.4	6.7	1.0	NA	**1.00**
11.20-15.00	50	570	20.1	41.7	26.9	31.9	5.8	3.0	0.6	0.6	**1.41**
11.20-15.00	50	700	11.2	45.1	24.0	38.7	6.2	6.7	1.0	4.0	**1.34**
11.20-15.00	50	800	7.6	47.5	17.0	47.5	7.2	9.8	2.5	4.0	**1.23**
11.20-15.00	50	1000	7.6	53.1	6.5	63.3	7.6	7.8	1.4	0.2	**1.08**
11.20-15.00	80	816	7.2	51.3	16.7	52.6	6.9	7.9	0.4	3.9	**1.21**
11.20-15.00	80	1000	13.5	47.7	0.05	61.6	7.8	7.4	1.9	0.2	**1.00**
30.00-40.00	50	800	7.2	54.6	32.2	44.2	1.5	7.7	0.5	1.4	**1.37**
30.00-40.00	50	1000	7.4	55.0	9.7	63.1	2.2	6.3	1.2	0.9	**1.11**

Chemical analysis of reaction products at 800°C for particle size 11.20-15.00 mm and 30.00-40.00 mm confirmed that the carbonates were yet to be decomposed at this temperature. Further, the contents of CO_2 are low (0.2%) at 1000°C for both samples, which shows that the carbonates were decomposed at temperature range 800-1000°C. The 11.20-15.00 mm sample heated in 50% CO terminated at 570°C shows a low content of CO_2, however it is also seen that the content of CaO was considerably lower in this sample compared to the remaining samples. Hence, it is believed that the low content of CO_2 in this sample is not due to a decomposition of carbonates, but rather due to a low content of calcite. While the relative total contents of manganese and iron changes with the reduction degree, the manganese to iron ratio should remain similar if the samples are homogeneous. With this in mind, the smaller particle sizes appear to be homogeneous, as highly similar Mn/Fe-ratios are obtained, i.e. within range 4.4-4.8. The samples composed of larger sized particles exhibit a larger degree of heterogeneity, where values between 2.1-7.4 are found.

The total weight loss (from weighing sample prior and subsequent to experiment) is shown as a function of the analysed oxidation level of manganese (x in MnOx) in Figure 4.55. In the figure to the left, a varying weight loss is observed for samples obtaining a complete reduction of higher manganese oxides, i.e. x in MnOx equal to 1. As marked in the figure, the two lower values correlate to experiments terminated at 800°C, where the carbonates were observed to still be present. The remaining values at this oxidation level are from experiments terminated at 1000°C, where the majority of the carbonates were decomposed. The

right hand figure shows the weight loss as a function of x in MnOx, where the weight loss correlating to carbonate decomposition have been accounted for in the mentioned samples. The relation between the total weight loss and the oxidation level is overall linear. The largest deviation from the trend is observed for the oxidation level of 1.21, which was obtained for particle size 11.20-15.00 mm reduced in 80% CO up to 800°C. The size of the deviation is 1.9 wt%. The deviation could be related to inaccuracy of the analyses, meaning that the reported O/Mn-ratio is lower than the actual value. Another potential explanation is that the sample was subjected to carbon deposition at lower temperatures, which caused the overall weight loss to be lower than that correlating to the reduction of the ore.
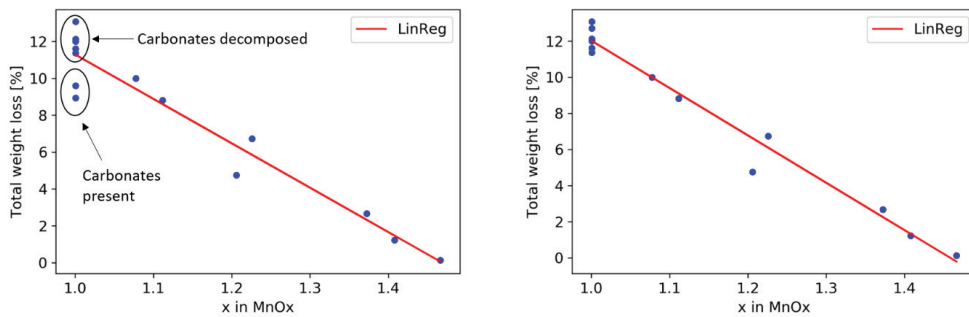
Figure 4.55: Total weight loss (from sample mass prior and subsequent to experiment) as a function of analysed oxidation level of manganese (x in MnOx). The linear regression obtains $R^2 = 0.98$

Selected samples were subjected to XRD analysis, which showed that the main constituting minerals were bixbyite (potentially braunite and/or braunite II) and monoxide, as seen in Table 4.11. Hausmannite was not detected in any of the investigated samples, which according to chemical analysis obtained reduction degrees in the range of 14-100%. This implies that, if present at all, hausmannite is only present in minor concentrations. In correlation with the chemical analysis, considerable concentrations of calcite were detected at temperatures up to and including 800°C, showing that carbonates have not been decomposed at 800°C. At 1000°C, small or insignificant concentrations of calcite were identified, whereas significant amounts of calcium was detected in solid solution in a monoxide phase. Several different oxidation states were identified for iron oxides, indicating that the reduction of hematite proceeds simultaneously as the manganese oxides.

The sample terminated at 700°C had obtained a 29% reduction of higher manganese oxides to MnO and was thus in the initial stages of reduction. The microstructure observed in three different particles from this experiment is shown in Figure 4.56-Figure 4.58. No evidence of a shrinking core reduction mechanism was observed in any of the particles. Particle 1 (Figure 4.56) displayed a two-phase structure, where the two phases appeared to be randomly distributed. EDS indicated that the bright grey phase was a braunite phase, as Ca, Si, and Mn was detected together with oxygen. The dark grey phase was largely calcium, carbon and oxygen, which indicates that the phase is calcite. Particle 2(Figure 4.57) showed a relatively homogeneous microstructure, appearing to consist of merely a single phase. A high concentration of pores of small size was observed. Particle 3 (Figure 4.59) was similar to particle 1, as a bright and dark grey phase coexisted

throughout the structure. The amount of dark grey phase, believed to be calcite, was considerably smaller in this particle. The unreduced ore showed mainly two microstructure types, i.e. type 1 being predominantly braunite II, and type 2 being braunite and calcite in coexistence. Hence, particle 1 and 3 appear to be of type 2, whereas particle 2 is type 1.

Table 4.11: Quantitative Rietveld analysis of mineralogy in partially reduced Nchwaning samples (11.20-15.00 mm)

Mineral	50% CO 570°C	50% CO 700°C	50% CO 800°C	80% CO 816°C	30% CO 1000°C
Bixbyite ($(Mn,Fe)_2O_3$)	62	61	26	29	19
Monoxide ($(Mn,Fe)O$)	7	11	42	47	
Monoxide ($(Mn,Ca,Fe)O$)					62
Calcite ($(Ca,Mg)CO_3$)	9	12	21	14	3
Braunite (Mn_7SiO_{12})	3	6	4	4	3
Braunite II ($CaMn_{14}SiO_{24}$)	5	2	3	4	2
Hematite (Fe_2O_3)	9	7	2	2	6
Magnetite (Fe_3O_4)	3				
Wüstite (FeO)	3	3	2	4	3
Reduction in MnOx from titration	14%	29%	51%	55%	NA
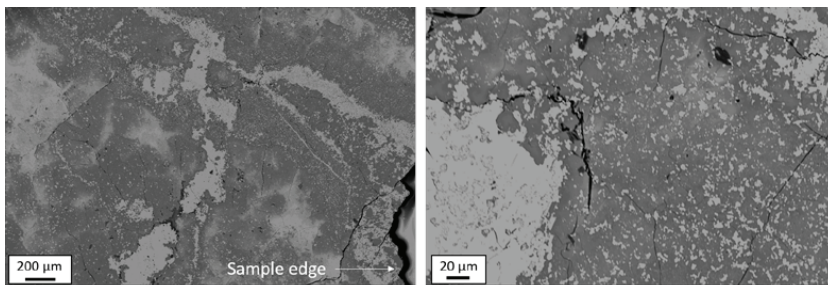
Figure 4.56: Microstructure observed in Nchwaning ore particle (11.20-15.00 mm) reduced non-isothermally (6°C/min) in 50% CO – 50% CO₂ at temperature 25-700°C. Chemical analysis gave a 29% reduction of higher manganese oxides to MnO
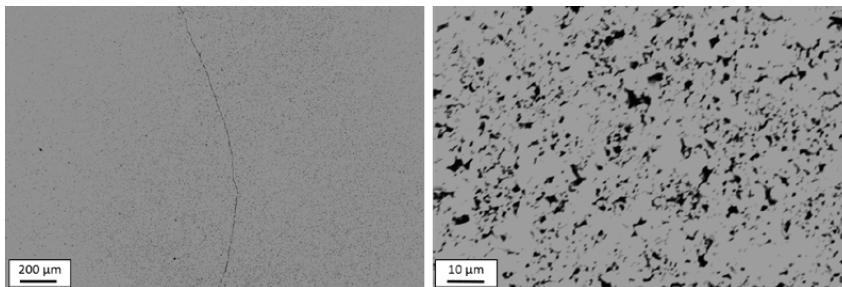
Figure 4.57: Microstructure observed in Nchwaning ore particle (11.20-15.00 mm) reduced non-isothermally (6°C/min) in 50% CO – 50% CO₂ at temperature 25-700°C. Chemical analysis gave a 29% reduction of higher manganese oxides to MnO
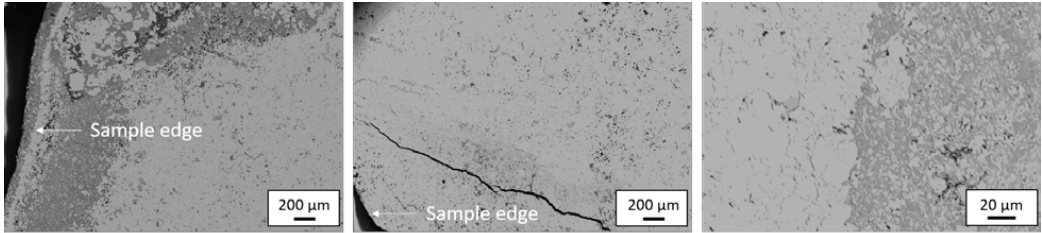
Figure 4.58: Microstructure observed in Nchwaning ore particle (11.20-15.00 mm) reduced non-isothermally (6°C/min) in 50% CO – 50% CO$_2$ at temperature 25-700°C. Chemical analysis gave a 29% reduction of higher manganese oxides to MnO

Microstructure in three particles of initial size 11.20-15.00 mm reduced in 80% CO terminated at 800°C are shown in Figure 4.59. According to chemical analysis, the average reduction degree of higher manganese oxides to MnO in this sample was 55%. Particle 1 displays a heterogeneous structure, where a bright and darker grey phase is dispersed in a random manner throughout the particle. A minor abundance of a white phase is also seen, which according to EDS was composed of manganese, barium, titanium, and sulphur, all of which in an 1:1 approximate ratio. A high extent of disintegration was observed in particle 2, where individual grains can be seen. Each grain appeared to be surrounded by a thin rim of (Mn,Fe,Ca)$_2$SiO$_4$. Further, a distinction between the core and outer layer of each grain was observed, where EDS indicated that both were in fact braunite II. This was deduced from the relation between Ca, Si, and (Mn+Fe), where the oxygen to manganese and iron ratio (O/(Mn+Fe)) was found to be 1.3:1 in the center, and 1:1 in the outer regions. The black areas observed in the image is epoxy. The microstructure in particle 3 appeared to consist of a center region and a product layer, where the potential product layer is observed to the right. Both center and exterior were observed to contain two distinct phases, where a darker grey matrix phase and a brighter grey phase was dispersed throughout. A higher porosity, as well as higher degree of heterogeneity, is observed in the outer layer. The different phases were analysed by EDS, where the results are presented in Table 4.12. In both center and product layer, the matrix was found to be a braunite phase, whereas brighter grey areas correlated to a (Mn,Fe)xOy-oxide. The difference between the phases in center and exterior, respectively, was due to the iron concentration.
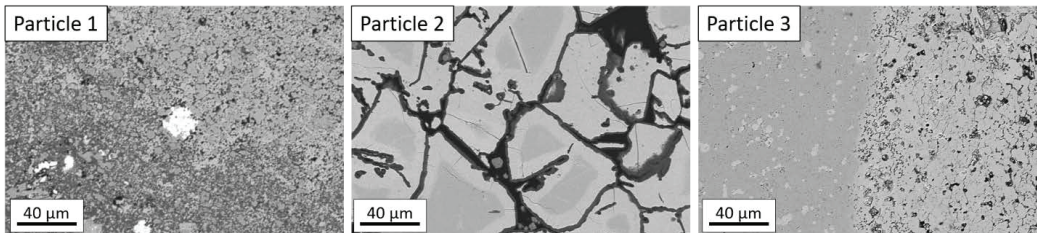
Figure 4.59: Microstructure observed in three separate particles (11.20-15.00 mm) reduced non-isothermally in 80% CO to 800°C. Reduction degree of 55% of higher manganese oxides to MnO according to chemical analysis

Table 4.12: EDS analysis (at%) of partially reduced Nchwaning particle (11.20-15.00 mm) correlating to particle 3 in Figure 4.59, where the average reduction of manganese oxides was 55% according to chemical analysis

Location	Mn [at%]	Fe [at%]	Si [at%]	Ca [at%]	O [at%]	Stochiometry from EDS	Total [wt%]	Suggested phase
Center	3.3	45.6	-	-	50.7	$(Fe,Mn)O$	94.4	$(Mn,\mathbf{Fe})_xO_y$
	41.1	-	5.7	-	51.7	$(Mn,Fe)_7SiO_9$	86.6	Braunite
Outer layer	31.7	20.8	-	-	46.0	$(Mn,Fe)O_{0.9}$	87.4	$(\mathbf{Mn},Fe)_xO_y$
	37.1	10.4	6.0	-	46.3	$(Mn,Fe)_8SiO_8$	87.8	Braunite

The microstructure in two different particles from experiment run in 50% CO terminated at 800°C is shown in Figure 4.60. According to chemical analysis the average reduction degree in this experiment was 51% of higher manganese oxides to MnO. The two particles exhibit structures highly similar to the two main structures observed in the untreated ore. Both particles show a relatively homogeneous structure with no indications of a topochemical reaction mechanism. EDS analysis showed that the matrix phase in particle 1 showed minor differences compared to the analysed composition of braunite identified in the original ore. Areas of a brighter grey phase is dispersed throughout, which was identified as a MnOx-phase. Particle 2 shows a clear distinction between a dark grey phase and a brighter grey phase, where investigations in higher resolution showed that the dark grey phase were composed of two individual phases. Both were found to contain mainly calcium and magnesium, and it is believed that the phases are $CaCO_3$ and $(Ca,Mg)CO_3$, with a 1:1 ratio of calcium and magnesium in the latter. The bright grey phase showed a composition correlating to that of braunite.
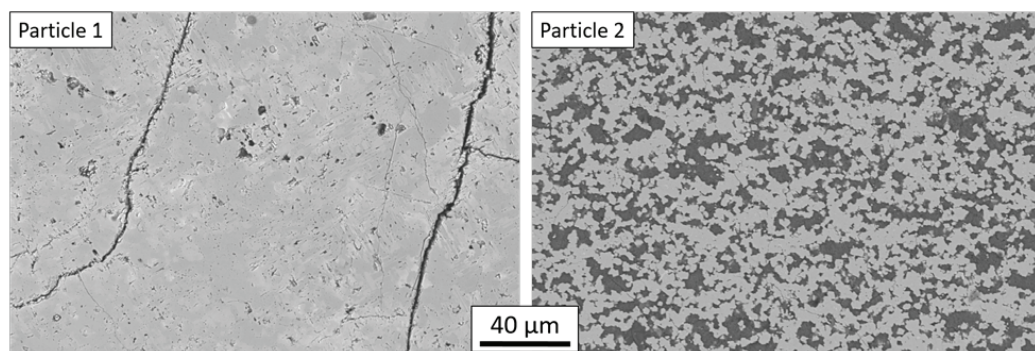
Figure 4.60: Microstructure observed in two separate particles (11.20-15.00 mm) reduced non-isothermally in 50%CO to 800°C. Reduction degree of 51% of higher manganese oxides to MnO according to chemical analysis

The lack of knowledge on the valence state of manganese, and the unreliable analysis of oxygen, complicates the identification of the specific mineral and oxidation state of manganese from EDS analyses. The investigations of reduced samples showed no indications of a shrinking core mechanism at various reduction degrees. Further, metallic iron was not observed in any of the samples subjected to non-isothermal reduction at any evaluated experimental conditions.

<u>Different particle types</u>

After the reduction experiments with particle size 30.00-40.00 mm it was observed that the particles appeared to be of two distinct categories, as some particles were black and others were green with small regions of white color, as is shown in Figure 4.61. The difference between these two particle types were examined through chemical composition, mineralogy, and microstructure.

The chemical composition is shown in Table 4.13, which shows that the total manganese content is similar in both particles, while the iron content is slightly lower in the green particle compared to the black, i.e. 6.4% compared to 8.4%. The green particle contains 3 times the amount of SiO_2 found in the black particle, in addition to 1.9 times the amount of CaO. Further, the concentrations of barium, sulphur and phosphorous are considerably larger in the green particle, i.e. 15.9, 5.4 and 3.4 times the amount in the black particle, respectively. From titration it was observed that the reduction degree of higher manganese oxides to MnO was relatively similar in both particles, where an oxidation level (x in MnOx) of 1.10 was found for the green particle, and 1.12 for the black particle. This correlates to a reduction degree of 78.9% and 73.7%, respectively.
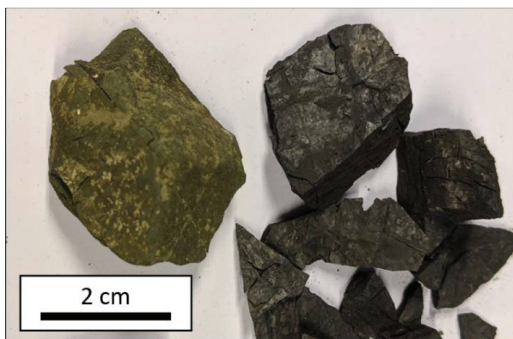
Figure 4.61: Particles from experiment with Nchwaning ore (30.00-40.00 mm) reduced in 50% CO – 50% CO2 at 6°C/min up to 1000°C

The mineralogy was investigated by XRD, where phase identification was performed using the EVA Software. The obtained XRD spectrums with the identified phases are shown in Figure 4.62. The XRD spectrum obtained for the visually green particle showed the presence of bixbyite, braunite and small amounts of hausmannite, in addition to manganosite. The quantified amounts, as shown in Table 4.14, correlate to an oxidation level of 1.11, which is highly in line with the x in MnOx obtained by titration.

All peaks observed in the black particle were successfully described by manganosite (MnO). The quantitative Rietveld analysis gave 99% MnO and 1% Mn_2O_3. Chemical analysis showed that this particle contained 4.4% calcium, which is assumed to be found in solid solution in the monoxide phase identified as MnO by XRD. CaO and MnO shows highly similar XRD spectrums, where merely a slight shift in the diffracted angles are observed between the two. The chemical analysis reported an oxidation level (x in MnOx) of 1.12, which implies that the particle contains more oxygen than that correlating to MnO. No additional peaks were recorded by the spectrum, which may suggest that the phase(s) were amorphous.

Table 4.13: *Chemical composition of reaction products from non-isothermal experiments conducted with Nchwaning ore (30.00-40.00 mm) in 50% CO at 6°C/min from room temperature to 1000°C*

Color	Fe, tot [wt%]	Mn, tot [wt%]	MnO_2 [wt%]	MnO [wt%]	SiO_2 [wt%]	CaO [wt%]	MgO [wt%]	CO_2 [wt%]	BaO [wt%]	S [wt%]	**MnOx**
Green	6.4	55.8	8.8	64.9	3.3	8.1	0.8	0.3	1.3	0.3	**1.10**
Black	8.4	54.3	10.7	61.4	1.1	4.4	1.2	1.6	0.2	0.0	**1.12**

The particles were cut to expose the cross-section, which revealed that both particles were mainly of black color, where merely a thin product layer formed the green color in the green appearing particle. An overview of the microstructure observed in the green particle at low magnification is shown in Figure 4.63. The microstructure showed the presence of two distinct product layers, where the porosity was larger in the outermost layer. A close-up of the different sections is presented in Figure 4.64. Two phases were seen to co-exist in the outer product layer, where the bright grey phase contained manganese, iron and oxygen. It is known that manganosite exhibit a green color, and it is thus believed that the bright grey phase is a manganosite with small amounts of iron in solid solution. The darker grey phase contained manganese, iron, calcium, silicon and oxygen, which may be the braunite identified by XRD. An intermediate layer is observed between the green outer layer and the center. In this layer, the phase compositions were similar to that of the outer layer, i.e. bright grey phase containing Mn, Fe, and O, and a darker grey phase which contained Ca and Si in addition to the former.
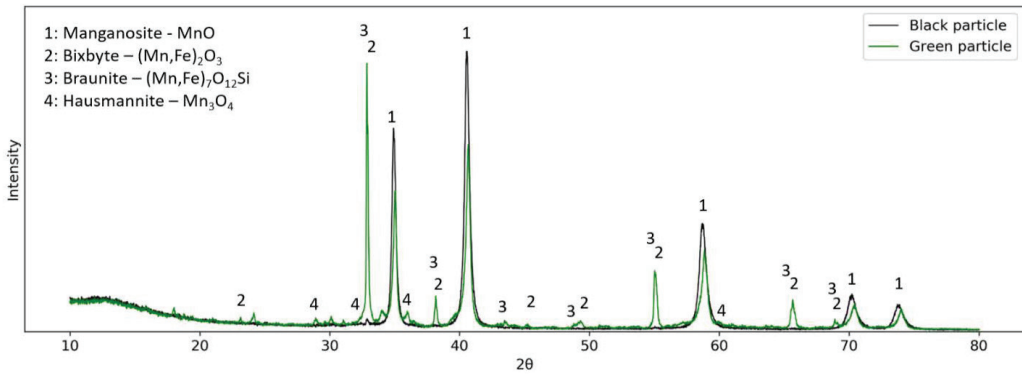
Figure 4.62: *XRD spectrum with identified phases from EVA of green and black appearing Nchwaning ore particle reduced in 50% CO up to 1000°C*

Table 4.14: *Mineralogy in green and black Nchwaning ore particle as determined by Rietveld analysis using TOPAS 5 Software*

Mineral	Formula	Green particle	Black particle
Monoxide	$(Mn,Fe,Ca)O$	77	99
Bixbyite	Mn_2O_3	2	1
Bixbyite	$(Mn,Fe)_2O_3$	19	
Braunite	Mn_7SiO_{12}	2	
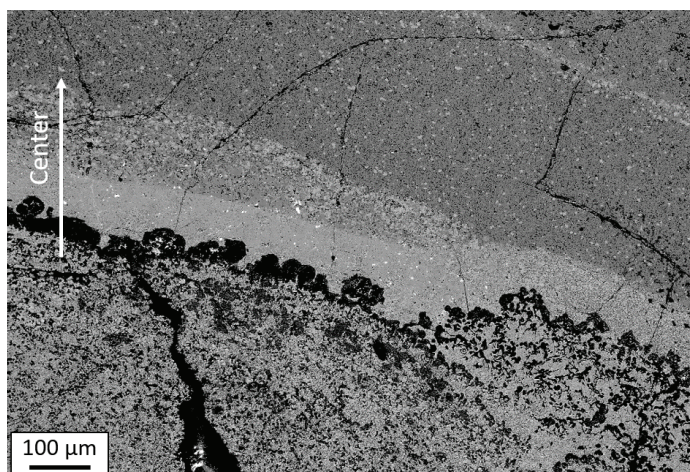
Figure 4.63: Microstructure observed in cross-section of particle appearing green in Figure 4.61 at low magnification
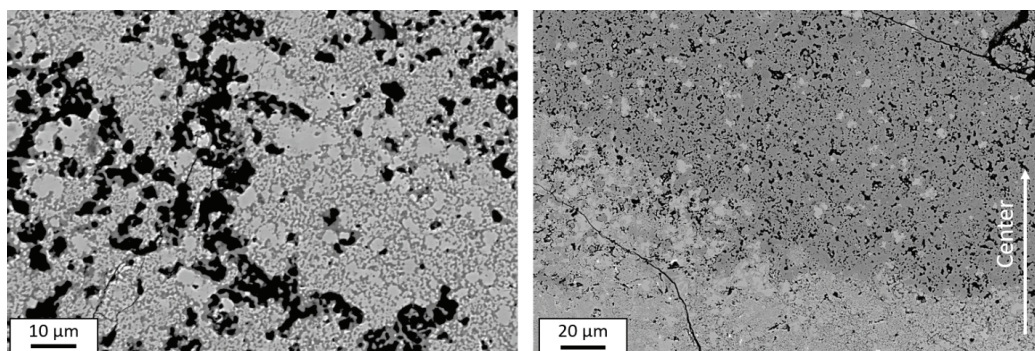
Figure 4.64: Product layer (left) and inner microstructure (right) observed in cross-section of particle appearing green in Figure 4.61

The microstructure observed in the black particle is shown in Figure 4.65 at low and high magnification, respectively. No trends were observed between phase distribution and distance from center in this particle. The structure is composed of brighter and darker grey regions randomly dispersed throughout the particle, where darker regions correlated to areas of higher porosity, as is seen in the image to the right.

The main difference between the particles appear to be the presence of the outermost layer of manganosite in the green particle. Whether this layer was a result of the reduction or related to an initial mineral distribution is not known. The majority of both particles appeared to be a monoxide containing manganese, iron and calcium. It is shown that despite different concentrations of iron, calcium and silicon, the two particles obtained highly similar reduction degree at the evaluated temperature.

133
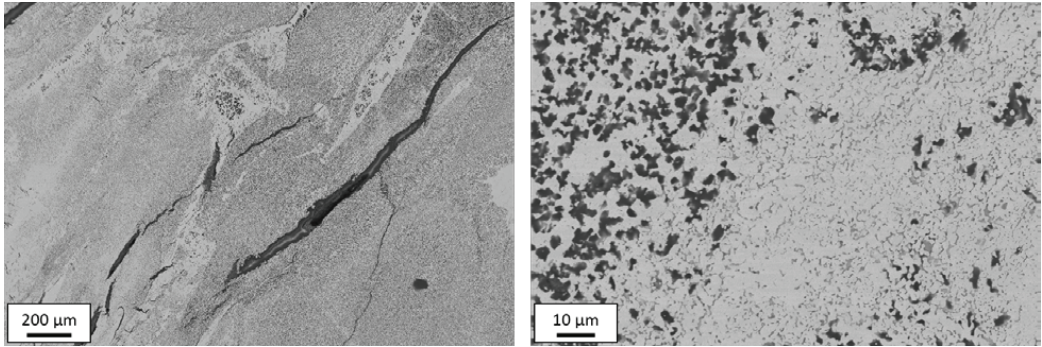
Figure 4.65: Microstructure observed in cross-section of particle appearing black in Figure 4.61

4.2.2 Isothermal reduction - CO-CO$_2$ atmosphere

Weight reduction behavior

11.20-15.00 mm particles were reduced isothermally in 50% and 70% CO at temperatures 600-900°C. Small sample sizes were evaluated due to limitations in furnace geometry. 4-5 particles were used in each experimental run, correlating to a weight of 20-25 g. This implies that the weight loss obtained at a total prereduction is merely 2.4-3.0 g. The combination of small weight loss, an open furnace, and a high frequency of the weight recordings resulted in fluctuations in the weight behavior. The conversion degree (reduction extent) was calculated from the recorded weight loss relative to the theoretical weight loss. Figure 4.66 shows the recorded weight and corresponding conversion for samples reduced in 50%CO–50%CO$_2$. The curves show an increasing reaction rate and reaction extent with increasing temperature and holding time. At 600°C, the weight loss converges at 20% conversion, whereas a full conversion extent is obtained at 800°C and 900°C.
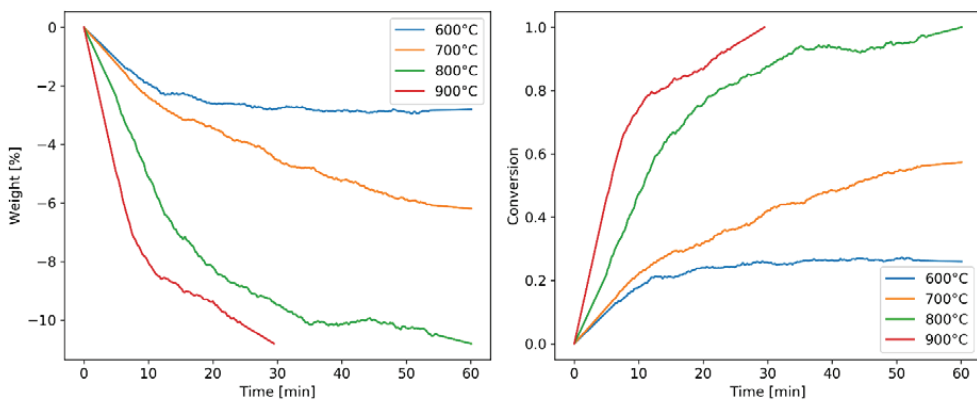
Figure 4.66: Recorded weight and conversion, respectively, as a function of time for Nchwnaing ore samples (11.20-15.00 mm) reduced isothermally at 600-900°C in 50% CO – 50% CO$_2$

Figure 4.67 shows the recorded weight and corresponding conversion for Nchwaning ore reduced in 70%CO–30%CO$_2$. In this atmosphere, a higher reduction extent is obtained at 600°C compared to 700°C, which is due to a faster rate in the initial stages of the experiment. An intermediate region where the weight remains approximately constant is observed at both 600°C and 700°C, i.e. between 15-45 minutes process time.
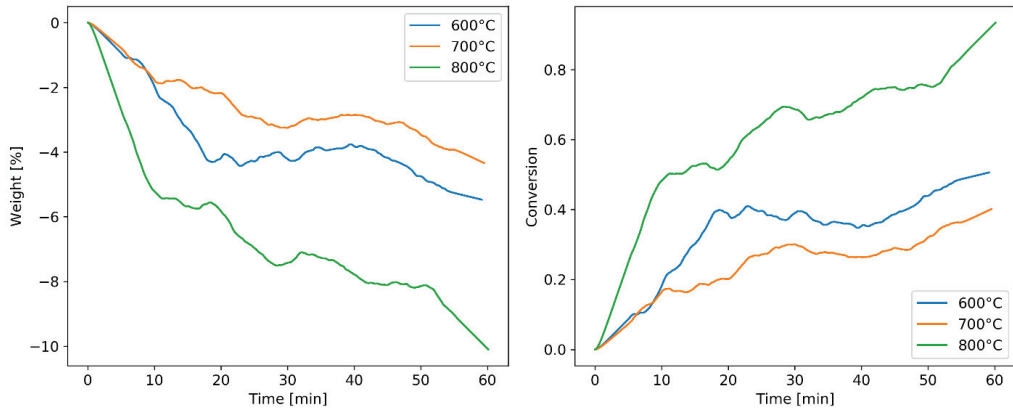
Figure 4.67: Recorded weight and conversion, respectively, as a function of time for Nchwnaing ore samples (11.20-15.00 mm) reduced isothermally at 600-900°C in 70% CO – 30% CO$_2$

Decrepitation

The samples were manually sieved into various size fractions after reduction to estimate the extent of disintegration. The variance between different runs can be evaluated from Figure 4.68 (left), which shows the size distribution of Nchwaning ore after reduction in 50% CO – 50% CO$_2$ at 800°C with a holding time of 30 minutes. These specific conditions were repeated three times, where the size distribution of each run, as well as the average, is presented in the figure. A low amount of fines have been produced in all four parallels, where approximately 80% of the sample remains at sizes larger than 10 mm. It is indicated that the decrepitation has occurred in a manner where only small pieces of ore have broken off, as the particle size has only been slightly decreased. The effect of temperature is evaluated in Figure 4.68 (right), which shows the average size distribution obtained at temperatures 600-800°C with holding time of 60 minutes in 50% CO – 50% CO$_2$. It can be seen that the majority of Nchwaning ore remains in the original size throughout the experiment at all evaluated temperatures. More than 90% of the samples remain at particle sizes larger than 10 mm. Figure 4.69 shows a comparison of the size distribution of experiments conducted in 50% CO and 70% CO, respectively, at temperatures 600-800°C. A low extent of decrepitation is seen for all conditions, where a clear effect of increasing CO in the reducing atmosphere is not observed.
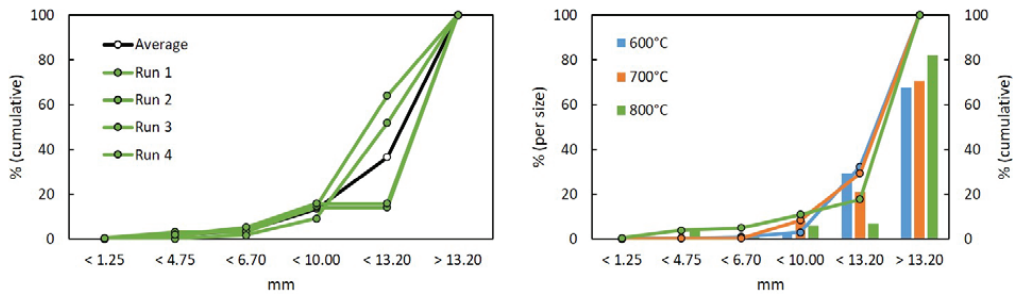
Figure 4.68: Size distribution after reduction experiments for Nchwaning ore (initial size 11.20-15.00 mm) reduced in 50% CO(remainder CO₂) for repeated runs at 800°C (left), and average size distribution at temperatures 600°C, 700°C and 800°C(right)
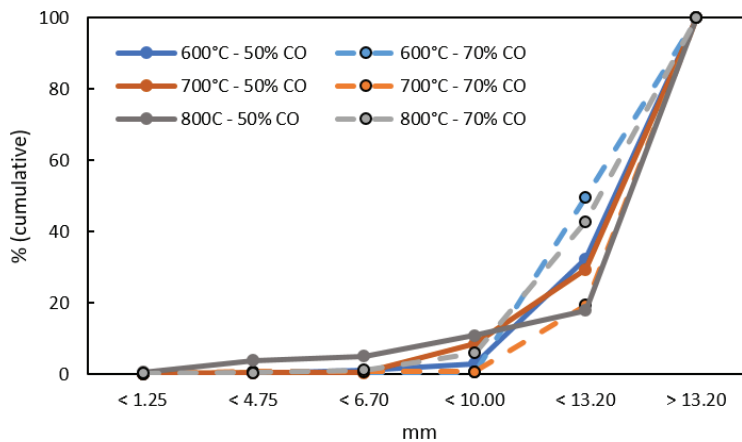
Figure 4.69: Size distribution after reduction experiments for Nchwaning ore (initial size 11.20-15.00 mm) reduced in either 50% CO or 70 % CO (remainder CO₂) at 600-800°C

Analysis

The chemical analysis of the samples reduced in 50%CO showed a 47% reduction of higher manganese oxides after 60 minutes reduction at 600°C, whereas a 75% reduction was obtained after 30 minutes at 900°C, as presented in Table 4.15. Some discrepancies are seen between the analyses. The sample reduced at 600°C shows a manganese to iron ratio of 2.1, whereas the sample reduced at 700°C shows a Mn/Fe ratio of 8.3. The former also show a low concentration of CO_2 compared to the remaining analyses. According to the raw material analyses, it was observed that the carbonates present in Nchwaning ore was largely

found in one of two particle types. Due to the small sample size, it is thus possible that the particles evaluated in this experiment were of type 1, i.e. low in carbonates.

Table 4.15: Chemical analysis of isothermal Nchwaning reduction products. 11.20-15.00 mm particles reduced in 50%CO-50%CO₂

Temperature	Time	Fe, tot	Mn, tot	MnO$_2$	MnO	SiO$_2$	CaO	MgO	CO$_2$	**MnOx**	**RD**
600°C	60 min	20.2	41.6	16.6	40.1	3.7	5.8	1.0	0.5	**1.25**	47
700°C	60 min	6.3	52.0	26.5	45.5	5.2	5.9	1.8	4.2	**1.32**	
800°C	60 min	10.6	44.2	13.0	46.5	7.1	9.4	2.9	4.5	**1.19**	
900°C	30 min	13.3	47.4	8.7	54.1	6.8	5.8	1.9	1.5	**1.12**	75

The samples were subjected to XRD analysis, where the results quantified by Rietveld analysis in TOPAS are shown in Table 4.16. While the quantified values should merely be used to indicate the distribution of major and minor phases, the obtained values are supported by the chemical analysis. The manganese was found as a combination of bixbyite and manganosite at all temperatures. The intermediate oxide hausmannite was not detected in any of the samples, which may suggest that the reduction of hausmannite to manganosite is fast. Calcium was detected as a carbonate at all temperatures, however in minor amounts at 600°C and 900°C. It is believed that the low abundance at 600°C is due to a low content of calcite in the sample prior to the experiment. Iron was found in the form of hematite and wüstite, which could suggest that the reduction of intermediate iron oxide magnetite (Fe$_3$O$_4$) is fast. The reduction of iron oxides to metallic iron will be dependent on temperature, oxygen pressure, and the activity of iron. According to thermodynamics, metallic iron is the stable iron phase when reduced in 80%CO-20%CO$_2$ at 1000°C in an ideal system. However, as the activity of iron in the manganese ore may be lower compared to an ideal system and the evaluated gas composition lies close to the phase boundary of wüstite, it is possible that the conditions are not sufficient in order to obtain a complete reduction to metallic iron. In accordance with the chemical analysis presented in Table 4.15, the XRD analysis shows a considerably higher abundance of iron oxides in the sample reduced at 600°C compared to sample reduced at 700°C.

Selected particles from each experiment were cut to expose the cross-section and examined by SEM and/or optical microscope. No correlation between phases and distance from surface was observed, implying that no evidence of a shrinking core mechanism was found. The observed microstructures showed high resemblance to the structures observed in the raw material. Further, the chemical composition of the observed phases obtained by EDS also showed high resemblance to the composition found in the initial material. In some cases, an increased abundance of cations was found, which could indicate that the oxygen content in the phase was lowered. The microstructure observed in a particle reduced in 50%CO-50%CO$_2$ at 600°C for 60 minutes is shown in Figure 4.70. Two phases of major size are observed at a random distribution throughout the structure. Both of these phases have been suggested to be braunite phases according to the relation between the analysed elements, as well as the similarity of the composition to the analysed phases in the raw material. Small areas of a third phase were observed, which was identified as hematite, as the composition was similar to that obtained for hematite in the initial material.

Table 4.16: Quantitative Rietveld analysis of isothermally reduced Nchwaning ore (11.20-15.00 mm) in 50% CO – 50% CO₂

Mineral	Formula	600°C (60 min)	700°C (60 min)	800°C (60 min)	900°C (30 min)
Monoxide	$(Mn,Fe)O$	30	41	53	64
Bixbyite	$(Mn,Fe)_2O_3$	44	32	37	9
Braunite	Mn_7SiO_{12}	4	10	10	7
Hematite	Fe_2O_3	22	2	7	9
Magnetite	Fe_3O_4	2	-	-	-
Wüstite	FeO	3	4	4	5
Calcite	$(Ca,Mg)CO_3$	5	12	18	5
MnOx from titration		47% reduction			75% reduction

Braunite II
38.4 at% Mn, 6.3 at% Fe, 3.0 at% Si, 3.0 at% Ca, 48.0 at% O
O/(Mn+Fe) = 1.1, (Mn+Fe)/Si = 14.7
Total wt% = 84.9

Braunite/Braunite II
37.0 at% Mn, 2 at% Fe, 6.0 at% Si, 5.0 at% Ca, 49.3 at% O
O/(Mn+Fe) = 1.3, (Mn+Fe)/Si = 6.6
Total wt% = 82.1

Hematite
6.3 at% Mn, 48.6 at% Fe, 43.1 at% O
Total wt% = 91.8
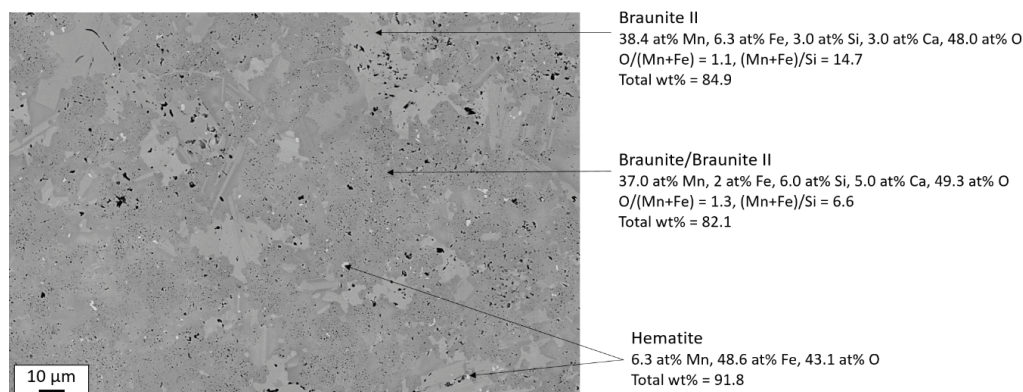
Figure 4.70: Microstructure observed in Nchwaning ore particle reduced in 50%CO-50%CO₂ at 600°C for 60 minutes. Suggested phases and the correlating chemical composition obtained by EDS are included

Figure 4.71 shows the microstructure observed in a particle subjected to isothermal reduction at 700°C in 70%CO-30%CO₂ for 60 minutes. This particle shows resemblance to the type 1 particles observed in the original sample. Three main phases were observed, identified as braunite, hematite, and carbonate. The compositions as obtained by EDS are shown in Table 4.17. Hematite was identified as brightest grey phase, as marked in the figure. The medium grey phase showed a composition according to EDS highly similar to that identified as braunite in the untreated ore. The braunite was depleted in calcium. The darker grey phase contained all calcium and magnesium present in the particles, which were detected at concentrations up to 26 at% and 16 at%, respectively. The analyses indicated that the carbonates were $CaCO_3$ and $(Ca,Mg)CO_3$.

It was seen that the formation of reduction products was not observed by SEM and EDS investigation of the reduced samples. This may suggest that the solid state diffusion of elements is slow. The investigated particles showed no indications of a topochemical mechanism. Rather, the visual appearance of the particles resembled the initial structures observed in the ore.
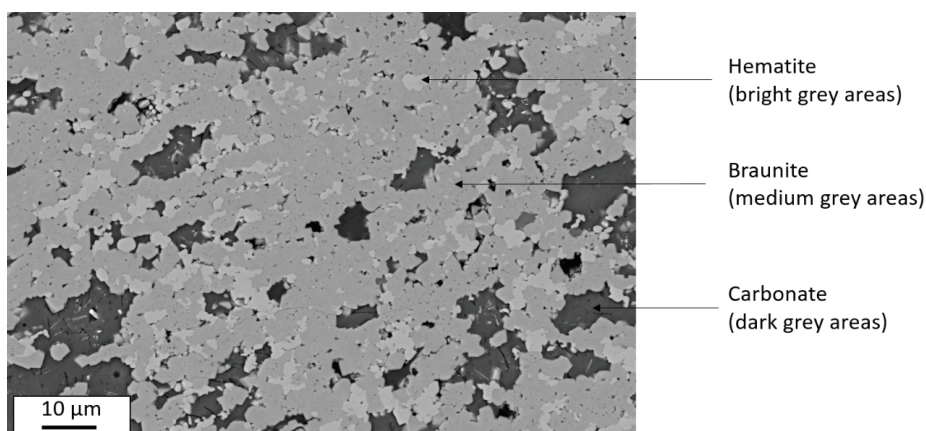
Figure 4.71: Microstructure observed in Nchwaning ore particle reduced in 70%CO-30%CO₂ at 700°C for 60 minutes. Phases identified correlate to analyses shown in Table 4.17

Table 4.17: Chemical analysis obtained by EDS of phases shown in Figure 4.71

Mn [at%]	Fe [at%]	Si [at%]	Ca [at%]	Mg [at%]	O [at%]	Total [wt%]	Suggested phase
3.3	52.0	-	-	-	43.6	90.2	Hematite
38.4	5.0	5.2	-	-	48.7	83.3	Braunite
1.7	0.0	0.2	18.3	16.3	57.3	78.1	$(Ca,Mg)CO_3$
2.0	0.0	0.3	26.0	1.7	65.8	80.7	$\mathbf{(Ca},Mg)CO_3$

4.2.3   Non-isothermal reduction – effect of inert material

The ore is fed to the furnace premixed in proper ratios with the remaining required raw materials, such as quartz and coke. While these materials do generally not take part in any reactions at low temperatures in the prereduction zone, they may have an effect on the temperature development, and thus the reduction rates of the ore. This section presents the observations made from the investigation of this potential effect on the temperature development by the use of quartz, which was mixed with the ore in various weight ratios during reduction. It is assumed that quartz behaves as an inert material in the temperature range used in this investigation.

Weight reduction behavior

All experiments presented in this section have been conducted at 6°C/min up to 1000°C in 50%CO-50%CO₂. Figure 4.72 shows the temperatures recorded by the thermocouple submerged in the sample as a function of time for the experimental runs with particle size 3.3-4.00 mm and 11.20-15.00 mm, respectively.

It can be seen that the temperature development shows similar behavior for all experiments, where a slightly higher temperature is obtained for experiments conducted without any quartz addition, particularly in the initial stages of the experiments.

Figure 4.73 shows the calculated weight behavior as a function of time and temperature, respectively, for Nchwaning ore in particle size 3.33-4.00 mm mixed with various ratios of inert material (quartz). Figure 4.74 shows the corresponding reaction rate, calculated from the change in weight at a 2-minute process time interval, where it was observed that all characteristics present at shorter time frames were conserved. Highly similar reduction behavior is observed for the experiments, as both weight and reaction rate show high degree of overlap. A slightly higher weight loss is obtained at a given process time for the experiment conducted without quartz, according to the slightly higher temperature experienced by the sample.
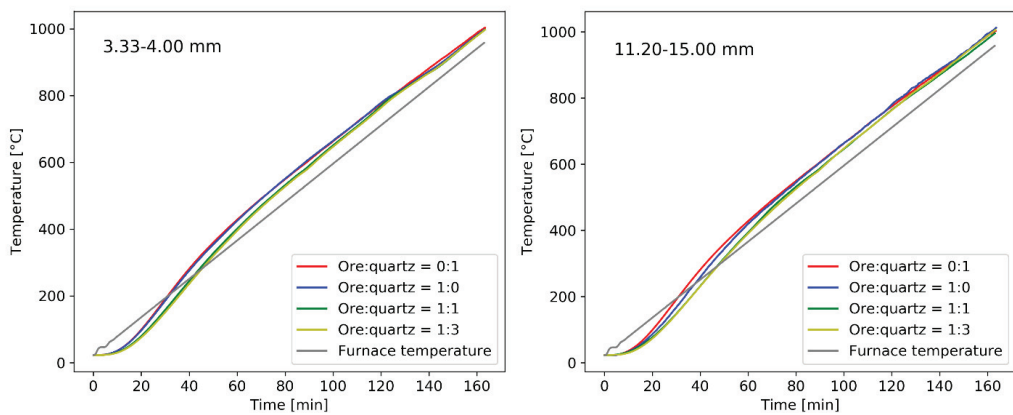
Figure 4.72: Temperature as a function of time for Nchwaning ore in size fraction 3.33-4.00 mm and 11.20-15.00 mm, respectively, mixed with quartz in various ratios
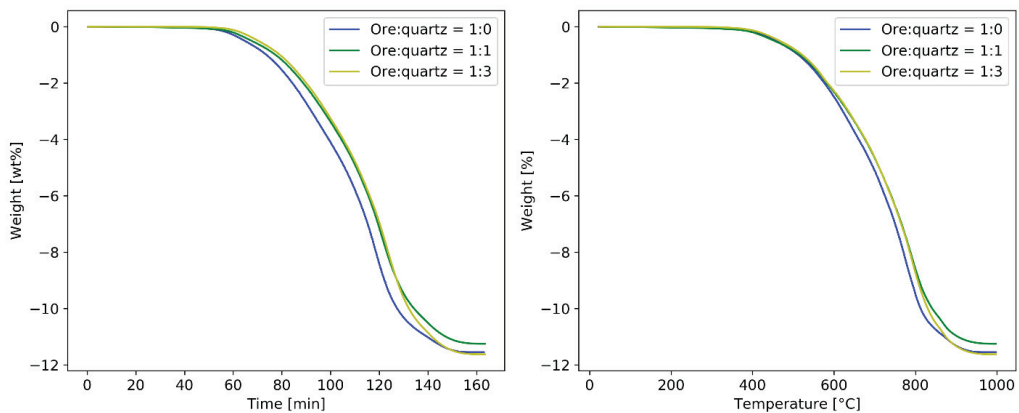
Figure 4.73: Calculated weight as a function of time and temperature, respectively, for Nchwaning ore in size 3.33-4.00 mm mixed with quartz in various ratios

The reaction rate starts to increase at temperatures close to 350°C for all experimental runs, where a local maximum is observed at approximately 430°C. According to experiments conducted with empty crucible, as well as experiments in CO-CO_2 presented in the previous section, it is believed that this small initial peak in the reaction rate correlates to the reverse Boudouard reaction, where CO-gas is decomposed to solid carbon and CO_2. The magnitude of this reaction appears to be unaffected by the presence of inert material. A change in the reaction rate is observed at 485°C, from which the rate increases with a steeper slope up to second peak position at 630°C. A further increase in the rate is observed between 650°C up to main peak position to 780°C, where all experiments experience the maximum obtained rate. The rate then shows a continuous decrease, interrupted by a slight increase at 866°C, likely due to carbonate decomposition.
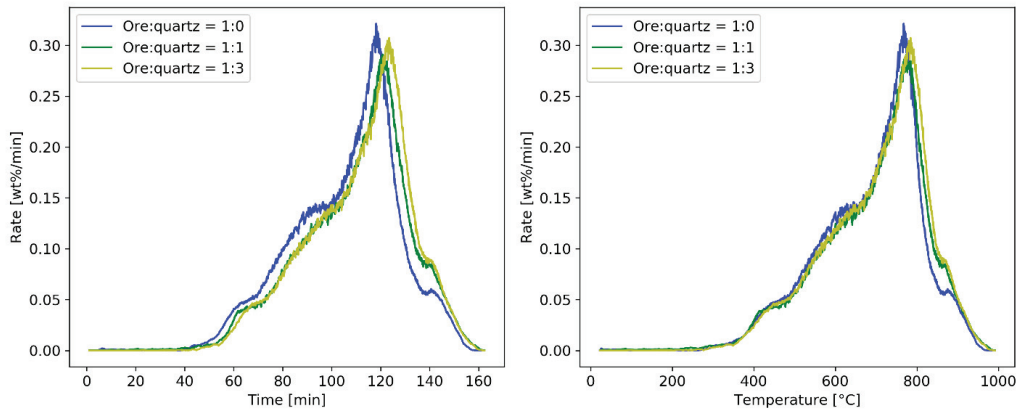
Figure 4.74: Reaction rate [wt%/min] as a function of time and temperature, respectively, for Nchwaning ore in size 3.33-4.00 mm with quartz in various ratios

The calculated weight behavior and the correlating reaction rate is for particle size 11.20-15.00 mm are shown in Figure 4.75 and Figure 4.76, respectively. The weight behavior curves indicate that the experiment conducted with merely the ore starts to reduce at a higher temperature and process time compared to the experiments conducted with ore mixed with inert material. However, evaluation of the correlating reaction rate shows that this is largely related to the initial peak in the reaction rate located at approximately 400°C, believed to be due to carbon deposition. Hence, it appears that the extent of carbon deposition increased with the presence of quartz. The maximum obtained rate is experienced at temperatures close to 800°C for all experiments. While the experiment conducted with Nchwaning ore shows a continuous increase up to the peak, followed by a continuous decrease in the reaction rate, the experiment conducted with a mixing ratio of 1:3 with inert material, show two additional minor peaks in the reaction rate behavior. Firstly, a local maximum is observed at 700°C. This additional peak was also observed when the heating rate in CO-CO_2 atmosphere was decreased from 6°C/min to 3°C/min (as shown in Figure 4.50). It is hence shown that the reduction at temperatures up to 800°C involves at least two reaction steps, which occur at largely overlapping temperature ranges. Secondly, an additional local maximum at 900°C is more profound and easily observed when the ore is heated in presence of quartz. As previously mentioned, it is believed that this is due to the decomposition of carbonates.
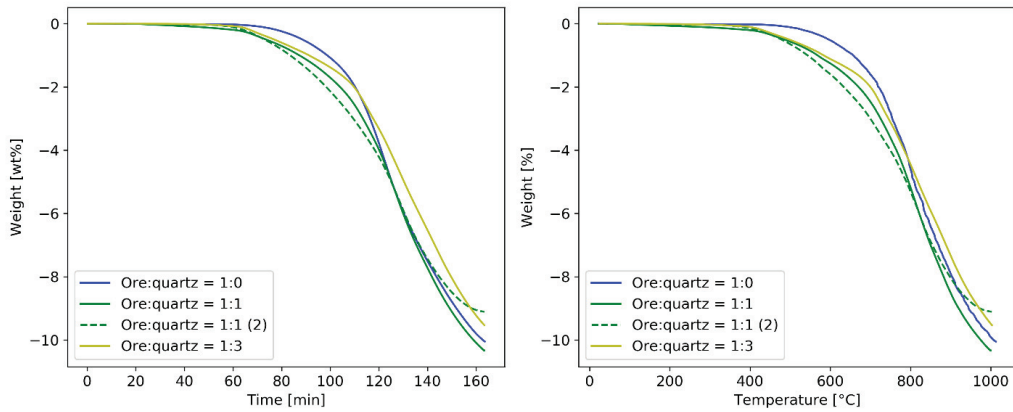
Figure 4.75: Calculated weight as a function of time and temperature, respectively, for Nchwaning ore in size 11.20-15.00 mm mixed with quartz in various ratios
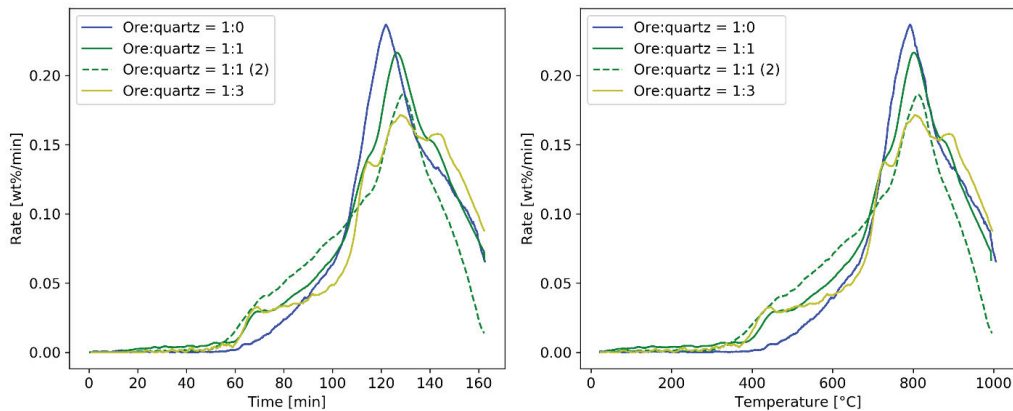
Figure 4.76: Reaction rate [wt%/min] as a function of time and temperature, respectively, for Nchwaning ore in size 11.20-15.00 mm with quartz in various ratios

Decrepitation

The extent of decrepitation was quantified by sieving the reduced samples into various size fractions. Figure 4.77 shows the size distribution of the Nchwaning ore particles after reduction experiments for initial particle size 3.33-4.00 mm and 11.20-15.00 mm, respectively. No significant difference in the disintegration extent is observed between experiments run with 1:1 and 1:3 weight mixing ratio of ore and quartz. For initial particle size 11.20-15.00 mm, 25.6 ± 7.4% of the sample was of size smaller than 10 mm after the reduction when ore and quartz was mixed in 1:1 ratio. Similarly, 23.9 ± 10.3 % was smaller than 10 mm for mixing ratio 1:3 for original and repeated experiment.
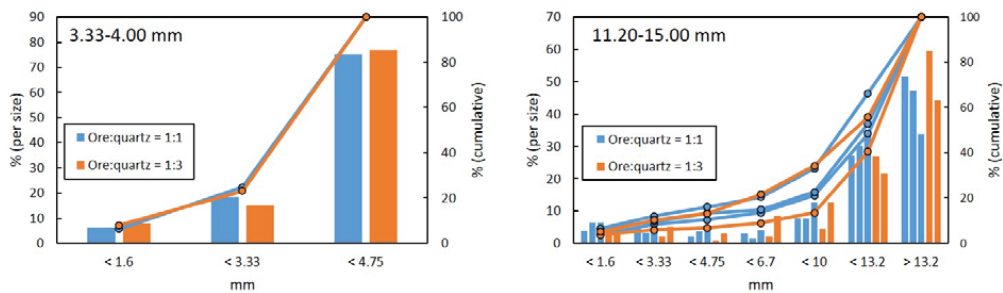
Figure 4.77: Size distribution after reduction experiments where ore and quartz were mixed in 1:1 or 1:3 weight ratio for Nchwaning ore. Particle size 3.33-4.00 mm (left) and 11.20-15.00 mm (right), respectively

Analysis

The reduced samples were analysed for chemical composition, where the results are presented in Table 4.18. All experiments have obtained a complete reduction of higher manganese oxides to MnO, except for particle size 11.20-15.00 mm mixed in weight ratio 1:3 with inert material (quartz). The analysed oxidation level (x in MnOx) in this sample was 1.04, which merely correlates to 3% of analysed MnO_2.

Table 4.18: Chemical composition of Nchwaning ore reduced while mixed with inert material (quartz). All experiments were conducted at 6°C/min up to 1000°C in 50% CO – 50% CO_2

Size [mm]	Ore:quartz [g]	Fe, tot [wt%]	Mn, tot [wt%]	MnO_2 [wt%]	MnO [wt%]	SiO_2 [wt%]	CaO [wt%]	MgO [wt%]	CO_2 [wt%]	**MnOx**
3.33-4.00	1:1	12.5	50.4	0.0	65.1	6.8	6.7	1.1	0.4	**1.00**
3.33-4.00	1:3	12.3	48.7	0.0	62.9	8.9	7.0	1.1	0.2	**1.00**
11.2-15.0	1:1	11.3	50.2	0.2	64.7	5.5	7.6	2.1	0.2	**1.00**
11.2-15.0	1:3	9.4	52.6	3.1	65.4	5.8	7.7	1.2	0.2	**1.04**

4.2.4 Non-isothermal reduction – effect of $H_2(g)/H_2O(g)$

The experiments presented in this section include the use of CO-CO_2, CO-CO_2-H_2, and CO-CO_2-H_2O atmospheres. As a relatively unstable behavior was observed for the mass balance, the reduction data in this section is discussed in terms of the behavior of the CO and CO_2 in the off-gas.

Five different gas atmospheres correlating to two different theoretical oxygen partial pressures were used in the experiments presented in this section. The standard atmospheres were 50%CO-50%CO_2 ($p(O_2)_1$) and 80%CO-20%CO_2 ($p(O_2)_2$), where gas atmospheres consisting of CO-CO_2-H_2 and CO-CO_2-H_2O, respectively, giving the same oxygen partial pressures as $p(O_2)_1$ and $p(O_2)_2$ were investigated. All

experiments presented in this section were conducted at a heating rate of 6°C/min using particle size 11.20-15.00 mm. Some of the experiments conducted in CO-CO_2 atmosphere, which were presented in section 4.2.1, are also reprinted here for comparison.

Figure 4.78 shows the temperature as a function of time for the two different theoretical oxygen pressures evaluated. The figure to the left shows the gas atmospheres correlating to oxygen pressure 1, where a highly similar temperature development is seen throughout the experimental runs. The right hand figure shows the temperature behavior in the two experiments correlating to the second oxygen pressure, where some dissimilarities are seen between the temperatures in CO-CO_2 and CO-CO_2-H_2 atmosphere. Experiments terminated at the same target temperature, shows highly similar sample temperatures, as can be seen in Table 4.19. The maximum attained sample temperature is approximately 10°C higher in the hydrogen atmosphere correlating to the lowest oxygen pressure ($p(O_2)_2$), which may indicate a faster rate.
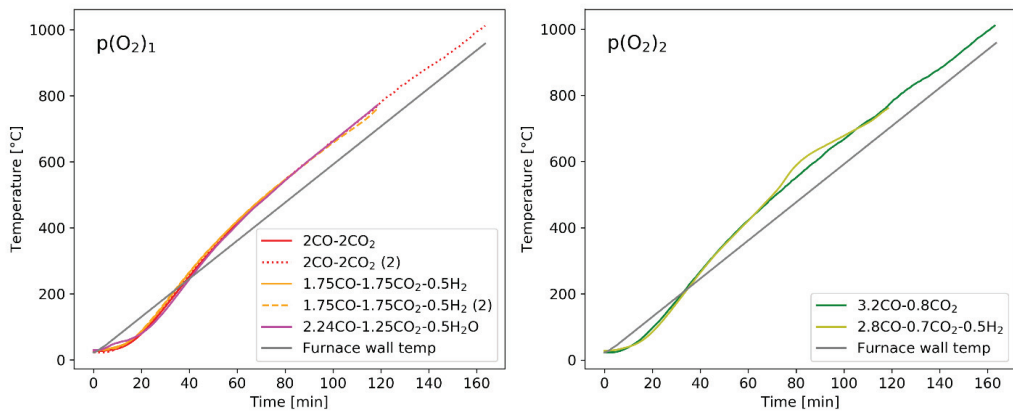
Figure 4.78: Temperature behavior in experiments conducted with Nchwaning ore in atmospheres correlating to two different oxygen partial pressures

Table 4.19: Maximum obtained temperature during reduction of Nchwaning ore in various atmospheres

Gas components	Oxygen pressure	Maximum furnace temperature [°C]	Maximum sample temperature [°C]
CO:CO_2	$p(O_2)_1$	500	567
CO:CO_2:H_2	$p(O_2)_1$	500	568
CO:CO_2:H_2	$p(O_2)_1$	700	763
CO:CO_2:H_2O	$p(O_2)_1$	700	761
CO:CO_2:H_2	$p(O_2)_2$	700	772

The recorded concentration of CO and CO_2 as analyzed by the off-gas analyzer was adjusted to set point value to compare the relative changes. %CO_2 relative to set point value for the experiments conducted in CO-CO_2 and CO-CO_2-H_2 atmosphere correlating to two different theoretical oxygen pressures is shown in

Figure 4.79. Similarly, Figure 4.80 shows the analyzed CO-concentrations relative to set point. To simplify the comparison of the trends in the CO and CO_2, the CO-concentrations have been presented with inverse values on the y-axis. Several observations can be made from the off-gas behavior. In general, the CO_2 concentrations are increased relative to set point throughout the experiments, which implies that CO_2 is produced. This is expected as the reduction of the ore results in CO_2-production. The exception from this is found in the experiment conducted in CO-CO_2-H_2 atmosphere correlating to oxygen pressure 1 ($p(O_2)_1$). In this experiment, the CO_2 shows an increase relative to set point at temperatures 400-550°C, whereas a negative (relative to set point) CO_2 is observed at higher temperatures. From 730°C, the concentration of CO_2 starts to increase again and reaches set point value at 750°C, slightly prior to experiment termination. The CO-concentration shows a continuous increase at temperatures up 750°C, from which it starts to decrease.

The potential reactions in a system of Nchwaning ore in CO-CO_2-H_2 atmosphere is the reduction of ore, the Boudouard reaction and the water-gas shift reaction. According to this, two potential explanations may be provided for the behavior of CO and CO_2. Firstly, a reaction between H_2 and CO_2 by the left shifted water-gas shift reaction($H_2 + CO_2 = H_2O + CO$) would result in a decreasing CO_2 and increasing CO. According to themodynamics, this reaction is not likely to occur at temperatures below 800°C. A second potential explanation is related to the right shifted Boudouard reaction ($CO_2 + C = 2\ CO$). As is seen from the reaction equation, this may explain why the consumed %CO_2 and produced %CO was not directly inversely related. This implies that the presence of hydrogen lowers the initiation temperature of the Boudouard reaction. This behavior is not seen in the CO-CO_2-H_2 atmosphere correlating to oxygen pressure 2 ($p(O_2)_2$). Rather, this experiment shows a considerable increase in the CO_2 concentrations, initiated at approximately 400°C, which continues to increase up to peak position at 700°C. The increased CO_2 may be due to the ore reduction or the left shifted Boudouard reaction, or a combination of the two. As this gas composition contains larger amounts of CO, it is likely that the Boudouard reaction is favored towards the decomposition of CO into solid carbon and CO_2.
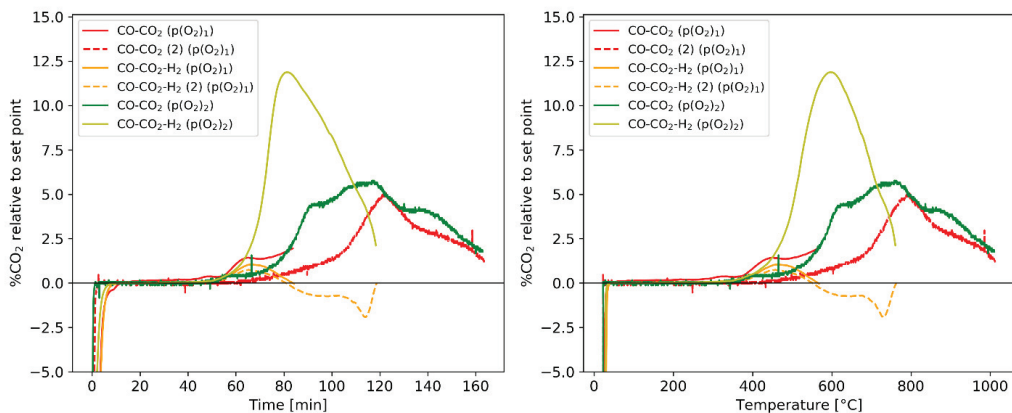
Figure 4.79: %CO_2 relative to set point for experiments with Nchwaning ore in different gas atmospheres based on CO-CO_2 and CO-CO_2-H_2 correlating to two different theoretical oxygen pressures.
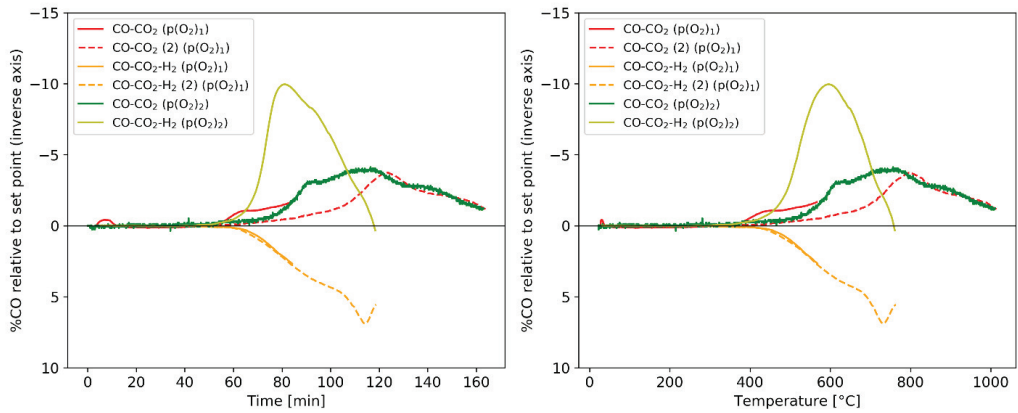
Figure 4.80: %CO relative to set point for experiments with Nchwaning ore in different gas atmospheres based on CO-CO$_2$ and CO-CO$_2$-H$_2$ correlating to two different theoretical oxygen pressures. Y-axis is inverted

The relative concentrations of CO$_2$ and CO in the experiment conducted with water vapor is shown in Figure 4.81 and Figure 4.82, respectively, where the results for the experiments conducted in CO-CO$_2$ and CO-CO$_2$-H$_2$ atmosphere with similar oxygen pressures have been included for comparison. It is observed that the experiment with water vapor shows positive amount of CO$_2$ and negative amount of CO throughout the reduction. The trends are inversely related, however the magnitudes are slightly dissimilar. Oscillating trends are observed in both CO and CO$_2$, where the oscillations appear to be initiated at temperatures close to 550°C, and the magnitude of the oscillations increase with increasing temperature.
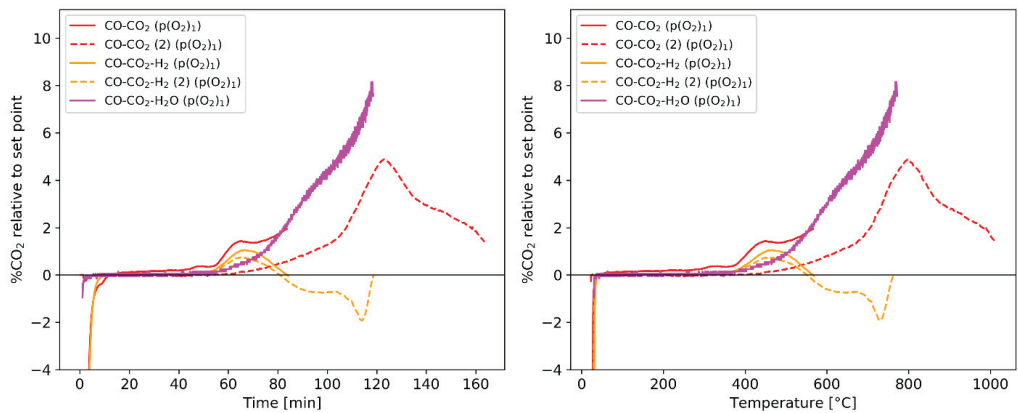
Figure 4.81: %CO$_2$ relative to set point for experiments with Nchwaning ore in different gas atmospheres based on CO-CO$_2$, CO-CO$_2$-H$_2$ and CO-CO$_2$-H$_2$O correlating to the same theoretical oxygen pressures.
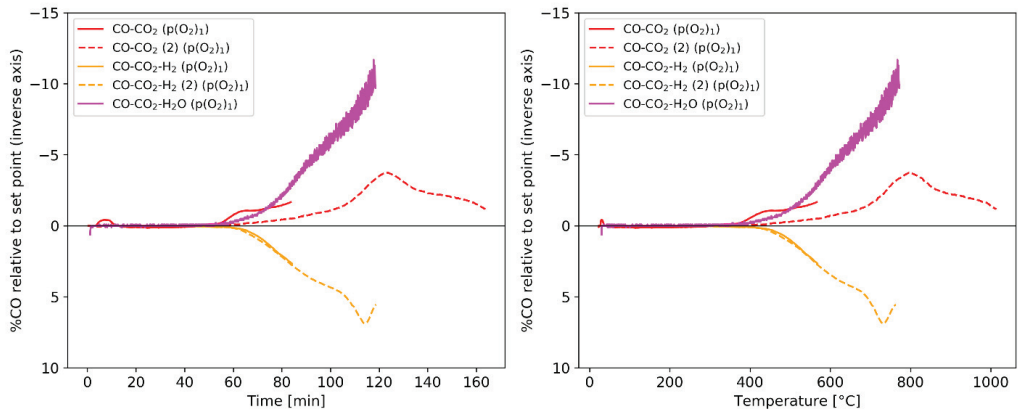
Figure 4.82: %CO relative to set point for experiments with Nchwaning ore in different gas atmospheres based on CO-CO$_2$, CO-CO$_2$-H$_2$ and CO-CO$_2$-H$_2$O correlating to the same theoretical oxygen pressures

Decrepitation

The samples were sieved into various size fraction after heating in reducing atmosphere to estimate the extent of decrepitation and disintegration. Figure 4.83 shows the results for the experiments conducted in reducing atmospheres correlating to oxygen pressure 1, i.e. that correlating to 50%CO-50%CO$_2$.
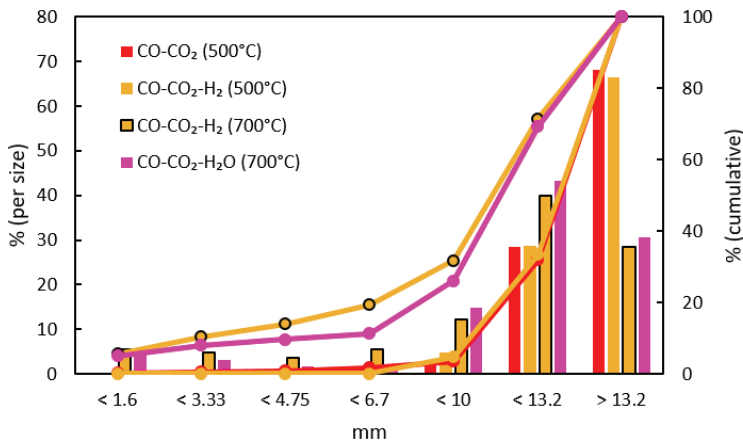
Figure 4.83: Size distribution after heating in reducing atmosphere composed of CO-CO$_2$, CO-CO$_2$-H$_2$, and CO-CO$_2$-H$_2$O, respectively, for Nchwaning ore of initial size fraction 11.20-15.00 mm

147

A highly similar low extent of disintegration was obtained in the experiments conducted in CO-CO_2 and CO-CO_2-H_2 terminated at 500°C. Similarly, the experiments conducted in CO-CO_2-H_2 and CO-CO_2-H_2O terminated at 700°C show highly similar size distribution after reduction. This could indicate that the disintegration of Nchwaning ore is more dependent on temperature rather than reducing atmosphere or reduction degree, however the amount of data is scarce, and more should be obtained to conclude.

Analysis

The samples were analysed for chemical composition after the reduction experiments, where the results may be found in Table 4.20. A varying extent of reduction of higher manganese oxides were attained in the different experiments. At 500°C, a highly similar reduction degree was obtained for the CO-CO_2 and CO-CO_2-H_2 atmosphere correlating to oxygen pressure 1. This indicates that the gas was at equilibrium, obtaining a similar oxygen pressure in the two atmospheres. An increased rate with the presence of hydrogen is not observed for Nchwaning, as it was observed for Comilog. Further, a highly similar reduction degree was also obtained for CO-CO_2-H_2 and CO-CO_2-H_2O atmospheres correlating to oxygen pressure 1 terminated at 700°C. This may indicate that equilibrium, and thus a similar oxygen pressure, was obtained.

Table 4.20: Chemical analysis of reduced Nchwaning ore (11.20-15.00 mm) samples

Gas	°C	Fe, tot [wt%]	Mn, tot [wt%]	MnO_2 [wt%]	MnO [wt%]	SiO_2 [wt%]	CaO [wt%]	MgO [wt%]	CO_2 [wt%]	**MnOx**
$CO:CO_2$ $(p(O_2)_1)$	500	20.1	46.4	26.9	31.9	5.8	3.0	0.6	0.6	**1.41**
$CO:CO_2:H_2$ $(p(O_2)_1)$	500	13.5	47.6	31.7	35.6	5.9	3.4	0.3	0.9	**1.42**
$CO:CO_2:H_2$ $(p(O_2)_1)$	700	8.0	50.8	23.5	46.4	5.5	7.5	1.0	3.3	**1.29**
$CO:CO_2:H_2O$ $(p(O_2)_1)$	700	11.5	47.0	22.3	42.5	5.1	6.7	1.2	2.5	**1.30**
$CO:CO_2:H_2$ $(p(O_2)_2)$	700	9.7	50.0	13.5	53.5	5.3	7.9	1.1	4.5	**1.17**

Microstructures observed in particles reduced in CO-CO_2-H_2 and CO-CO_2-H_2O terminated at 500°C and 700°C are shown in Figure 4.84-Figure 4.86. The observed structures appeared similar to those observed for samples partially reduced in CO-CO_2 atmosphere (as shown in Figure 4.56 and Figure 4.57). No indications of a topochemical mechanism is observed in any of the particles. A high concentration of pores was observed in some of the particles, however no correlation between pore concentration and center distance was seen.
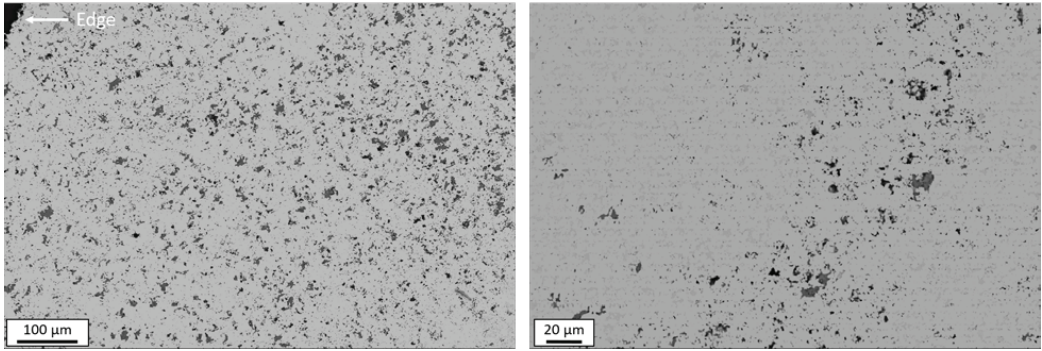
Figure 4.84: Microstructure observed in Nchwaning ore particle reduced in CO-CO$_2$-H$_2$ at 6°C/min up to target temperature 500°C
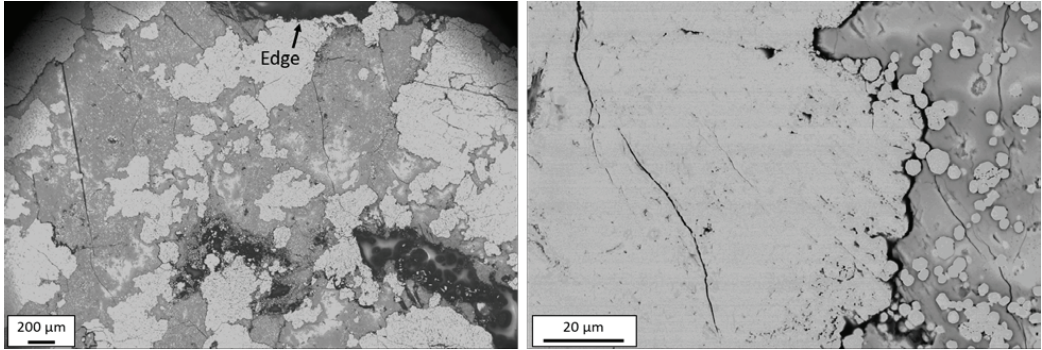
Figure 4.85: Microstructure observed in Nchwaning ore particle reduced in CO-CO$_2$-H$_2$ at 6°C/min up to target temperature 700°C
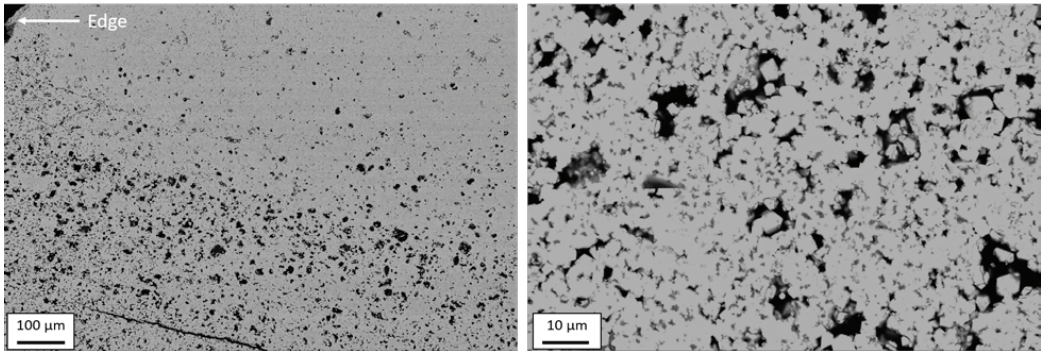
Figure 4.86: Microstructure observed in Nchwaning ore particle reduced in CO-CO$_2$-H$_2$O at 6°C/min up to target temperature 700°C

4.3 Calculated vs measured temperature

Dissimilar temperature behavior was observed during the reduction of Comilog- and Nchwaning-ore, respectively. Overall, the temperature development observed for Comilog ore was indicated to largely correlate to the reaction rate, implying that the same trends were observed in the temperature behavior as in the rate behavior. This is shown for particle size 0.50-1.36 mm and 11.20-15.00 mm, respectively, reduced in 50%CO-50%CO$_2$ in Figure 4.87. It is seen for both particle sizes that the temperature increase is initiated at a slightly higher process time compared to the reaction rate.
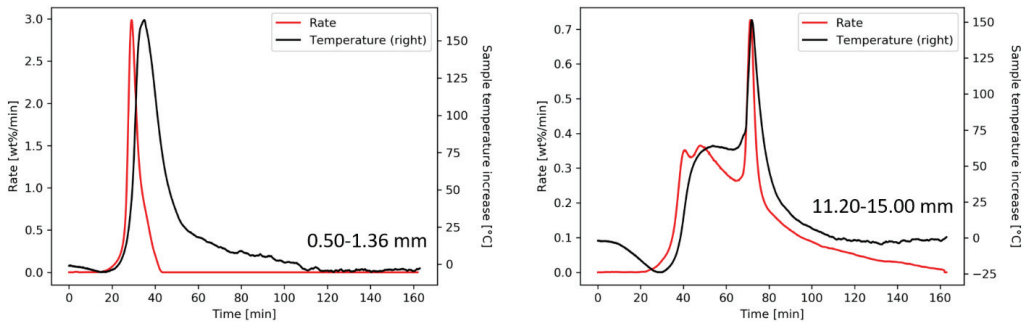
Figure 4.87: Reaction rate and temperature increase in sample (relative to furnace temperature of heating rate 6°C/min) for Comilog ore in particle size 0.50-1.36 mm and 11.20-15.00 mm, respectively, reduced in 50%CO-50%CO$_2$. A strong correlation between the reaction rate and the sample temperatures is seen

To confirm whether the observed temperature behavior was attributed to the reaction rates, the theoretical temperature was calculated. The temperature experienced by the sample will be affected by thermal radiation heat from the crucible walls, convective heat transfer between gas and solid phase, and reaction heat from the reduction of the ore samples. In addition, there are heat losses in the system to consider. This gives rise to a complicated energy balance. The heat generated by the reaction can however be analytically estimated using equation 4.1.

$$\Delta H_{rx} = m \cdot Cp \cdot \Delta T \qquad\qquad 4.1$$

Where ΔH_{rx} is the reaction enthalpy, m is the mass of sample [g], Cp is the heat capacity [J/K·g], and ΔT is the temperature change experienced by the sample [K]. The heat capacities for Comilog and Nchwaning ore reported by Ksiazek were utilized in the calculations[113], who reported values for temperature range 25-1000°C at every 100°C. The heat capacity of Nchwaning ore showed a continuous increase from 0.7 J/g·K to 1.0 J/g·K at 700°C. From this temperature it decreased to approximately 0.6 J/g·K at 1000°C. For Comilog ore, the specific heat capacity increased slowly from ca 0.8 J/g·K to 0.9 J/g·K at 25-500°C. At this temperature, the heat capacity started to decrease, where a value of 0.5 J/g·K was found at 1000°C. The values are similar to that of pure Mn-oxides at temperatures up to 600°C[17], where MnO_2, Mn_3O_4 and MnO has Cp = 0.62-0.63 J/g·K and Mn_2O_3 has 0.70 J/g·K. at 25°C.

150

The reaction enthalpies were calculated based on the reaction steps that was presented in the previous chapter. In the case of Comilog, the reduction of the two smaller particle sizes were estimated by the overall reduction of MnO_2 to MnO, as the reaction rate behavior showed a single peak. For the larger particle sizes, the reaction course was described according to the steps that was presented in the previous chapter. As such, the overall reduction of MnO_2 to MnO was used to determine the temperature development at temperatures below the main exothermic peak. The exothermic peak was described by the rapid reduction of MnO_2 to Mn_2O_3, and reduction after peak position was described by Mn_2O_3 to MnO. For Nchwaning ore, the reaction enthalpy was calculated for the reduction of Mn_2O_3 to MnO in a single step for all particle sizes. To simplify the calculations, the temperature was estimated by combining the temperature increase from the heat effects and the temperature measured during the heating of a crucible containing quartz. As such, the temperature recorded when the sample is quartz is assumed to be an approximation of the heat effects of the radiation heat, as well as the heat transfer from solid to gas phase and vice versa.

$$T_{calc} = T(crucible\ with\ quartz) + \Delta T(reaction\ heat) \qquad 4.2$$

The calculated temperatures of the sample due to the heat of exothermic reactions are presented together with the temperatures measured by the thermocouple in Figure 4.88 and Figure 4.89 for Comilog- and Nchwaning-ore, respectively. The calculated temperatures agree with the experimental temperatures, showing that Nchwaning follows the gas temperature during reduction. As observed in Figure 4.89 there is a reasonable agreement between the calculated temperature increase due to the exothermic reactions and the temperatures measured during the experiment for Comilog ore. While the calculated temperature displays the same trends as the recorded temperature, some discrepancies are observed. The calculated temperature is generally lower than that which was recorded. Furthermore, the width of the exothermic peak is narrower in the calculated temperatures. The calculated temperatures do not account for the fact that the sample exist in smaller size particles in a cluster, but rather views the mass as a single particle. As such, it is likely that the differences in the calculated and measured temperature is related to heat transfer effects encountered in a cluster of particles.
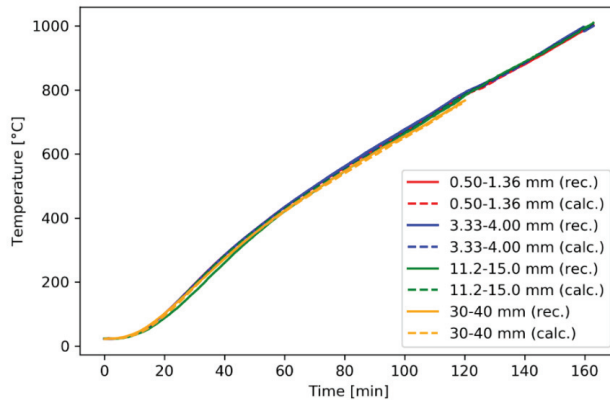
Figure 4.88: Recorded and calculated temperature, respectively, for four different particle size fractions of Nchwaning ore reduced in 50%CO-50%CO₂ at 6°C/min from 25-1000°C
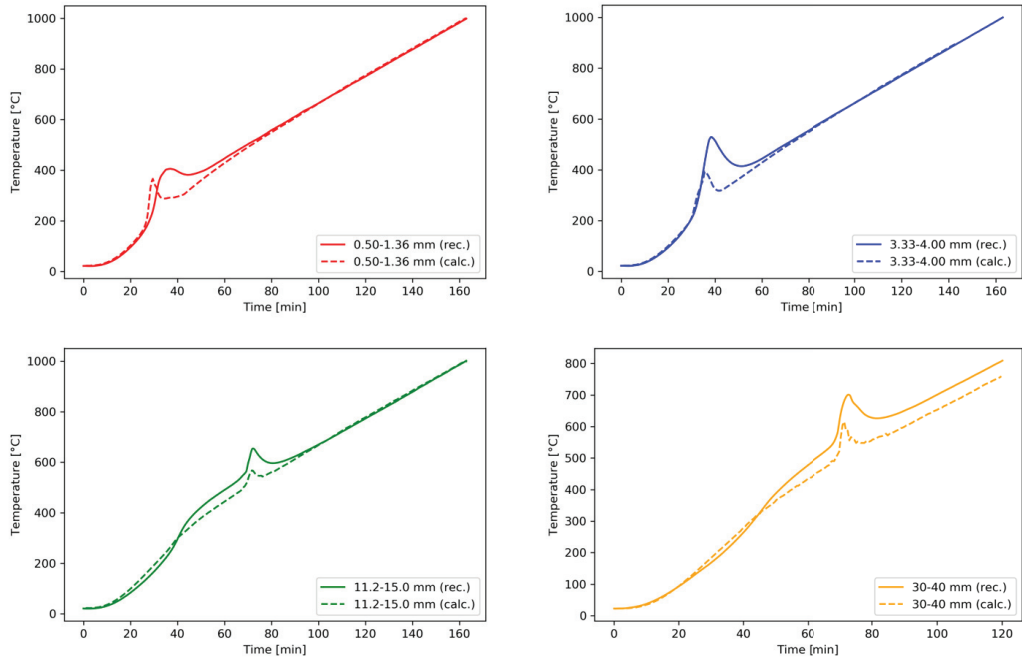
Figure 4.89: Recorded and calculated temperature, respectively, for four different particle size fractions of Comilog ore reduced in 50%CO-50%CO₂ at 6°C/min from 25-1000°C

5   Discussion

The previous chapter presented the results obtained from the experimental investigation of the reduction of Comilog- and Nchwaning-ore, respectively. The ores were exposed to varying conditions, including particle size, gas composition and temperature, in order to evaluate how the ores behave in the industrial furnace. The experimental results obtained for reduction of Comilog- and Nchwaning-ore will be analysed and discussed in this chapter. The first section elucidates the changes of the ore during reduction, focusing on reaction steps and observations from microstructure investigations. The second section will present an analysis of the reaction rates. The observations and measurements were used to construct a simple model which is presented in this section. The third section is dedicated to the disintegration and decrepitation that occurs during the reduction of manganese ore. Finally, the relevance of the experimental results to the industrial operation is evaluated.

5.1   Mechanisms

This section discusses the reaction steps involved in reduction of Comilog and Nchwaning manganese ore, and the developments in the microstructure. As the ores differ in chemical composition, mineralogy, and physical parameters, the ores are discussed separately.

5.1.1   Comilog ore

Comilog ore is largely composed of a variety of tetravalent manganese oxides, i.e. pyrolusite(MnO_2), ramsdellite(MnO_2), cryptomelane(KMn_8O_{16}), nsutite($Mn^{4+}_{1-x}Mn^{2+}_xO_{2-2x}(OH)_{2x}$), and lithiophorite ((Al, Li,)$Mn^{4+}O_2(OH)_2$). In addition, minor concentrations of gibbsite(Al(OH)₃), goethite(Fe(OH)₂) and quartz(SiO₂) was detected by XRD. The identified minerals are in correlation with previously reported mineralogy of Comilog ore[11], [114]. Comilog contains some chemically bound moisture, which is largely found as nsutite and lithiophorite. The amount of chemically bound moisture was estimated to be 5 wt%, which is in high agreement with the values previously reported by Tangstad et al. for various grades of Comilog ore[10]. During prereduction, Comilog ore experience a weight loss due to evaporation of chemically bound moisture and reduction of higher manganese oxides (x in $MnO_x > 1$) to MnO. The reduction of higher manganese oxides to MnO is reflected in the off-gas behavior, whereas the chemically bound moisture is evaporated and condensed in a separate container. As such, the difference between the weight loss behavior from the mass balance and the off-gas behavior is the weight loss related to the chemically bound water. From this assumption, it was observed that the chemically bound moisture evaporated at temperatures 200-400°C, as can be seen in Figure 5.1. This was supported by the quantitative XRD, which showed that the nsusite phase was removed after non-isothermal heating (6°C/min) up to 400°C, as well as by isothermal reduction at 400°C at 40 minutes holding time. XRD further indicated that nsutite decomposed to pyrolusite. This agrees well with the results presented by Ngoy[56], who observed a weight loss of approximately 5 wt% in Comilog ore by heating at 6°C/min up to 500°C in CO₂, where chemical analysis showed that no reduction of manganese oxides had occurred during this stage.
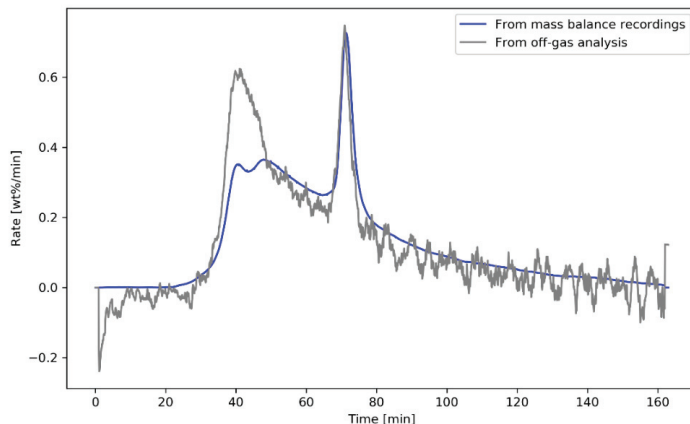
Figure 5.1: Reaction rate (wt%/min) as found from mass balance recordings and off-gas analysis, respectively, for the reduction of Comilog ore (11.20-15.00 mm) at 6°C/min in 50%CO-50%CO₂. The difference in the curves represent the H₂O-volatilization from nsutite and lithiophorite

Several distinct peaks were observed in the reaction rate, exemplified for particle sizes 11.20-40.00 mm. The reduction steps were deduced from the quantitative XRD results of reduced samples. Figure 5.2 shows the observations made for particle size 11.20-15.00 mm reduced in 50%CO-50%CO$_2$ at 6°C/min up to 1000°C, where the reactions correlating to the characteristics of the rate behavior have been marked. Similar observations were made for particle size 11.20-15.00 mm and 30.00-40.00 mm, respectively, reduced non-isothermally. Furthermore, the reaction sequence observed during non-isothermal reduction was also observed in the isothermal reduction experiments conducted at 400-600°C. Two main regions of the reaction rate behavior was observed in non-isothermal experiments, separated at approximately 70 minutes process time. The first stage could be further separated, as a relatively small decrease in the rate was observed in a local minimum at 370°C between two individual peaks at 310°C and 410°C, respectively. The initial stages of reduction, initiated at 200°C, was the reduction of MnO_2 to a combination of Mn_2O_3, Mn_3O_4, and MnO. Hausmannite (Mn_3O_4) was the main reduction product at temperatures below 370°C, however a certain amount of the hausmannite had already been further reduced to MnO. At 550°C (obtained at 70 minutes process time), only minor amounts of Mn_2O_3 and Mn_3O_4 was found, and the manganese was mainly distributed between MnO_2 and MnO, i.e. initial and final oxidation state. This indicates that the reduction of tetravalent oxides proceeds through all intermediate stable oxide phases, where a slightly higher temperature is required to initiate reduction of Mn_3O_4 to MnO compared to MnO_2 to Mn_3O_4. This difference in temperature is believed to be the cause of the slight decrease in reaction rate at 370°C. Considering the small decline in the rate, and the similarity of the reduction products, the reduction during temperature range 200-550°C may be approximated as the overall reduction of MnO_2 to MnO. At approximately 550°C, a rapid increase was observed in the reaction rate, accompanied by a large exothermic temperature peak. This was found to be the rapid removal of any MnO_2 remaining at this temperature, which was found to proceed to Mn_2O_3. This step was merely dependent on temperature, and was unaffected by particle size, gas composition, and heating rate. Nonetheless, the extent of the rapid removal is indirectly

154

dependent on these variables, as this decides the amount of MnO_2 that is present at the threshold temperature. The decomposition temperature of pure MnO_2 to Mn_2O_3 in oxygen is 510°C, which agrees with that the MnO_2 experiences decomposition rather than reduction. The produced Mn_2O_3 continued to be reduced further to MnO.
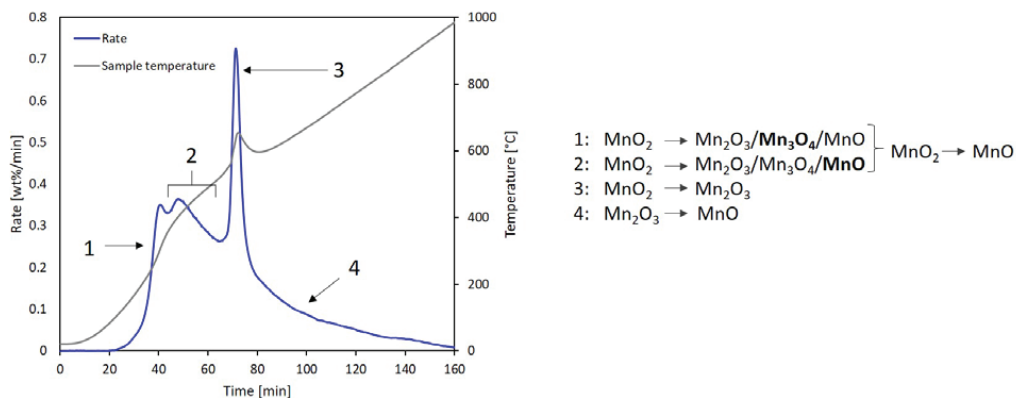
Figure 5.2: Reaction steps observed during non-isothermal (6°C/min) reduction of Comilog ore (11.20-15.00 mm) in 50%CO-50%CO2. Oxide marked in bold represents main reaction product

Fully reduced samples were found to be 97% manganosite, where the remaining 3% was attributed to quartz(SiO_2), kalsillite($KAlSiO_4$), and galaxite($MnAl_2O_4$). Excluding kalsillite, these are the same phases reported by Ishak in fully reduced precalcined Comilog ore[34]. The rapid decomposition/reduction of MnO_2 resulting in a large exothermic peak in temperature has also been observed previously for Comilog ore, both by Tangstad[21] and Ksiazek[113]. The latter observed a decline in thermal diffusivity in Comilog ore at this temperature range, which was credited to the reduction of MnO_2 to Mn_2O_3[113]. This behavior is observed to be typical for MnO_2 ores, where Tangstad observed the rapid reduction to be initiated at 80°C higher temperature in Groote Eylandt (BHP) ore compared to Comilog. This may be due to the lower thermal diffusivity of Groote Eylandt ore compared to Comilog ore, as reported by Ksiazek, who further stated that the thermal diffusivity was mainly dependent on mineralogy and particle size[30].

Comilog ore was observed to exhibit large variations in microstructure, where each particle was composed of several different minerals. The phase regions were small, and few clear phase boundaries were observed in the majority of the particles. This was also observed by Simon et al, who showed the distribution of lithiophorite, pyrolusite, and cryptomelane and hollandite in various samples in different size fractions of Comilog ore[114]. Large variations were also observed during investigation of microstructure in partially or fully non-isothermally reduced samples in this study. Common for all was however the lack of a visual reaction front. In contrast to the non-isothermal reduction products, a reaction front was observed in several of the particles subjected to isothermal reduction. It is possible that some Comilog ore particles reduce through a shrinking core mechanism, despite the majority obeying a different mechanism. However, the

particles appeared to initially be of similar type as the investigated particles from non-isothermal experiments which did not display the formation of a product layer. It has been observed by several other researchers that the reduction kinetics are highly affected by the pretreatment of the ore[32], [34], [48]. As such, it is possible that the rapid heating of the particles, which the particles are subjected to through the isothermal setup, causes alterations to the pore structure of the particles, which leads to additional diffusion resistance. The longer holding time may also have this effect.

Available literature on microstructure development during reduction of manganese ores is scarce, and the literature is generally on ores subjected to pretreatment prior to reduction. Through the investigation of precalcined Comilog ore (MnO_2 oxides decomposed to Mn_3O_4), reduced isothermally at 900-1100°C in CO-atmosphere, Ishak[34] observed varying microstructure development in particles that had been subjected to similar conditions. Some particles obtained a full reduction to MnO, whereas other remained unreduced, i.e. as Mn_3O_4. In the partially reduced samples, some particles showed an unreacted core of Mn_3O_4, whereas other showed the unreacted Mn_3O_4 dispersed throughout the structure or contained in the outer regions. Hence, the observations made by Ishak correlates to the observations in this study, which also showed varying microstructures and no specific trend in the distribution of phases. Ishak further reported that the reduction was highly dependent on the pretreatment of the material, where a considerably faster reaction rate was observed when the ore was prereduced to Mn_3O_4 compared to precalcined to Mn_3O_4. It was found that the surface area of the prereduced sample was 14.13 m^2/g compared to 0.71 m^2/g in the precalcined sample. Similar trends were observed for the porosities. As such, it is clear that the precalcination causes alterations to the microstructure, which could imply that the observations are not comparable to the particles investigated in this study. However, as a shrinking core mechanism was not observed in the precalcined samples by Ishak, it is highly unlikely that this would be observed in untreated material, as the diffusional resistance should be larger in the precalcined material.

5.1.2 Nchwaning ore

Nchwaning ore is largely composed of Mn_2O_3-oxides, which were found to be bixbyite (($Mn,Fe)_2O_3$), braunite (Mn_7SiO_{12}), and braunite II($CaMn_{14}SiO_{24}$). In addition, considerable amounts of hematite(Fe_2O_3) and smaller amounts of calcite($CaCO_3$) is present. The theoretical prereduction of Nchwaning ore in gaseous atmosphere involves the reduction of trivalent Mn-oxides to MnO, the reduction of hematite to metallic iron, and the decomposition of carbonates. The reaction rate curves displayed several peaks, implying that the reaction proceeds through several steps. Generally, the reduction of smaller particles (< 4.00 mm) proceeded through two main steps, where peak positions were at 550°C and 750-800°C. The initial peak was less profound with increasing particle size and decreasing CO-concentration. The occurrence of a small additional reaction step was indicated at temperature range 800-900°C, deduced from a change in the reaction rate. Larger particles (> 11.20 mm) also displayed two main stages in the reaction rate, characterized by a slow rate in the initial stages, and a faster rate with increasing temperature. The maximum obtained rate for these particles was observed at temperatures close to 800°C. As for the smaller sized particles, the reaction rate behavior also indicated a small additional reaction step at temperatures close to 900°C.

The reduction of Mn_2O_3-oxides to MnO may proceed through the stable intermediate oxide phase hausmannite (Mn_3O_4). However, in this study the trivalent manganese oxides were found to reduce to manganosite in a single step. Partially reduced samples, which according to chemical analysis obtained a reduction of manganese oxides in range 14-100%, did not contain any hausmannite according to XRD investigations. Hence, the reduction of hausmannite to manganosite is rapid, where any formed hausmannite quickly proceeds to manganosite upon formation. This agrees with the observations made by Berg and Olsen, who found bixbyite and manganosite to be the main constituting oxides during isothermal reduction of Nchwaning ore at temperatures 700-1100°C[36]. Only minor concentrations of hausmannite were detected. The reduction of hematite subsided with the formation of wüstite at the conditions evaluated in this study. Furthermore, hematite and wüstite were the only detected oxidation states of iron at the evaluated experimental conditions, according to the observations by XRD and SEM. As such, the prereduction of Nchwaning ore is described by the reduction of trivalent oxides to manganosite, the reduction of hematite to wüstite, and the decomposition of calcite.

For smaller particle sizes it was found that the reduction of manganese oxides was initiated at a lower temperature than the reduction of hematite. Further, the manganese oxides were found to obtain a full reduction to MnO while iron oxides remained unreduced (relative to FeO). This was deduced from comparison of the weight loss and chemical analysis of experiments terminated early and late in the reduction course, respectively, i.e. at low and high weight loss. Nonetheless, the reduction of manganese and iron oxides proceeded at highly overlapping temperature ranges. The reaction steps have been marked in Figure 5.3 for size fraction 3.33-4.00 mm heated at 6°C/min in 50%CO-50%CO_2 at temperature range 25-1000°C. As previously mentioned, small extents of carbon deposition were observed, of which the peak attributed to this have been marked in the figure. The reduction of larger sized particles (> 11.20 mm) showed relatively similar trends, however the initial peak was less profound. For these particles, the weight loss showed a relatively linear correlation with the changing MnOx, implying that the reduction of manganese and iron oxides likely proceed simultaneously with increasing temperature. The decomposition of calcite occurred at temperature range 850-1000°C for all particle sizes. As the content of carbonates is relatively low, the weight loss attributed to the decomposition is also fairly low, however a change in the weight loss rate was observed at this temperature range at all conditions. It was also confirmed by chemical analysis, which showed that the carbonates remained at 800°C and had been decomposed at 1000°C.

SEM/EDS investigations of partially reduced samples showed no indications of a topochemical reaction mechanism. The reduction appeared to occur throughout the samples in both isothermal and non-isothermal temperature regimes. Furthermore, the observed structures, and analysed compositions by EDS, showed high correlation to those observed in the particles prior to reduction, implying that no developing phase regions were observed. This supports that the reduction is occurring throughout the particle.
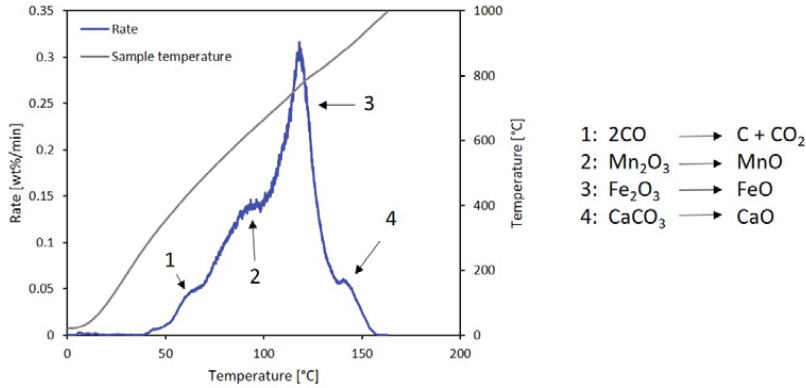
Figure 5.3: Reaction steps observed during non-isothermal (6°C/min) reduction of Nchwaning ore (11.20-15.00 mm) in 50%CO-50%CO₂. The reduction of manganese and iron oxides proceed at highly overlapping temperature ranges, so the full size of the peak is not attributed to the single marked reaction step. Rather, it shows that the reduction of manganese oxides is initiated prior to the iron oxide reduction

5.2 Reaction rates

The prereduction behavior of manganese ores have a large impact on the energy consumption and the off-gas characteristics of a ferromanganese furnace. This is largely attributed to the occurrence of the Boudouard reaction, which will proceed at temperatures exceeding 800°C in the industrial furnace. The CO_2 that is released from the ore at temperatures exceeding 800°C will be a reactant in the Boudouard reaction ($C + CO_2 = 2CO$), which is highly endothermic and produces $CO(g)$. Industrial manganese ores have been found to have varying ore chemistry and mineralogy. This was shown in the previous section for Comilog- and Nchwaning-ore. Furthermore, different ore types have also been found to have differing physical characteristics, such as mechanical strength and porosity. Due to these differences, the prereduction behavior is different for dissimilar ores. To evaluate the effect of the ore prereduction on the energy efficiency and the off-gas characteristics, it is important to know how the ores respond to the varying conditions that it may be exposed to in the industrial furnace. This section presents an evaluation of the experimental reaction rates, where the quantitative effect of the investigated parameters is discussed and analysed.

The non-isothermal reduction data is described by equation 5.1 with a reasonably well agreement. dX/dT is the non-isothermal reaction rate, k is the Arrhenius rate constant, X is the conversion (reduction) degree, p_{CO} is the partial pressure of CO, and r_p is the average particle size.

$$\frac{dX}{dT} = k(T(t)) \cdot (1 - X) \cdot p_{CO}^m \cdot r_p^n \qquad 5.1$$

158

The values in equation 5.1 valid for Comilog- and Nchwaning-ore have been summarized in Table 5.1. The experimental time and temperature values were utilized to find the best bit of the model. While the dependency on average particle size and partial pressure of CO was determined from the apparent rate constants, the activation energy and frequency factor were found through simultaneous model-fitting utilizing all obtained TGA data. For the model-fitting, 17 Comilog experiments and 14 Nchwaning experiments were used.

Table 5.1: Values used for modelling of the reduction of Comilog and Nchwaning ore, respectively, according to equation 5.1

	Description	Comilog	Nchwaning
k_0	Frequency factor	0.53 cm/atm·min	60.4 cm/atm·min
Ea	Activation energy	16.9 kJ/mol	62.6 kJ/mol
m (in p_{CO}^m)	Order of partial pressure	0.7	1.5
n (in r_p^n)	Order of particle size	-1	-1

The experimental data is presented together with the model data for Comilog ore at the various experimental conditions in Figure 5.4. The curves include four different particle size fractions in range 0.50-40.00 mm, CO-concentrations in range 30-80% in CO-CO$_2$ atmosphere, and heating rates between 3-9°C/min. The obtained model results are presented together with the experimental data for Nchwaning ore in Figure 5.5. The curves include four different particle size fractions in range 0.50-40.00 mm, CO-concentrations in range 30-80% in CO-CO$_2$ atmosphere, and heating rates between 3-6°C/min. A comparison of the reaction rates of the experiments and model are presented for both ores in appendix E.
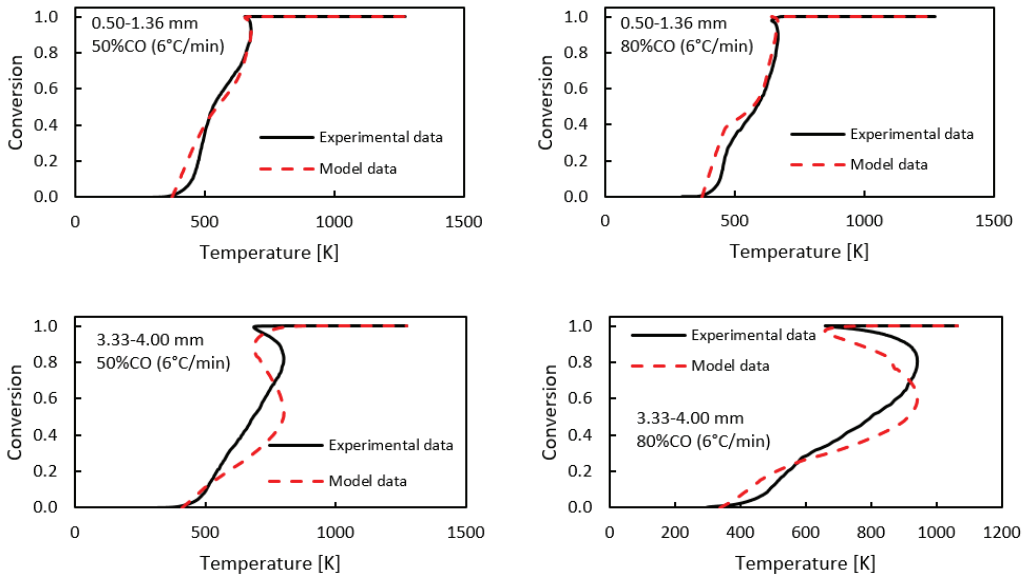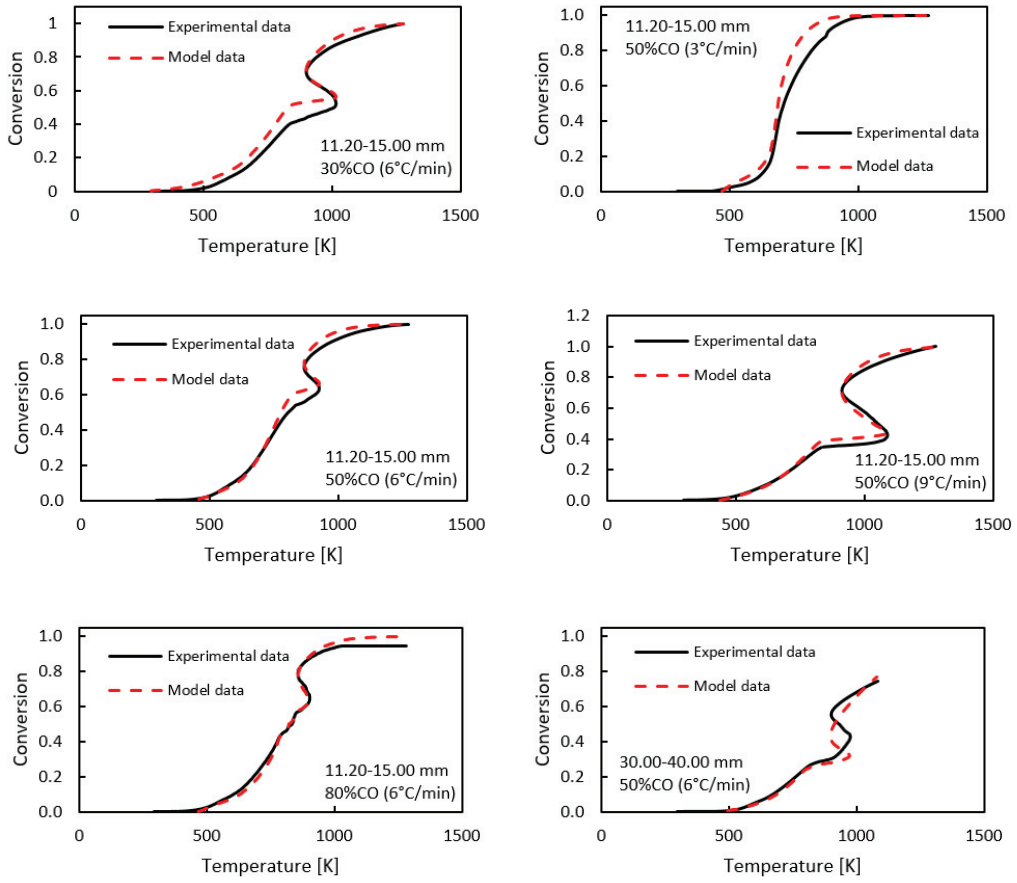
Figure 5.4: Experimental data and model data for Comilog ore, where the experiment conditions are marked in each figure
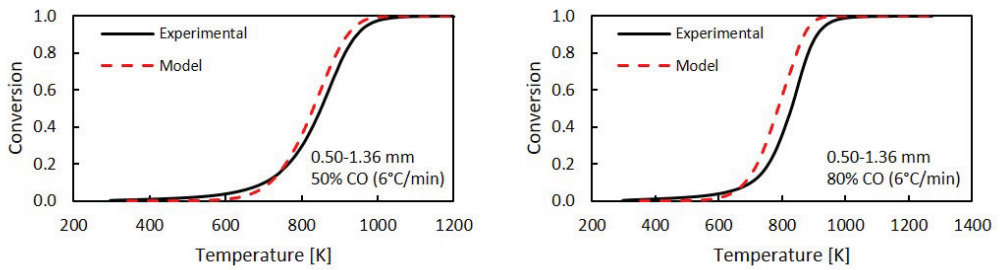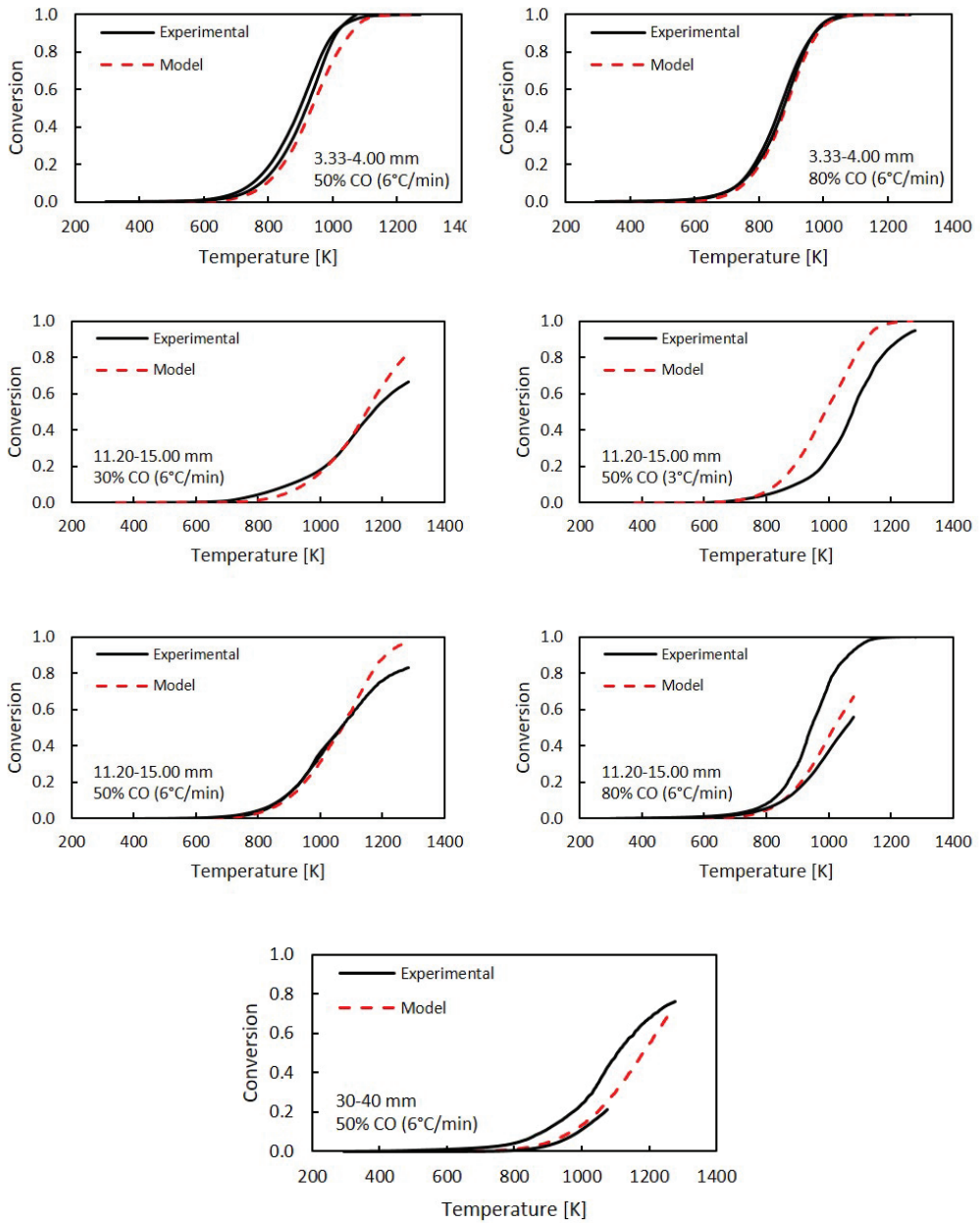
Figure 5.5: Experimental data and model data for Nchwaning ore, where the experiment conditions are marked in each figure

Temperature dependency

The activation energy and the frequency factor were obtained by simultaneous model-fitting of the thermogravimetric data, including various particle sizes, heating rates and CO-concentrations. The activation energy obtained for Comilog ore was 16.9 kJ/mol, whereas 62.6 kJ/mol was found for Nchwaning ore. The activation energy is a measure of the temperature sensitivity of a reaction. As such, the obtained values indicate that the reduction of Nchwaning ore is more dependent on the temperature compared to Comilog. The experimental results showed that the reduction of Nchwaning was initiated at a higher temperature compared to Comilog, which correlates with the higher activation energy. The effect of the activation energy on the reaction rates should be viewed together with the temperature range at which the reaction is occurring. The reduction of 11.2-15.0 mm Comilog particles was initiated at approximately 200-250°C. With an activation energy of 16.9 kJ/mol, the reaction rate is increased by a factor of 1.4 when the temperature is increased from 250°C to 300°C, if not considering the reduced amount of material. The experimental reaction rate obtained for 11.2-15.0 mm particles reduced in 50%CO showed an increase in the reaction rate of factor 1.7 when the temperature was increased from 250°C to 300°C, which shows high agreement with the model increase. The reduction of 11.2-15.0 mm particles of Nchwaning ore was initiated at 600-650°C. With a temperature increased from 650°C to 700°C, the reaction rate is increased by a factor of 1.5 with an activation energy of 62.6 kJ/mol. The experimental reaction rate curves obtained for the reduction of 11.2-15.0 mm particles reduced in 50%CO-50%CO$_2$ (6°C/min at 25-1000°C) showed that the rate increased by a factor of 1.7 at the mentioned temperature increase. This confirms that the obtained activation energies describe the temperature dependency that was observed in the experimental data obtained in this study.

The amount of representative data found in literature for the activation energies for the reduction of manganese ores is scarce. The majority of the reduction studies performed on manganese ore have focused on the reduction of Mn$_3$O$_4$ to MnO, implying that the ores were precalcined. In addition, some values have been reported for synthetic oxides or calcined ore heated in hydrogen or argon atmosphere, or with the use of solid carbon as reductant. Furthermore, several of the studies report a large variation in the presented activation energies. Ishak[34] reported values between 12-230 kJ/mol for the reduction of Mn$_3$O$_4$ to MnO in calcined Comilog ore. El-Geassy et al.[57] investigated the reduction of MnO$_2$ in a Baharia iron ore, and reported an activation energy of 9.6 kJ/mol in the initial stages of the reduction, whereas 36.4 kJ/mol was found for the later stages. Furthermore, De Bruijn et al.[33] reported an activation energy of 79 kJ/mol for the initial reduction step observed for a calcined unspecified MnO$_2$ ore in hydrogen atmosphere at 275-400°C. Berg[14] reported an activation energy of 41 kJ/mol for the reduction of braunite in calcined Nchwaning ore, and further 50-70 kJ/mol for the reduction of braunite in a Namibian ore. The calculated activation energies presented in previous literature are thus of similar magnitude as the ones obtained in this study. It is evident that the activation energy varies with the investigated material and/or experimental conditions.

Particle size

The TGA curves showed that the reduction of Comilog and Nchwaning ore was affected by the ore particle size. Four different particle sizes were evaluated in 50% CO, whereas the three smaller size fractions were evaluated in 80% CO for both ores. The effect of the average particle size fraction was estimated by evaluating the apparent frequency factors as a function of particle size.

Apparent rate constants assuming the rate is merely described by the rate constant and the extent of reduction was calculated according to 5.2. The standard form of the non-isothermal rate law includes the heating rate, as it is generally applied to linear temperature programs. In the present case, the heating rate was included in the temperature integral, as the actual temperature varies with the reaction. As such, the equation and calculation procedure is similar to that described by Vyazovkin[93]. The temperature integral was estimated by the trapezoidal method at each given step size. As such, the full equation that was utilized to calculate apparent rate constants is as given in equation 5.3. This specific form of the equation was used to account for the time dependency of the temperature in the Arrhenius constant.

$$\frac{dX}{dT} = k_{app}(T) \cdot (1 - X) \tag{5.2}$$

$$g(X) = -\ln(1 - X) = \int_{t_1}^{t_2} k_{app}\, dt = k_{0,app} \cdot \int_{t_X}^{t_{X+\Delta X}} \exp\left(-E_a/RT(t)\right) dt \tag{5.3}$$

For Comilog ore in particle size > 11.20 mm, the reduction data prior to the exothermic peak was utilized, whereas for smaller particle sizes the whole reduction curve was utilized. The reaction rate profiles showed that the reduction of smaller particle sizes of Nchwaning ore displayed two distinct peaks corresponding to two distinct reaction steps. The steps were not fully separated, but rather occurred at largely overlapping temperature ranges. At larger particle sizes, the reaction rate did not display well separated reaction steps, however a linear correlation was obtained between the weight loss and the oxidation level of manganese. This implies that the reaction rate curves for larger sizes represent the conversion of manganese oxides in Nchwaning. A variance was observed between the reduction curves obtained at similar conditions for Nchwaning ore. As such, the apparent rate constants were estimated for all parallels. The apparent rate constant includes the effect of particle size and CO partial pressure according to equation 5.4. As such, the constant n was found from the slope in $\ln(k_{0,app})$ vs $\ln(r_p)$.

$$k_{app} = k_0^* \cdot e^{-E_a/R \cdot T} = k_0 \cdot p_{CO}^m \cdot r_p^n \cdot e^{-E_a/R \cdot T} \tag{5.4}$$

The effect of the average particle size fraction for Comilog ore is deduced from the slopes of the linear regressions presented in Figure 5.7. The reaction rate of Comilog ore is found to be proportional to the inverse particle size, i.e. rate α $(1/r_p)$. A high correlation between the behavior in 50% CO and 80% CO is seen, where both give a slope of approximately -1, which implies that the factor n in equation 5.3 is -1. The

accuracy of the fit is relatively high in both cases. The main contribution to the deviation of the linear regression is found for the smaller particle sizes, either for size 0.50-1.36 mm or 3.33-4.00 mm, which shows a negative and positive deviation, respectively. It is possible that the size distribution of the smallest particle size does not follow a normal distribution. There may potentially also be some differences in heat losses. The largest deviation between the experimental and modelled conversion curves was found for particle size 3.33-4.00 mm, as was shown in Figure 5.4. This is likely related to the deviation observed for the average particle size dependency.
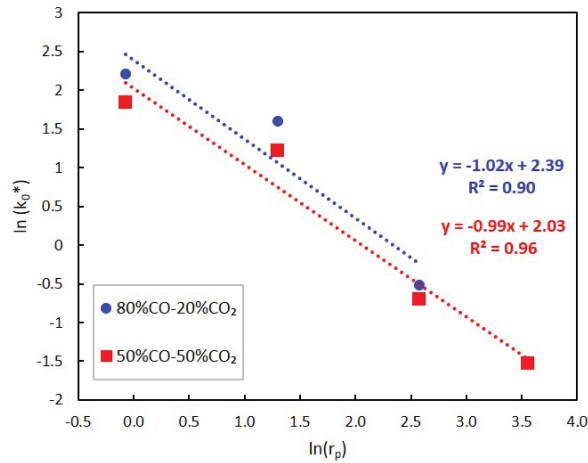
Figure 5.6: ln($k_{0,app}$) vs ln(r_p), where r_p is the particle size, for Comilog ore. Relation between reaction rate and particle size is deduced from the slope, where the slope is constant n in r_p^n

The dependency of Nchwaning ore is more uncertain due to the larger variation between parallels. The results are shown in Figure 5.7, where the data from all parallels have been included in the figure to the left. In the figure to the right, the data from experiment conducted with 30-40 mm particles in 50%CO terminated at 1000°C have been excluded from the linear regression. It is believed that the reduction data obtained at the experiment terminated at 800°C was more representative, as it was observed that these particles remained intact in the original particle size throughout the experiment, whereas the sample terminated at 1000°C had been subjected to severe decrepitation. As such, the values obtained in 80%CO shows a slope of -0.75, whereas the data obtained in 50%CO shows a slope of -1. As the regression in the former is obtained from three particle sizes, whereas the latter is obtained from four, it is believed that the data from 50% CO is more accurate. Thus, it is found that the reaction rate of Nchwaning ore is proportional to the inverse particle size, i.e. rate α (1/r_p). Similar as for Comilog ore, it is observed that the largest deviation from the regression is obtained for the two smallest particle sizes.
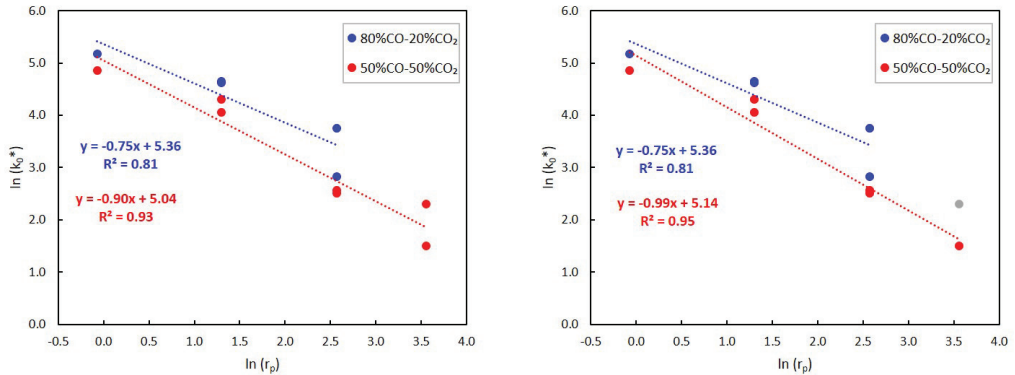
Figure 5.7: $ln(k_{0,app})$ vs $ln(r_p)$, where r_p is the particle size, for Nchwaning ore. Left: all values have been included in linear regression. Right: Data from 30-40 mm particles reduced in 50%CO terminated at 1000°C is not included in regression. Relation between reaction rate and particle size is deduced from the slope, where the slope is constant n in r_p^n

According to gas-solid reaction theory for topochemical reactions, a reaction rate proportional to ($1/r_p$) describes chemical reaction control, whereas a rate proportional to ($1/r_p^2$) is valid for diffusion control. This indicates that the reduction of both Comilog and Nchwaning ore follows a chemical reaction controlled mechanism. However, this relation is valid for the effect of the reaction area for ideal solid samples, which has no initial porosity. Furthermore, in the case of reduction of highly oxidized manganese ores, several other aspects may be incorporated in a changing particle size. Highly oxidized ores may be subjected to extensive decrepitation during heating in reducing atmosphere. Hence, the effective particle size may vary throughout the reduction course, where larger particles may be more likely to decrepitate compared to smaller particles[115]. Disintegration is further discussed in a separate chapter. Furthermore, it is likely that a changing particle size affects the heat transfer, and thus temperature development, of the particle cluster. A decreasing particle size will increase the contact area, hence promoting heat transfer between the particles, as well as between particles and ambient. It may also introduce larger temperature gradients within a single particle. A changing temperature gradient in both single particles and clusters of varying particle sizes were shown by Ksiazek[113]. It is hence suggested that the obtained relation between the average particle size and the reaction rate should not be viewed as a relation between the surface reaction area and the reaction rate, but rather an average dependency on geometrical effects.

Few representative studies covering the effect of particle size on the prereduction of industrial manganese ores were found. The available studies generally agree that a decreasing particle size promotes the reduction extent, however the effect is yet to be quantified according to the author's knowledge. Pochart et al. compared the oxidation level (x in MnOx) obtained at 1100°C for Comilog, BHP, and Nchwaning ore after reduction in CO-CO2 atmosphere[20]. A lower oxidation level was found with decreasing particle size for all three ores. The effect on the reduction rate was not quantified, however the decrease in the O/Mn ratio when decreasing the particle size was highly similar for Comilog and Nchwaning ore. As such, the results presented by Pochart et al. agrees with the findings in this study. Biørnstad[115] also obtained a lower oxidation level in particle size 3.35-6.7 mm compared to 10.0-13.2 mm when reducing Comilog and Nchwaning ore at 6°C/min in 70%CO-30%CO2. Ishak observed an effect of particle size (2.4-4.8 mm vs

6.7-9.5 mm) during the reduction of precalcined (decomposing all manganese oxides to Mn_3O_4) Comilog ore[34]. The experiments were conducted at fairly high temperatures, i.e. 900-1100°C, in CO-CO_2 atmosphere. A slightly increased rate was observed with decreasing particle size at 900-1000°C, however no effect was observed at 1100°C. Berg observed the formation of a product layer in precalcined reduced Nchwaning and BHP ore, which implies that the particle radius affects the kinetics[14]. Due to the ore being precalcined, as well as the high temperatures evaluated, the observations by Ishak and Berg may not be directly comparable to the results in this study. Another study on precalcined ore was presented by Gao[38], who observed no effect of decreasing particle size. However the sizes compared were all small and within range of what is considered as fine, i.e from < 45 μm to 500-1000 μm.

Gas composition

The TGA curves indicated that the reduction was affected by the CO-concentration in the CO-CO_2 atmosphere. The extent at which the reaction rate was affected was quantified in a similar manner as the average particle size. The results are shown in Figure 5.8, where the dependency is obtained from the slope of the linear regressions. While merely two partial pressures of CO were evaluated for the two smaller particles sizes, the relation for these have also been included for comparison. Four and three different partial pressures were evaluated for particle size 11.20-15.00 mm for Comilog and Nchwaning ore, respectively. The reduction rate of Comilog ore appear to be proportional to the CO partial pressure by an order of 0.7. It is observed that the two smaller particles sizes show dependencies of 0.77 and 0.78, respectively, which correlates well with that obtained for 11.20-15.00 mm. A larger effect is observed for Nchwaning ore, where the data obtained for 11.20-15.00 mm particles shows a slope of 1.5, i.e. that the reaction rate is proportional to the partial pressure of CO to the power of 1.5. It may be noted that the variation between the two parallels obtained at 80%CO is relatively large. If the regression is based on the data obtained from the experiment terminated at 800°C, the reaction rate would be proportional to the partial pressure. Similarly, if the data obtained at 1000°C is used, the slope is 2.0. A lower dependency is observed for the two smaller particle sizes, however as these are only based on two data points, a linear regression is not valid.
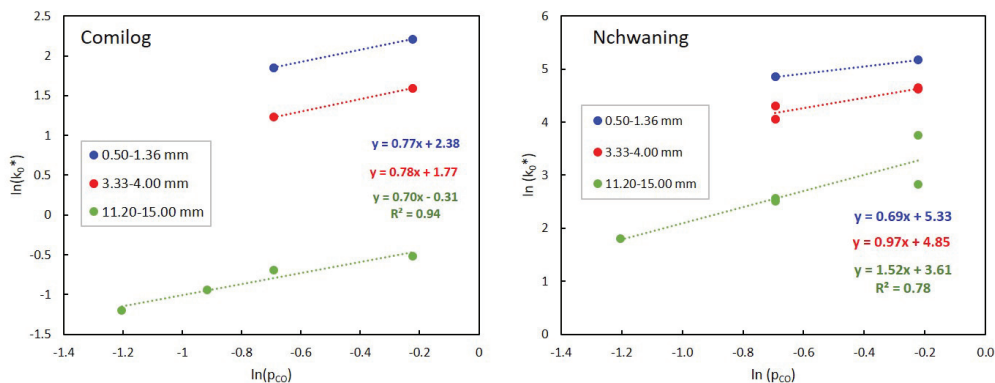
Figure 5.8: Intercepts from Arrhenius plot as a function of CO-concentration for Comilog ore (left)) and Nchwaning ore (right)

The effect of CO has been investigated by previous researchers, both through non-isothermal experiments[21], [56] and isothermal reduction of precalcined samples[14], [38]. The isothermal studies presented by Berg[14] and Gao[38] both showed an increasing reaction rate with increasing concentration of CO. The former investigated precalcined BHP-, Nchwaning-, and Namibian-ore. The latter utilized a precalcined manganese ore of unknown origin, where the rate was found to be proportional to the CO partial pressure. The increased reduction rate with increasing CO-concentration may be due to a lower oxygen pressure, however it may also be related to the increased specific gas flow (L/min) of CO. According to the non-isothermal studies presented by Tangstad[21] and Ngoy[56], the component gas flow had a larger effect than the partial pressures during non-isothermal reduction of Comilog and Nchwaning ore. The experimental set ups used in these investigations were highly similar to that of this work. Tangstad observed the reduction rate to be unaffected by the presence of CO_2 up to 30% in CO-CO_2 atmosphere, whereas Ngoy et al. obtained a highly similar reaction rate when evaluating 70%CO-30%CO_2 and 50%CO-50%CO_2. In both studies, the gas flow of CO was constant at 2 L/min, and the composition was varied through the gas flow of CO_2. In the work presented by Tangstad, the presented normalized weight reduction curves showed a nearly full overlap for atmospheres of 100% CO and 70%CO-30%CO_2. It was observed that in the case of Nchwaning ore, the former experiment resulted in a weight loss of 5.6 wt%, whereas the latter obtained a weight loss of 10.1 wt%. This may suggest that the samples that were reduced may not be directly comparable through a normalized weight loss behavior. In the case of Comilog ore, it is suggested that the CO gas flow of 2 L/min was insufficient, resulting in the highly similar rate. The work reported by Tangstad utilized Comilog and Nchwaning ore in similar particle size as this study, however the sample size was 2.5-3.0 times larger. In addition, a heating rate of 9°C/min was used, compared to 6°C/min in this study. Both of these parameters result in a higher CO-consumption at a given time and temperature. Ngoy introduced the reducing atmosphere at 500°C, which is a considerably higher temperature compared to the temperature at which reduction was seen to be initiated in this study, i.e. 200°C. As such, the reduction is expected to proceed rapidly in the initial stages, potentially consuming all available CO(g). This was confirmed by the off-gas analysis, which showed that after the reducing gas was introduced, the recorded %CO in the off-gas was 0 during the first 5 minutes. During this stage, the weight reduction indicated that 50% of the total reduction had occurred. Thus, the input amount of CO(g) was clearly a limiting factor of the reaction rate. Hence, it is believed that the lack of observed effect of CO-concentration in CO-CO_2 atmosphere during reduction of Comilog and Nchwaning ore in the non-isothermal studies presented by Tangstad and Ngoy, respectively, is mainly due to insufficient supply of CO, as well as non-representative samples.

The reduction of manganese ores with varying CO gas flow has been reported previously. Berg[14] evaluated the effect of gas flow in the investigation of precalcined BHP-, Nchwaning- and Namibian-ore. No correlation between the gas flow and the reaction rate was observed, where a gas flow of 4 L/min and 3 L/min correlated to the slowest and fastest reduction, respectively, for precalcined BHP particles (0.45-0.51 cm). As such, the natural variance between the experimental runs due to inhomogeneity of the ore was larger than the potential effect of varying gas flow rate. In addition, Berg evaluated single particles, which implies that the amount of CO required for reduction is fairly low, and most likely achieved by all gas flows that were evaluated. When investigating the reduction of precalcined Comilog ore, Ishak reported an insignificant effect of increasing the CO gas flow from 3 L/min to 6 L/min at temperatures 900-1000°C[34]. The off-gas recordings for the various experiments in this study showed that the CO was present in the off-gas throughout the experiments, indicating that the CO input gas flow was sufficient, thus not limiting the

reaction rate. It is mentioned that Ishak had precalcined the Comilog ore, decomposing all manganese oxides to Mn_3O_4, which results in a lower CO required to complete the reduction.

The feed of CO in the present study may be observed in Figure 5.9 for Comilog ore. The sample reduced in 30%CO-70%CO₂ (CO gas flow = 1.2 L/min) shows the lowest obtained CO-concentration, which is observed in relation to the rapid reduction of MnO_2 at 580°C, where the CO level is 1.5% in the off-gas at peak position. However, as the rate decreases rapidly, it is likely that this did not limit the rate. Furthermore, this minimum of CO-concentration occurs at the rapid decomposition step, which was not observed to be significantly affected by the CO/CO_2 ratio. As such, it is concluded that the increased reaction rate observed for increasing CO/CO_2 ratios observed in this study is due to an increased partial pressure of CO, and not by an increased CO flow. The reaction is promoted by the increased CO partial pressure due to the decreased oxygen pressure, which introduces a larger driving force for the reduction. From the curves shown in Figure 5.9, it is clear that the CO/CO_2 ratio is affected by the ongoing reduction. As such, it may be argued that the CO-concentration that the ore is exposed to throughout the reduction will vary. For Nchwaning ore, it is a fair approximation that the gas composition remains constant, as the lower oxidation level and slower reaction rate does not result in large changes in the CO-concentration in the bulk phase.
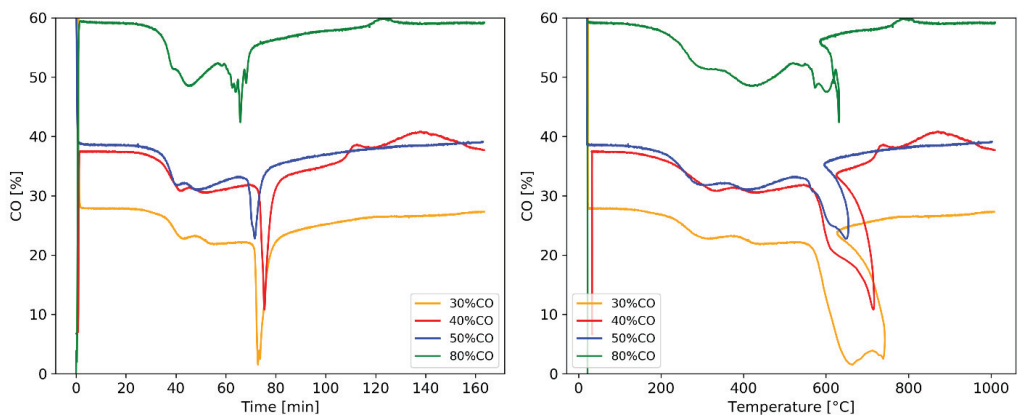
Figure 5.9: CO-concentrations as analyzed by off-gas analyzer during reduction of Comilog ore in CO-CO₂ atmosphere at various CO-concentrations

The off-gas composition showed that the CO_2-concentrations decreased below set point values at temperatures exceeding 800°C for several of the experiments conducted with Nchwaning ore. As all reactions related to the reduction of Nchwaning ore, i.e. Mn-oxide reduction, Fe-oxide reduction and carbonate decomposition, all correlate to an increase in CO_2, it was concluded that the "negative" CO_2 was due to the Boudouard reaction ($C + CO_2 = 2CO$). The reaction was left shifted at temperatures 400-800°C, resulting in an increased CO_2 and weight due to carbon deposition. When the temperature reached approximately 800°C, the reaction was observed to be shifted to the right, implying that the deposited carbon reacted with CO_2 in the gas to form CO. As the only available source of carbon in the system was the carbon deposited at low temperatures, the extent of left and right shifted Boudouard reaction was

directly related. The extent of carbon deposition was affected by the CO-concentration in the atmosphere, and the rate decreased as the CO was consumed by the ore reduction. Furthermore, it was indicated that the extent of carbon deposition varied with the particle size of the ore, where a decreasing particle size correlated to an increased amount of carbon deposition. This correlates to the increasing surface area with decreasing particle size. As such, in CO-CO_2 atmosphere, the largest amount of carbon deposition was observed for particle size 0.50-1.36 mm reduced in 80%CO-20%CO_2. As the weight reduction curves were constructed from the changing CO_2 concentration in the off-gas, the left shifted Boudouard reaction will result in an apparent weight reduction which is larger than that attributed to the ore reduction. Nonetheless, the estimated amount of deposited carbon was merely 0.4 g, which is not believed to have a large effect on the reaction rates. The Boudouard reaction was observed to occur to a low extent in the experiments with Comilog ore. This is likely due to that the reduction of Comilog ore is initiated at temperatures lower than the left shifted Boudouard reaction, which decreases the available concentration of CO. This is supported by the reduction data observed for particle size 0.50-1.36 mm (as shown in Figure 3.21), where the reduction of the ore was completed at temperatures below 400°C, and the carbon deposition was initiated at approximately 430°C. The temperatures at which the left and right shifted Boudouard reaction, respectively, were initiated were highly similar to those observed when Comilog ore or quartz was the sample material. It is well known that the Boudouard reaction is catalyzed by the presence of iron, mainly in metallic state, however also in the form of oxides. These results indicate that the concentration of iron in Nchwaning ore is not sufficient to affect the kinetics of the Boudouard reaction.

A few experiments were also conducted where hydrogen was introduced to the gas phase. Hydrogen was found to promote the reduction rate of Comilog ore, where a considerably larger reaction rate was observed in the initial stages of reduction. Hydrogen has been found to reduce the ore faster compared to $CO(g)$ by several previous researchers[21], [51], [54], [56]. Two different compositions of CO-CO-H_2 were used, which correlated to the theoretical oxygen pressure obtained in 50%CO-50%CO_2 and 80%CO_2-20%CO_2, respectively. The results showed that the rate was more affected by the presence of hydrogen compared to the oxygen pressure. This was also observed by Ngoy[56] for Comilog ore reduced in CO-CO_2 and CO-CO_2-H_2.

To evaluate whether the water-gas shift reaction was at equilibrium, the hydrogen was also added to the gas mixture as water vapor, i.e. $H_2O(g)$. The gas flow of each component was calculated so that the theoretical oxygen pressure correlated to that of 50%CO-50%CO_2. The weight as a function of time and temperature, respectively, are presented in Figure 5.10 for samples reduced in CO-CO_2, CO-CO_2-H_2, and CO-CO_2-H_2O, where all atmospheres have similar theoretical oxygen pressure. The faster reduction in CO-CO_2-H_2 compared to CO-CO_2 may be explained by the higher reduction potential of hydrogen compared to CO as reducing agent. However, this does not explain the different reduction behavior observed for CO-CO_2-H_2 and CO-CO_2-H_2O. According to the water-gas shift reaction, these two atmospheres give highly similar partial pressures of hydrogen at the evaluated temperature range, as shown in Figure 5.11. This indicates that the water-gas shift reaction is not at equilibrium.
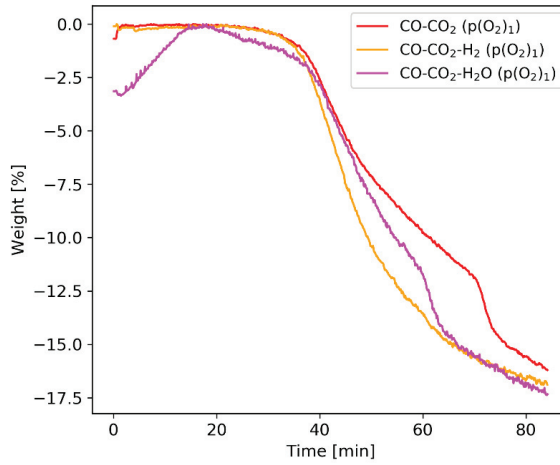
Figure 5.10: Weight as a function of time for gas atmospheres containing CO-CO2, CO-CO2-H2 and CO-CO2-H2O, where the specific compositions correlate to the same theoretical oxygen pressure. It is seen that the reduction behavior is different for all three compositions, indicating that the gas is not at equilibrium
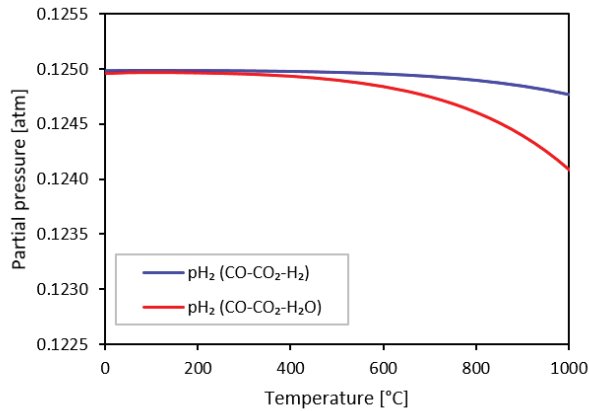
Figure 5.11: Partial pressures of hydrogen in CO-CO2-H2 and CO-CO2-H2O atmosphere according to the water-gas shift reaction. Highly similar hydrogen pressures of both gas mixtures is shown at temperatures 0-1000°C

While it is found that the water-gas shift reaction is not at equilibrium, it is clear that the gas components have reacted to some extent. The weight reduction obtained in CO-CO2-H2O is presented together with two different CO-CO2 atmospheres in Figure 5.12, where the legend indicates the specific gas flow [L/min] of each gas component. According to the legend, the specific gas flow of CO was 2 L/min and 3.2 L/min in the CO-CO2 atmospheres, respectively, whereas the CO-CO2-H2O contained 2.25 L/min CO. Evaluating the weight loss as a function of time shows that the CO-CO2-H2O atmosphere gives a highly similar

behavior as the CO-CO₂ atmosphere conducted with 3.2 L/min CO. As the CO-CO₂-H₂O atmosphere had a CO gas flow of 2.24 L/min, the reduction would be slower if the water-gas shift reaction did not occur.

Similar oxidation levels were obtained utilizing CO-CO₂ and CO-CO₂-H₂ atmospheres of corresponding theoretical oxygen pressures for Nchwaning ore. This is shown in Figure 5.13, which presents the analysed x in MnOx as a function of temperature for CO-CO₂ and CO-CO₂-H₂, where both atmospheres correlates to the oxygen pressure obtained in 50%CO-50%CO₂. The results further indicated a similar trend for atmospheres correlating to the oxygen pressure of 80%CO-20%CO₂. An oxidation level of 1.21 was obtained in CO-CO₂ at 816°C, whereas 1.21 was obtained in CO-CO₂-H₂ at 772°C. This indicates that the obtained reduction rates of the manganese oxides are highly similar. This agrees well with the observations made by Ngoy, who found the reduction of Nchwaning ore to be merely slightly affected by the presence of hydrogen[56].
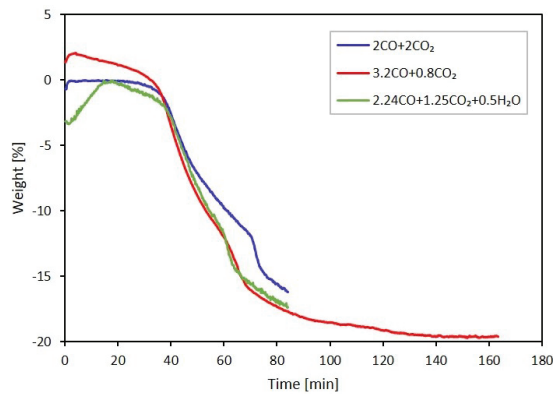
Figure 5.12: Weight as a function of time for Comilog ore reduced in CO-CO₂ and CO-CO₂-H₂O. The legend shows the gas flow [L/min] of each component. The figure shows that the CO-CO₂-H₂O atmosphere shows highly similar weight reduction as a function of time as the CO-CO₂ atmosphere with 3.2 L/min gas flow CO
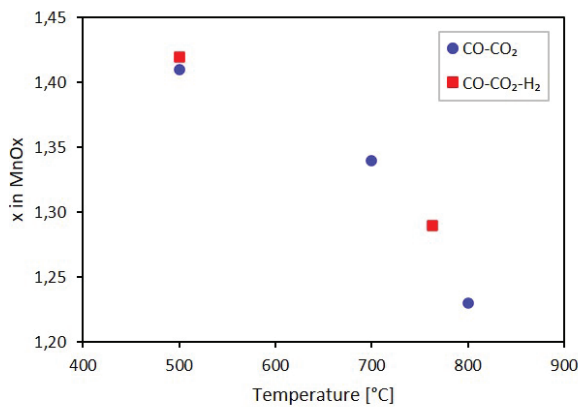
Figure 5.13: x in MnOx as a function of temperature for Nchwaning ore, showing that similar trends are obtained for CO-CO₂ and CO-CO₂-H₂ atmospheres of correlating theoretical oxygen pressure

Correlation to isothermal data

Comilog and Nchwaning ore was reduced isothermally in the Tammann furnace at RWTH Aachen. The data obtained in 50%CO at temperatures 400-600°C and 600-900°C for Comilog ore and Nchwaning ore, respectively, was analysed by the isoconversional method, as well as by conventional model-fitting. Isoconversional methods allows for calculation of the activation energy at a progressive conversion, without requiring the assumption of the governing reaction mechanism. As the calculation is performed at progressive conversion, it may also reveal the occurrence of individual reaction steps. A common procedure utilized to determine the reaction mechanisms for gas-solid reactions is the conventional model-fitting approach. This method involves the fitting of various reaction models to the TGA data, where it is assumed that the relation obtaining the more optimal fit is the governing mechanism. Common reaction models include nucleation and growth, reaction order models, diffusion models, and geometrical contraction model. An overview of the reaction models may be found in the paper presented by Khawam and Flanagan[83].

The activation energies obtained at progressive conversion by the isoconversional method for the isothermal reduction data of Comilog ore are presented in Figure 5.14. The R^2-values indicate a relatively good fit at all conversions. Furthermore, the values may indicate the occurrence of two distinct reaction stages, as a shift is observed at conversion range 0.42-0.46. The initial stage correlate to an average activation energy of 27.8 kJ/mol, whereas the latter stage correlate to 51.3 kJ/mol. This may suggest that the reduction of Comilog ore becomes more temperature sensitive at the latter stages of reduction.
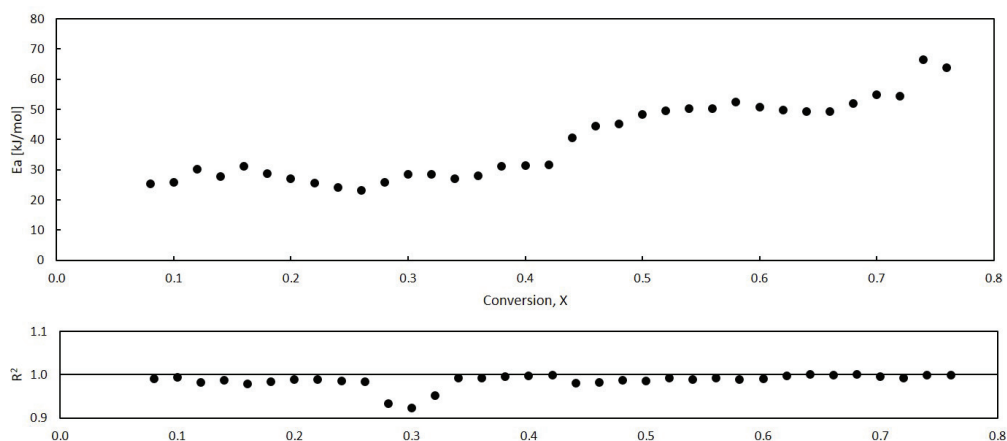
Figure 5.14: Activation energies at progressive conversion calculated by the standard isoconversional method for isothermal reduction of Comilog ore

The activation energies calculated from the isoconversional method for Nchwaning ore are seen in Figure 5.15. The calculations were only possible at conversions up to 50%, as a minimum of three points are required. Furthermore, the average R^2-values in the initial stages (< 20% conversion) were merely 0.61, which implies large uncertainties in the data. An average R^2 value of 0.958 was found for conversion range

20-50% conversion. The activation energy was determined to be 60.0 kJ/mol for conversion range 20-32%, whereas 111.5 kJ/mol was obtained for 34-50% conversion.
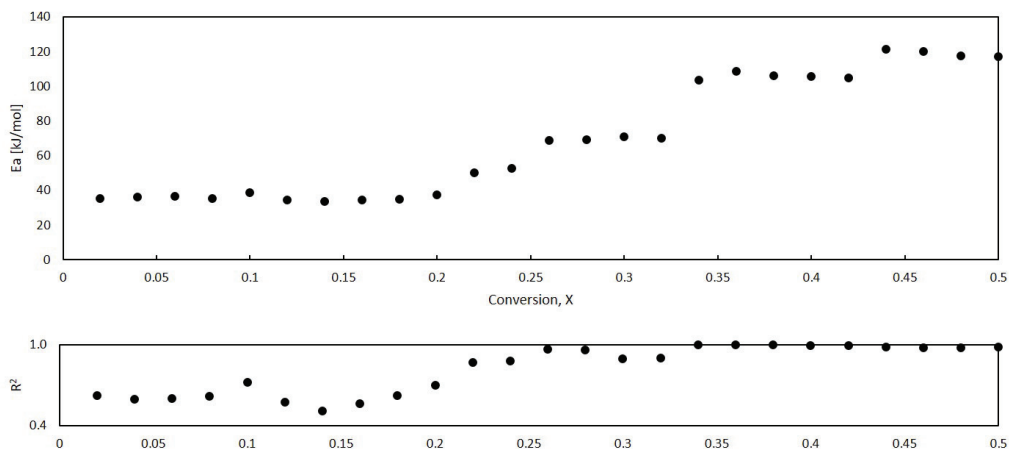
Figure 5.15: Isoconversional calculation of activation energy of isothermal reduction of Nchwaning ore in 50% CO

The activation energies obtained in the initial stages of reduction was found to show a relatively good agreement with the values obtained from the non-isothermal experiments. An activation energy of 27.8 kJ/mol was obtained for Comilog ore at reduction degrees in range 0-40% from the isothermal reduction experiments, whereas 17 kJ/mol was deduced from the non-isothermal data. For Nchwaning ore, 60.0 kJ/mol was found from isothermal reduction at 20-50% reduction degree, whereas 62.6 kJ/mol was obtained from the non-isothermal experiments. For both ores, the isothermal calculations indicated that the activation energy was larger towards the last part of the reduction. It is not known whether this represents the actual change in the reduction, or if it is related to the uncertainties related to the TGA data. It has been shown that artifactual variations in activation energy may be introduced by the calculation methods employed in the isoconversional method[83], [91].

The model-fitting approach was applied to the full conversion range for Comilog ore. In addition, according to the observations made from the isoconversional calculations indicating two potential steps, the conversion up to 42% and exceeding 46%, respectively, were also evaluated separately. The three mechanisms that obtained the highest statistical fit are presented in Table 5.2. According to the results, nucleation and growth kinetics as described by the Avrami Erofe'ev equation obtained the best fit in the initial stages, as well as the full reduction stage evaluated simultaneously. For conversion stage 0.46-0.72, the mechanism of contracting volume obtained the best fit, which is a topochemical mechanism for chemical reaction control. It is however mentioned that the obtained fit were between 0.963-0.999 for all evaluated models at conversion range 0.08-0.42, and 0.973-0.997 for conversion range 0.46-0.72. The model-fitting results for nucleation and growth kinetics are shown in Figure 5.16 for the two evaluated

conversion ranges. According to nucleation and growth theory, the nucleation constant, which describes the dimensions at which the nucleation occur, may be deduced from the slope of the linear regressions in Figure 5.16. It is seen that while there are some deviations at the high conversion range, the slopes may be approximated to 1. The reaction model for nucleation and growth kinetics where the Avrami constant is equal to 1 is shown in equation 5.5, and it may be noted that it is identical to the reaction model of a first order chemical reaction. A more optimal fit was obtained in the conventional model-fitting for nucleation kinetics compared to a first order reaction, as the data of the Avrami equation is evaluated in logarithmic form, which causes the initial values to be weighted less.

$$\frac{dX}{dt} = k_{app} \cdot (1 - X) \qquad\qquad 5.5$$

Table 5.2: R^2 values for model fitting of isothermal experiments for different reaction models for isothermal reduction of Comilog ore in 50% CO

	Mechanism (R^2)		
Fit	X = 0.08-0.42	X = 0.46-0.72	X = 0.08-0.72
Best	Avrami Erofe'ev (0.999)	Contracting volume (0.997)	Avrami Erofe'ev (0.996)
Second	1. order chemical rx. (0.997)	Avrami Erofe'ev (0.991)	1. order chemical rx. (0.994)
Third	Power law (0.997)	3D diffusion (0.990)	Contracting volume (0.991)
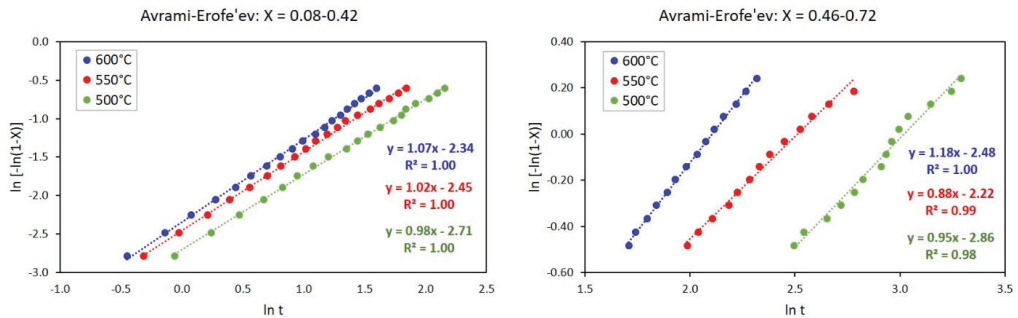
Figure 5.16: ln[-ln(1-X)] vs ln t (Avrami plot) for isothermal reduction of Comilog ore

Conventional model-fitting was also performed for the isothermal reduction data obtained for Nchwaning ore. Several different models were observed to provide similar high degree of linear relation to the data, however all of these indicated that there was a transition stage at conversion 0.74-0.76. The obtained R^2 values for the four models obtaining the best fit at conversion range 0.06-0.74 is shown in Table 5.3. There are some discrepancies between different temperatures, where the data obtained at 700°C did not show a high degree of fit towards any of the evaluated models, whereas the data obtained at 900°C showed R^2 values between 0.993-0.998 for four of the models. The lack of consistency may be due to non-representative data due to small sample size and inhomogeneity of the ore.

174

As was previously stated, the reliability of the isothermal reduction data obtained in this study is not clear, as the data was subjected to fluctuations, and the small sample size implies a potentially large effect of the ore's heterogeneity. Comilog is known to be a relatively homogeneous ore, which may suggest that representative data may be obtained from small sample sizes. Nchwaning ore exhibits a larger degree of heterogeneity, which implies that the data may to larger extent be influenced by the natural variation in the ore. This correlates to the observations made in this section, where a lower consistency was observed for Nchwaning ore.

Table 5.3: Fit (R^2) of experimental data according to various models by conventional isothermal model-fitting approach at conversions below 0.74 for Nchwaning ore

	Avrami	Area contraction	Volume contraction	First order ch. rx.
600°C	0.9930	0.9893	0.9897	0.9904
700°C	0.9267	0.8777	0.8813	0.8884
800°C	0.9615	0.9663	0.9720	0.9795
900°C	0.9991	0.9928	0.9960	0.9979
Average	0.9701	0.9593	0.9598	0.9641

The conventional model-fitting approach indicated that the reduction of Comilog ore was best described by a first order chemical reaction, whereas the results for Nchwaning ore was inconclusive. Nonetheless, it may be argued that the governing mechanism may not be extracted from the isothermal experiments, as several reactions occur simultaneously. Furthermore, the majority of the evaluated reaction models provided highly similar statistical fits with the TGA data, which also indicates that it is not a reliable approach to determine the reaction mechanism.

The model parameters obtained from non-isothermal reduction data (shown in Table 5.1) were used to model the isothermal reduction experiments. The comparison of the model and the experimental curves are shown in Figure 5.17 for Comilog ore. It is seen that the model prediction is consequently lower than the experimental values for all evaluated temperatures throughout the holding time. It is possible that this is related to decrepitation. During the isothermal reduction of Comilog ore, it was observed that the ore started to decrepitate relatively early in the experiment, which implies that the effective particle size was decreased from the initial average of 13.1 mm. The disintegration decreases the effective particle size, which further promotes the reduction rate. Figure 5.18 shows the results of the model where an average particle size of 7 mm was used to model reduction at 400-500°C and 9 mm was used at 550-600°C.

The model curves together with the experimental conversion curves for Nchwaning ore are presented in Figure 5.19. The correlation is observed to be considerably low. The experimental conversion curves were constructed from the recorded weight loss relative to the theoretical weight loss. It is possible that this has provided an increased conversion at a given holding time compared to the actual reduction extent. Nonetheless, due to the heterogeneous nature of Nchwaning ore, the reproducibility of the experiments was low. As such, it is not believed that the conversion curves are representative for the overall reduction behavior.
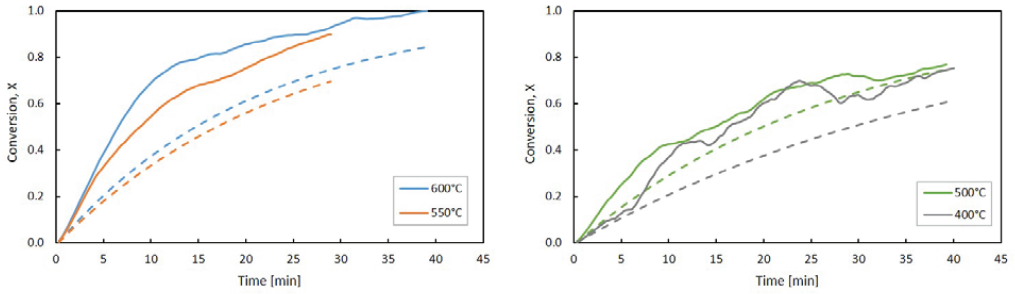
Figure 5.17: Model parameters found from non-isothermal TGA data used to model isothermal reduction data for Comilog ore, given by Table 5.1 for 13.1 mm particles. Model gives lower conversion compared to experimental throughout the experiments
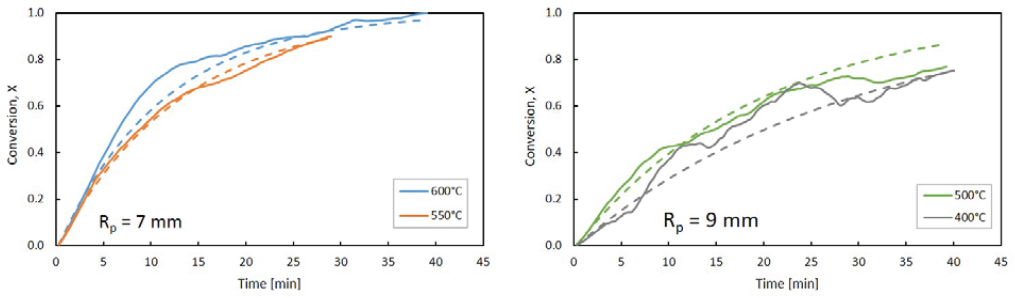
Figure 5.18: Isothermal reduction data modelled by using the parameters obtained from non-isothermal reduction data for Comilog ore. The average particle size was decreased from 13.1 mm (initial size) to 7 mm at high temperature and 9 mm at low temperature to estimate the effect of decrepitation
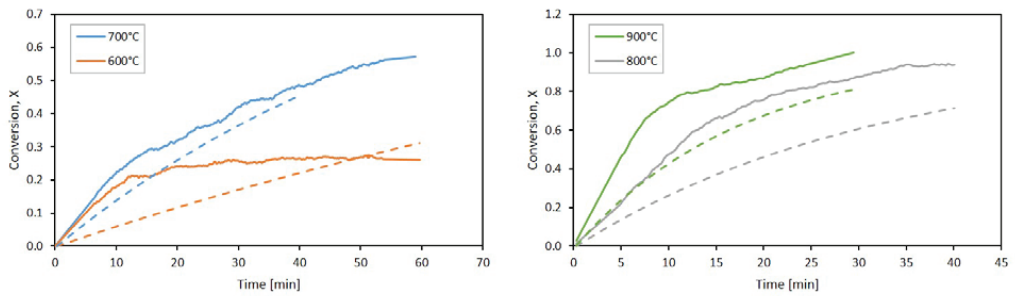
Figure 5.19: Model parameters found from non-isothermal TGA data used to model isothermal reduction data for Nchwaning ore given by Table 5.1 for 13.1 mm particles. Model gives lower conversion compared to experimental throughout the experiments

176

Evaluation of model

The model was able to describe the reduction behavior with a relatively good agreement to the experimental data. As the model was relatively simple and modelled a multistep reaction mechanism in a single step, there are of course deviations observed. The aim was to produce a simple and robust model that was able to describe the reduction extent with varying particle size, CO-concentrations and temperature. As such, the constructed model describes overall reduction trends rather than focusing on the specific mechanisms. The limitations and simplifications of the model will be discussed in this section.

A limitation of the model is that is does not include the thermodynamic driving force. The driving force of the reduction of the manganese oxides can be expressed by the oxygen pressure in the ore relative to the equilibrium oxygen pressure. Considering that the ores contain various different oxides, a representative quantification of the oxygen pressure is considered complicated, however a simplified representation should be obtainable. In the present study, the effect of the oxygen pressure was simplified by including the partial pressure of CO. The CO partial pressure was assumed constant according to the input composition, however, the CO/CO_2 ratio will change throughout the reduction course as it is affected by the ore reduction, particularly for Comilog ore. This was shown in Figure 5.9. A more representative model should incorporate the changing $CO-CO_2$ concentrations.

The geometrical factor was expressed through the correlation between the particle size and the reaction rate. Generally, the particle size of a sphere may be included in a reaction model to express the effect of available surface area for reduction. However, changing the ore particle size does not merely change the available surface area, but further affects other characteristics that may affect the reaction rate. This includes decrepitation, which will decrease the effective particle size. In general, larger particle sizes are more susceptible towards decrepitation.

A first order chemical reaction mechanism was utilized. This was to a certain degree an assumption, where it was desired to correlate the reaction rate and the reduction extent in a simple manner. In addition, it is believed that if the reduction was governed by a topochemical reaction mechanism, this should have been possible to observe during microstructure investigation of partially reduced samples. It is further argued that due to the heterogeneous nature of the ore, the ore reduction will likely not be fully described by a single reaction mechanism.

Rather than describing the individual reactions, the model described the overall reduction extent. For Comilog ore, the rapid reduction of remaining MnO_2 present at threshold temperature of 550-600°C was not accounted for in the model. The TGA data showed that the decomposition of MnO_2 initiated at this temperature proceeded at a rate much faster than the prior reduction. As such, samples experiencing a high amount of reduction in this step shows a larger deviation respective to the model data. For Nchwaning ore, the model does not separate between the manganese and iron oxides, and does not account for the decomposition of carbonates. It is believed that it is a fair approximation that the reduction extent of manganese and iron oxides is closely related, particularly for larger particles. The amount of carbonates present in the ore is relatively low, and does not have a large impact on the reduction. Furthermore, it was observed that the carbonates were decomposed at temperature range 800-1000°C, regardless of the particle size and gas atmosphere. A variation of considerable size was observed between the parallels obtained for larger particle sizes (> 11.2 mm) for Nchwaning ore. The variation is likely related to the natural variation

of the ore. The heterogeneity is not displayed in the chemical analysis, which indicates that the variance is introduced either through differing mineralogy or through physical parameters, e.g. porosity.

Comparison of the obtained activation energies with previously reported findings could indicate that the magnitude is dependent on the characteristics of the investigated manganese material and/or the experimental conditions. As such, the model developed in this work may potentially only be used for similar time and temperature set ups.

5.3   Decrepitation

Overall, it was found that Nchwaning ore shows low degree of disintegration and decrepitation compared to Comilog ore during heating in reducing atmosphere. This is illustrated by the amount of sample of size less than 4.75 mm after reduction of ore mixed with quartz in 50%CO-50%CO$_2$ at 6°C/min at 25-1000°C in Figure 5.20. According to chemical analysis, all of these experiments resulted in a full prereduction of manganese oxides to MnO. The difference in decrepitation of Comilog and Nchwaning ore agrees well with previous investigations[10], [12], [115].
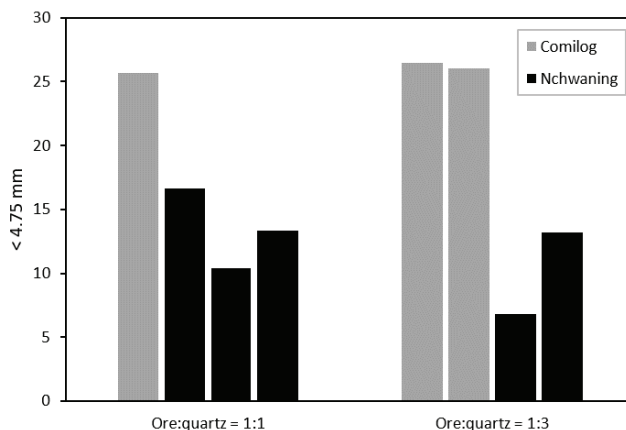
Figure 5.20: Amount of sample of size less than 4.75 mm after reduction experiments in 50%CO-50%CO$_2$ for Nchwaning and Comilog (both in size 11.20-15.00 mm) mixed with quartz in weight ratio 1:1 and 1:3, respectively. Samples were heated at 6°C/min up to 1000°C, where a full prereduction to MnO was obtained according to chemical analysis. It is seen that Comilog experience a higher degree of disintegration compared to Nchwaning

It was found that the decrepitation of Comilog ore was a function of the reduction extent, implying that the decrepitation was related to the reduction of higher manganese oxides, but not credited to a specific reaction step. Hence, the decrepitation of Comilog is not largely attributed to the rapid reduction of MnO$_2$ giving the large exothermic temperature peak. This was supported by the similar extent of decrepitation in the

178

experiments conducted with mixed ore and quartz, where it was observed that the exothermic peak was suppressed. Furthermore, a similar extent of disintegration was obtained in $CO-CO_2$ and $CO-CO_2-H_2$ atmospheres, respectively. The relation between the amount of disintegrated material and analysed MnOx in the reduced sample is shown in Figure 5.21. It is clear that the extent of decrepitation is a function of the decreasing MnOx. This was also observed by Biørnstad[115], who investigated the disintegration of Comilog ore (sample size of 2 kg) during non-isothermal heating in $CO-CO_2$ atmosphere at temperature range 25-800°C (3°C/min heating rate). While the magnitude of the exothermic temperature peak decreased when the ore was heated in presence of quartz, the extent of disintegration did not decrease. Rather, Biørnstad observed a slightly larger decrepitation extent when the ore was mixed with quartz, despite the magnitude of the exothermic peak being lowered.
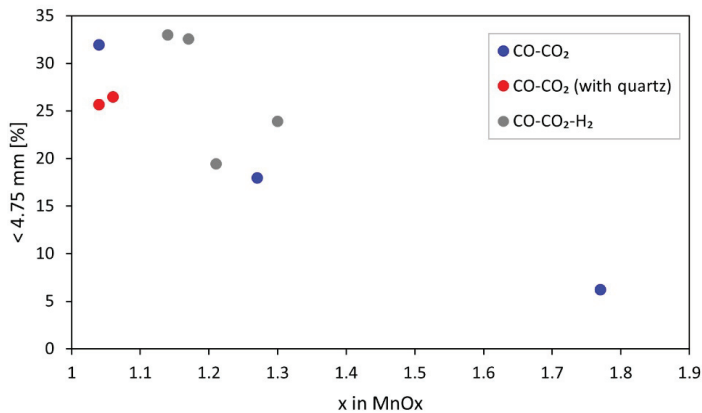
Figure 5.21: Amount of sample of size smaller than 4.75 mm after reduction experiments as a function of MnOx for Comilog ore. Figure shows that the decrepitation increases with decreasing MnOx (reduction extent). All experiments have been conducted with a heating rate of 6°C/min up to various target temperatures.

Figure 5.22 shows the sample fraction of size smaller than 4.75 mm for experiments conducted with initial size fraction 11.20-15.00 mm after heating in reducing atmosphere as a function of MnOx for Nchwaning ore. The figure indicates a relation between the extent of decrepitation and the reduction extent, however due to generally low decrepitation, the trend is less clear than for Comilog. The samples of oxidation level equal to 1.41 and 1.42 shows nearly no disintegration, in spite of being heated at 6°C/min up to 500°C. This indicates that the increasing temperatures is not a large factor in the decrepitation of Nchwaning ore. Similar observations were made by Biørnstad[115], who observed a near linear relation between the decrepitation and MnOx of Nchwaning by non-isothermal reduction (3°C/min) in $CO-CO_2$ atmosphere.

According to the studies presented by Faria with colleagues, the main factors responsible for the decrepitation of manganese ores are moisture elimination, hydrated minerals decomposition, and higher oxides and braunite decompositions[23]–[26], [116]. Faria suggested that the thermal decomposition of

manganese oxides were the major contributing factor, which was also indicated by Biswas[27]. In this study, it was found that the decrepitation was mainly a function of the reduction extent. It is thus not believed that the removal of chemically bound moisture has a large impact on the decrepitation of Comilog ore. As was shown in section 5.1.1, the chemically bound moisture was removed in the early stages of the reduction. Thus, if this process was a main factor, the ore would show a larger disintegration in the early stages. The lower extent of decrepitation of Nchwaning compared to Comilog have previously been explained by the lower porosity[10], [12]. However, according to the observed relation between the oxidation level and the disintegration, it is likely that the difference is at least partly related to the higher concentration of manganese oxides, as well as the higher oxidation level, in Comilog ore.
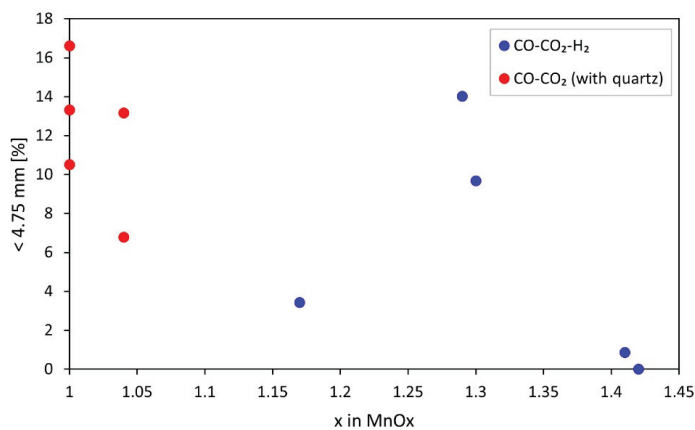
Figure 5.22: Amount of sample of size smaller than 4.75 mm after reduction experiments as a function of MnOx for Nchwaning ore. Figure shows that the decrepitation increases with decreasing MnOx (reduction extent). All experiments have been conducted with a heating rate of 6°C/min up to various target temperatures.

It was found that the decrepitation of Comilog ore decreased with increasing heating rate. Figure 5.23 shows that the results obtained in this study shows a high correlation to the results obtained by Biørnstad, who evaluated the decrepitation of Comilog ore in CO-CO_2 atmosphere heated at 3°C/min. An increased heating rate leads to increased thermal stresses experienced by the ore. As such, it would be expected that an increased heating rate would cause increased disintegration. The results obtained in this study are contradictory to this. However, the results support the conclusion that the rapid reduction step and corresponding rapid temperature increase is not a large factor in the decrepitation. The extent of the exothermic temperature peak was highly dependent on the heating rate. At 9°C/min, a large amount of MnO_2 remained at the threshold temperature, leading to a large extent of reduction occurring in this rapid step. At a heating rate of 3°C/min, nearly all MnO_2 had been reduced when the threshold temperature was reached, and an insignificant temperature increase was observed. As such, the results support the conclusion that the rapid reduction step is not a large factor in the decrepitation. However, the results indicate that the decrepitation may not be merely expressed as a function of the reduction extent. The reduction of Comilog

ore at 3°C/min is nearly fully described by the reduction of MnO_2 to MnO. In comparison, the reduction at 9°C/min may be divided into three steps. The initial stages are described by MnO_2 to MnO, whereas MnO_2 to Mn_2O_3 occurs in the rapid reduction step, followed by Mn_2O_3 to MnO. This could indicate that it is the reduction of MnO_2 to MnO that is the main contributing reaction towards decrepitation. However, this is not supported by the observations made from the decrepitation as a function of x in $MnOx$, presented in Figure 5.21. It is possible that the increasing disintegration with decreasing heating rate is due to that the ore is more susceptible towards decrepitation when the reduction proceeds at lower temperatures.
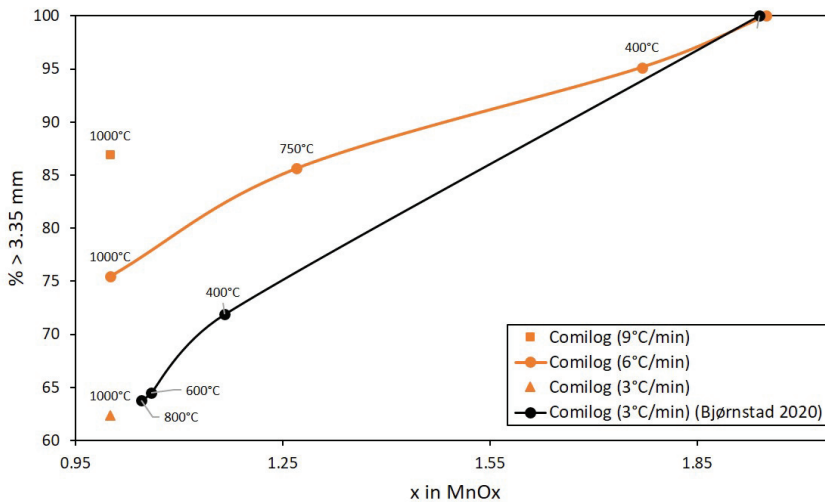
Figure 5.23: Amount of sample of size larger than 3.35 mm after reduction in CO-CO₂ atmosphere at various heating rates, showing that the decrepitation of Comilog ore obtained in this study shows high correlation to the results presented by Biørnstad[115]

5.4   Industrial significance

The behavior of the manganese ores as they descend in the prereduction zone of the industrial furnace is largely decisive for the overall energy consumption, as well as the off-gas characteristics of the process. Both the energy consumption and amount, composition and temperature of the off-gas are affected by the oxygen level of the ores, as well as its CO-reactivity. The CO-reactivity determines the *prereduction degree*, which is reduction extent that is obtained at 800°C, whereas the oxygen level determines to which extent the reduction of higher manganese oxides by CO(g) occurs. The previous sections have discussed the results obtained through the experimental investigation of the prereduction behavior of two commercial manganese ores, i.e. Comilog and Nchwaning. This section will illustrate and discuss some of the main findings in relation to the industrial ferromanganese furnace.

The first section demonstrates how the ores behave as they descend in the prereduction zone when exposed to various conditions. Further, the results were used to calculate the effect on the off-gas characteristics, including amount, temperature, and composition. The latter is important for any further processing of the off-gas, e.g. through electric energy production.

5.4.1 Prereduction degree

The ore is at ambient temperature when it is fed to the industrial furnace and exposed to the charge surface, being of temperature 200-400°C. The upper temperature limit of the prereduction zone may be said to be 1200-1400°C, which is when a slag phase is formed in the lower parts of the furnace. The heating rates the materials are exposed to depends on its location in the furnace. According to Pochart et al.[20], the heating rate varies from 2°C/min to 8°C/min, where rate decreases with distance from the electrodes. As such, the results obtained for heating rates 3°C/min, 6°C/min and 9°C/min in this study may be used to illustrate the reduction at different locations in the furnace. The oxidation level (x in MnOx) obtained at 3°C/min, 6°C/min and 9°C/min for Comilog ore is illustrated in Figure 5.24. A similar figure for Nchwaning ore at 3°C/min and 6°C/min is shown in Figure 5.25. The values are valid for 11.20-15.00 mm ore particles with a furnace gas of 50%CO-50%CO_2. In these figures, it is assumed that the raw materials descend in the furnace while being heated by the ascending gases at a heating rate of 3°C/min, 6°C/min and 9°C/min, respectively, where the lowest rate is obtained near the furnace wall. The oxidation level of Comilog ore at 800°C varies from 1.01 to 1.06 at 3°C/min to 9°C/min. For Nchwaning ore, an oxidation level of 1.15 was obtained at 800°C when the ore was heated at 3°C/min, whereas 1.20 was obtained at a heating rate of 6°C/min. This implies that at a given furnace depth, the oxidation level will be lower in the outer regions of the furnace for both Comilog and Nchwaning ore.

The reduction extent obtained at 800°C was observed to vary with the particle size for both ores. The oxidation level of manganese (x in MnOx) as the ores descend in the prereduction zone is shown in Figure 5.26 for the initial average particle size fractions that were evaluated. It is assumed that the ores are heated by the ascending gases, of composition 50%CO-50%CO_2, at a rate of 6°C/min. Solid lines are valid for Comilog ore, whereas Nchwaning ore is shown in dashed lines. Particle size fractions are noted by similar color for both ores. It is seen that Comilog ore has obtained a complete prereduction at 800°C for the three smaller particle sizes. In correlation to industrial operation, this implies that merely larger lumps (> 13.1 mm) will provide CO_2 that may be consumed in the Boudouard reaction. For Nchwnaning ore, particles of average size of 3.7 mm have almost obtained complete prereduction at 800°C. While Figure 5.26 showed the reduction behavior of Comilog and Nchwaning ore for the various initial average particle size fractions, the effective particle size of the ores will decrease as the ores descend in the prereduction zone due to decrepitation. This is illustrated for Comilog ore in Figure 5.27, which shows how the average particle size changes as the ore descends in the prereduction zone at different locations. The average particle size remains relatively unchanged as the ore descends in the inner section of the furnace, while significant changes are observed towards the outer regions.

182
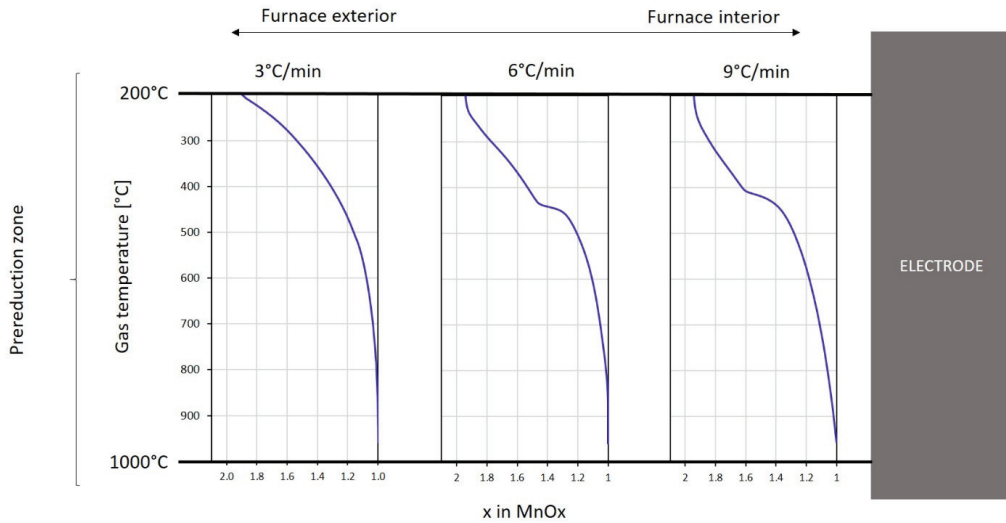
Figure 5.24: Oxidation level of manganese (x in MnOx) at different locations in the furnace for Comilog ore, when the ore is exposed to a gas of 50%CO-50%CO₂ ascending the furnace. The values show that a given MnOx is obtained at similar depth in the prereduction zone for the various heating rates
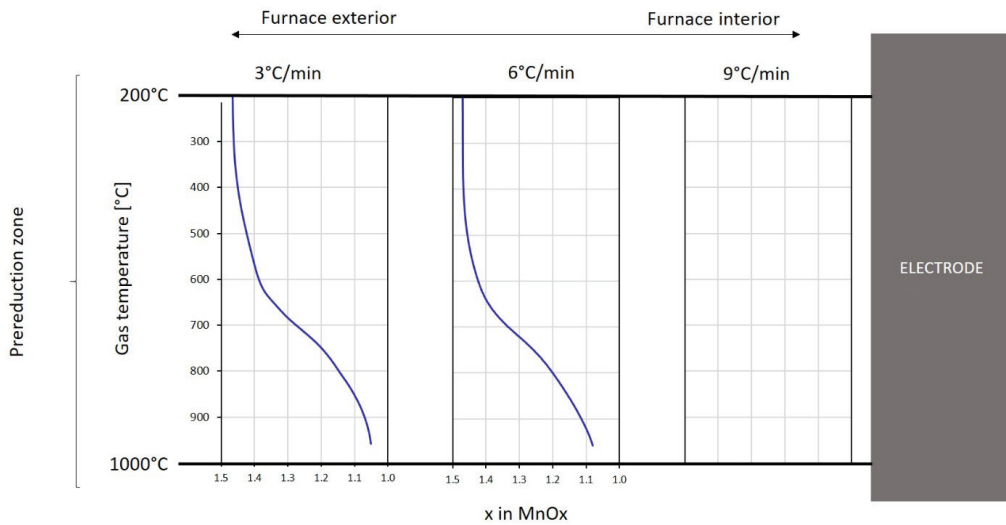
Figure 5.25: Oxidation level of manganese (x in MnOx) at different locations in the furnace for Nchwaning ore, when the ore is exposed to a gas of 50%CO-50%CO₂ ascending the furnace. The values show that a given MnOx is obtained at similar depth in the prereduction zone for both heating rates. Reduction behavior was not evaluated at 9°C/min
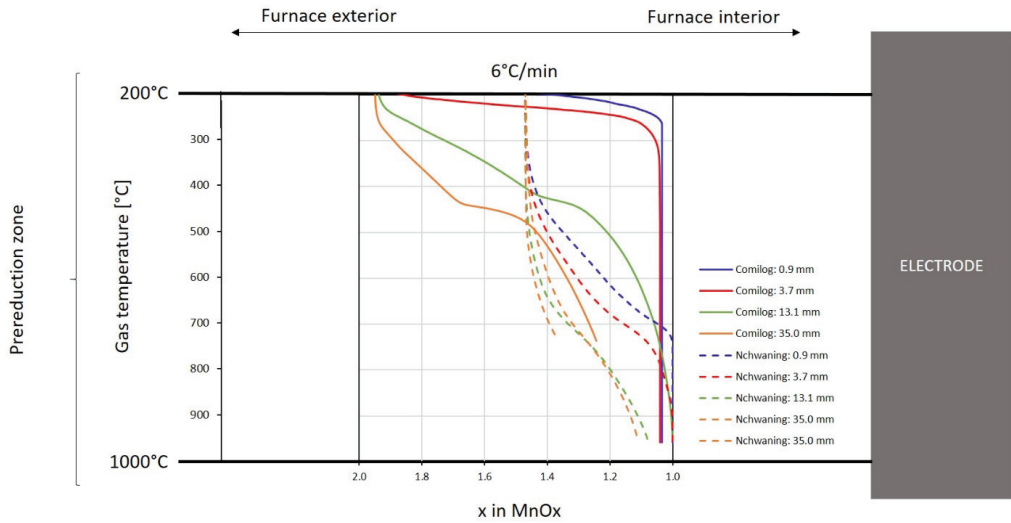
Figure 5.26: Oxidation level of manganese in Comilog and Nchwaning ore in various particle sizes as it descends through the prereduction zone (200-1000°C) at a rate of 6°C/min
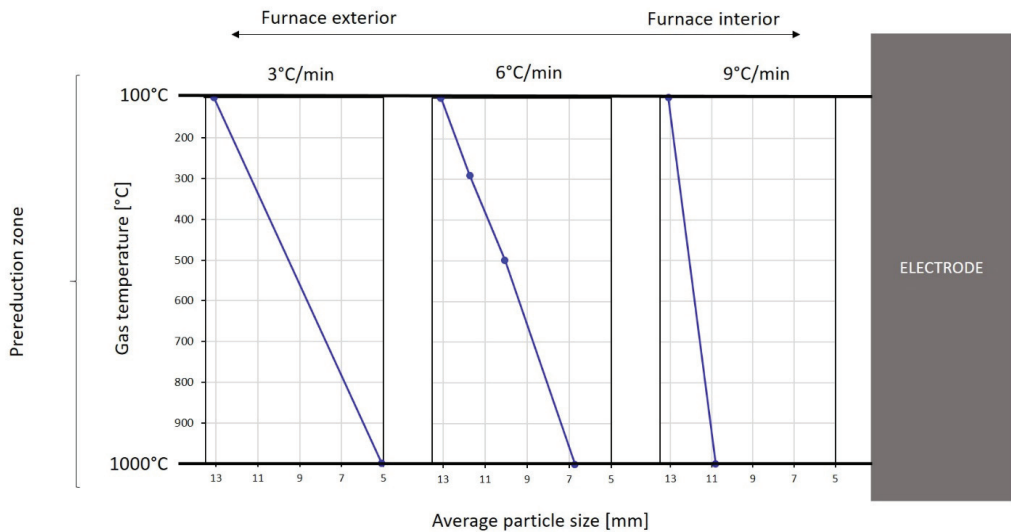
Figure 5.27: Change in average ore particle size of Comilog ore as it descend in the prereduction zone being heated by furnace gas of composition of 50%CO-50%CO$_2$ at 3°C/min, 6°C/min and 9°C/min for initial particle size of 13.1 mm

Figure 5.28 shows the oxidation level of manganese (x in MnOx) in Comilog and Nchwaning ore as it descends in the prereduction zone at various concentrations of CO(g) in the ascending furnace gas. The ore, of average particle size equal to 13.1 mm, is heated by the ascending furnace gas at a heating rate of 6°C/min. Comilog ore has obtained a complete prereduction at 800°C at CO-concentrations in range 40-80%, whereas an oxidation level of 1.1 is obtained in 30%CO at this temperature. Nchwaning ore is seen to partially reduce at temperatures exceeding 800°C for concentrations in range 30-80%, where an oxidation level of 1.1 was obtained at 800°C in 80%CO.
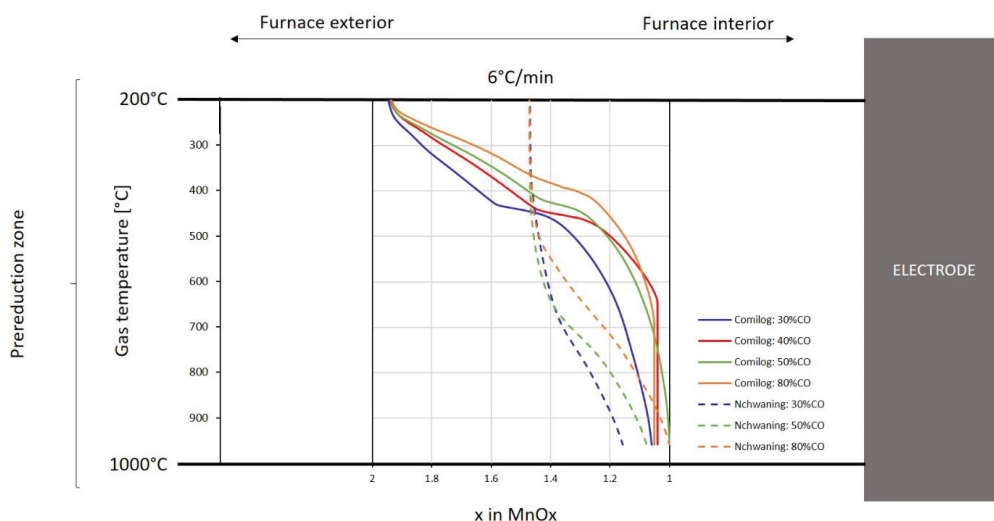
Figure 5.28: Oxidation level of manganese in Comilog and Nchwaning ore as it descends through the prereduction zone (200-1000°C) at a rate of 6°C/min exposed to ascending CO-CO$_2$ furnace gas of various CO-concentrations

From Figure 5.24-Figure 5.28 it is clear that Comilog ore will lead to a lower consumption of carbon compared to Nchwaning ore, as less oxygen is released at temperatures exceeding 800°C. Furthermore, it may also decrease the required amount of electrical energy fed to the system, due to the higher oxidation level leading to a larger extent of the exothermic reduction reactions. Figure 5.29 shows the temperature of Comilog and Nchwaning ore at different locations in the furnace for various average particle sizes. It is assumed that the ores are heated by the ascending gases, of composition 50%CO-50%CO$_2$, at a rate of 6°C/min. While Nchwaning ore follows the gas temperature, a clear effect of the exothermic reactions is observed for Comilog ore. Furthermore, it is seen that smaller sized particles will result in a large heat production in the upper part of the prereduction zone, whereas larger sized particles correlate to a lower temperature increase, occurring further down in the furnace. The heat production is closely related to the reduction rates.
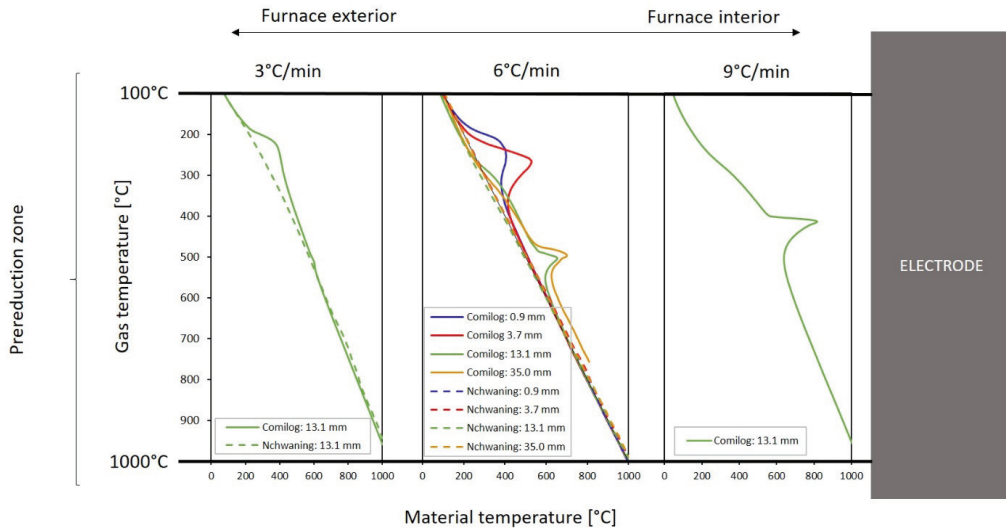
Figure 5.29: Temperature of Comilog and Nchwaning ore as it descends at different locations in the prereduction zone, while being heated by ascending furnace gas of composition 50%CO-50%CO$_2$ at a heating rate of 6°C/min

5.4.2 Off-gas characteristics

As was shown in the previous section, Comilog and Nchwaning ore show dissimilar reaction rates as they descend in the prereduction zone. This leads to a varying prereduction degree, i.e. ore reduction obtained at 800°C. The varying extent of prereduction degree, as well as the different oxygen content of the ores, will lead to different off-gas characteristics. Varying prereduction degree (reduction extent at 800°C) was obtained at varying ore particle size and varying CO-concentration in the furnace gas. The composition, and thus chemical energy, was calculated for each of the evaluated particle size fractions, and for each of the evaluated CO-CO$_2$ concentrations that the ore was exposed to as in descends in the prereduction zone.

The off-gas characteristics obtained at the various evaluated conditions were estimated by the use of HSC Chemistry through mass and energy balances. Chapter 2.6 presented mass and energy balances constructed for the production of HC FeMn and SiMn. To evaluate the off-gas characteristics, it was decided to use the example of HC FeMn, as this process involves a larger extent of prereduction compared to SiMn. Overall, the included process chemistry and assumptions were similar to that presented in section 2.6. This implies the amount of ore fed to the process was calculated to produce 1 tonne of alloy, and the required amount of carbon was calculated accordingly. The differences were as follows:

- The supply of manganese in the calculations for HC FeMn shown in chapter 2.6 were based on two different manganese ores and sinter. In this section, it is assumed that all required manganese was fed as Comilog ore or Nchwaning ore, respectively.
- The amount of fluxes (here as pure CaCO$_3$) was calculated to obtain a basicity of 0.9 for both ores. This implies that the calculations have been adjusted to obtain similar amount of MnO in the slag

phase. The alloy compositions will be different for Comilog and Nchwaning due to different Mn/Fe ratio in the ores.

- In the case presented in section 2.6, the prereduction degree was set to 25%, which implied that 75% of all CO_2 produced from reduction of Mn_3O_4, iron oxides and carbonate decomposition would react in the Boudouard reaction. In this section the prereduction degree will be varied according to the results obtained for the various conditions. This implies that the CO_2 production from the carbonate decomposition will always react according to the Boudouard reaction, as it was found that carbonates decompose at temperatures exceeding 800°C. The amount of CO_2 from the manganese and iron oxide reduction was determined by the MnOx obtained at 800°C.

Varying prereduction degree (reduction extent at 800°C) was obtained at varying ore particle size and varying CO-concentration in the furnace gas. The composition, and thus chemical energy, was calculated for each of the evaluated particle size fractions, and for each of the evaluated CO-CO_2 concentrations that the ore was exposed to as it descends the prereduction zone. The values calculated for each of the evaluated particle size fractions are shown in Table 5.4. In these calculations, the ore particles were exposed to a furnace gas of 50%-50%CO_2, heating the material at a rate of 6°C/min. At a full prereduction (x in MnOx = 1 at 800°C), a lower carbon consumption is observed for Nchwaning ore compared to Comilog ore. This is due to that the produced alloy from Nchwaning ore has a higher content of iron, which is assumed to be reduced to metallic state prior to slag formation. Furthermore, Comilog ore generally gives a higher content of CO_2 in the off-gas, due to the higher oxidation level of the ore. Figure 5.30 shows the chemical energy in the off-gas as a function of average particle size for Comilog and Nchwaning ore, respectively. More carbon is consumed in the Boudouard reaction when using Nchwaning ore compared to Comilog, which correlates to an increased amount of chemical energy in the off-gas. This is valid also when both ores obtain a complete prereduction at temperatures below 800°C, as the lower oxygen level of Nchwaning results in a lower CO-consumption in the prereduction zone.

The oxidation level obtained at 800°C is dependent on the CO-concentration in the furnace gas that the ore is exposed to as it descends in the prereduction zone. By assuming that the concentration of CO is constant at temperatures 25-800°C, the energy content in the off-gas at various CO-concentrations was calculated. The values are calculated for 11.20-15.00 mm particles, where it is assumed that the materials are heated by the gas at a heating rate of 6°C/min. An overview of the off-gas characteristics is shown in Table 5.6. The chemical energy as a function of the CO-concentration in the furnace gas at temperatures 25-800°C is shown in Figure 5.31. In general, observations that were made in the previous paragraph applies. It is further seen that the energy content in the off-gas decreases when the ores have been exposed to a furnace gas of higher CO-concentration, as a higher prereduction degree has been obtained at 800°C. The increase is more substantial for Nchwaning, as it was found that the reduction of Nchwaning ore was more dependent on the CO-concentration compared to Comilog ore.

Ore	Particle size [mm]	x in MnOx at 800°C	Carbon consumption [kg]	Total amount of gas [kmol]	CO [kmol]	CO_2 [kmol]	Chemical energy in off-gas [kWh]
Comilog	0.9	1.00	288.0	21.5	2.5	18.7	196.9
	3.7	1.00	288.0	21.5	2.5	18.7	196.9
	13.1	1.04	297.4	22.3	4.1	17.9	320.4
	35	1.24	344.6	26.2	11.9	13.9	937.9
Nchwaning	0.9	1.00	247.6	16.4	4.5	11.9	351.0
	3.7	1.03	256.8	17.2	6.0	11.2	470.6
	13.1	1.20	308.5	21.5	14.6	6.9	1148.4
	35	1.37	360.3	25.8	23.2	2.5	1826.1
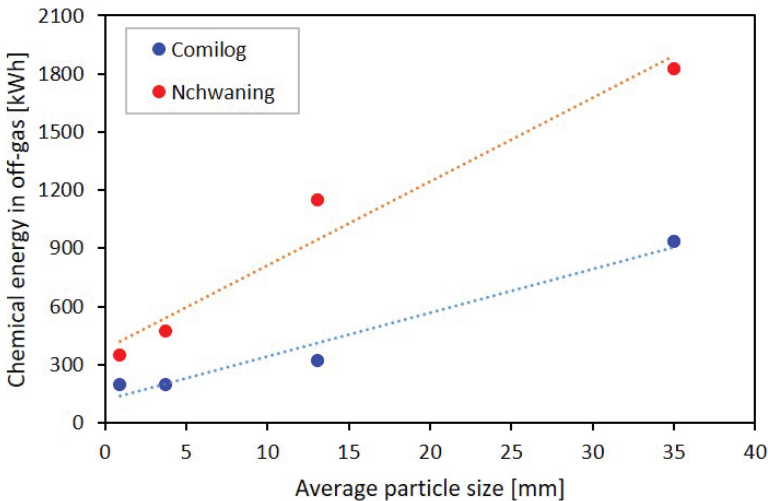
Figure 5.30: Energy content in off-gas [kWh] as a function of average particle size for Comilog and Nchwaning ore, respectively. Data from experiments conducted in 50%CO-50%CO_2 have been used. The energy content increases with increasing particle size for both ores, however the increase is steeper for Nchwaning. In addition, Nchwaning generally gives a higher amount of energy in the off-gas

Table 5.5: Carbon consumption, off-gas composition and chemical energy in off-gas for various degrees of prereduction obtained when exposed to varying CO-concentration in the furnace gas at temperatures 25-800°C for Comilog and Nchwaning ore, respectively. Values are valid for the production of 1 tonne of HC FeMn where all required manganese have been fed as Comilog or Nchwaning ore, respectively

Ore	%CO in furnace gas	x in MnOx at 800°C	Carbon consumption [kg]	Total amount of gas [kmol]	CO [kmol]	CO_2 [kmol]	Chemical energy in off-gas [kWh]
Comilog	30	1.11	313.2	23.6	6.7	16.6	526.9
	40	1.10	312.0	23.5	6.4	16.7	508.7
	50	1.03	293.9	22.0	3.5	18.2	274.1
	80	1.00	288.0	21.5	2.5	18.7	258.6
Nchwaning	30	1.27	328.6	23.1	18.0	5.2	1410.7
	50	1.20	307.8	21.4	14.5	6.9	1139.2
	80	1.11	283.0	19.3	10.2	10.2	804.9
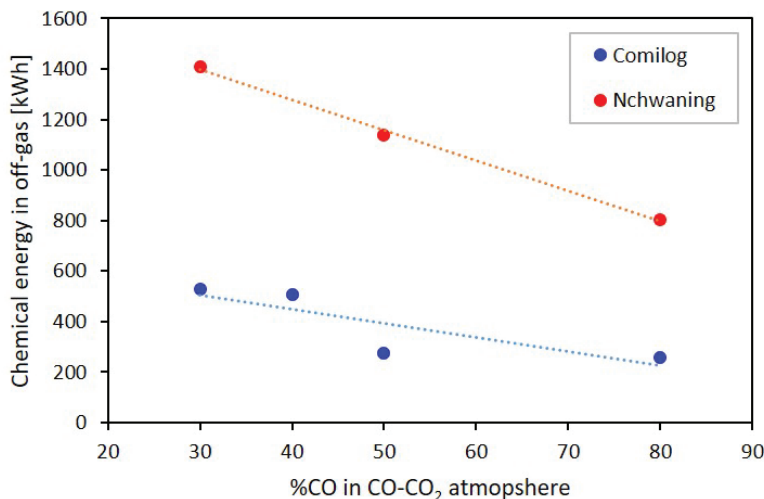
Figure 5.31: Energy content in off-gas [kWh] for various CO-concentrations that the ore is exposed to as it descends the prereduction zone. A decreasing energy content in the off-gas with increasing CO-concentration is observed for both Comilog and Nchwaning, however the effect is more substantial for Nchwaning

While the main components of the furnace gas are CO(g) and CO_2(g), a certain amount of hydrogen and water vapor is also found in the industrial off-gas. Water vapor is largely introduced to the system through the moisture in the raw materials, which may either be surface moisture or chemically bound moisture. Hydrogen may be formed by the reaction between water vapor and CO(g) according to the water-gas shift

reaction (WGSR). As such, the amount of hydrogen present in the off-gas will be dependent on the kinetics of the water-gas shift reaction. While surface moisture is rapidly evaporated at 100°C, chemically bound moisture is expelled at temperatures between 200-400°C. This implies that water vapor (and hydrogen) is not present in the furnace at temperatures exceeding 400°C. An effect of increased moisture content in the raw materials is that the energy consumption of the overall furnace process increases, as evaporation of water is an endothermic process. The presence of water vapor will further lead to a different off-gas composition. In Table 5.4 it was shown that when Comilog ore of particle size 35 mm ascends the prereduction zone exposed to a furnace gas of 50%CO-50%CO$_2$, a an oxidation level of 1.24 was obtained. The resulting off-gas composition was approximately 12 kmol CO and 14 kmol CO$_2$, correlating to 46%CO-54%CO$_2$. If 10% of moisture is added to the raw materials, the off-gas composition is changed to 32%CO-38%CO$_2$-30%H$_2$O. If assuming no extent of the water gas shift reaction, the chemical energy in the off-gas remains unchanged, as the content of CO has not been affected by the presence of water vapor. If the water-gas shift reaction is at equilibrium, nearly all present water vapor will react with CO(g) to form H$_2$(g) and CO$_2$(g). The off-gas composition (given in kmol) when the raw materials contain 10% moisture is shown in Figure 5.32, where values are shown for when the water gas shift reaction does not occur and when it is at equilibrium. The equilibrium constant of the WGSR at 400°C was used. It is seen that the off-gas composition is highly dependent on to which extent the WGSR occurs. The oxidation of CO, which increases the H$_2$ content, also leads to an increased chemical energy in the off-gas, where the specific increase was 30 kWh. This correlates to a relative increase of 3%. From the laboratory experiments conducted in this study, it was indicated that the WGSR occurred to some extent, but was not at equilibrium. As such, the composition and chemical energy in the off-gas is likely to be somewhere on the lines between the points marked in the figure.
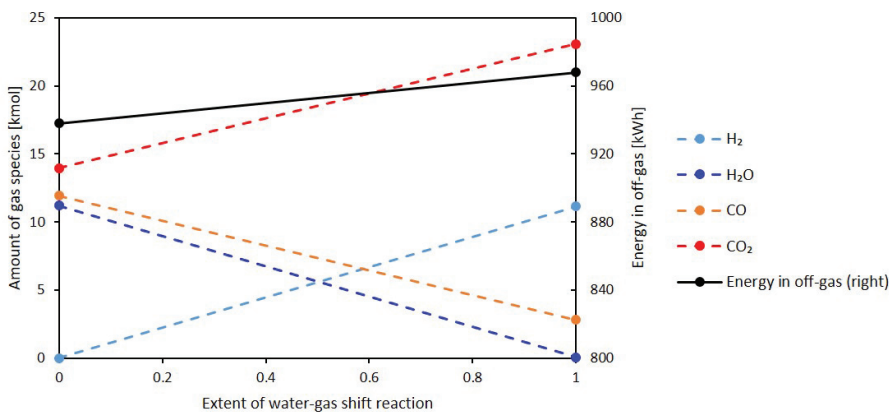
Figure 5.32: Change in off-gas composition (given in kmol) when the water-gas shift reaction does not occur and when it is at equilibrium. Values valid for the calculation of off-gas values obtained for Comilog ore in size 35 mm exposed to furnace gas of 50%CO-50%CO2 heating the ore at 6°C/min.

As any moisture introduced to the system will be expelled at temperatures below 400°C, the water vapor will have a low effect on the reduction rates. For Nchwaning ore, the water/hydrogen is removed from the system at temperatures lower than that required for the ore reduction. It may however influence the

reduction rates of Comilog ore, which will start to reduce at 150-250°C, depending on particle size. If the water vapor and/or hydrogen is present at temperatures when Comilog ore starts to reduce, it is likely that this will promote the reduction rate.

To estimate off-gas temperatures, the mass and energy balances were expanded from one to three zones. It is here assumed that the material- and gas-temperatures will not be the same. The prereduction zone was evaluated in two zones, which was separated at 800°C indicating the temperature at which the Boudouard reaction is initiated. Zone 3 was the coke-bed zone, which also included the slag formation. All material temperatures were defined, where zone 1 was given as temperature range 25-800°C and zone 2 was defined as 800-1250°C. Zone 3 was then set to be 1250-1500°C. It is mentioned that the materials descend towards increasing temperatures, while the furnace gas moves from the coke-bed zone towards the charge surface. This implies that the furnace gas from zone 3 will ascend to zone 2. It was assumed that the temperature of the gas ascending from the coke-bed zone to the Boudouard zone was of similar temperature as alloy and slag, i.e. 1500°C.

To estimate an off-gas temperature, an assumption regarding the heat balance of zone 2 is required to obtain the temperature of the gas ascending from zone 2 to zone 1. The heat balance of zone 2 was assumed to be affected by the extent of prereduction occurring in zone 1. A varying prereduction in zone 1 gives rise to a varying extent of the endothermic Boudouard reaction in zone 2, as well as the amount and composition of the materials in zone 2 that is heated from 800°C to 1250°C. An electrical energy feed was added to zone 2, which was calculated to be 50% (case 1) and 75%(case 2) of the energy consumed in the Boudouard reaction, in addition to the heat required to increase the temperature of the specific material composition from 800°C to 1250°C. The reaction enthalpy of the Boudouard reaction is 47.895 kWh/kmol[17]. Including this energy supply, the temperature of the gas ascending to zone 1 was calculated by assuming a zero heat balance within zone 2(±1 kWh). The off-gas temperature was then adjusted to obtain a zero heat balance (±1 kWh) in zone 1.

The off-gas temperature was calculated for a varying oxidation level of manganese obtained at 800°C, i.e. for various amounts of CO_2 consumed in the Boudouard reaction. The present calculations considered all available CO_2 in the system, i.e. from reduction of manganese oxides to MnO, reduction of iron oxides to FeO, and decomposition of carbonates. It was assumed that these three reactions proceeded to similar extent. As such, the zones were defined as presented in Table 5.6. The off-gas temperatures are presented graphically in Figure 5.33. The calculated values are presented in Table 5.7 and Table 5.8 for Comilog- and Nchwaning-ore, respectively. The reduction extent at 800°C has been presented in terms of the oxidation level of manganese.

Table 5.6: HC FeMn furnace reactions divided into three zones used to calculate off-gas temperatures for various experimental conditions used in this study

Zone	Reactions occurring in zone	Description
1	$H_2O = H_2O(g)$ $x(MnO_2 + CO = MnO + CO_2)$ $x(Fe_2O_3 + 3CO = 2FeO + 3CO_2)$ $x(CaCO_3 = CaO + CO_2)$	x is determined from the experimental results Input temperature of materials: 25°C Output temperature of materials: 800°C
2	$(1-x)(MnO_2 + CO = MnO + CO_2)$ $(1-x)(Fe_2O_3 + CO = 2Fe + 2CO_2)$ $(1-x)(CaCO_3 = CaO + CO_2)$ $C + CO_2 = 2\ CO$	Active region of the Boudouard reaction. Input temperature of materials: 800°C Output temperature of materials: 1250°C
3	$MnO + C = Mn + CO$ $SiO_2 + 2C = Si + 2CO$ $C = \underline{C}$	Coke-bed zone: metal producing reactions. Input temperature of materials: 1250°C Output temperature of materials and gas: 1500°C
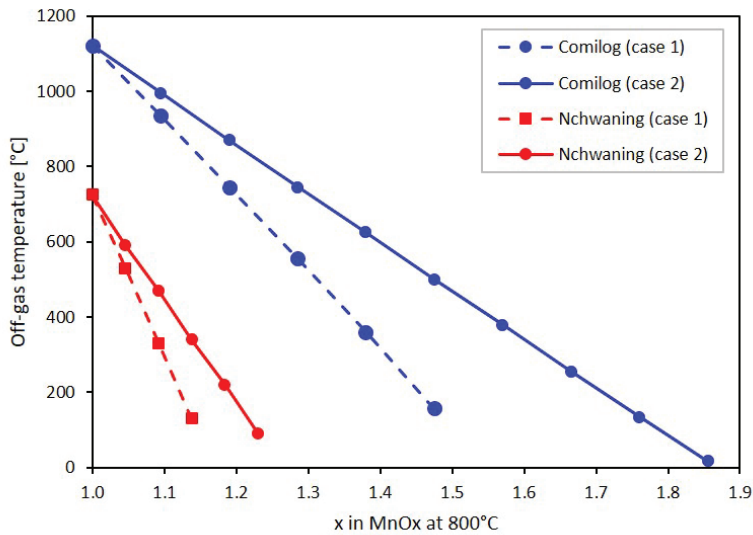
Figure 5.33: Off-gas temperature for Comilog and Nchwaning ore, respectively, as a function of oxidation level of manganese (x in MnOx) obtained at 800°C. Case 1 and 2 illustrated different electrical energy consumption in zone 2 (Boudouard zone)

Table 5.7: Calculated values for a three-zone HC FeMn furnace where Comilog ore is the manganese raw material. Case 1 and case 2 assumed an electrical energy feed to zone 2 of 50% and 75%, respectively, of the energy consumed by the Boudouaurd reaction, in addition to the energy required to heat the materials from 800°C to 1250°C

Case	MnOx at 800°C	Electrical energy feed to zone 2 [kWh]	Temperature of gas ascending from zone 2 to zone 1 [°C]	Off-gas temperature [°C]
1	1.00	236.7	1500	1122
	1.10	269.0	1380	935
	1.19	303.7	1280	745
	1.29	333.7	1200	555
	1.38	366.0	1130	360
	1.48	398.4	1070	158
	1.57	430.7	1020	< 25
2	1.00	236.7	1500	1122
	1.10	294.5	1500	995
	1.19	352.4	1495	870
	1.29	410.2	1495	745
	1.38	468.1	1495	625
	1.48	525.9	1495	500
	1.57	583.8	1495	380
	1.67	641.6	1492	255
	1.76	699.5	1492	135
	1.86	758.4	1492	17

Table 5.8: Calculated values for a three-zone HC FeMn where Nchwaning ore is the manganese raw material. Case 1 and case 2 assumed an electrical energy feed to zone 2 of 50% and 75%, respectively, of the energy consumed by the Boudouaurd reaction, in addition to the energy required to heat the materials from 800°C to 1250°C

Case	MnOx at 800°C	Electrical energy feed to zone 2 [kWh]	Temperature of gas ascending from zone 2 to zone 1 [°C]	Off-gas temperature [°C]
1	1.00	202.3	1500	725
	1.10	223.5	1355	530
	1.19	244.7	1230	330
	1.29	265.8	1125	130
	1.38	287.0	1028	< 25
2	1.00	202.3	1500	725
	1.10	239.2	1440	590
	1.19	276.1	1395	470
	1.29	313.1	1350	340
	1.38	349.9	1320	220
	1.48	386.9	1282	90

Several observations can be made from the tabulated values and the graphical representation. Firstly, it is clear that Comilog ore results in a higher off-gas temperature compared to Nchwaning. This is due to the higher oxygen level, which leads to a larger extent of the exothermic reactions. Comilog ore in particle size 30-40 mm obtained an oxidation level of 1.24 at 800°C when reduced in 50%CO-50%CO_2 at 6°C/min. This correlates to an off-gas temperature of 600-800°C. Nchwaning ore in similar conditions obtained an oxidation level of 1.37, which correlates to an off-gas temperature of 100-200°C. While it is seen that the off-gas temperature is affected by the prereduction degree, it is also clear that the temperature is affected by the temperature of the gas ascending from zone 2 to zone 1. This temperature will be determined by the heat balance of zone 2. At an oxidation level of 1.38 (correlating to a 60% reduction at 800°C) obtained for Comilog ore, where the gas ascending from zone 2 has a temperature of 1130°C, the off-gas temperature is found to be 360°C. However, at the same oxidation level and a furnace gas from zone 2 of temperature 1495°C, an off-gas temperature of 620°C is obtained. The values show that if the reduction extent is low, i.e. a high x in MnOx at 800°C, the amount of heat produced in the upper part of the prereduction zone (zone 1) is low, as a small extent of the exothermic reactions occur. As an electrical energy supply was not included in the low temperature zone, this lead to off-gas temperatures lower than 25°C at low prereduction degrees for case 1 in Comilog ore, and both cases for Nchwaning ore. These high oxidation levels are likely not observed at 800°C in the industrial furnace[34]. In an industrial furnace, heat is generated when the current runs from the electrodes through the charge material in an industrial furnace. The majority of the electrical energy will go to the coke-bed zone, where the resistivity of low. According to the simulations presented by Dhainaut[117], some of the electrical energy will also dissipate higher up in the furnace, where the amount is affected by the electrode position. When the electrode was positioned 1 m above the metal bath, less than 5% of the electrical energy could be dissipated at temperatures below 1200°C, whereas less than 3% was dissipated at an electrode height of 3 m. It was however argued by Olsen and Tangstad[3], that this is unlikely, as these potential current paths would have short lifetime. As such, it is possible that the energy feed supplied to zone 2 in these calculations was not representative. Nonetheless, the values may still be used to evaluate the effect of increased reduction extent on the off-gas temperature.

These sections have discussed effects on operation using Comilog or Nchwaning ore, respectively, as the manganese raw material. The chemical energy in the off-gas was presented for varying conditions in the prereduction zone. The amount of this energy that may be recovered, i.e. the exergy, will depend on the recovery technique. As such, the values were not discussed in terms of exergy. In industrial practice, it is more common to use a combination of manganese materials, rather than relying on a single type of ore. Generally, a combination of high oxygen ores and semi-oxygen ores (or sinter) may be used, which implies that the industrial practice may observe an average of the values calculated here.

6 Conclusions and further work

The prereduction behavior of Comilog and Nchwaning manganese ores was investigated as a function of particle size, gas composition and temperature. The results were analysed through TGA curves, chemical composition, mineralogy, and microstructure investigations.

Comilog ore is a high oxygen ore, where the majority of the ore is composed of different MnO_2-minerals. It was found that the initial stages of the prereduction was the reduction of these MnO_2 minerals to MnO in an overall single step, implying that intermediate oxidation states Mn_2O_3 and Mn_3O_4 were insignificant. The reaction rate obtained in this step was found to be proportional to the inverse average particle size, i.e. $(1/r_p)$. Further, the rate was found to increase with the partial pressure of CO to the power of 0.7. The rapid decomposition temperature of MnO_2 was found to be 580-600°C. As such, any remaining MnO_2 at this threshold temperature experienced a rapid reduction, where Mn_2O_3 was formed. The Mn_2O_3 continued to be reduced to MnO. The reaction rate obtained in the rapid reduction step was merely dependent on the amount of material that was present at this threshold temperature, which implies that it was indirectly affected by the same parameters that affect the reduction at lower temperatures. The chemically bound moisture (5 wt%) was found to be expelled in the initial stages of reduction, i.e. at temperatures 200-400°C. It was found that the reduction steps observed during isothermal experiments were similar to those observed in non-isothermal experiments. Dissimilar phase development was however observed between isothermal and non-isothermal reduction, where a topochemical reaction front was formed during isothermal reduction at low temperature. This was not observed in samples reduced non-isothermally (6°C/min). Thus, the isothermal temperature regime causes alterations to the microstructure, either due to rapid initial heating, or the low reaction temperature.

Nchwaning ore is mainly constituted by different Mn_2O_3-minerals, hematite and calcite. It was found that the reduction of manganese and iron oxides occurred at highly similar temperature ranges, however the reduction of manganese oxides was initiated prior to the iron oxides. The rate was dependent on the particle size and the CO-concentration in the gas atmosphere, where the effect of the average particle size on the reaction rate was quantified to $(1/r_p)$. Further, the rate was promoted by the CO partial pressure to the power of 1.5. The trivalent manganese oxides in Nchwaning reduced to manganosite(MnO) in a single step, where the potential intermediate oxide hausmannite (Mn_3O_4) was not observed at any stage. It was found that the reduction of hematite subsided with the formation of wüstite (FeO) at the conditions evaluated in this study, where the reduction occurred in a single step. Carbonates were found to decompose at temperatures between 800-1000°C, regardless of particle size and gas composition. Nchwaning ore was found to be more heterogeneous compared to Comilog, which gave rise to a larger variance in the TGA curves. The reduction of Nchwaning ore followed the same reaction steps in both non-isothermal and isothermal reduction. Investigations of microstructure development showed no indications of a topochemical reaction mechanism.

The reduction of MnO_2 in Comilog ore was initiated at a lower temperature compared to the reduction of Mn_2O_3 in Nchwaning ore. Furthermore, the reduction rate of MnO_2 to MnO in Comilog ore was higher than that of Mn_2O_3 to MnO in Nchwaning. The temperature behavior during reduction was affected by the oxidation level of the ore and the obtained reaction rates. While it was found that the temperature of

Nchwaning ore will be similar to the gas temperature in an industrial furnace, the temperatures of Comilog ore is strongly affected by the exothermic reduction reactions. This is due to the higher oxidation level of Comilog which gives a larger amount of heat that is released compared to Nchwaning, in combination with the faster reaction rate for MnO_2 to MnO in Comilog compared to Mn_2O_3 to MnO in Nchwaning. A model was developed that was able to describe the reduction of manganese oxides with reasonable accuracy. It was found that the activation energy of Comilog ore was 17 kJ/mol, whereas 63 kJ/mol was determined for Nchwaning ore. The magnitudes showed high correlation to the experimental temperature dependency of the reaction rates. Due to the different reduction behavior, it was found that the use of Nchwaning ore generally leads to an increased energy and carbon consumption, as a larger extent of the reduction occurred in the active region of the Boudouard reaction. Furthermore, this leads to a higher content of $CO(g)$ in the off-gas.

Hydrogen had a promoting effect on the reduction rate of Comilog ore, both when added as $H_2(g)$ and $H_2O(g)$ to a CO-CO_2 mixture for a fixed oxygen pressure. A faster reaction rate was however observed in CO-CO_2-H_2, and it was concluded that the water-gas shift reaction did proceed, but was not at equilibrium. For Nchwaning ore, a highly similar reduction behavior was obtained in CO-CO_2 and CO-CO_2-H_2 atmospheres correlating to similar theoretical oxygen pressure. As such, the water-gas shift reaction is likely at or close to equilibrium during the reduction of Nchwaning ore. Water vapor (and hydrogen) will not be present in the industrial furnace at temperatures exceeding 400°C. Increased moisture content increases the energy consumption, but will likely not have a large effect on the prereduction behavior. A moisture content of 10% in a given charge composition will experience an increased energy in the off-gas of 1.5% relative to the total energy consumption if the water-gas shift reaction is at equilibrium.

It was found that the decrepitation of both ores were largely a function of the reduction extent. This is particularly interesting for Comilog ore, as it implies that the thermal stresses resulting from the rapid decomposition step is not affecting the decrepitation. The decrepitation of Comilog ore was further found to be affected by the heating rate, where the disintegration increased with decreasing heating rate. This observation could be related to the observation of a topochemical reaction front forming in Comilog ore subjected to isothermal reduction at low temperatures, which indicated that the particles were more dense compared to the ones subjected to non-isothermal reduction at 6°C/min.

Further work

It is believed that the work presented in this study is an important step towards an increased understanding of the behavior of the prereduction zone. The majority of the previous studies have investigated manganese ores subjected to various pretreatments, which have shown to result in a highly different reduction behavior compared to the untreated ore. However, at the same time, investigating the untreated ore in non-isothermal reduction schemes gives rise to a complex system, where it is difficult to quantify the effect of single parameters. Nonetheless, the results are believed to be more representative towards the industrial process.

In the present study, the reduction behavior of Comilog ore and Nchwaning ore was evaluated separately. As the industrial practice usually involves a mixture of manganese ores in the charge mix, it would be interesting to investigate if and to what extent the presence of Comilog ore affects the reduction of

Nchwaning and vice versa. This will show whether the temperature behavior observed for an ore mix can be determined by using average values from the behavior of the single ores. This could be further expanded to include the remaining raw materials, such as metallurgical coke and fluxes for the investigation of HC FeMn.

A general objective is to obtain a model that can predict the prereduction behavior with reasonable accuracy. An initial step to doing this would be to obtain TGA data for the reduction of Comilog and Nchwaning utilizing various experimental set ups, to determine to which extent the equipment that is utilized affects the kinetic parameters. Furthermore, it is clear that more experiments should be conducted for Nchwaning ore to account for the heterogeneity of the ore. Another step towards a representative model is to describe the driving force through the oxygen potential. A changing CO-concentration is experienced by the ore as it descends the prereduction zone, and as such, a representative model should account for this.

In the present study, it was found that the decrepitation of Comilog ore was dependent on the reduction extent and the heating rate. The decrepitation was found to increase with decreasing heating rate. The explanation for this is not known. It is possible that the pore structure is altered when the reduction is allowed to proceed at lower temperatures, making the particle more susceptible towards disintegration. This would agree with the observations of a topochemical reaction mechanism in the Comilog ore samples reduced isothermally at low temperatures, however more experiments should be performed to confirm.

7 References

[1] S. E. Olsen and M. Tangstad, "Silicomanganese production - Process understanding," INFACON X, 2004.

[2] K. N. Swamy, D. G. C. Robertson, P. Calvert, and D. Kozak, "Factors affecting carbon consumption in the production of high carbon ferromanganese," *INFACON IX*, vol. 9, pp. 293–301, 2001.

[3] S. E. Olsen, S. Olsen, M. Tangstad, and T. Lindstad, *Production of manganese ferroalloys*. Tapir Academic Press, 2007.

[4] J. Kaczorowski, T. Lindstad, and M. Syvertsen, "The influence of potassium on the Boudouard reaction in manganese production," *ISIJ Int.*, vol. 47, no. 11, pp. 1599–1604, 2007.

[5] J. Ostwald, "Mineralogy of the Groote Eylandt manganese oxides: A review," *Ore Geol. Rev.*, vol. 4, no. 1–2, pp. 3–45, 1988.

[6] A. S. E. Kleyenstuber, "A review of the geology and mining of the Kalahari manganese field," 1982.

[7] J. P. R. de Villiers, "A Mineralogical Investigation of Mamatwan and Wessels Manganese Ores," *Natl. Inst. Metall.*, p. 10, 1979.

[8] K. Turkova, D. Slizovskiy, and M. Tangstad, "CO reactivity and porosity of manganese materials," *ISIJ Int.*, vol. 54, no. 6, pp. 1204–1208, 2014.

[9] J. Gutzmer and N. J. Beukes, "Mineral paragenesis of the Kalahari managanese field, South Africa," *Ore Geol. Rev.*, vol. 11, no. 6, pp. 405–428, 1996.

[10] M. Tangstad, P. Calvert, H. Brun, and A. G. Lindseth, "Use of comilog ore in ferromanganese production," in *Proceedings: Tenth International Ferroalloys Congress*, 2004, vol. 1, p. 4.

[11] B. Sorensen, S. Gaal, E. Ringdalen, M. Tangstad, R. Kononov, and O. Ostrovski, "Phase compositions of manganese ores and their change in the process of calcination," *Int. J. Miner. Process.*, vol. 94, no. 3–4, pp. 101–110, 2010.

[12] M. Visser, H. Smith, E. Ringdalen, and M. Tangstad, "Properties of Nchwaning and Gloria ore in the production of Mn ferro-alloys," INFACON XIII, Kazakhstan, Jun. 2013.

[13] R. Kononov, O. Ostrovski, and S. Ganguly, "Carbothermal solid state reduction of manganese ores: 1. Manganese ore characterisation," *ISIJ Int.*, vol. 49, no. 8, pp. 1099–1106, 2009.

[14] K. L. Berg, "Gaseous Reduction of Manganese Ores," Dr. Ing thesis, The Norwegian University of Science and Technology, 1998.

[15] I. M. Varentsov and G. Grasselly, "Geology and geochemistry of manganese. General Problems—Mineralogy, Geochemistry," *Methods Vol IE Schweiz. Verlagsbuchhandlung Stuttg.*, 1980.

[16] B. E. Sørensen, "Mineral quantification of Manganese ores," Internal report, NTNU, 2010.

[17] Outotec, *HSC Chemistry*. .

[18] M. Eissa, H. El-Faramawy, A. Ahmed, S. Nabil, and H. Halfa, "Parameters affecting the production of high carbon ferromanganese in closed submerged arc furnace," *J. Miner. Mater. Charact. Eng.*, vol. 11, no. 01, p. 1, 2012.

[19] I. S. Çardakli, N. Sevinc, and T. Öztürk, "Production of high carbon ferromanganese from a manganese ore located in Erzincan," *Turk. J. Eng. Environ. Sci.*, vol. 35, no. 1, pp. 31–38, 2011.

[20] G. Pochart, L. Joncourt, N. Touchard, and C. Perdon, "Metallurgical benefit of reactive high grade ore in manganese alloys manufacturing," *World*, vol. 800, no. 1000, p. 1200, 2007.

[21] M. Tangstad, "Summary of prereduction experiments in the Disvadri furnaces with industrial materials in Gasferrosil v.2," NTNU, Internal report, 2017.

[22] P. P. Kim, "Reduction Rates of SiMn Slags from Various Raw Materials," 2018.

[23] G. L. de Faria, N. C. da S. Viana, N. Jannotti Júnior, C. B. Vieira, and F. G. da S. Araújo, "Decrepitation of Brazilian manganese lump ores.," 2010.

[24] G. L. Faria, N. Jannotti, and F. G. da Silva Araújo, "Decrepitation behavior of manganese lump ores," *Int. J. Miner. Process.*, vol. 102, pp. 150–155, 2012.

[25] G. L. de Faria, J. A. S. Tenório, N. Jannotti Jr, and F. da S. Araújo, "Disintegration on heating of a Brazilian manganese lump ore," *Int. J. Miner. Process.*, vol. 124, pp. 132–137, 2013.

[26] G. L. Faria, N. Jannotti, and F. G. da S. Araújo, "Particle disintegration of an important brazilian manganese lump ore," *Rem Rev. Esc. Minas*, vol. 67, no. 1, pp. 55–60, 2014.

[27] A. Biswas, P. K. Das, and V. Singh, "Investigation of the decrepitation phenomenon of polymorphic materials: A theoretical and experimental study," *Powder Technol.*, vol. 294, pp. 119–133, 2016.

[28] Bragstad, "Bestemmelse av porøsitet," Sintef Bygg og miljøteknikk, Report no. 00072, Project number 22B007.00. + Appended results, 2000.

[29] M. Ksiazek, M. Tangstad, and E. Ringdalen, "The thermophysical properties of raw materials for ferromanganese production," *South. Afr. Pyrometallurgy 2011*, 2012.

[30] M. Ksiazek, T. Maik, E. Ringdalen, and M. Tangstad, "The thermal diffusivity of raw materials for ferromanganese production," *INFACON XIII, Kazakhstan 2013*, 2013.

[31] R. Ishak and M. Tangstad, "Degree of prereduction without coke consumption in industrial furnaces," *INFACON XI*, pp. 268–279, 2007.

[32] M. Tangstad, S. Wasbø, and R. Tronstad, "Kinetics of the Pre-reduction of Manganese Ores," in *Conference proceedings, Infacon IX (Quebec)*, 2001, pp. 202–207.

[33] T. J. W. De Bruijn, T. H. Soerawidjaja, W. A. De Jongt, and P. J. Van Den Berg, "Modelling of the reduction of manganese oxides with hydrogen," *Chem. Eng. Sci.*, vol. 35, no. 7, pp. 1591–1599, 1980.

[34] R. J. Ishak, "Reaction Kinetics for Reduction of Manganese Ore with Carbon Monoxide in the Presence of Carbon," Dr. Ing thesis, NTNU, 2002.

[35] W. M. Dressel and H. Kenworthy, *Thermal behavior of manganese minerals in controlled atmospheres*, vol. 5761. US Dept. of the Interior. Bureau of Mines, 1961.

[36] K. L. Berg and S. E. Olsen, "Kinetics of manganese ore reduction by carbon monoxide," *Metall. Mater. Trans. B*, vol. 31, no. 3, pp. 477–490, 2000.

[37] M. S. Fahim, H. El Faramawy, A. M. Ahmed, S. N. Ghali, and A. E. H. T. Kandil, "Characterization of Egyptian manganese ores for production of high carbon ferromanganese," *J. Miner. Mater. Charact. Eng.*, vol. 1, no. 02, p. 68, 2013.

[38] Y. B. Gao, H. G. Kim, and H. Y. Sohn, "Kinetics of pre-reduction of manganese ore by CO," *Miner. Process. Extr. Metall.*, vol. 121, no. 2, pp. 109–116, 2012.

[39] G. J. W. Kor, "The thermal decomposition of Mn 2 O 3 and the reduction of Mn 3 O 4 by C and CO," *Metall. Trans. B*, vol. 9, no. 2, pp. 307–311, 1978.

[40] G. Akdogan and R. H. Eric, "Solid state carbothermic reduction of manganese ores," *Int. J. Mater. Prod. Technol.*, vol. 8, no. 1, pp. 29–42, 1993.

[41] G. Akdogan and R. H. Eric, "Carbothermic reduction behaviour of wessel manganese ores," *Miner. Eng.*, vol. 7, no. 5–6, pp. 633–645, 1994.

[42] G. Akdogan and R. H. Eric, "Kinetics of the solid-state carbothermic reduction of Wessel manganese ores," *Metall. Mater. Trans. B*, vol. 26, no. 1, pp. 13–24, 1995.

[43] M. Yastreboff, O. Ostrovski, and S. Ganguly, "Effect of gas composition on the carbothermic reduction of manganese oxide," *ISIJ Int.*, vol. 43, no. 2, pp. 161–165, 2003.

[44] R. H. Eric and E. Burucu, "The mechanism and kinetics of the carbothermic reduction of Mamatwan manganese ore fines," *Miner. Eng.*, vol. 5, no. 7, pp. 795–815, 1992.

[45] M. A. Reuter and J. S. J. Van Deventer, "Kinetic model for the carbothermic reduction of manganese dioxide," *Thermochim. Acta*, vol. 125, pp. 99–106, 1988.

[46] H. Li and D. G. C. Robertson, "Effect of moisture, combined water, and volatile elements on fixed carbon requirement in a ferro-manganese smelting furnace," 1997.

[47] M. Gustum, "Smart utilization of CO gas in industrial clusters," NTNU, Specialization project, 2017.

[48] H. E. Barner and C. L. Mantell, "Kinetics of hydrogen reduction of manganese dioxide," *Ind. Eng. Chem. Process Des. Dev.*, vol. 7, no. 2, pp. 285–294, 1968.

[49] R. Kononov, O. Ostrovski, and S. Ganguly, "Carbothermal solid state reduction of manganese ores: 2. Non-isothermal and isothermal reduction in different gas atmospheres," *ISIJ Int.*, vol. 49, no. 8, pp. 1107–1114, 2009.

[50] H. H. A. El-Gawad, M. M. Ahmed, N. A. El-Hussiny, and M. E. H. Shalabi, "Reduction of low grade Egyptian manganese ore via hydrogen at 800 C-950°C," *Open Access Libr. J. L*, vol. 1, p. e427, 2014.

200

[51] T. Beck, "Forreduksjon av manganmalm med H$_2$/CO blandinger," NTNU, Internal report, 1998.

[52] T. Beck, "Forreduksjon av Comilog manganmalm med H$_2$ og CO gass," Internal report, 1998.

[53] T. Beck, "Kinetikk og mekanisme ved reduksjon av manganmalm," MSc thesis, NTNU, 1998.

[54] S. Lobo, "Reduction of manganese ores using CO, H$_2$, CO$_2$ and H$_2$O blends," Unpublished work, 2015.

[55] P. Perreault and G.-S. Patience, "Pyrolusite–CO reduction kinetics," *Chem. Eng. J.*, vol. 295, pp. 227–236, 2016.

[56] D. Ngoy, "Pre-reduction of manganese ores with CO and H$_2$ gas," 2019.

[57] A. A. El-Geassy, M. I. Nasr, M. A. Yousef, M. H. Khedr, and M. Bahgat, "Behaviour of manganese oxides during magnetising reduction of Baharia iron ore by CO–CO$_2$ gas mixture," *Ironmak. Steelmak.*, vol. 27, no. 2, pp. 117–122, 2000.

[58] N. A. El-Hussiny, H. H. A. El-Gawad, F. M. Mohamed, and M. E. H. Shalabi, "Pelletization and Reduction of Egyptian Low Grade Manganese Ore Pellets via Hydrogen at 750-950ºC," *Int. J. Sci. Eng. Res.*, vol. 6, no. 5, pp. 339–346, 2015.

[59] A. A. El-Geassy, M. I. Nasr, A. A. Omar, and E. A. Mousa, "Isothermal reduction behaviour of MnO$_2$ doped Fe$_2$O$_3$ compacts with H$_2$ at 1073–1373 K," *Ironmak. Steelmak.*, vol. 35, no. 7, pp. 531–538, 2008.

[60] I. R. Leith and M. G. Howden, "Temperature-programmed reduction of mixed iron—manganese oxide catalysts in hydrogen and carbon monoxide," *Appl. Catal.*, vol. 37, pp. 75–92, 1988.

[61] A. Zare Ghadi, M. S. Valipour, S. M. Vahedi, and H. Y. Sohn, "A Review on the Modeling of Gaseous Reduction of Iron Oxide Pellets," *Steel Res. Int.*, vol. 91, no. 1, p. 1900270, 2020.

[62] T. L. Joseph, "Porosity, reducibility and size preparation of iron ores," *Trans AIME*, vol. 120, pp. 72–89, 1936.

[63] W. M. McKewan, "Steelmaking, The Chipman Conference," *JF Elliott TR Meadowcroft Eds*, p. 142, 1965.

[64] E. T. Turkdogan and J. V. Vinters, "Gaseous reduction of iron oxides: Part I. Reduction of hematite in hydrogen," *Metall. Mater. Trans. B*, vol. 2, no. 11, pp. 3175–3188, 1971.

[65] E. T. Turkdogan and J. V. Vinters, "Gaseous reduction of iron oxides: Part III. Reduction-oxidation of porous and dense iron oxides and iron," *Metall. Trans.*, vol. 3, no. 6, pp. 1561–1574, 1972.

[66] E. T. Turkdogan, R. G. Olsson, and J. V. Vinters, "Gaseous reduction of iron oxides: Part II. Pore characteristics of iron reduced from hematite in hydrogen," *Metall. Mater. Trans. B*, vol. 2, no. 11, pp. 3189–3196, 1971.

[67] A. Bonalde, A. Henriquez, and M. Manrique, "Kinetic analysis of the iron oxide reduction using hydrogen-carbon monoxide mixtures as reducing agent," *ISIJ Int.*, vol. 45, no. 9, pp. 1255–1260, 2005.

[68] A. Pineau, N. Kanari, and I. Gaballah, "Kinetics of reduction of iron oxides by H2: Part I: Low temperature reduction of hematite," *Thermochim. Acta*, vol. 447, no. 1, pp. 89–100, 2006.

[69] J. I. Rodero *et al.*, "Blast furnace and metallurgical coke's reactivity and its determination by thermal gravimetric analysis," *Ironmak. Steelmak.*, vol. 42, no. 8, pp. 618–625, 2015.

[70] H. Zhang, J. Bai, W. Li, and F. Cheng, "Comprehensive evaluation of inherent mineral composition and carbon structure parameters on CO$_2$ reactivity of metallurgical coke," *Fuel*, vol. 235, pp. 647–657, 2019.

[71] T. Hilding *et al.*, "Effect of temperature on coke properties and CO$_2$ reactivity under laboratory conditions and in an experimental blast furnace," in *AISTech 2005: 09/05/2005-12/05/2005*, 2005, pp. 497–505.

[72] R. Sakurovs and L. Burke, "Influence of gas composition on the reactivity of cokes," *Fuel Process. Technol.*, vol. 92, no. 6, pp. 1220–1224, 2011.

[73] D. A. Aderibigbe and J. Szekely, "Studies in coke reactivity: Part 1. Reaction of conventionally produced coke with CO-CO$_2$ mixtures over temperature range 850-1000°C," *Ironmak. Steelmak.*, vol. 1, pp. 11–19, 1981.

[74] Y. K. Rao, A. Adjorlolo, and J. H. Haberman, "On the mechanism of catalysis of the Boudouard reaction by alkali-metal compounds," *Carbon*, vol. 20, no. 3, pp. 207–212, 1982.

[75] M. Alam and T. DebRoy, "A comparative study of the roles of KCN and NaCN as catalytic precursors in the Boudouard reaction," *Fuel*, vol. 66, no. 1, pp. 103–112, 1987.

[76] L. A. Haas, S. E. Khalafalla, and P. L. Weston, *Kinetics of formation of carbon dioxide and carbon from carbon monoxide in presence of iron pellets*, vol. 7064. US Department of the Interior, Bureau of Mines, 1968.

[77] A. El-Geassy and M. Nasr, "Influence of original structure on the kinetics and mechanisms of carbon monoxide reduction of hematite compacts," *ISIJ Int.*, vol. 30, no. 6, pp. 417–425, 1990.

[78] W. K. Jozwiak, E. Kaczmarek, T. P. Maniecki, W. Ignaczak, and W. Maniukiewicz, "Reduction behavior of iron oxides in hydrogen and carbon monoxide atmospheres," *Appl. Catal. Gen.*, vol. 326, no. 1, pp. 17–27, 2007.

[79] N. Towhidi and J. Szekely, "The influence of carbon deposition on the reduction kinetics of commercial grade hematite pellets with CO, H_2, and N_2," *Metall. Trans. B*, vol. 14, no. 3, pp. 359–367, 1983.

[80] J. Szekely, J. W. Evans, and H. Y. Sohn, *Gas-solid reactions*. Elsevier, 1976.

[81] O. Levenspiel, *Chemical reaction engineering*. 1999.

[82] S. Vyazovkin, A. K. Burnham, J. M. Criado, L. A. Pérez-Maqueda, C. Popescu, and N. Sbirrazzuoli, "ICTAC Kinetics Committee recommendations for performing kinetic computations on thermal analysis data," *Thermochim. Acta*, vol. 520, no. 1–2, pp. 1–19, 2011.

[83] A. Khawam and D. R. Flanagan, "Basics and applications of solid-state kinetics: a pharmaceutical perspective," *J. Pharm. Sci.*, vol. 95, no. 3, pp. 472–498, 2006.

[84] P. E. Sánchez-Jiménez, L. A. Pérez-Maqueda, A. Perejón, and J. M. Criado, "Clarifications regarding the use of model-fitting methods of kinetic analysis for determining the activation energy from a single non-isothermal curve," *Chem. Cent. J.*, vol. 7, no. 1, p. 25, 2013.

[85] M. E. Brown *et al.*, "Computational aspects of kinetic analysis: part A: the ICTAC kinetics project-data, methods and results," *Thermochim. Acta*, vol. 355, no. 1–2, pp. 125–143, 2000.

[86] M. Maciejewski, "Computational aspects of kinetic analysis.: Part B: The ICTAC Kinetics Project—the decomposition kinetics of calcium carbonate revisited, or some tips on survival in the kinetic minefield," *Thermochim. Acta*, vol. 355, no. 1–2, pp. 145–154, 2000.

[87] S. Vyazovkin, "Computational aspects of kinetic analysis.: Part C. The ICTAC Kinetics Project—the light at the end of the tunnel?," *Thermochim. Acta*, vol. 355, no. 1–2, pp. 155–163, 2000.

[88] A. K. Burnham, "Computational aspects of kinetic analysis.: Part D: The ICTAC kinetics project—multi-thermal–history model-fitting methods and their relation to isoconversional methods," *Thermochim. Acta*, vol. 355, no. 1–2, pp. 165–170, 2000.

[89] B. Roduit, "Computational aspects of kinetic analysis.: part E: the ICTAC kinetics project—numerical techniques and kinetics of solid state processes," *Thermochim. Acta*, vol. 355, no. 1–2, pp. 171–180, 2000.

[90] S. Vyazovkin and C. A. Wight, "Model-free and model-fitting approaches to kinetic analysis of isothermal and nonisothermal data," *Thermochim. Acta*, vol. 340, pp. 53–68, 1999.

[91] A. Khawam and D. R. Flanagan, "Role of isoconversional methods in varying activation energies of solid-state kinetics: I. Isothermal kinetic studies," *Thermochim. Acta*, vol. 429, no. 1, pp. 93–102, 2005.

[92] A. Khawam and D. R. Flanagan, "Role of isoconversional methods in varying activation energies of solid-state kinetics: II. Nonisothermal kinetic studies," *Thermochim. Acta*, vol. 436, no. 1–2, pp. 101–112, 2005.

[93] S. Vyazovkin, "Evaluation of activation energy of thermally stimulated solid-state reactions under arbitrary variation of temperature," *J. Comput. Chem.*, vol. 18, no. 3, pp. 393–402, 1997.

[94] H. Y. Sohn, "Developments in gas-solid reaction analysis," in *Julian Szekely Memorial Symposium on Materials Processing*, 1997, pp. 35–65.

[95]   J. B. Joshi and L. K. Doraiswamy, "Chemical reaction engineering," *Albright's Chem. Eng. Handb.*, pp. 737–968, 2008.

[96]   H. Y. Sohn, "Review of fluid-solid reaction analysis—Part 2: Single porous reactant solid," *Can. J. Chem. Eng.*, vol. 97, no. 7, pp. 2068–2076, 2019.

[97]   M. Ishida and C. Y. Wen, "Comparison of zone-reaction model and unreacted-core shrinking model in solid—gas reactions—I isothermal analysis," *Chem. Eng. Sci.*, vol. 26, no. 7, pp. 1031–1041, 1971.

[98]   J. Szekely and J. W. Evans, "A structural model for gas—solid reactions with a moving boundary," *Chem. Eng. Sci.*, vol. 25, no. 6, pp. 1091–1107, Jan. 1970, doi: 10.1016/0009-2509(70)85053-9.

[99]   H. Y. Sohn and J. Szekely, "A structural model for gas-solid reactions with a moving boundary—III: A general dimensionless representation of the irreversible reaction between a porous solid and a reactant gas," *Chem. Eng. Sci.*, vol. 27, no. 4, pp. 763–778, 1972.

[100] S. K. Bhatia and D. D. Perlmutter, "A random pore model for fluid-solid reactions: I. Isothermal, kinetic control," *AIChE J.*, vol. 26, no. 3, pp. 379–386, 1980.

[101] H. Y. Sohn, "The law of additive reaction times in fluid-solid reactions," *Metall. Trans. B*, vol. 9, no. 1, pp. 89–96, 1978.

[102] T. A. Larssen, M. Tangstad, and I. T. Kero, "Energy distribution in HC FeMn and SiMn energy vs exergy analyses," *J. South. Afr. Inst. Min. Metall.*, vol. 119, no. 12, pp. 1071–1076, 2019.

[103] T. J. Kotas, *The exergy method of thermal plant analysis*. Elsevier, 2013.

[104] J. Szargut, A. Valero, W. Stanek, and A. Valero, *Towards an international reference environment of chemical exergy. Technical paper*. Elsevier Science Publishers, Netherlands, 2005.

[105] T. Lindstad, B. Monsen, and K. S. Osen, "How the ferroalloy industry can meet greenhouse gas regulations," *INFACON XII*, 2010.

[106] ERAMET-NORWAY, "Eramet Sustainability Report 2016," 2017. [Online]. Available: https://issuu.com/erametnorway/docs/eramet_b__rekraftrapp2016_eng-issuu.

[107] M. Tangstad, S. E. Olsen, and E. Sverre, "The ferromanganese process–Material and Energy balance," *INFACON*, vol. 7, pp. 621–630, 1995.

[108] D. E. Newbury and N. W. Ritchie, "Is scanning electron microscopy/energy dispersive x-ray spectroscopy (SEM/EDS) quantitative? Effect of specimen shape," in *Scanning Microscopies 2011: Advanced Microscopy Technologies for Defense, Homeland Security, Forensic, Life, Environmental, and Industrial Sciences*, 2011, vol. 8036, p. 803602.

[109] "Standard Test Methods for Determination of Manganese (IV) in Manganese Ores by Redox Titrimetry." https://compass.astm.org/EDIT/html_annot.cgi?E465+11(2017) (accessed Oct. 28, 2019).

[110] J. P. De Villiers, "The crystal structure of braunite II and its relation to bixbyite and braunite," *Am. Mineral.*, vol. 65, no. 7–8, pp. 756–765, 1980.

[111] T. Kohler, T. Armbruster, and E. Libowitzky, "Hydrogen bonding and Jahn–Teller distortion in groutite, α-MnOOH, and manganite, γ-MnOOH, and their relations to the manganese dioxides ramsdellite and pyrolusite," *J. Solid State Chem.*, vol. 133, no. 2, pp. 486–500, 1997.

[112] C. Naganna, "Thermal study of some manganese oxide and hydrous oxide minerals," in *Proceedings of the Indian Academy of Sciences-Section A*, 1963, vol. 58, no. 1, pp. 16–28.

[113] M. Ksiazek, "The thermophysical properties of raw materials for ferromanganese production.," Dr. Ing thesis, NTNU, Trondheim, 2012.

[114] S. Blancher, "Geology and mining of the Comilog manganese ore body (Gabon)," presented at the 3rd School on Manganese Ferroalloy Production, Aug. 2020.

[115] O. Biørnstad, "Decrepitation of Comilog, Assman and UMK manganese ores during prereduction," MSc thesis, NTNU, 2020.

[116] G. L. de Faria, J. A. S. Tenório, N. Jannotti Jr, and F. da S. Araújo, "A geometallurgical comparison between lump ore and pellets of manganese ore," *Int. J. Miner. Process.*, vol. 137, pp. 59–63, 2015.

[117] M. Dhainaut, "Simulation of the electric field in a submerged arc furnace," in *Proceedings of the Tenth International Ferroalloy Congress*, 2004, pp. 605–613.

Appendix A   Weight behavior vs off-gas behavior

Abnormal weight behavior in the initial stages was observed for the majority of the experiments. For a few of the experiments, the mass balance recorded a decreasing weight from initiation of the experimental run. As the weight started to decrease before the temperature had started to increase in the sample, it is believed that the behavior was due to an error related to the balance. For the majority of the remaining experiments, a weight increase was observed in the initial stages, prior to any weight loss related to the sample. At a certain time and temperature, weight reduction due to sample reduction exceeded the weight gain due to drifting and an overall weight reduction is observed. As such, the weight recordings are the combined effect of drifting and reduction, and separation of the two is challenging as varying extent of drifting was observed for different experiments. This also complicates the assessment of the time and temperature at which reduction is initiated, as there will be a certain time period and temperature range where the weight increase due to drifting exceeds the weight loss due to reduction.

In order to confirm that the observed behavior was related to the mass balance and not the sample behavior, quartz was heated in argon from room temperature up to 1000°C at 6°C/min. Thus, this experiment was conducted with what can be viewed as an inert material and an inert gas atmosphere, implying that the weight should remain unchanged. Figure A.1 shows that the balance does an initial jump in the weight of 2 g and 2.5 g weight increase for the two runs, respectively. This is likely due to effects from the applied heating and/or the gas flow. From the new off-set point, it can be observed that the recorded weight show a continuous increase up to target temperature. The total recorded weight gains observed at 1000°C from the new off-set points were 4 g and 2.5 g, respectively. Hence, it is clear that the mass balance is subjected to inconsistent drifting, which will influence the TGA data obtained during the reduction experiments.
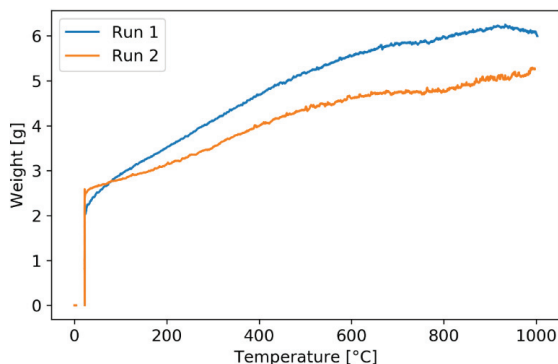
Figure A.1: Recorded weight during heating of quartz in 1 L/min argon gas

Due to this unreliable weight behavior, it was decided to utilize the off-gas analysis to describe the reduction behavior, where the specific procedure was described in section 3.3.1. Another benefit of relying on the

off-gas behavior compared to the mass balance values was that the mass balance showed larger extent of fluctuations compared to the off-gas values.

The following two subsections shows the comparison of the weight behavior data obtained from the mass balance and the off-gas analysis for Comilog and Nchwaning ore, respectively.

Comilog ore

An example of the inconsistent weight recordings are presented in Figure A.2, which shows the four investigated temperatures for Comilog ore in size fraction 3.33-4.00 mm heated at 6°C/min in 50% CO - 50% CO_2. As the only changed parameter was the target temperature, these experiments can be viewed as duplicates. For the experiment heated to 1200°C, a weight decrease is observed for all times and temperatures, including the very initial stages of the experiment where the sample temperature has not increased relative to room temperature. On the contrary, the experiment stopped at 500°C shows a clear increase in the recorded weight up to approximately 25 minutes process time, correlating to a sample temperature of 150°C, where it reaches a maximum of 4% weight increase. The experiment stopped at 800°C and 1000°C shows an intermediate behavior compared to 1200°C and 500°C. The weight remains relatively stable during the first 20 minutes process time, however a weight increase of 1-3% is observed.

For Comilog ore, the difference between the off-gas behavior and the weight behavior will be the removal of the chemically bound moisture. This removal results in a weight loss detected by the mass balance, however it is not detected by the off-gas analyzer, as any evaporated water escaping the crucible is condensed prior to the gas entering the analyzer.
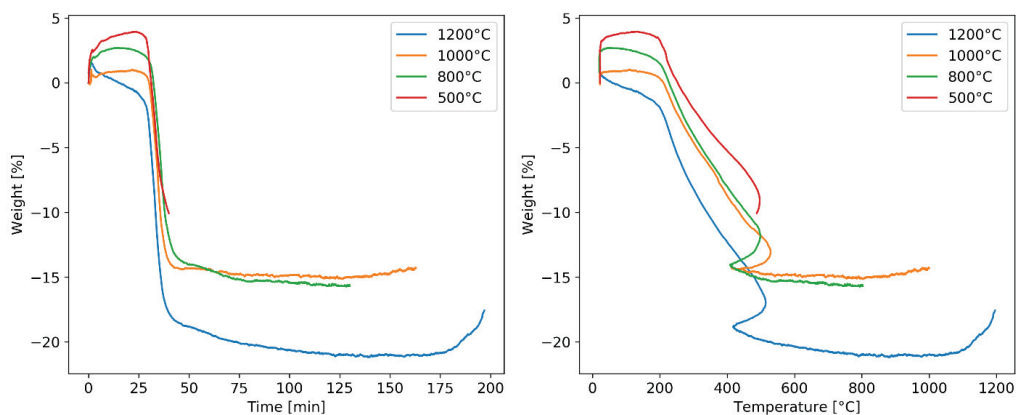
Figure A.2: Recorded weight for Comilog ore (3.33-4.00 mm) in 50%CO-50%CO₂
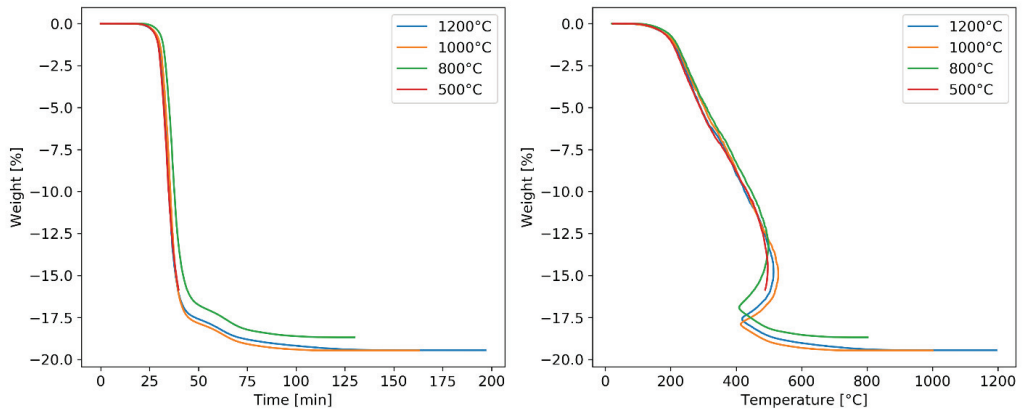
Figure A.3: Weight reduction behavior calculated from off-gas analysis normalized to total mass loss found from weighing sample prior and subsequent to reduction experiment

Nchwaning ore

Nchwaning ore does not contain any surface of chemically bound water, and as such, reactions related to the prereduction of Nchwaning ore will be registered by the off-gas composition. As such, if the extent of mass balance drifting is low, the behavior of the weight as recorded by the mass balance and the weight calculated from the off-gas analysis should show high correlation. This was observed in the experiment conducted with 30%CO-70%CO_2 with size fraction 11.20-15.00 mm, which is shown in Figure A.4. The correlating reaction rates, shown to the right, shows that he weight calculated from the off-gas exhibit a lower extent of fluctuations.
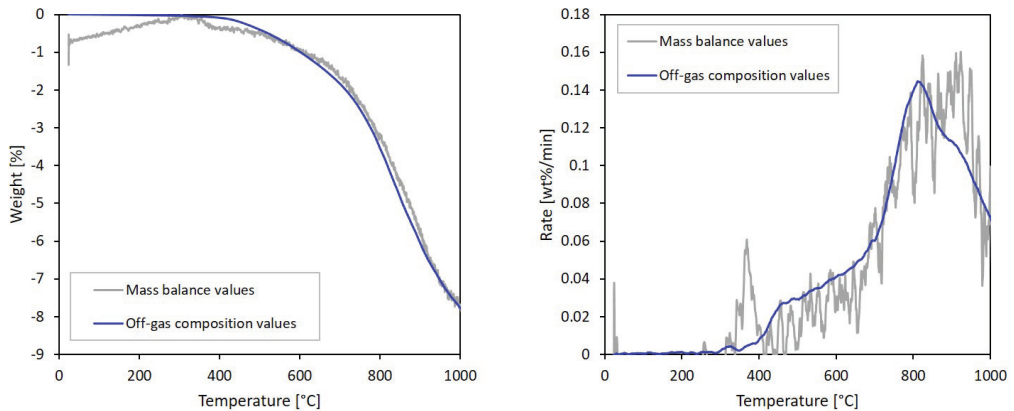
Figure A.4: Recorded weight and calculated weight behavior for Nchwaning ore (11.20-15.00 mm) in 30%CO-70%CO_2

Appendix B   Additional weight behavior data

As was stated in section 4.2.4, the weight reduction data obtained for Nchwaning ore reduced in CO-CO_2-H_2 and CO-CO_2-H_2O atmospheres were highly influenced by the drifting of the weight balance, potentially in combination with the left shifted Boudouard reaction. As such, the weight curves, and corresponding reaction rates are presented here.

Figure B.1 shows the weight behavior as given by the mass balance as function of time and temperature, respectively, for the experiments conducted in CO-CO_2 and CO-CO_2-H_2 atmospheres, where the composition of the CO-CO_2-H_2 atmospheres were calculated in order to correlate to the same theoretical oxygen pressures as the CO-CO_2 atmospheres. It is clearly seen that these experiments have been subjected to the previously mentioned drifting of the mass balance recordings, as all experiments show a continuous increase in the weight from the initial stages of the experimental runs.
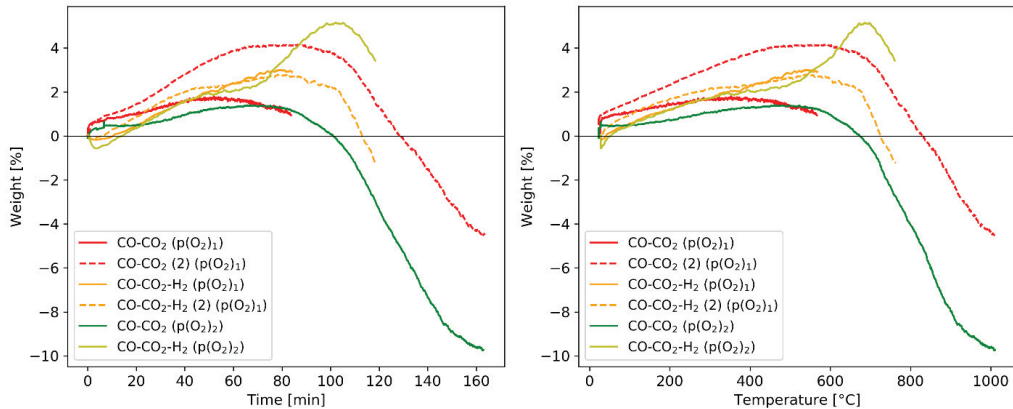
Figure B.1: Weight (as given by the mass balance recordings) as a function of time and temperature, respectively, for reduction experiments with Nchwaning ore in atmospheres based on CO-CO_2 and CO-CO_2-H_2 correlating to two distinct theoretical oxygen pressures

The majority of the curves exhibit a behavior that may be separated into three regions, i.e. an initial stage where the weight increases due to drifting, an intermediate stage where both weight increase due to drifting and weight decrease due to reduction occur simultaneously resulting in a relatively stable weight, and a final stage where the weight loss due to reduction dominates. The experiment conducted in CO-CO_2-H_2 composition correlating to the lowest theoretical oxygen pressure ($p(O_2)_2$) shows additional characteristics. This experiment is noted by the yellow curve in the figure, and it may be seen that the weight increase stage consists of two regions. The initial stages show a relatively slow weight increase, where the magnitude is similar to the other experiments, however a shift in the weight increase rate is observed at approximately 400-500°C. At this temperature, the weight starts to increase more rapidly up to peak at 690°C. A potential explanation is that the initial weight increase is due to drifting, and the change in rate at 500°C is due to the

left shifted Boudouard reaction, resulting in carbon deposition. Previous observations has shown that this reaction obtains sufficient kinetics at approximately 400°C in the experimental set ups used in this work. As such, in an attempt to present the weight behavior in a more representative manner, the weight values were shifted relative to the maximum obtained value at temperature range 25-400°C. The shifted weight curves are presented in Figure B.2. According to this figure, it is indicated that carbon deposition occurred in atmospheres containing hydrogen, where a lower oxygen pressure (increased amount of CO) in the atmosphere correlates to a higher extent of carbon deposition.
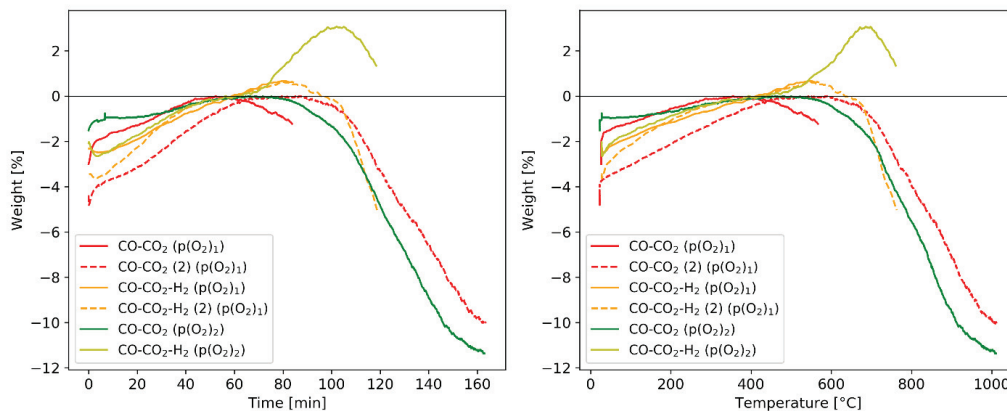
Figure B.2: Weight from mass balance recordings shifted relative to maximum obtained weight at temperatures 25-400°C as a function of time and temperature, respectively, for reduction experiments with Nchwaning ore in atmospheres based on CO-CO₂ and CO-CO₂-H₂ correlating to two distinct theoretical oxygen pressures

The reaction rates were calculated from the change in weight per minute interval from the values presented in Figure B.3. A high extent of fluctuation/noise is observed in the calculated reaction rate, where fluctuations are observed throughout. As these fluctuations are observed in all curves, including the ones not subjected to carbon deposition, it is believed that this is mainly due to the sensitivity of the mass balance combined with a low reaction rate, rather than an effect of any reactions related to gas or sample. The reaction rate starts to increase (indicating weight loss from reduction) at similar process time and temperature, i.e. approximately 550-600°C. A steeper slope is observed for experiments conducted with hydrogen compared to the corresponding atmospheres of CO-CO₂.

The shifted weight curves for the experiments conducted in CO-CO₂, CO-CO₂-H₂, and CO-CO₂-H₂O, respectively, where all compositions correlated to the same theoretical oxygen pressure, are shown in Figure B.4. The experiment conducted with water vapor shows an increase from the initiation of the experimental run similar to as the other experiments, however the rate of weight increase is considerably higher. The rapid weight increase subsides when the sample temperature reaches 100°C, from which the weight remains relatively stable at temperature range 100-230°C. As the rapid weight increase subsides at 100°C, it is suggested that the increasing weight is due to the water vapor that condenses as it is exposed to the sample. At temperatures exceeding 230°C, a two stage weight loss is observed. The weight decreases between 230-400°C, at which the weight remains stable until the temperature reaches approximately 500°C. If the increasing weight at temperatures below 100°C was due to the condensation of water vapor, it is likely that

the initial weight reduction stage is due to the evaporation of this condensed water. Further, the weight reduction stage initiated at 500°C is then assumed to be due to the reduction of oxides in the ore.
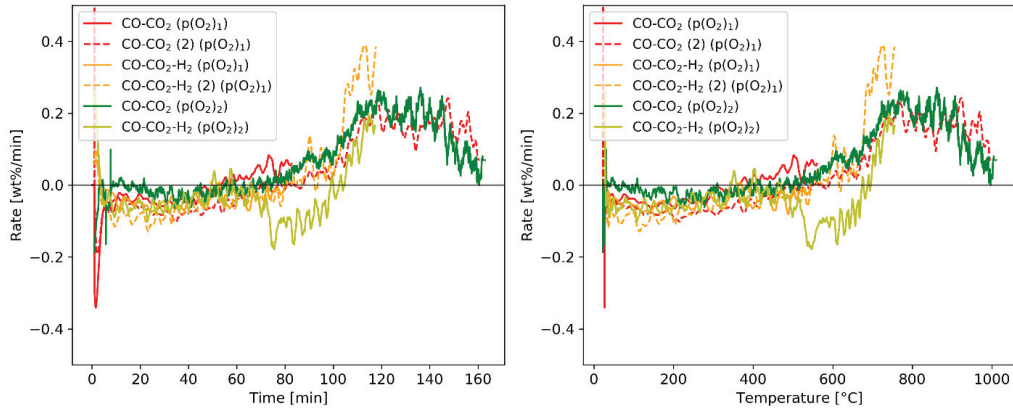
Figure B.3: Reaction rate [wt%/min] calculated from change in weight per two minute interval from values as given by mass balance for Nchwaning ore heated in CO-CO₂ and CO-CO₂-H₂ correlating to similar theoretical oxygen pressures

The reaction rate calculated from the change in weight per 2 minute intervals are presented in Figure B.5. A low reaction rate is observed throughout the experimental runs for all three atmospheres. In general, a high extent of fluctuations are observed, which complicates the identification of potential distinct reaction steps. The highest reaction rate is obtained in the experiment conducted with hydrogen, followed by CO-CO₂ atmosphere, and lastly by the experiment with water vapor.
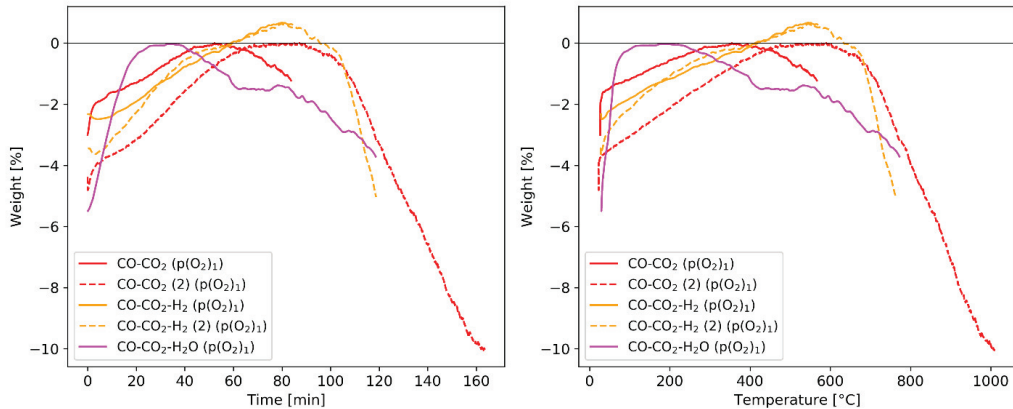
Figure B.4: Weight from mass balance recordings shifted relative to maximum obtained weight at temperatures 25-400°C as a function of time and temperature, respectively, for reduction experiments with Nchwaning ore in atmospheres based on CO-CO₂, CO-CO₂-H₂ and CO-CO₂-H₂O correlating to the same theoretical oxygen pressure
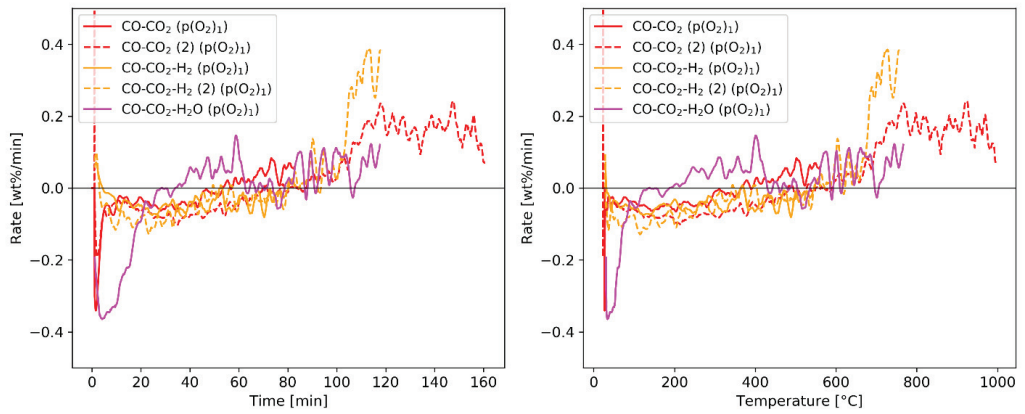
Figure B.5: Reaction rate [wt%/min] calculated from change in weight per two minute interval from values as given by mass balance for Nchwaning ore heated in $CO-CO_2$, $CO-CO_2-H_2$ and $CO-CO_2-H_2O$, respectively, correlating to similar theoretical oxygen pressures

Appendix C   XRD spectrums

This section shows the XRD spectrums with identified phases for both raw materials and reduced samples. XRD analyses were obtained using a D8 A25 DaVinci X-ray Diffractometer with CuKα-radiation. Mineral identification was performed using the PDF database in the BRUKER EVA Software.

Spectrums with identified phases are presented for the raw materials, as well as reduced samples subjected to isothermal and non-isothermal reduction.

Comilog ore

Raw material:
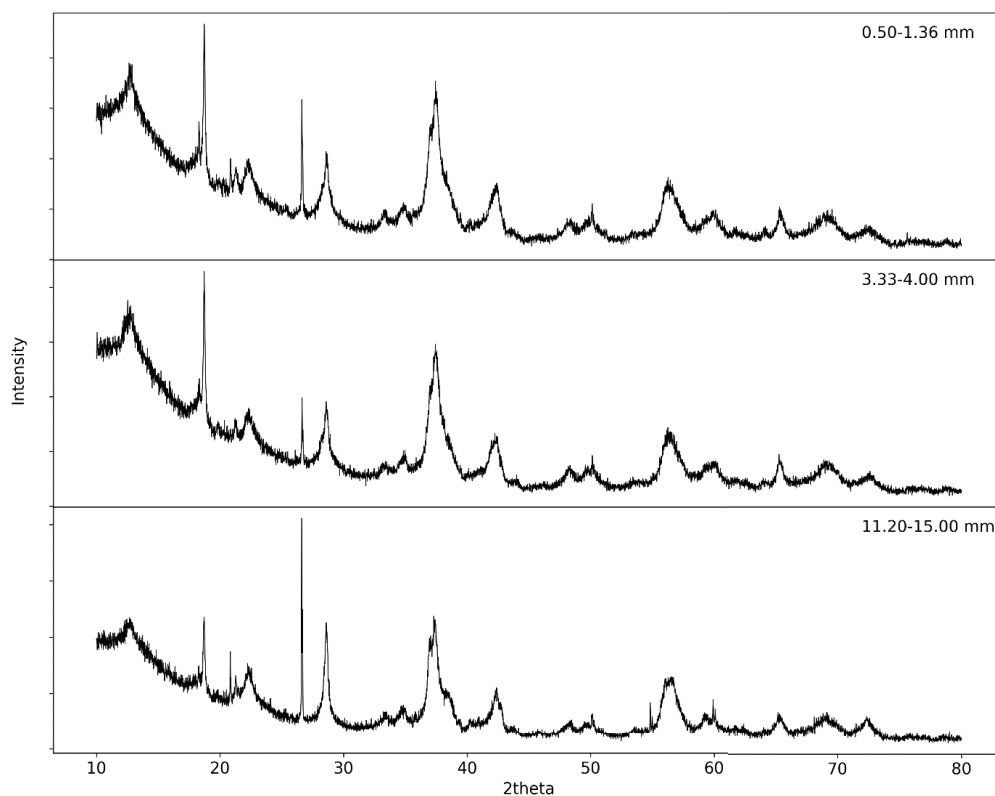
Figure C.1: XRD spectrum of Comilog ore in particle size 0.50-1.36 mm, 3.33-4.00 mm, and 11.20-15.00 mm, respectively
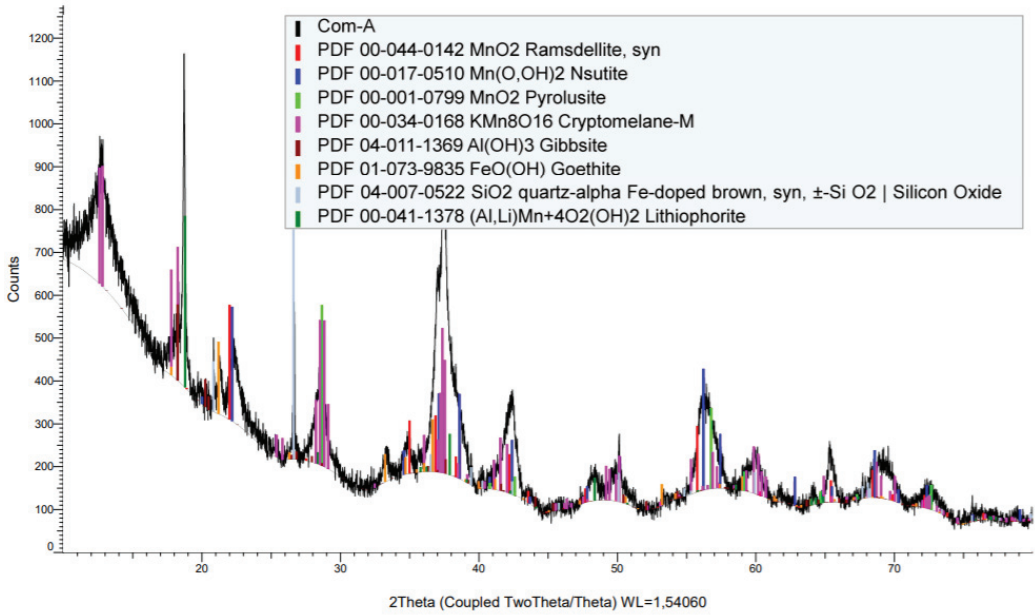
Figure C.2: XRD spectrum with phases identified using the PDF database in EVA Software for Comilog ore in particle size 0.50-1.36 mm
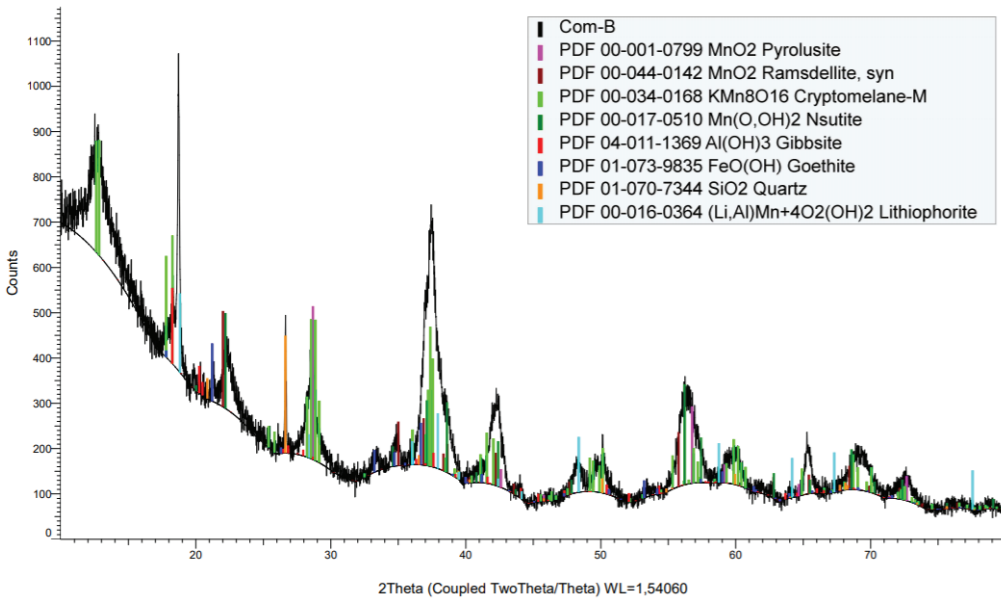
Figure C.3::XRD spectrum with phases identified using the PDF database in EVA Software for Comilog ore in particle size 3.33-4.00 mm

214

Reduced samples (non-isothermal reduction experiments):
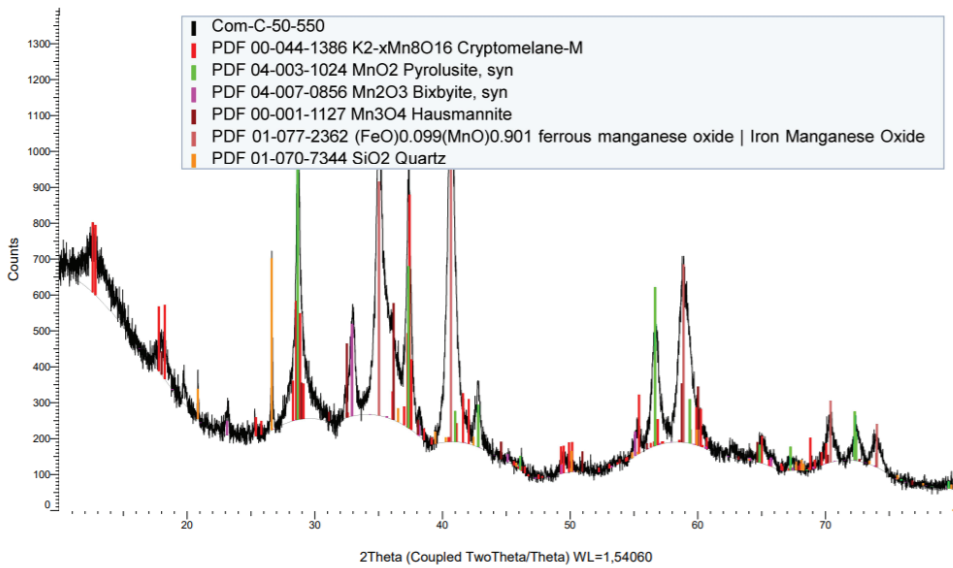
Figure C.4: XRD spectrum with phases identified using the PDF database in EVA Software for Comilog ore in particle size 11.20-15.00 mm heated at 6°C/min in 50%CO-50%CO2 at temperatures up to 550°C
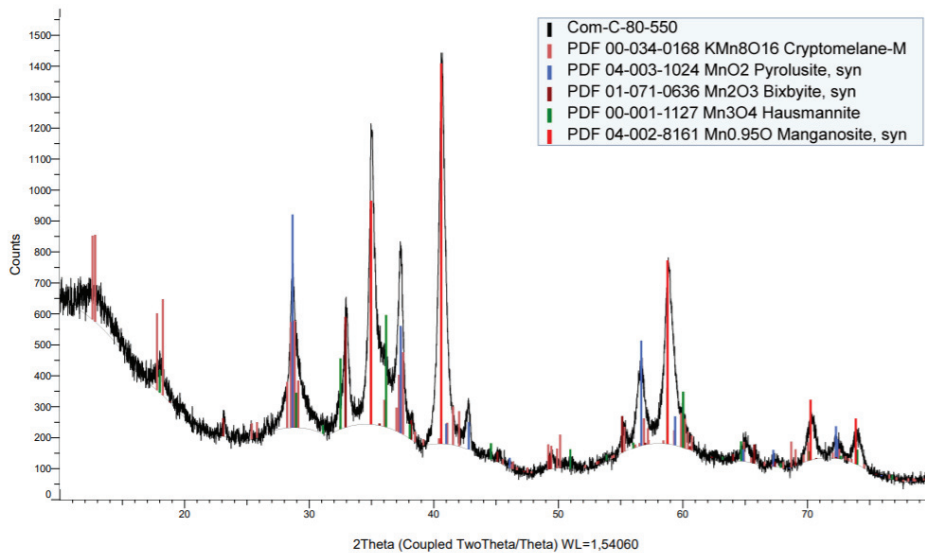
Figure C.5: XRD spectrum with phases identified using the PDF database in EVA Software for Comilog ore in particle size 11.20-15.00 mm heated at 6°C/min in 80%CO-20%CO2 at temperatures up to 550°C

Nchwaning ore

Raw material:
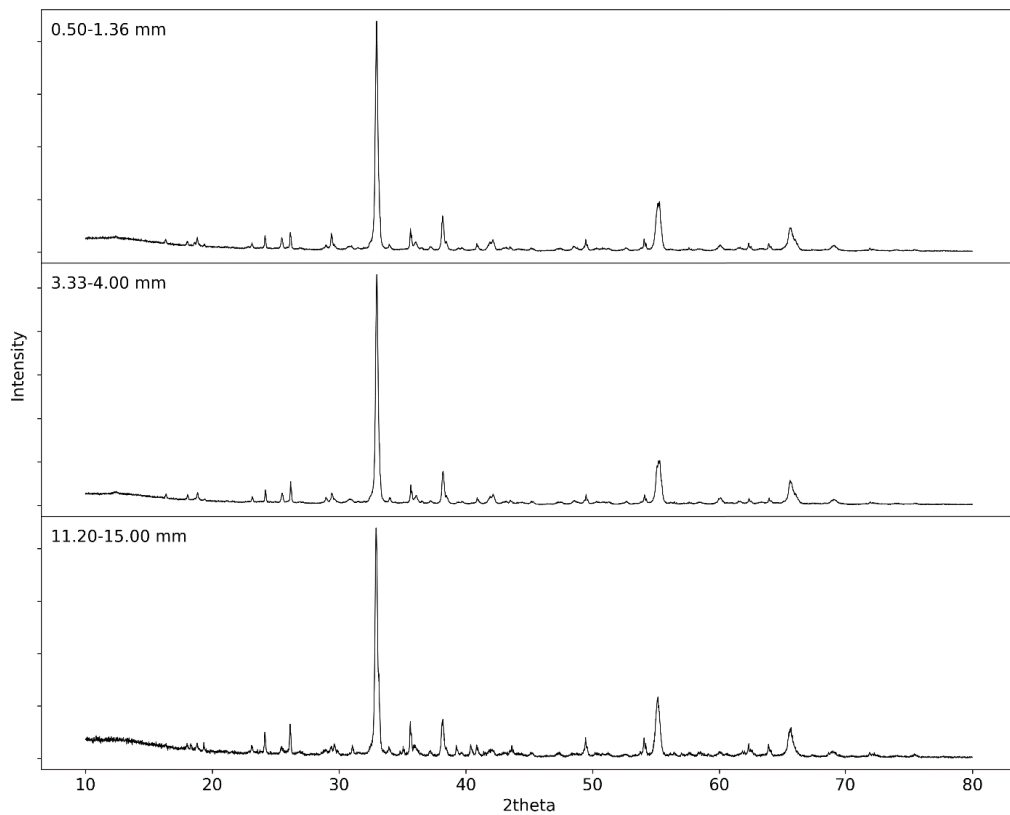
Figure C.6: XRD spectrum of Nchwaning ore in particle size 0.50-1.36 mm, 3.33-4.00 mm, and 11.20-15.00 mm, respectively
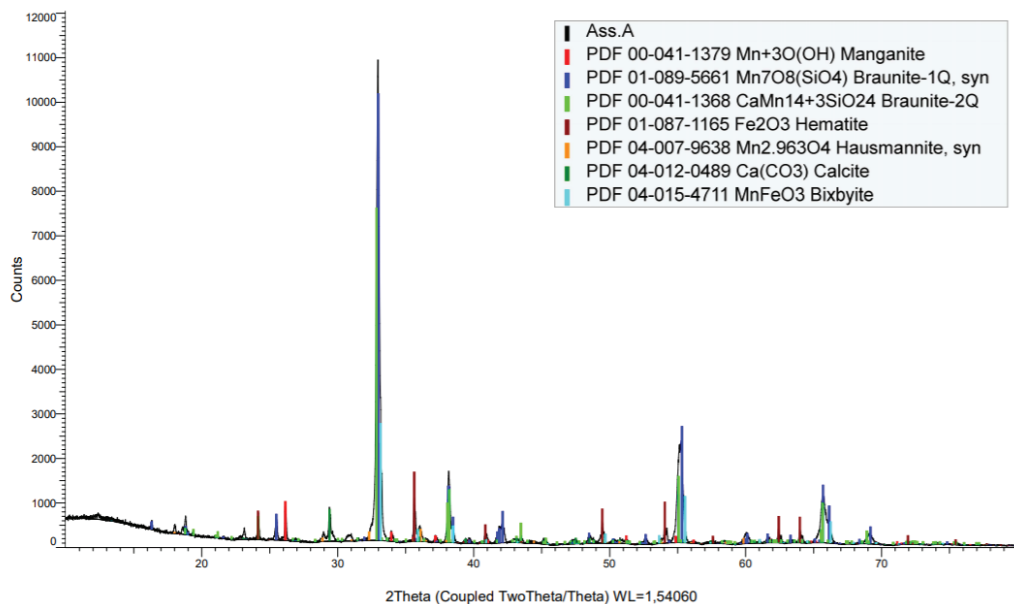
Figure C.7: XRD spectrum with phases identified using the PDF database in EVA Software for Nchwaning (Assmang) ore in particle size 0.50-1.36 mm
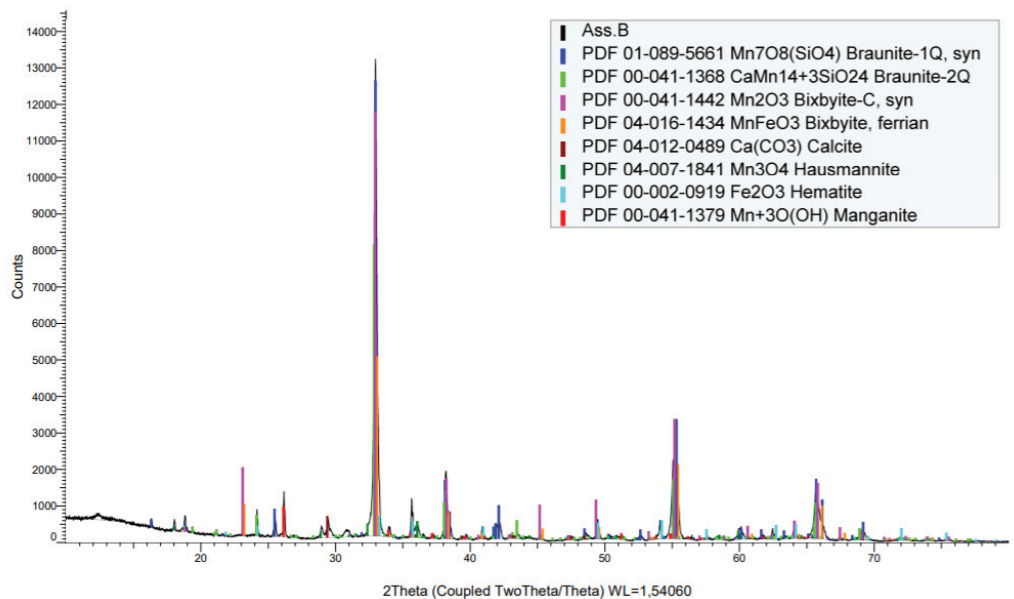
Figure C.8: XRD spectrum with phases identified using the PDF database in EVA Software for Nchwaning (Assmang) ore in particle size 3.33-4.00 mm
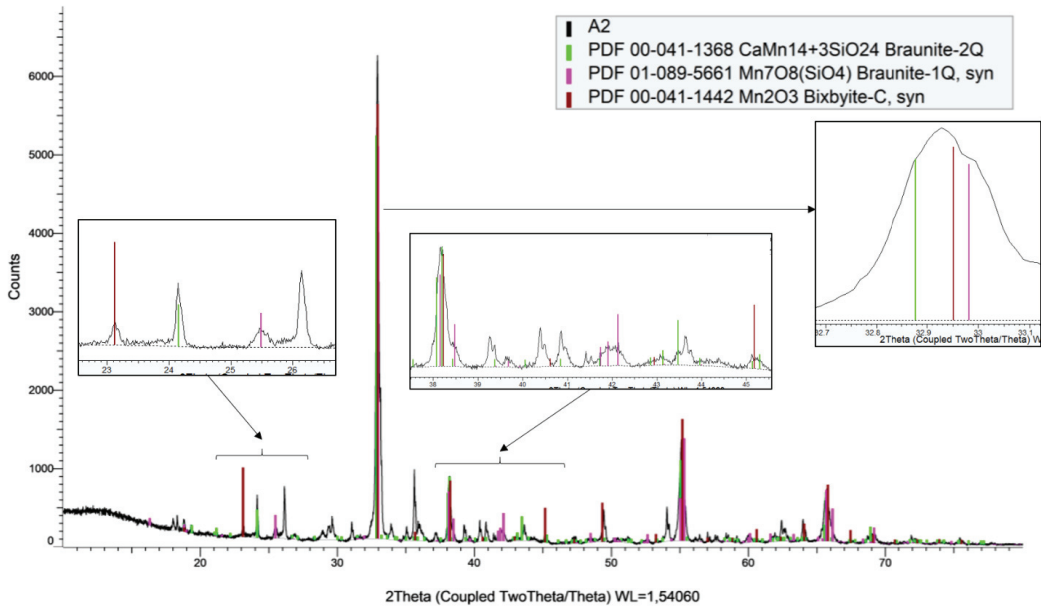
Figure C.9: XRD spectrum of Assmang ore (11.20-15.00 mm) with XRD patterns of bixbyite, braunite and braunite II

Reduced samples (non-isothermal reduction experiments in DisVaDri furnace):
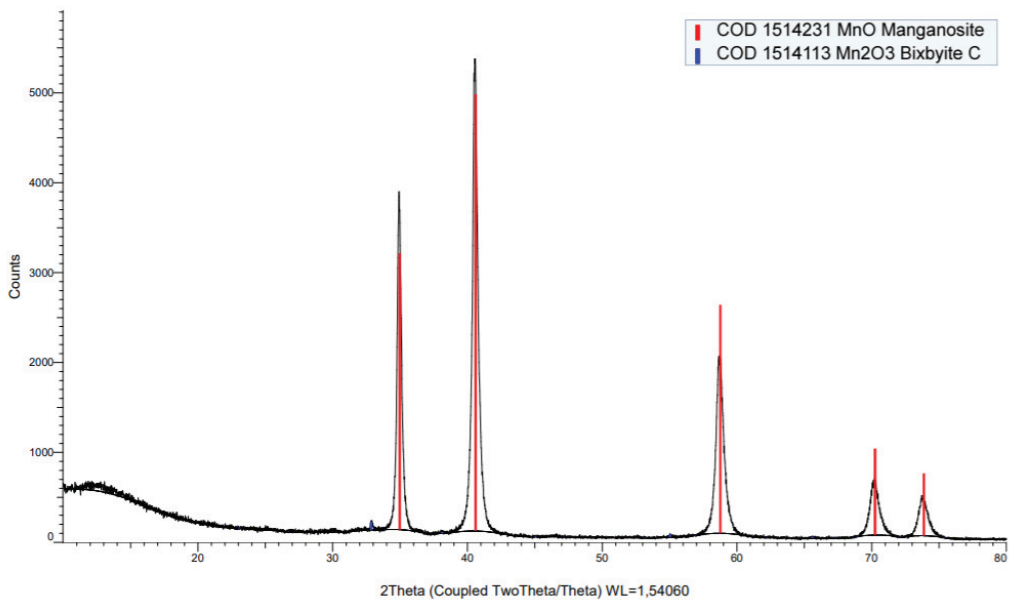
Figure C.10: Nchwaning ore in size fraction 30-40 mm heated to 1000°C in 50%CO-50%CO₂. Particle of black color
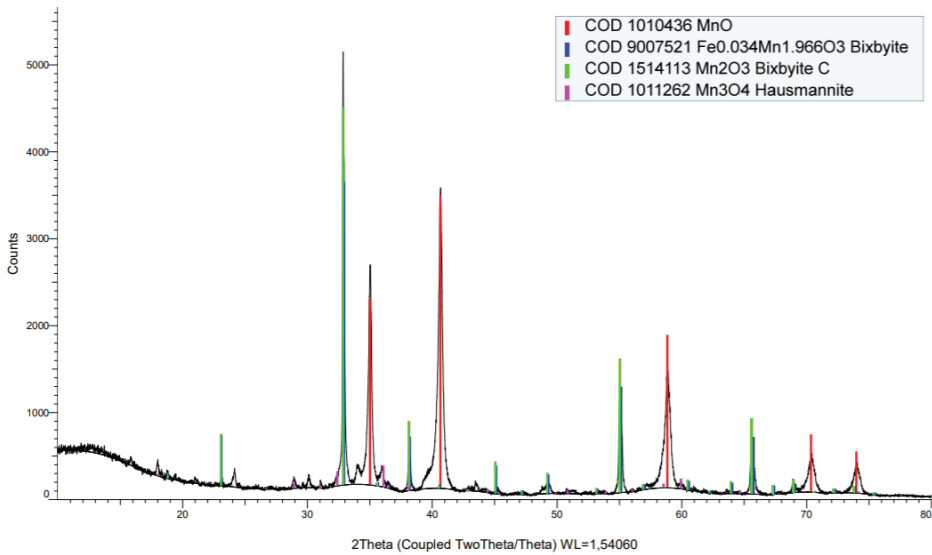
Figure C.11: Nchwaning ore in size fraction 30-40 mm heated to 1000°C in 50%CO-50%CO₂. Particle of green color

Reduced samples (isothermal reduction experiments in Tammann furnace):
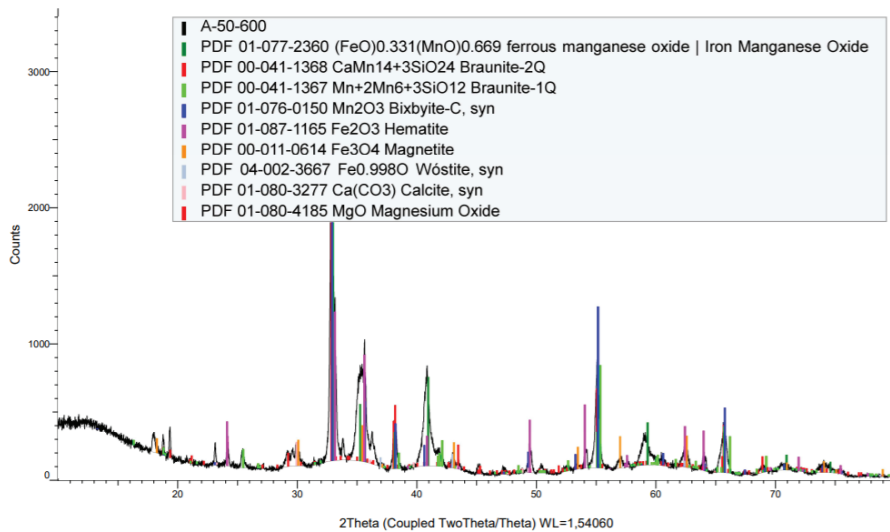
Figure C.12: Nchwaning ore (11.20-15.00 mm) reduced in Tammann furnace in 50%CO-50%CO₂ at 600°C for 60 minutes
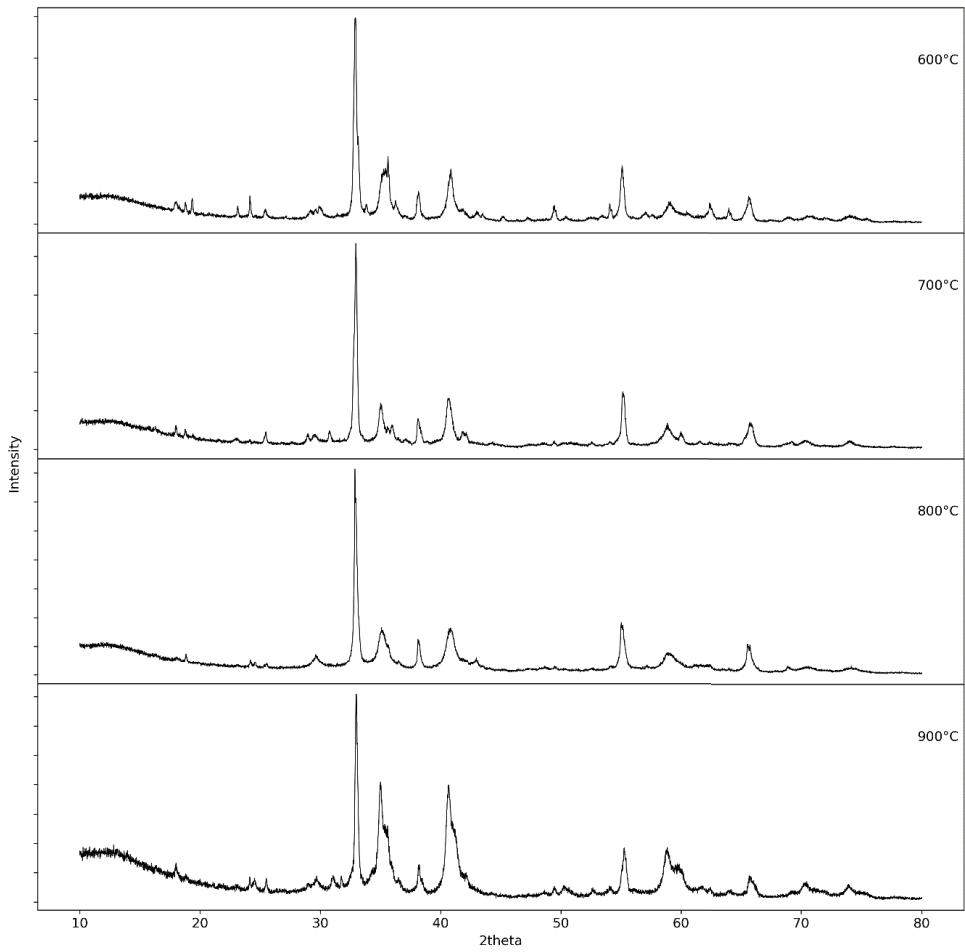
Figure C.13: XRD spectrum of Nchwaning ore (11.20-15.00 mm) reduced in 50%CO-50%CO₂ at 600°C, 700°C, 800°C, and 900°C, respectively. Samples from reduction experiments in Tammann furnace

Appendix D   Weight loss values

Weight loss from experiments in DisVadri furnace:

Table D.1: Overview of weight loss of Comilog ore non-isothermally in CO-CO$_2$ atmosphere

Size [mm]	%CO	Temperature	Weight in [g]	Weight out [g]	Loss [g]	Loss [%]
0.5-1.36	50	1000°C	74.98	60.20	14.18	19.71
0.5-1.36	80	1000°C	75.07	59.79	15.28	20.35
3.33-4.00	50	500°C	75.00	63.11	11.89	15.85
3.33-4.00	50	800°C	75.05	61.03	14.02	18.68
3.33-4.00	50	1000°C	72.02	60.43	14.59	19.45
3.33-4.00	80	360°C	75.02	68.01	7.01	9.34
3.33-4.00	80	790°C	75.05	60.86	14.19	18.91
3.33-4.00	80	1000°C	75.00	60.20	14.82	19.76
11.2-15.0	30	1000°C	76.43	61.67	14.77	19.32
11.2-15.0	40	1000°C	76.45	61.68	14.77	19.32
11.2-15.0	50	400°C	74.96	70.76	4.21	5.61
11.2-15.0	50	550°C	74.81	66.43	8.38	11.20
11.2-15.0	50	1000°C	75.31	60.26	15.05	19.99
11.2-15.0	80	550°C	75.20	65.65	9.55	12.70
11.2-15.0	80	1000°C	75.09	60.29	14.81	19.72
30.0-40.0	50	800°C	77.20	62.76	14.44	18.70

Table D.2: Overview of weight loss of Comilog ore non-isothermally in CO-CO$_2$-H$_2$O-H$_2$-atmosphere

Gas	Furnace temperature [°C]	Weight in [g]	Weight out [g]	Loss [g]	Loss [%]
CO:CO$_2$ (p(O$_2$)$_1$)	500	76.40	64.02	12.38	16.21
CO:CO$_2$:H$_2$ (p(O$_2$)$_1$)	400	75.60	63.77	11.84	15.65
CO:CO$_2$:H$_2$ (p(O$_2$)$_1$)	500	75.63	62.84	12.79	16.91
CO:CO$_2$:H$_2$O (p(O$_2$)$_1$)	500	74.63	61.67	12.97	17.38
CO:CO$_2$:H$_2$ (p(O$_2$)$_2$)	500	76.00	63.14	12.86	16.92

Table D.3: Overview of weight loss of Nchwaning ore non-isothermally in CO-CO$_2$-H$_2$O-H$_2$-atmosphere

Gas	Furnace temperature [°C]	Weight in [g]	Weight out [g]	Loss [g]	Loss [%]
CO:CO$_2$ (p(O$_2$)$_1$)	500	75.75	74.82	0.93	1.23
CO:CO$_2$:H$_2$ (p(O$_2$)$_1$)	500	75.33	75.31	0.03	0.03
CO:CO$_2$:H$_2$ (p(O$_2$)$_1$)	700	75.10	71.15	3.95	5.26
CO:CO$_2$:H$_2$O (p(O$_2$)$_1$)	700	74.94	72.00	2.94	3.92
CO:CO$_2$:H$_2$ (p(O$_2$)$_2$)	700	74.65	71.20	3.45	4.62

Table D.4: Overview of weight loss of Nchwaning ore non-isothermally in CO-CO₂ atmosphere

Size [mm]	%CO	Temperature [°C]	Weight in [g]	Weight out [g]	Loss [g]	Loss [%]
0.5-1.36	50	1000°C	75.00	66.00	9.00	12.00
0.5-1.36	80	1000°C	75.04	65.20	9.84	13.11
3.33-4.00	50	300°C	75.02	74.85	0.17	0.23
3.33-4.00	50	800°C	75.04	68.31	6.73	8.97
3.33-4.00	50	1000°C	74.99	66.33	8.66	11.55
3.33-4.00	80	800°C	75.01	67.80	7.21	9.61
3.33-4.00	80	1000°C	75.07	66.01	9.06	12.07
11.20-15.00	30	1000°C	75.04	69.12	5.92	7.89
11.20-15.00	50	570°C	75.75	74.82	0.93	1.23
11.20-15.00	50	800°C	75.37	70.29	5.08	6.73
11.20-15.00	50	1000°C	75.01	67.47	7.54	10.05
11.20-15.00	80	816°C	74.80	71.24	3.55	4.75
11.20-15.00	80	1000°C	75.27	66.71	8.55	11.36
30.00-40.00	50	800°C	75.46	73.44	2.01	2.67
30.00-40.00	50	1000°C	75.21	68.58	6.63	8.81

Weight loss from experiments in Tammann furnace:

Table D.5: Overview of weight loss of Nchwaning ore reduced isothermally in Tammann furnace at 600-900°C

Ore	Gas	[°C]	Time [min]	Weight in [g]	Weight out [g]	Loss [g]	Loss [%]
Nchwaning	50%CO+50%CO₂	600	60 (1)	23.94	22.99	0.95	3.98
Nchwaning	50%CO+50%CO₂	600	60 (2)	25.34	25.22	0.13	0.50
Nchwaning	50%CO+50%CO₂	600	30 (1)	24.63	24.61	0.02	0.08
Nchwaning	50%CO+50%CO₂	700	60 (1)	26.87	26.45	0.43	1.58
Nchwaning	50%CO+50%CO₂	700	60 (2)	25.22	23.84	1.36	5.40
Nchwaning	50%CO+50%CO₂	700	30 (1)	25.44	20.46	4.99	19.59
Nchwaning	50%CO+50%CO₂	700	30 (1)	22.98	19.71	3.27	14.23
Nchwaning	50%CO+50%CO₂	800	60 (1)	24.30	20.75	4.49	17.79
Nchwaning	50%CO+50%CO₂	800	30 (1)	25.24	21.38	2.00	8.54
Nchwaning	50%CO+50%CO₂	800	30 (2)	23.38	25.81	0.40	1.52
Nchwaning	50%CO+50%CO₂	800	30 (3)	26.21	19.31	2.21	10.26
Nchwaning	50%CO+50%CO₂	800	30 (4)	21.52	21.26	3.04	12.53
Nchwaning	50%CO+50%CO₂	900	30 (1)	21.30	17.86	3.44	16.17
Nchwaning	50%CO+50%CO₂	900	30 (2)	18.21	16.42	1.79	9.84
Nchwaning	70%CO+30%CO₂	600	60 (1)	22.82	22.17	0.65	2.87
Nchwaning	70%CO+30%CO₂	700	60 (1)	23.83	0.65	0.69	2.89
Nchwaning	70%CO+30%CO₂	700	30 (1)	24.84	20.73	4.10	16.51
Nchwaning	70%CO+30%CO₂	700	30 (2)	27.41	25.65	1.76	6.41
Nchwaning	70%CO+30%CO₂	800	60 (1)	22.62	21.12	1.49	6.60
Nchwaning	70%CO+30%CO₂	800	30 (1)	21.85	19.55	2.30	10.54

Table D.6: Overview of weight loss of Comilog ore reduced isothermally in Tammann furnace at 600-900°C

Ore	Gas	Temperature [°C]	Time [min]	Weight in [g]	Weight out [g]	Loss [g]	Loss [%]
Comilog	50%CO+50%CO$_2$	400	40 (1)	19.00	17.36	1.63	8.60
Comilog	50%CO+50%CO$_2$	500	40 (1)	22.57	20.23	2.34	10.37
Comilog	50%CO+50%CO$_2$	500	40 (2)	16.00	14.23	1.77	11.09
Comilog	50%CO+50%CO$_2$	500	40 (3)	18.20	16.06	2.15	11.79
Comilog	50%CO+50%CO$_2$	500	20 (1)	22.23	20.85	1.39	6.23
Comilog	50%CO+50%CO$_2$	550	40 (1)	15.48	13.91	1.58	10.18
Comilog	50%CO+50%CO$_2$	550	30 (1)	17.64	13.61	4.03	22.87
Comilog	50%CO+50%CO$_2$	550	30 (2)	19.94	15.62	4.32	21.68
Comilog	50%CO+50%CO$_2$	550	30 (3)	21.09	18.18	2.91	13.80
Comilog	50%CO+50%CO$_2$	600	40 (1)	16.72	13.81	2.92	17.43
Comilog	50%CO+50%CO$_2$	600	40 (2)	17.89	15.44	2.45	13.69
Comilog	50%CO+50%CO$_2$	600	20 (1)	19.54	15.39	4.16	21.28
Comilog	50%CO+50%CO$_2$	600	20 (2)	18.64	16.43	2.21	11.85
Comilog	70%CO+30%CO$_2$	400	40 (1)	18.33	15.92	2.41	13.16
Comilog	70%CO+30%CO$_2$	400	40 (2)	22.05	19.64	2.41	10.94
Comilog	70%CO+30%CO$_2$	400	20 (1)	19.47	17.92	1.55	7.98
Comilog	70%CO+30%CO$_2$	400	20 (2)	26.64	24.66	1.98	7.42
Comilog	70%CO+30%CO$_2$	500	40 (1)	18.20	15.92	2.28	12.54
Comilog	70%CO+30%CO$_2$	500	40 (2)	19.80	16.78	3.02	15.26
Comilog	70%CO+30%CO$_2$	500	20 (1)	19.27	17.40	1.87	9.72
Comilog	70%CO+30%CO$_2$	600	40 (1)	19.24	11.12	8.12	42.18
Comilog	70%CO+30%CO$_2$	600	40 (2)	21.99	17.74	4.25	19.33

Appendix E   Rate curves from modelling (non-isothermal data)

In section 5.2, the experimental conversion curves were presented together with the model results. The reaction rate curves from the experimental data and model data are presented in this section.

Comilog ore
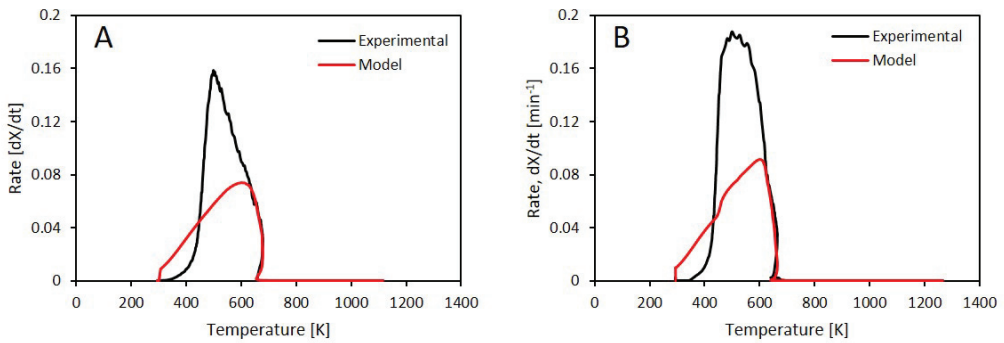
Figure E.1: Reaction rates from experimental data compared to reaction rates from modelled data for Comilog ore in size fraction 0.50-1.36 mm reduced in A: 50%CO-50%CO₂ and B: 80%CO-20%CO₂. Heated at 6°C/min up to 1000°C
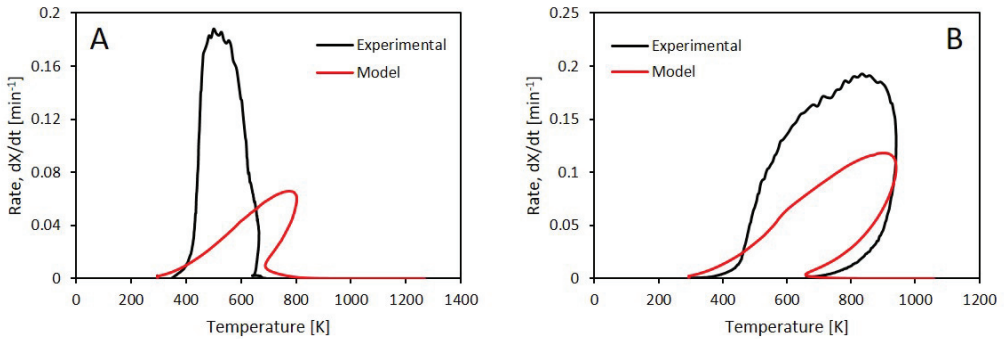
Figure E.2:: Reaction rates from experimental data compared to reaction rates from modelled data for Comilog ore in size fraction 3.33-4.00 mm reduced in A: 50%CO-50%CO₂ and B: 80%CO-20%CO₂. Heated at 6°C/min up to 1000°C
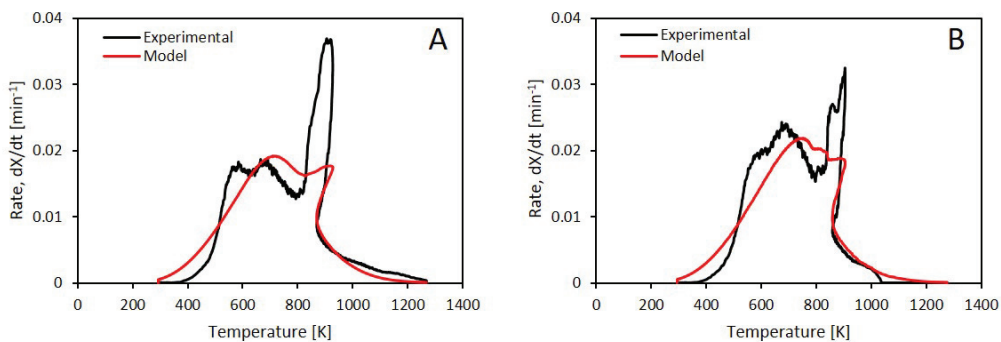
Figure E.3:: Reaction rates from experimental data compared to reaction rates from modelled data for Comilog ore in size fraction 11.20-15.00 mm reduced in A: 50%CO-50%CO2 and B: 80%CO-20%CO2. Heated at 6°C/min up to 1000°C
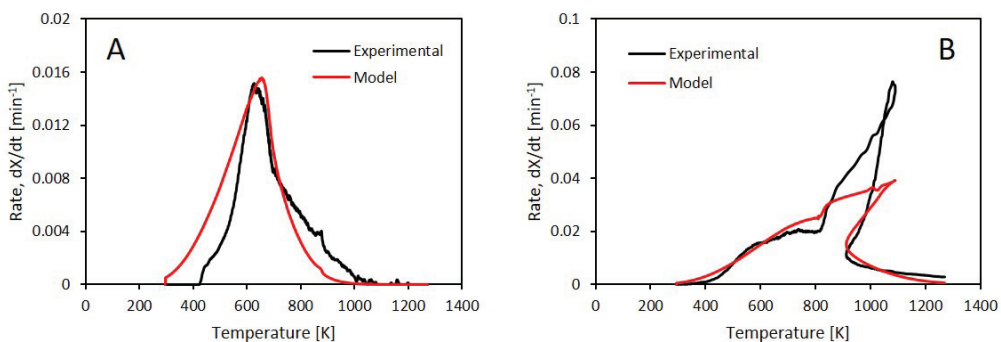
Figure E.4: Reaction rates from experimental data compared to reaction rates from modelled data for Comilog ore in size fraction 11.20-15.00 mm reduced in 50%CO-50%CO2 at A: 3°C/min and B: 9°C/min
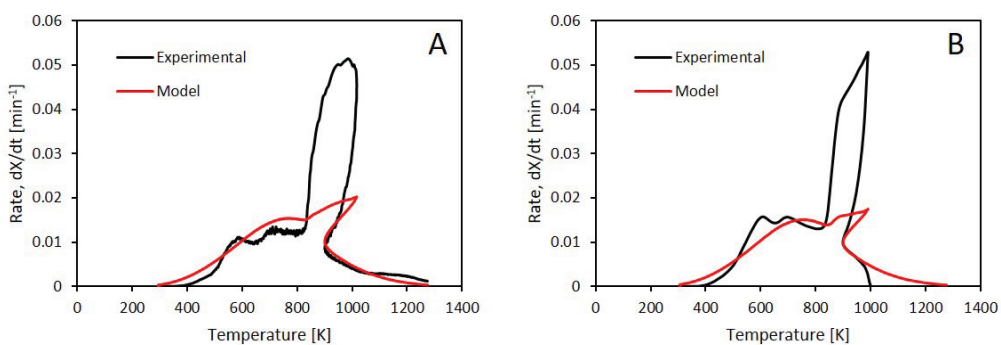
Figure E.5: Reaction rates from experimental data compared to reaction rates from modelled data for Comilog ore in size fraction 11.20-15.00 mm reduced in A: 30%CO-70%CO2 and B: 40%CO-60%CO2. Heated at 6°C/min up to 1000°C
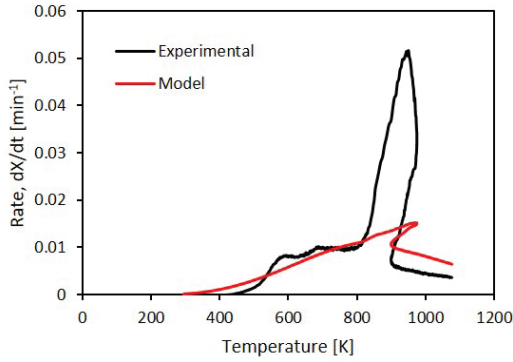
Figure E.6: Reaction rates from experimental data compared to reaction rates from modelled data for Comilog ore in size fraction 30-40 mm in 50%CO-50%CO₂ at 6°C/min at 25-1000°C

Nchwaning ore
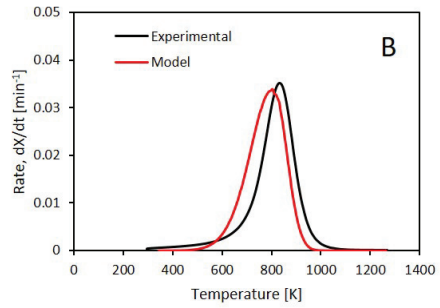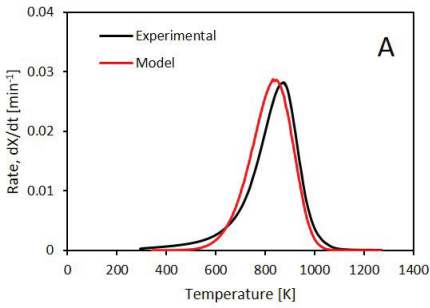
Figure E.7: Reaction rates from experimental data compared to reaction rates from modelled data for Nchwaning ore in size fraction 0.50-1.36 mm reduced in A: 50%CO-50%CO₂ and B: 80%CO-20%CO₂. Heated at 6°C/min up to 1000°C
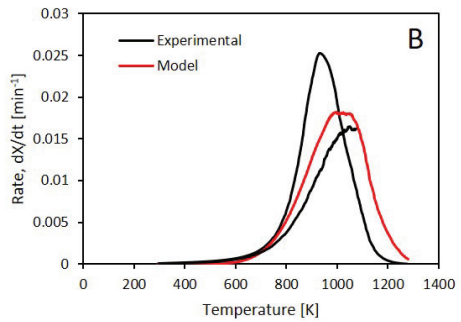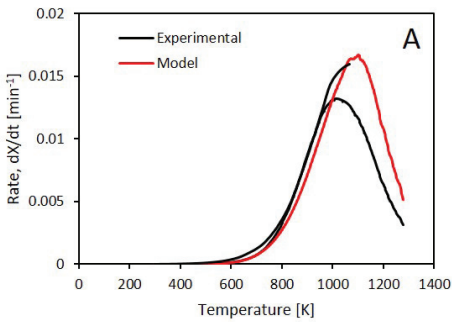
Figure E.8: Reaction rates from experimental data compared to reaction rates from modelled data for Nchwaning ore in size fraction 11.20-15.00 mm reduced in A: 50%CO-50%CO₂ and B: 80%CO-20%CO₂. Heated at 6°C/min up to 1000°C

227
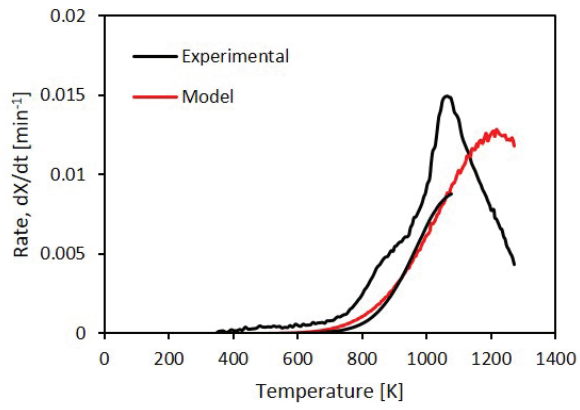
Figure E.9: Reaction rates from experimental data compared to reaction rates from modelled data for Nchwaning ore in size fraction 30-40 mm in 50%CO-50%CO₂ at 6°C/min at 25-1000°C

NTNU
Norwegian University of
Science and Technology